frontiers | Research Topics

Advances in PET-CT imaging

Edited by
Nataliya Lutay and Francesco Dondi

Published in
Frontiers in Medicine
Frontiers in Neuroimaging

ISSN 1664-8714
ISBN 978-2-8325-7232-0
DOI 10.3389/978-2-8325-7232-0

Generative AI statement
Any alternative text (Alt text) provided alongside figures in the articles in this ebook has been generated by Frontiers with the support of artificial intelligence and reasonable efforts have been made to ensure accuracy, including review by the authors wherever possible. If you identify any issues, please contact us.

About Frontiers

Frontiers is more than just an open access publisher of scholarly articles: it is a pioneering approach to the world of academia, radically improving the way scholarly research is managed. The grand vision of Frontiers is a world where all people have an equal opportunity to seek, share and generate knowledge. Frontiers provides immediate and permanent online open access to all its publications, but this alone is not enough to realize our grand goals.

Frontiers journal series

The Frontiers journal series is a multi-tier and interdisciplinary set of open-access, online journals, promising a paradigm shift from the current review, selection and dissemination processes in academic publishing. All Frontiers journals are driven by researchers for researchers; therefore, they constitute a service to the scholarly community. At the same time, the *Frontiers journal series* operates on a revolutionary invention, the tiered publishing system, initially addressing specific communities of scholars, and gradually climbing up to broader public understanding, thus serving the interests of the lay society, too.

Dedication to quality

Each Frontiers article is a landmark of the highest quality, thanks to genuinely collaborative interactions between authors and review editors, who include some of the world's best academicians. Research must be certified by peers before entering a stream of knowledge that may eventually reach the public - and shape society; therefore, Frontiers only applies the most rigorous and unbiased reviews. Frontiers revolutionizes research publishing by freely delivering the most outstanding research, evaluated with no bias from both the academic and social point of view. By applying the most advanced information technologies, Frontiers is catapulting scholarly publishing into a new generation.

What are Frontiers Research Topics?

Frontiers Research Topics are very popular trademarks of the *Frontiers journals series*: they are collections of at least ten articles, all centered on a particular subject. With their unique mix of varied contributions from Original Research to Review Articles, Frontiers Research Topics unify the most influential researchers, the latest key findings and historical advances in a hot research area.

Find out more on how to host your own Frontiers Research Topic or contribute to one as an author by contacting the Frontiers editorial office: frontiersin.org/about/contact

Advances in PET-CT imaging

Topic editors
Nataliya Lutay — Skåne University Hospital, Sweden
Francesco Dondi — Università degli Studi di Brescia, Italy

Citation
Lutay, N., Dondi, F., eds. (2025). *Advances in PET-CT imaging*.
Lausanne: Frontiers Media SA. doi: 10.3389/978-2-8325-7232-0

Table of contents

05 Editorial: Advances in PET-CT imaging
Francesco Dondi

08 Comprehensive literature review of oral and intravenous contrast-enhanced PET/CT: a step forward?
Gilles Metrard, Clara Cohen and Matthieu Bailly

17 Association between vascular FDG uptake during follow-up and the development of thoracic aortic aneurysms in giant cell arteritis
Daniel Blockmans, Lien Moreel, Albrecht Betrains, Steven Vanderschueren, Walter Coudyzer, Lennert Boeckxstaens and Koen Van Laere

24 Diagnostic yield of FAP-guided positron emission tomography in thyroid cancer: a systematic review
Alessio Rizzo, Domenico Albano, Francesco Dondi, Martina Cioffi, Barbara Muoio, Salvatore Annunziata, Manuela Racca, Francesco Bertagna, Arnoldo Piccardo and Giorgio Treglia

35 Preliminary evidence of localizing CD8+ T-cell responses in COVID-19 patients with PET imaging
Hans J. P. M. Koenen, Ilse J. E. Kouijzer, Michel de Groot, Steffie Peters, Daphne Lobeek, Evelien A. J. van Genugten, Dimitri A. Diavatopoulos, Nienke van Oosten, Sanne Gianotten, Mathias M. Prokop, Mihai G. Netea, Frank L. van de Veerdonk and Erik H. J. G. Aarntzen

43 Multimodal imaging findings of primary liver clear cell carcinoma: a case presentation
Xianwen Hu, Xiaotian Li, Wei Zhao, Jiong Cai and Pan Wang

50 Case report: A rare case of isolated sigmoid Rosai-Dorfman disease on contrast-enhanced CT and ^{18}F-FDG PET/CT
Wanling Qi, Zhehuang Luo, Mingyan Shao, Min Chen, Fengxiang Liao and Linfeng Hu

55 ^{68}Ga-PSMA-11 PET and mpMRI in the diagnosis of initial lymph node staging of prostate cancer: a head-to-head comparative meta-analysis
Yuanrong Wang, Ren Jing, Haiyan Wang and Qiuyan Zhao

68 Clinical and imaging features of pulmonary mixed squamous cell and glandular papilloma: a case report and literature review
Xianwen Hu, Wei Zhao, Fangming Li, Pan Wang and Jiong Cai

75 Imaging findings of inflammatory myofibroblastic tumor of sigmoid colon: literature review and case report
Xianwen Hu, Wei Zhao, Ronghua Yu and Pan Wang

81 Detection of cardiac neuroendocrine tumour metastases by somatostatin receptor PET/CT: a systematic review and meta-analysis
Daniela Campanale, Alessio Imperiale, Domenico Albano, Alessio Rizzo, Arnoldo Piccardo and Giorgio Treglia

92 Impact of fat intake on [^{18}F]AlF-NOTA-FAPI-04 uptake in normal abdominal organs
Jiashun Dai, Wanjing Zhou, Huaping Liu, Chengzhi Jiang and Hui Ye

100 [^{18}F]FDG PET/CT versus [^{18}F]FDG PET/MRI in staging of non-small cell lung cancer: a head-to-head comparative meta-analysis
Dandan Yu and Chaolin Chen

110 Diagnostic efficacy and necessity of 18F-FDG PET/CT in fever of unknown origin: insights from a retrospective cohort study
Xiaoman Yu, Shuang Wang, Na Du, Hongguang Zhao and Haiying Chen

125 Ultra-low dose immunoPET using ^{64}Cu-rituximab tracer for a human CD20 mouse model
Frezghi Habte and Arutselvan Natarajan

132 Assessing the accuracy of automated CT perfusion software in excluding acute stroke: a comparative study of two software packages
Maximilian Thormann, Maria Faltass, Roland Schwab, Stefan Klebingat and Daniel Behme

frontiers | Frontiers in Medicine

TYPE Editorial
PUBLISHED 29 October 2025
DOI 10.3389/fmed.2025.1722348

OPEN ACCESS

EDITED AND REVIEWED BY
Giorgio Treglia,
Ente Ospedaliero Cantonale (EOC), Switzerland

*CORRESPONDENCE
Francesco Dondi
francesco.dondi@unibs.it

RECEIVED 10 October 2025
ACCEPTED 15 October 2025
PUBLISHED 29 October 2025

CITATION
Dondi F (2025) Editorial: Advances in PET-CT imaging. *Front. Med.* 12:1722348. doi: 10.3389/fmed.2025.1722348

Editorial: Advances in PET-CT imaging

Francesco Dondi*

Nuclear Medicine, Università degli Studi di Brescia and ASST Spedali Civili di Brescia, Brescia, Italy

KEYWORDS

[^{18}F]fluorodesoxyglucose ([^{18}F]FDG), non-small cell lung cancer (NSCLC), fibroblast activation protein (FAP) inhibitor (FAPI), prostate specific membrane antigen (PSMA), [^{68}Ga]Ga-PSMA-11 PET, multiparametric magnetic resonance imaging (mpMRI), PET/CT

Editorial on the Research Topic
Advances in PET-CT imaging

This Research Topic collected 15 articles that underlined the advances of positron emission tomography/computer tomography (PET/CT) imaging both in clinical and preclinical settings. In recent years, the use of PET/CT imaging has grown steadily, demonstrating its added value in the assessment of a wide range of diseases, including for example, neoplasms and inflammatory-infectious conditions. In this setting, the continuous development of different radiopharmaceuticals allows an expansion of the application scope of this imaging modality, providing ongoing new research opportunities and potential future clinical applications.

[^{18}F]fluorodesoxyglucose ([^{18}F]FDG) is currently the most widely used radiotracer, since its ability to underline the increased glycolytic activity of cells and tissue in different pathological conditions. In this setting, Yu et al. assessed the diagnostic efficacy and necessity of [^{18}F]FDG PET/CT in fever of unknown origin, demonstrating sensitivity of 79.5%, specificity of 61.1%, positive predictive value of 75.6% and negative predictive value of 66.3% for the final diagnosis. In addition, in the case of true-positive PET imaging, correlations with localized pain and prolonged activated partial thromboplastin time were found, identifying therefore clinical factors associated with PET positivity.

Blockmans et al. applied [^{18}F]FDG PET/CT imaging for the evaluation of giant cell arteritis, revealing that in addition to the extent and the intensity of the initial vascular inflammation, aortic inflammation may contribute to the development of aneurysms of the thoracic aorta.

An interesting case reported by Qi et al. underlined the possible clinical application of [^{18}F]FDG PET/CT in the evaluation of Rosai-Dorfman disease, reporting a rare case of unifocal extranodal localization that occurred in the sigmoid. Interestingly, a sort of similar pattern of appearance between the contrast-enhanced CT scan (mild to moderate enhancement) and the PET/CT scan (mild to moderate tracer uptake) was reported. Similarly, Hu, Zhao, Yu, et al. presented an interesting case of a 10-year-old girl diagnosed with inflammatory myofibroblastic tumor of the sigmoid colon, a rare site for its presentation, characterized as a mass with uneven enhancement on contrast-enhanced CT and increased [^{18}F]FDG uptake.

Not moving from the oncological setting, a case report by Hu, Li, et al. provided a valuable reference for imaging findings in primary clear cell carcinoma of the liver, a rare subtype of hepatocellular carcinoma, which presented at [^{18}F]FDG PET/CT as unevenly low-density with increased tracer uptake, while on contrast-enhanced CT or T1WI it may

present significant enhancement. Hu, Zhao, Li, et al. reported an interesting and rare case of a pulmonary mixed squamous cell and glandular papilloma that presented as a lung solid nodule with no lobulation or spiculation but with significant enhancement on contrast-enhanced CT and increased [^{18}F]FDG uptake on PET/CT; the subsequent literature review revealed that tracer uptake can range from mild to significant.

Yu and Chen performed a head-to-head comparative meta-analysis to evaluate [^{18}F]FDG PET/CT vs. [^{18}F]FDG PET/magnetic resonance imaging (MRI) in the staging of non-small cell lung cancer (NSCLC). The sensitivity and specificity for detecting nodal metastases were 0.82 (0.68–0.94) vs. 0.86 (0.70–0.97) and 0.88 (0.76–0.96) vs. 0.90 (0.85–0.94), for the two modalities respectively, while focusing on distant metastases, the values were 0.86 (0.60–1.00) vs. 0.93 (0.63–1.00) and 0.89 (0.65–1.00) vs. 0.90 (0.64–1.00), respectively. No significant differences were reported, showing that the two modalities has similar value for the evaluation of NSCLC localization.

As mentioned, different radiotracers can be used to image different metabolic pathways with PET imaging. Fibroblast activation protein (FAP) inhibitor (FAPI) is used for the assessment of fibroblasts activity. In this setting Dai et al. evaluate the impact of milk consumed prior to PET/CT on [^{18}F]AlF-NOTA-FAPI-04 uptake in normal abdominal organs to avoid gallbladder and biliary tract uptake, revealing that there was a reduction in gallbladder uptake in treated group ($p < 0.001$, average SUVmean 2.19 $\pm$ 2.01 vs. 10.04 $\pm$ 9.66). A subgroup analysis revealed that [^{18}F]FAPI uptake of liver and small intestine was significantly lower than [^{18}F]FDG uptake in both the treated and control group ($p < 0.001$). The diagnostic yield of FAPI tracers in the evaluation of thyroid cancer was investigated in a systematic review by Rizzo et al.. In a per-patients analysis on the detection of local recurrence and distant metastases of differentiated thyroid cancer, overall detection rate of approximately 85%, overall sensitivity and specificity of 96% and 50% respectively and detection rate for lymph node metastases of 86%, for lung lesions of 81.7% and bone secondaries of 100% were reported. In a per-lesion analysis, sensitivity and specificity for neck lesions were 83% and 42% respectively and detection rate for distant and nodal metastases of 79% and 95.4%, respectively. FAPI imaging was able to reveal a higher number of lesions in lymph nodes, lung, bone and liver compared to [^{18}F]FDG, however its superiority was not statistically significant in most of the cases. Additionally, FAPI PET demonstrated high accuracy for detecting local recurrences and distant metastases of medullary thyroid cancer when compared to [^{68}Ga]Ga-DOTANOC PET/CT.

The detection of cardiac neuroendocrine tumor metastases with somatostatin receptor PET/CT was evaluate in a meta-analysis by Campanale et al. Compared to other radiological techniques, PET/CT was able to detect earlier these metastases and patients were often asymptomatic and had other disease localization. The pooled prevalence of cardiac metastases of neuroendocrine neoplasm among those performing PET/CT was 1.5% [95% confidence interval (CI) 1.0%−1.9%].

Prostate specific membrane antigen (PSMA) is a radiopharmaceutical typically used for the evaluation of prostate cancer. A meta-analysis comparing [^{68}Ga]Ga-PSMA-11 PET and multiparametric magnetic resonance imaging (mpMRI) in the diagnosis of initial lymph node staging was performed by Wang et al. PET imaging demonstrated an overall sensitivity of 73% (95% CI 51%−91%) and an overall specificity of 94% (95% CI 88%−99%), while mpMRI showed a sensitivity of 49% (95% CI 30%−68%) and a specificity of 94% (95% CI 88%−99%). Despite that, the differences in sensitivity and specificity were not statistically significant.

Immuno-PET is an innovative medical imaging technique that combines antibodies or similar immuno-targeting molecules with positron-emitting radionuclides, enabling therefore the detection of specific cells. In this setting, Koenen et al. reported a case series of patients imaged with [^{89}Zr]Zr-crefmirlimab berdoxam PET/CT to assess CD8$^+$ T-cell localization during active COVID-19 infection. In particular, PET imaging demonstrated the differential distribution of CD8$^+$ T-cells in the mucosa and associated lymphoid organs of the upper respiratory tract during early and later stages of the infection, underscoring the concept of spatial and temporal compartmentalization of T-cell responses to respiratory viral infection. Moreover, differences in patterns of CD8$^+$ T-cell distribution across mucosa, primary and secondary lymphoid organs, blood pool, and peripheral tissues could be correlated with changes in CD8$^+$ T-cell functional phenotypes and had a coincidence with different intensity of tracer uptake. Habte and Natarajan proposed the basis for the initial validation of the potential usage of ultra-low-dose clinical practices using target-specific immuno-PET, by developing a novel immuno-PET with an intact rituximab antibody labeled with [^{64}Cu]Cu to image human CD20 in a transgenic mouse model for non-Hodgkin's lymphoma imaging. They underlined that an ultra-minimal dose administered in a mouse model [25 μCi] showed good image quality with high signal-to-noise ratio without compromising quantitative accuracy.

Moving to a more technical field, Metrard et al. proposed an interesting literature review of contrast-enhanced PET/CT, reporting that the use of iodinated contrast enhanced its overall performances by combining sensitivity and specificity of PET with those of diagnostic CT. In addition, improvement in patient dosimetry, facilitating pathology management and decreasing the administered volumes of contrast agent were important factors taken into account. Despite that, side effects related to contrast agents injection may be present and needs therefore to evaluated when assessing their use. Lastly, Thormann et al. compared two different software packages for the evaluation of acute ischemic stroke at perfusion CT (CTP), underscoring significant variability in their ability to reliably rule out small lacunar infarcts. In particular, one of them demonstrated a good specificity, suggesting that dependable CTP-based stroke exclusion is achievable with advanced post-processing.

In conclusion, this Research Topic includes different papers that underline the potential applications of PET/CT in different fields. Different radiotracers will probably constantly gain relevant role for the assessment of several pathological conditions, aiming therefore a more personalized evaluation of the patients.

Author contributions

FD: Writing – original draft.

Conflict of interest

The author declares that the research was conducted in the absence of any commercial or financial relationships that could be construed as a potential conflict of interest.

Generative AI statement

The author(s) declare that no Gen AI was used in the creation of this manuscript.

Any alternative text (alt text) provided alongside figures in this article has been generated by Frontiers with the support of artificial intelligence and reasonable efforts have been made to ensure accuracy, including review by the authors wherever possible. If you identify any issues, please contact us.

Publisher's note

frontiers | Frontiers in Medicine

TYPE Review
PUBLISHED 19 March 2024
DOI 10.3389/fmed.2024.1373260

OPEN ACCESS

EDITED BY
Nataliya Lutay,
Skåne University Hospital, Sweden

REVIEWED BY
Natale Quartuccio,
Azienda Ospedaliera Ospedali Riuniti Villa Sofia Cervello, Italy
Akram Al-Ibraheem,
King Hussein Cancer Center, Jordan
Alexandru Florea,
University Hospital RWTH Aachen, Germany

*CORRESPONDENCE
Gilles Metrard
gilles.metrard@chu-orleans.fr

†These authors have contributed equally to this work

RECEIVED 19 January 2024
ACCEPTED 06 March 2024
PUBLISHED 19 March 2024

CITATION
Metrard G, Cohen C and Bailly M (2024) Comprehensive literature review of oral and intravenous contrast-enhanced PET/CT: a step forward?
Front. Med. 11:1373260.
doi: 10.3389/fmed.2024.1373260

Comprehensive literature review of oral and intravenous contrast-enhanced PET/CT: a step forward?

Gilles Metrard[1,2*†], Clara Cohen[3†] and Matthieu Bailly[1,2†]

[1]Nuclear Medicine Department, Orléans University Hospital, Orléans, France, [2]Centre de Biophysique Moléculaire, CNRS UPR 4301, Université d'Orléans, Orléans, France, [3]Radiology Department, Orléans University Hospital, Orléans, France

The integration of diagnostic CT scans into PET/CT facilitates a comprehensive single examination, presenting potential advantages for patients seeking a thorough one-shot check-up. The introduction of iodinated contrast media during PET scanning raises theoretical concerns about potential interference with uptake quantification, due to the modification of tissue density on CT. Nevertheless, this impact appears generally insignificant for clinical use, compared to the intrinsic variability of standardized uptake values. On the other hand, with the growing indications of PET, especially ^{18}F-FDG PET, contrast enhancement increases the diagnostic performances of the exam, and provides additional information. This improvement in performance achieved through contrast-enhanced PET/CT must be carefully evaluated considering the associated risks and side-effects stemming from the administration of iodinated contrast media. Within this article, we present a comprehensive literature review of contrast enhanced PET/CT, examining the potential impact of iodinated contrast media on quantification, additional side-effects and the pivotal clinically demonstrated benefits of an all-encompassing examination for patients. In conclusion, the clinical benefits of iodinated contrast media are mainly validated by the large diffusion in PET protocols. Contrary to positive oral contrast, which does not appear to offer any major advantage in patient management, intravenous iodine contrast media provides clinical benefits without significant artifact on images or quantification. However, studies on the benefit–risk balance for patients are still lacking.

KEYWORDS

PET/CT, iodine, contrast enhanced, one-shot, examination

1 Introduction

A recent editorial has brought forth the question: "PET/contrast-enhanced CT in oncology: to do, or not to do, that is the question" (1).

Positron Emission Tomography (PET) is a molecular imaging technique that enhances diagnostic performance (2), therapeutic response monitoring (3), prognosis evaluation (4, 5) and modifies the management of patients with hematological (6) or solid malignancy (7). However, it is sensitive to attenuation. Unlike Single Photon Emission Tomography (SPECT), PET reconstruction needs the detection of two simultaneous 511 keV photons produced by β+ annihilation. The increased interaction probability of at least one of two photons versus only one results in a decreased sensitivity with patient's depth.

This attenuation has been historically corrected with a 511 keV attenuation map generated using a ^{68}Germanium transmission source. The primary drawback of this technique was its inherent slowness, significantly elongating the examination duration. Subsequent PET generation introduced a shift where attenuation correction map was substituted with a simulated high-energy attenuation map derived from Computed Tomography (CT). The first hybrid PET/CT systems offered enhanced accuracy in pinpointing the anatomical uptake location.

Gradually, PET manufacturers integrated the same diagnostic CT used as in radiology. With the potentially comparable performances capabilities, the redundancy between radiological CT and PET/CT prompted physicians to enhance the CT parameters of PET for minimizing overall patient's exposure, especially in oncology, and the economic impact (8).

The quest to the one-stop-shop anatomic and metabolic exam potentially required contrast-enhanced CT but the attenuation map modification by contrast medium could potentially lead to PET artefacts (9, 10). In this article, we propose a comprehensive literature review on the physical and clinical impacts of intravenous and positive oral contrast-enhanced CT in PET (cePET/CT).

2 Physical impact on standardized uptake value

The standardized uptake value (SUV) is the main quantitative parameter in PET to assess the radiopharmaceutical concentrations in tissues, while accounting for radioactive decay.

SUV body weighted (SUV_{bw} or SUW) is determined by the ratio of the activity concentration in the tissue under examination to the activity concentration in the entire body.

However, SUV_{bw} assumed a uniform distribution of the radiopharmaceutical throughout the body which was not the case. Particularly for the mainly used radiopharmaceuticals, the activity level in white adipose tissue was considerably low and led to an SUV_{bw} overestimation in patients with obesity (11). To rectify this, a more accurate approach involved scaling the SUV according to the lean body mass (SUV_{lbm} or SUL) (12) for adults or to the body surface area (SUA) in pediatric patients (13).

Furthermore, various other factors could potentially interfere with radiopharmaceutical distribution, such as injected activity, post-injection uptake time, blood glucose level, attenuation correction (14).

There was also multiple methods for quantifying SUV in a region of interest (ROI). SUV_{mean} represented the average activity in the ROI while SUV_{max} captured only the maximum pixel value. However, SUV_{max} was more sensitive to noise (15) and SUV_{mean} tended to lower the quantitative values with a better repeatability (16). An alternative approach could involve SUV_{peak} which computed the mean pixel value in the vicinity of the pixel with the maximum value and is less sensitive to changes in reconstruction parameters (17).

2.1 Intravenous iodine contrast media

On anthropomorphic phantom with and without Iodine Contrast Media (ICM), the study conducted by Razac et al. revealed a marginal absolute difference ΔSUV_{max} and ΔSUV_{mean}, of 0.2 and 0.4, respectively (18). This disparity was more pronounced in the most metabolically active simulated lesion ($\Delta SUV = 1.5$ for a SUV_{max} of 22). Nevertheless, these discrepancies were not clinically or statistically significant. These findings corroborated those of Bunyaviroch et al. which indicated a maximum SUV relative difference of 7% on phantom studies and a lower variance with 5.9% in clinical application (19). A variability of up to 8% was also found in conventional and digital systems complying with EARL accreditation but a more than 30% SUV difference could be observed on a limited number of lesions (17).

In clinical practice, the SUV fluctuation was heightened in highly contrast-enhanced regions, although these differences were not deemed significant (20, 21). Even when the variability was statistically significant, the authors did not observe any discernible clinical impact (22). This ICM SUV induced difference remained relatively negligible compared to the 20–30% global SUV variability in tumors (16). For this reason, it was recommended to use a 25% SUV decreased threshold for tumor reduction and a 33% SUV increased threshold for tumor progression in follow-up (23).

To mitigate the effects of ICM on attenuation correction, numerous research groups have explored how to refine the injection protocol, such as adjusting the ICM dose, concentration, or flow rate.

Regarding dose adjustment, an adaptation to the body surface area demonstrated a decrease in SUV variability, compared to a fixed-dose approach, and an improved interpatient homogeneity of contrast enhancement (24).

Similarly, the same researchers compared the effects of ICM dosage, finding no significant difference between 300 and 370 mgI/ml (25). When using an even higher iodine concentration of 400 mgI/ml, in a multiphase contrast enhanced CT protocol, Aschoff et al. noted only a minimal to negligible influence on 2-[^{18}F]FDG (^{18}F-FDG) quantification (26). It was advisable to opt for a single-phase CT rather than a multiphasic protocol to minimize coregistration errors (27).

2.2 Oral contrast media

Similarly to ICM, positive oral contrast agents could influence SUV values. This effect was demonstrated on phantom with SUV overestimation for high-density oral contrast agent (28) and the absence of significant artifact for low-density barium oral contrast agents (29). However, in a small patient cohort, Otsuka et al. did not find a significant correlation between SUV and Hounsfield density (30).

On simulated PET reconstructions, Dizendorf et al. demonstrated that oral contrast agents overestimated PET attenuation coefficients by 26.2% with only a small effect on SUV PET. The error was measured at 4.4% and did not appear to be clinically significant (31).

3 Additional risks of contrast media in cePET/CT

In clinical use and because of their route of administration, positive oral contrast media were remarkably safe and side effects were exceedingly rare (32). Most complications were observed with intravenous contrast agents.

ICM allowed the enhancement of vascular structures and tissue contrast. They were classified into two major categories: highly hyperosmolar ICM and hypo- or iso-osmolar non-ionic ICM. Both

types could induce side effects, with a higher prevalence seen in ionic ICM. This discrepancy in side effects prevalence was the reason why non-ionic ICM were preferred (33).

Warming iodine contrast media at 37°C could also reduce the risk of allergic or physiologic reactions (34).

3.1 Pseudo-allergic and allergic reactions

While ionic ICM previously resulted in side effects for 12% of patients, the use of non-ionic ICM had significantly decreased this occurrence to 0.7–3.1% and the most severe reactions have been drastically reduced from 0.22 to 0.02–0.04%.

ICM reactions were mostly non-fatal and manifested in 70% of patients within the first 5 min following ICM injection (35).

The majority of ICM reactions were non-allergic. Hyperosmolality induced fast vascular volume changes or direct chemotoxicity which could lead to physiological responses such as flushing, nausea and altered taste. Another reaction came from a non-allergic hypersensitivity caused by the direct release of histamine from mast cells and basophils. This mechanism could result in allergic-like symptoms like urticaria. For mild reactions, simple monitoring or H1-antihistamines treatment was generally sufficient.

IgE-mediated allergy was uncommon. In more severe cases involving laryngeal edema, corticosteroid therapy was often initiated while resuscitation measures were implemented during anaphylactic shocks (36).

For at-risk patients, a prophylactic treatment could be implemented (H1-antihistamines, corticosteroids) (37).

3.2 Nephrotoxicity

ICM increased the risk of acute kidney injury within 48 h following injection. This risk, previously overestimated, could now be prevented by hydration when clearance was below 30 mL/min/1.73 m^2 or for high-risk patients without contra-indication (38). As contrast enhanced CT was optional in PET, it might be advisable to refrain from administering ICM to these patients. For the specific case of myeloma, a meta-analysis suggested that no special precaution was needed if the calcium level was within the normal range (39).

3.3 Metformin

Metformin is an oral antihyperglycemic medication commonly prescribed for diabetes. In the context of ICM injection, patients might potentially develop lactic acidosis coupled with renal failure (35). The European Society of Urogenital Radiology (ESUR) guidelines and American College of Radiology manual recommended discontinuing the treatment for 48 h and monitoring renal function when the baseline clearance was below 30 mL/min/1.73 m^2 or if there were signs of acute renal failure.

3.4 Extravasation

Compared to the low injected volume of radiopharmaceuticals, ICM injection is carried out at higher pressure and for a larger volume. The risk of extravasation reported in the literature ranged from 0.1 to 0.9% and was increased when using an automatic injector (40, 41) or in cancer patients (42).

The risks associated with extravasation increased with osmolality but also depended on its direct toxicity. This toxicity was notably more pronounced with ionic ICM, as well as the anatomical location or volume. While most cases were relatively benign resulting in minor issues like skin erythema, there was potential for more severe side effects such as compartment syndrome or necrosis (40).

The widespread use of non-ionic ICM usually did not expose patients to the risk of severe complications. Therefore, a surgical consultation might be advised only for volumes exceeding 150 mL or in case of compressive signs (impaired perfusion or altered sensibility) (40).

3.5 Contrast-induced thyroid dysfunction

A typical radiological dose of ICM contains a substantial amount of free iodine, equivalent to the iodine needs for several months. When the body encountered excess iodine, the Wolff-Chaikoff effect was triggered, causing a fast downregulation in thyroid hormone synthesis. Prolonged exposure to high iodine levels could disrupt this regulatory mechanism, potentially resulting in either hyperthyroidism or hypothyroidism.

Moreover, this excess iodine load had the potential to exacerbate existing thyroid pathology or even directly cause thyroid toxicity (43).

3.6 ICM transformation products and potential toxicity

While ICM themselves were not inherently toxic, their presence in source waters raised concerns due to the formation of potentially toxic transformation products detected in drinking water (44). Specifically, ICM could react with commonly used disinfectants like chlorine, leading to formation of iodinated disinfection byproducts (iodo-DBP). Studies indicated that these iodo-DBP were highly genotoxic or cytotoxic, surpassing the conventional DBPs in toxicity. This situation highlighted concerns regarding the effectiveness of current treatment technologies and raised serious questions about disinfecting water containing ICM (45). Recent proposals suggested measures aimed at reducing and collecting ICM residues (46).

These potential side effects needed to be balanced against the clinical benefits of an enhanced CT for the patients. Table 1 summarizes the main advantages and disadvantages of ICM injection in PET/CT.

4 Clinical added value of cePET/CT

4.1 Head and neck tumors

Squamous cell carcinoma (SCC) represents the most common head and neck tumor type (95%). ^{18}F-FDG cePET/CT with dual phase has been proved superior to conventional imaging by MRI or CT for diagnosis and staging of patients with laryngeal carcinoma, with an higher rate of regional nodal, distant metastasis, and synchronous tumors (5, 47). More globally, ^{18}F-FDG PET/CT is a recognized

TABLE 1 Main advantages and disadvantages of cePET/CT.

Pros	Cons
Better lesion contrast especially in low-contrast lesions	A more complex exam scheduling: kidney function, allergies, medications
Better delineation of anatomic structures (digestive and vascular structures, liver, muscles…)	Additional risks: pseudo-allergic and allergic reactions, kidney failure…
Better PET/CT performance: sensitivity, specificity, accuracy	Artefacts with SUV overestimation
Better visualization of urinary tract	No additional reimbursement in many countries
More comfortable for the patient	
Overall cost lower than 2 exams	

modality for the staging and follow-up of head and neck SCC (48, 49). In cases with cervical lymph node metastasis from an unknown primary tumor, ^{18}F-FDG PET/CT revealed primary tumors that went undetected by CT or MRI in about 25% of cases (50). However, in those studies the difference between PET/CT and cePET/CT was not evaluated.

Prognosis for head and neck SCC is partly influenced by Human Papilloma Virus (HPV) status, with evidence that virally induced tumors responded far better to radiotherapy (51, 52). Using the hypoxia-specific tracer ^{18}F-fluoroazomycin arabinoside (FAZA), Saksø et al. demonstrated that the risk of locoregional recurrence was higher among patients with more hypoxic, non-HPV tumors (57% [21–94%]), when comparing to less hypoxic, non-HPV tumors, with a risk difference of 45% [4–86%] (53).

Integrated ^{18}F-FDG PET/perfusion CT showed that tumoral perfusion was significantly increased compared to surrounding soft tissue, especially for advanced tumors, and that meant blood flow was decreased in HPV-negative tumors (54).

Suenaga et al. showed that cePET/CT and PET/CT statistically showed larger AUC than contrast enhanced CT (ceCT) for recurrent head and neck squamous cell carcinoma (55). Even though minimal, the difference between cePET/CT and PET/CT for local recurrence reached a significant level ($p = 0.039$).

These works highlighted the distinctions between HPV-positive and negative tumors and emphasized the utility of analyzing the microvasculature features of tumoral head and neck SCC to predict their aggressiveness. This illustrated the necessity of integrating non-morphologic parameters, and also looking beyond the SUV uptake.

4.2 Digestive tumors

^{18}F-FDG ceCT had a higher predictive positive value for any PET pathologic findings than CT in the whole gastrointestinal tract, as well as in the separate evaluation of the upper and lower gastrointestinal tract (56). The sensitivity for the detection of a malignant lesion was 100% for ceCT and 29.4% for CT ($p = 0.0001$). The false negative rate for any pathology was 31.1% for ceCT and 68.9% for CT; this rate was however lower in the lower gastro-intestinal tract for CT (12.5% vs. 37.5% for ceCT).

^{18}F-FDG PET and ceCT seemed to have similar value in the detection of unsuspected recurrence of high-risk colorectal cancer in a patient-based analysis: sensitivity and specificity of 86 and 88%, 86 and 92%, 86 and 85%, respectively for PET, ceCT and cePET/CT (57). However, the combined assessment of cePET/CT improved the accuracy in the lesion-based analysis: sensitivity of 56, 71 and 97%, respectively for PET, ceCT and cePET/CT.

Regarding rectal tumors, cePET/CT was superior to non-enhanced PET/CT for precise definition of regional nodal status in rectal cancer with a better characterization of pararectal, internal iliac and obturator lymph nodes (58).

A retrospective study explored the diagnostic value of the cross-modality fusion images provided by ^{18}F-FDG PET/CT and ceCT in differentiating malignant from benign pancreatic lesions and staging pancreatic cancer (59). The authors found higher sensitivity and accuracy of cePET/CT compared to PET/CT and ceCT conducted individually both for diagnosing pancreatic malignant tumor and peripancreatic vessel invasion. Regarding regional lymph node metastasis, there was no significant differences between the three methods: however, regarding distant metastasis, cePET/CT improved sensitivity and negative predictive value in comparison to ceCT alone. cePET/CT had also higher sensitivity and accuracy than PET/CT, but the difference was not statistically significant.

Considering neuroendocrine tumors, a recent study emphasized that ceCT in ^{68}Ga-DOTATATE PET should be included for staging. The overall lesion-based sensitivity, specificity, negative predictive value and positive predictive value were 97% versus 85, 86% versus 73, 93% versus 72, 93% versus 85%, respectively, for full-dose cePET/CT and low dose PET/CT (60).

In the case of positive oral contrast media, several studies have demonstrated an improvement in digestive distension which was a potential help for diagnosis (61–63), but few have been able to demonstrate a clinical benefit. Chen et al. reported a more accurate delayed PET/CT with laxative-augmented contrast medium than conventional PET/CT for the evaluation of colorectal foci (64) and Guo et al. reported a case of enterovesical fistula revealed with oral contrast (65). The main challenge in assessing the impact of oral contrast agents was the hyperfixation of digestive structures (66), particularly due to distension, increased motility, and irritative phenomena (30). Regarding these digestive fixations, they were less pronounced with negative oral contrast agents (67–69) or those with low iodine density (62, 70).

4.3 Gynecological tumors

Considering malignant ovarian tumors, ^{18}F-FDG cePET/CT outperformed ceCT with sensitivity, specificity, negative predictive value, positive predictive value, and accuracy of 96 versus 84%, 92 versus 59%, 90 versus 59%, 97 versus 84%, and 95 versus 76%, respectively for cePET/CT and PET/CT alone (71). cePET/CT represented an accurate imaging modality for staging ovarian cancer (72).

Regarding ovarian cancer recurrence, cePET/CT seemed to be more accurate. Some data suggested higher sensitivity, specificity, and accuracy of cePET/CT: 86.9, 95.9, and 92.5%, respectively, (compared to 78.3, 95.0, and 88.3%, respectively for PET/CT) ($p = 0.023$ at least) (73). Another study found a better identification of smaller peritoneal/lymph node lesions close to physiological FDG

uptake sources with cePET/CT (74). With a better accuracy compared to non-contrast PET/CT and enhanced CT, cePET/CT could lead to changes in patient management for 39% of them (75).

Similarly, for uterine cancer, cePET/CT seemed to perform slightly better (sensitivity and accuracy) for nodal staging ($p = 0.046$ and 0.047) (76). cePET/CT was accurate for recurrence, reducing the frequency of equivocal interpretations (77) and leading to more appropriate subsequent clinical management than that resulting from PET alone or ceCT alone (78).

4.4 Melanoma

A previous study recommended to perform ^{18}F-FDG PET/CT instead of cePET/CT for staging of malignant melanoma patients (79). Comparison between CT and ceCT alone clearly revealed higher sensitivity and specificity for ceCT. However, when directly comparing lesion-based evaluation of combined PET/CT and cePET/CT, there was a difference in sensitivity of 3% only and no difference in specificity. As a limit, this study was conducted on a non-time-of-flight PET/CT system.

4.5 Hematological cancers

Integrated cePET/CT could improve the evaluation of pelvic lymphatic pathways nodal status in patients with malignant lymphoma (external and internal iliac, common iliac lymph nodes); diagnostic accuracies of retroperitoneal lymph nodes seemed to be similar between PET/CT and cePET/CT (80). However, the contribution of ceCT in nodal staging (Ann Arbor) seemed to remain limited (81). Similarly, the response evaluation applying the Deauville score and Lugano classification criteria remained unchanged with cePET/CT (82).

Thus, cePET/CT could be performed in the management of lymphoma patients, especially for a precise target delineation before radiotherapy (83).

CePET/CT approach should also be considered in pediatric exams. It could offer dose savings at similar image quality for children and young adults with lymphoma who had indications for both PET and diagnostic CT examinations (84).

4.6 Other malignancies

^{18}F-FDG cePET/CT showed similar results compared with CT/MRI in the detection of primary renal tumors, but it was superior to conventional methods in the detection of metastasis and staging (85). Once again, in this study, the authors did not compare directly PET/CT and cePET/CT.

Similarly, the same authors also showed higher diagnostic accuracy of ^{18}F-FDG cePET/CT for staging bladder cancer (89% vs. 57% for conventional imaging: CT and MRI), with upstaging in 37% of patients, resulting in changes of patient management.

The use of contrast has also been described as useful in ^{18}F-FDG cePET/CT as an initial imaging modality in patients presenting with metastatic malignancy of undefined primary origin (86).

In the specific case of lung and breast cancers, although these cancers were frequent, the clinical contribution of iodinated contrast injection has not been studied. It had only been demonstrated for lung cancers that non-ionic contrast injection did not cause significant artifact (21).

Figure 1 illustrates the improved visualization of low-contrast lesions, especially in difficult areas for diagnosis.

4.7 Non-tumor pathologies: inflammation and infection

A recent study focused on the diagnostic challenge in suspected infected aortic aneurysms, showing the high diagnostic accuracy of PET/CT for the detection of infection (sensitivity between 85 and 100% vs. between 63 and 88% for ceCT) (87). However, the authors raised the question of specificity because of false positive findings. The combined acquisition and analysis of PET and ceCT could help to improve this specificity.

In vasculitis, cePET/CT could be useful for identifying stenotic lesions in Takayasu arteritis, but data are insufficient to support its routine use for giant cell arteritis large vessel vasculitis. Guidelines recommended a low-dose CT prior to ceCT for attenuation correction and subsequent SUV calculations (88).

Recent guidelines in the management of infectious endocarditis recommended cePET/CT, as it allowed the detection of metabolic findings (FDG uptake distribution and intensity) and anatomical findings (endocarditis-related lesions like abscess) within a single imaging procedure, resulting in the clinical clarification of indeterminate findings and change in the management of the patients. This might be particularly helpful in complex settings like aortic grafts (89).

Lastly, contrast enhancement with an ICM enabled the detection of others pathologies, mostly not visible in PET/CT, such as lesions below the system resolution or pulmonary embolism, which were common in oncology (90).

5 Clinical added value of cePET/CT with other radiotracers

5.1 ^{18}F-choline

Despite being widely used for prostate cancer in many countries, only a few studies on parathyroid glands have been published. In a meta-analysis, Piccardo et al. found a better pooled sensitivity for 4D cePET/CT compared to PET/CT in primary hyperparathyroidism (Sensitivity of 0.93 and 0.89, respectively) with an identical detection rate (0.86) (91). In a cohort comprising 44 primary hyperparathyroidism patients, the same researchers confirmed the higher sensitivity of cePET/CT over PET/CT (with sensitivity of 1.0 and 0.8, respectively) and a better detection rate of 0.72 compared to 0.56, respectively (92).

5.2 ^{68}Ga-DOTATOC

For neuroendocrine tumors, ^{68}Ga-DOTATOC cePET/CT demonstrated a minimal increase in sensitivity and specificity compared to unenhanced exam (93). Ruf et al. recommended the same multiphase protocol for cePET/CT as for CT scan (94, 95).

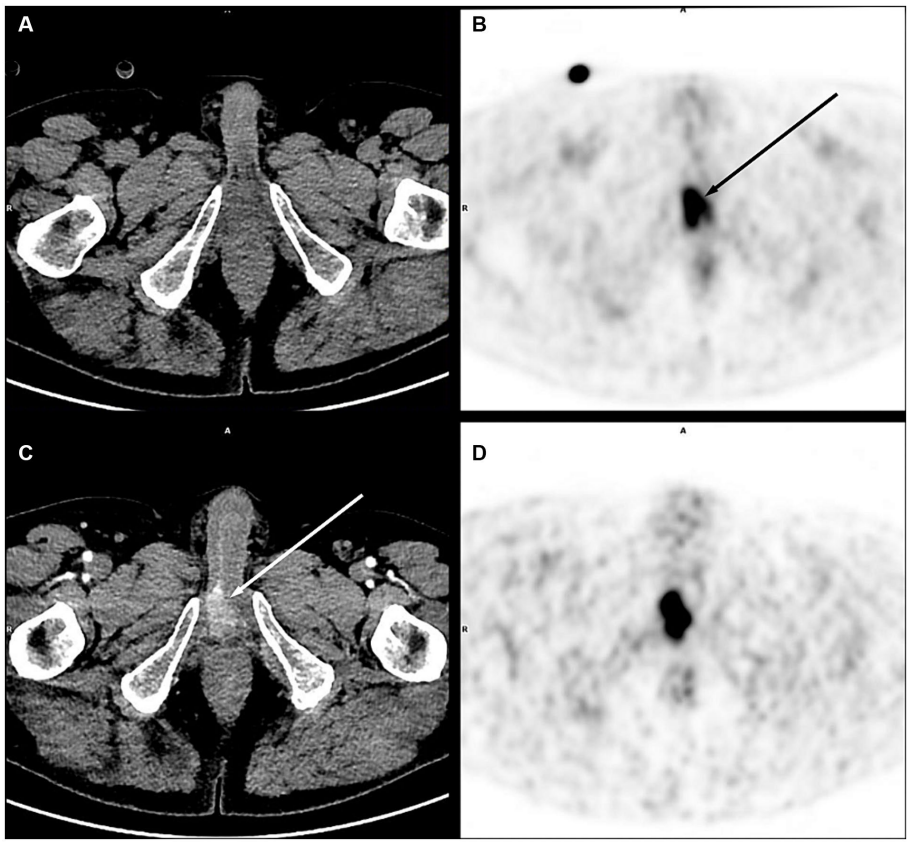

FIGURE 1
Right corpora cavernosa metastasis from penile carcinoma. on PET images (early acquisition **B**, late acquisition **D**), there was a focal uptake [**(B)** black arrow], without significant lesion on unenhanced CT **(A)**, in an area close to the physiological urinary activity. With contrast medium injection on a dedicated acquisition **(C)**, this uptake corresponded to a metastatic lesion clearly visible on CT (white arrow).

5.3 ^{68}Ga-PSMA ligand

Although the injection of contrast media did not yield a significant difference in diagnostic performance between PET/CT and cePET/CT, contrast enhancement seemed to improve the delineation of genitourinary system and increased the diagnostic certainty and interobserver agreement (96, 97).

However, CT acquisition during the contrast urinary excretion allowed for a better identification of the urinary tract. In a large retrospective study of 247 patients, Rosar et al. demonstrated that CT urography increased diagnostic confidence (in 48.6% of patients) while providing substantial support for interpretation (24.3%). In 12.1% of patients, urography changed the disease staging with a potential impact on patient management (98).

Tulipan et al. also showed that iodinated contrast agent sedimentation in the bladder created an activity gradient that improved visualization of the prostatic bed and the posterior bladder (99).

6 Issues raised by the all-in-one PET/CT exam

The one-stop-shop PET exam with ICM blurs the boundary between nuclear medicine and radiology. Depending on the country, this may rise issues of legislation and reimbursement. In addition, the choice of cePET/CT injection protocol is not standardized and differs from one nuclear medicine department to another (100).

7 Conclusion

The use of iodinated contrast media (ICM) in PET/CT scans enhanced the overall examination performance by combining the PET sensitivity and specificity with those of diagnostic enhanced CT. This synergistic performance enhancement was achievable through an all-in-one examination, improving patient dosimetry, facilitating pathology management, and decreasing the administered volumes of ICM especially in the field of oncology. In contrast, although positive oral contrast media enhanced distension and contrast of digestive structures, their clinical utility in PET imaging appeared more modest.

However, the ICM injection was not exempt from side effects, most of which were moderate. For the most severe forms, the additional risk remained low, as most patients would have undergone an ICM enhanced CT as part of their assessment. Apart from contraindications, injecting less than 150 mL of non-ionic ICM into patients with a renal clearance greater than 30 mL/min/1.75 m^2 could maximize the safety of

ICM use in PET as long as no benefit–risk studies have been carried out.

Author contributions

GM: Writing – original draft, Writing – review & editing. CC: Writing – original draft, Writing – review & editing. MB: Writing – original draft, Writing – review & editing.

Funding

The author(s) declare that no financial support was received for the research, authorship, and/or publication of this article.

Conflict of interest

The authors declare that the research was conducted in the absence of any commercial or financial relationships that could be construed as a potential conflict of interest.

Publisher's note

References

1. Scialpi M, Moschini TO, De Filippis G. PET/contrast-enhanced CT in oncology: "to do, or not to do, that is the question". *Radiol Med*. (2022) 127:925–7. doi: 10.1007/s11547-022-01496-3

2. Kim K, Ha M, Kim SJ. Comparative study of different imaging modalities for diagnosis of bone metastases of prostate cancer: a Bayesian network meta-analysis. *Clin Nucl Med*. (2024) 49:312–8. doi: 10.1097/RLU.0000000000005078

3. Wahl RL, Jacene H, Kasamon Y, Lodge MA. From RECIST to PERCIST: evolving considerations for PET response criteria in solid tumors. *J Nucl Med*. (2009) 50:122S–50S. doi: 10.2967/jnumed.108.057307

4. Xia Q, Liu J, Wu C, Song S, Tong L, Huang G, et al. Prognostic significance of (18) FDG PET/CT in colorectal cancer patients with liver metastases: a meta-analysis. *Cancer Imaging*. (2015) 15:19. doi: 10.1186/s40644-015-0055-z

5. Al-Ibraheem A, Abdlkadir AS, Al-Adhami D, Hejleh TA, Mansour A, Mohamad I, et al. The prognostic and diagnostic value of [(18)F]FDG PET/CT in untreated laryngeal carcinoma. *J Clin Med*. (2023) 12:3514. doi: 10.3390/jcm12103514

6. Valls L, Badve C, Avril S, Herrmann K, Faulhaber P, O'Donnell J, et al. FDG-PET imaging in hematological malignancies. *Blood Rev*. (2016) 30:317–31. doi: 10.1016/j.blre.2016.02.003

7. Al-Ibraheem A, AlSharif A, Abu-Hijlih R, Jaradat I, Mansour A. Clinical impact of (18)F-FDG PET/CT on the Management of Gynecologic Cancers: one center experience. *Asia Ocean J Nucl Med Biol*. (2019) 7:7–12. doi: 10.22038/AOJNMB.2018.11208

8. Picchio M, Mansueto M, Crivellaro C, Guerra L, Marcelli S, Arosio M, et al. PET/CT and contrast enhanced CT in single vs. two separate sessions: a cost analysis study. *Q J Nucl Med Mol Imaging*. (2012) 56:309–16.

9. Annunziata S, Testart N, Auf der Springe K, Cuzzocrea M, Nicod Lalonde M, Schaefer N, et al. Contrast enhanced CT on PET/CT imaging in clinical routine: an international survey. *Front Med (Lausanne)*. (2023) 10:1290956. doi: 10.3389/fmed.2023.1290956

10. Strobel K, Heinrich S, Bhure U, Soyka J, Veit-Haibach P, Pestalozzi BC, et al. Contrast-enhanced 18F-FDG PET/CT: 1-stop-shop imaging for assessing the resectability of pancreatic cancer. *J Nucl Med*. (2008) 49:1408–13. doi: 10.2967/jnumed.108.051466

11. Sarikaya I, Albatineh AN, Sarikaya A. Revisiting weight-normalized SUV and lean-body-mass-normalized SUV in PET studies. *J Nucl Med Technol*. (2020) 48:163–7. doi: 10.2967/jnmt.119.233353

12. Keramida G, Peters AM. The appropriate whole body metric for calculating standardised uptake value and the influence of sex. *Nucl Med Commun*. (2019) 40:3–7. doi: 10.1097/MNM.0000000000000935

13. Sarikaya I, Sarikaya A. Assessing PET parameters in oncologic (18)F-FDG studies. *J Nucl Med Technol*. (2020) 48:278–82. doi: 10.2967/jnmt.119.236109

14. Adams MC, Turkington TG, Wilson JM, Wong TZ. A systematic review of the factors affecting accuracy of SUV measurements. *AJR Am J Roentgenol*. (2010) 195:310–20. doi: 10.2214/AJR.10.4923

15. Boellaard R, Krak NC, Hoekstra OS, Lammertsma AA. Effects of noise, image resolution, and ROI definition on the accuracy of standard uptake values: a simulation study. *J Nucl Med*. (2004) 45:1519–27.

16. de Langen AJ, Vincent A, Velasquez LM, van Tinteren H, Boellaard R, Shankar LK, et al. Repeatability of 18F-FDG uptake measurements in tumors: a metaanalysis. *J Nucl Med*. (2012) 53:701–8. doi: 10.2967/jnumed.111.095299

17. Koopman D, Jager PL, Slump CH, Knollema S, van Dalen JA. SUV variability in EARL-accredited conventional and digital PET. *EJNMMI Res*. (2019) 9:106. doi: 10.1186/s13550-019-0569-7

18. Abdul Razak HR, Nordin AJ, Ackerly T, Van Every B, Martin R, Geso M. Quantifying the effects of iodine contrast media on standardised uptake values of FDG PET/CT images: an anthropomorphic phantom study. *Australas Phys Eng Sci Med*. (2011) 34:367–74. doi: 10.1007/s13246-011-0088-y

19. Bunyaviroch T, Turkington TG, Wong TZ, Wilson JW, Colsher JG, Coleman RE. Quantitative effects of contrast enhanced CT attenuation correction on PET SUV measurements. *Mol Imaging Biol*. (2008) 10:107–13. doi: 10.1007/s11307-007-0126-z

20. Mawlawi O, Erasmus JJ, Munden RF, Pan T, Knight AE, Macapinlac HA, et al. Quantifying the effect of IV contrast media on integrated PET/CT: clinical evaluation. *AJR Am J Roentgenol*. (2006) 186:308–19. doi: 10.2214/AJR.04.1740

21. An YS, Sheen SS, Oh YJ, Hwang SC, Yoon JK. Nonionic intravenous contrast agent does not cause clinically significant artifacts to 18F-FDG PET/CT in patients with lung cancer. *Ann Nucl Med*. (2007) 21:585–92. doi: 10.1007/s12149-007-0066-3

22. Behrendt FF, Temur Y, Verburg FA, Palmowski M, Krohn T, Pietsch H, et al. PET/CT in lung cancer: influence of contrast medium on quantitative and clinical assessment. *Eur Radiol*. (2012) 22:2458–64. doi: 10.1007/s00330-012-2515-1

23. Lodge MA. Repeatability of SUV in oncologic (18)F-FDG PET. *J Nucl Med*. (2017) 58:523–32. doi: 10.2967/jnumed.116.186353

24. Behrendt FF, Rebière M, Goedicke A, Pietsch H, Palmowski K, Kuhl CK, et al. Contrast medium injection protocol adjusted for body surface area in combined PET/CT. *Eur Radiol*. (2013) 23:1970–7. doi: 10.1007/s00330-013-2781-6

25. Verburg FA, Apitzsch J, Lensing C, Kuhl CK, Pietsch H, Mottaghy FM, et al. Body surface area adapted iopromide 300 mg/ml versus 370 mg/ml contrast medium injection protocol: influence on quantitative and clinical assessment in combined PET/CT. *Eur J Radiol*. (2013) 82:2348–52. doi: 10.1016/j.ejrad.2013.09.013

26. Aschoff P, Plathow C, Beyer T, Lichy MP, Erb G, Öksüz M, et al. Multiphase contrast-enhanced CT with highly concentrated contrast agent can be used for PET attenuation correction in integrated PET/CT imaging. *Eur J Nucl Med Mol Imaging*. (2012) 39:316–25. doi: 10.1007/s00259-011-1919-5

27. Brechtel K, Klein M, Vogel M, Mueller M, Aschoff P, Beyer T, et al. Optimized contrast-enhanced CT protocols for diagnostic whole-body 18F-FDG PET/CT: technical aspects of single-phase versus multiphase CT imaging. *J Nucl Med*. (2006) 47:470–6.

28. Antoch G, Jentzen W, Freudenberg LS, Stattaus J, Mueller SP, Debatin JF, et al. Effect of oral contrast agents on computed tomography-based positron emission tomography attenuation correction in dual-modality positron emission tomography/computed tomography imaging. *Investig Radiol*. (2003) 38:784–9.

29. Cohade C, Osman M, Nakamoto Y, Marshall LT, Links JM, Fishman EK, et al. Initial experience with oral contrast in PET/CT: phantom and clinical studies. *J Nucl Med*. (2003) 44:412–6.

30. Otsuka H, Kubo A, Graham M, Nishitani H. The relationship between standard uptake value (SUV) and Hounsfield unit (HU) of oral contrast agent for FDG-PET/CT study. *J Med Investig*. (2004) 51:226–9. doi: 10.2152/jmi.51.226

31. Dizendorf E, Hany TF, Buck A, von Schulthess GK, Burger C. Cause and magnitude of the error induced by oral CT contrast agent in CT-based attenuation correction of PET emission studies. *J Nucl Med*. (2003) 44:732–8.

32. Pickhardt PJ. Positive Oral contrast material for abdominal CT: current clinical indications and areas of controversy. *AJR Am J Roentgenol*. (2020) 215:69–78. doi: 10.2214/AJR.19.21989

33. Urrutia M, Macharaviaya A, Rodriguez R. Adverse reactions to contrast media for intravenous use. A comparison between ionic and nonionic media. *Rev Med Panama*. (1995) 20:20–4.

34. Nawras M, Alyousif Z, Beran A, Elsamaloty H. The relationship between iodinated contrast material temperature and adverse reactions: a meta-analysis of 307,329 injections. *Clin Imaging*. (2023) 100:54–9. doi: 10.1016/j.clinimag.2023.05.006

35. Rose TA Jr, Choi JW. Intravenous imaging contrast media complications: the basics that every clinician needs to know. *Am J Med*. (2015) 128:943–9. doi: 10.1016/j.amjmed.2015.02.018

36. Radiology ACO. *ACR Manual On Contrast Media*. (2023). American College or Radiology (ACR).

37. Hsieh C, Wu SC, Kosik RO, Huang YC, Chan WP. Pharmacological prevention of hypersensitivity reactions caused by iodinated contrast media: a systematic review and meta-analysis. *Diagnostics (Basel)*. (2022) 12:1673. doi: 10.3390/diagnostics12071673

38. Davenport MS, Perazella MA, Yee J, Dillman JR, Fine D, McDonald RJ, et al. Use of intravenous iodinated contrast Media in Patients with kidney disease: consensus statements from the American College of Radiology and the National Kidney Foundation. *Radiology*. (2020) 294:660–8. doi: 10.1148/radiol.2019192094

39. Stacul F, Bertolotto M, Thomsen HS, Pozzato G, Ugolini D, Bellin MF, et al. Iodine-based contrast media, multiple myeloma and monoclonal gammopathies: literature review and ESUR contrast media safety committee guidelines. *Eur Radiol*. (2018) 28:683–91. doi: 10.1007/s00330-017-5023-5

40. Mandlik V, Prantl L, Schreyer AG. Contrast media extravasation in CT and MRI - a literature review and strategies for therapy. *Rofo*. (2019) 191:25–32. doi: 10.1055/a-0628-7095

41. Heshmatzadeh Behzadi A, Farooq Z, Newhouse JH, Prince MR. MRI and CT contrast media extravasation: a systematic review. *Medicine (Baltimore)*. (2018) 97:e0055. doi: 10.1097/MD.0000000000010055

42. Silva HCS, Bitencourt AGV, Chojniak R. Extravasation of iodinated contrast medium in cancer patients undergoing computed tomography. *Radiol Bras*. (2018) 51:236–41. doi: 10.1590/0100-3984.2017.0064

43. Andreucci M, Solomon R, Tasanarong A. Side effects of radiographic contrast media: pathogenesis, risk factors, and prevention. *Biomed Res Int*. (2014) 2014:741018:1–20. doi: 10.1155/2014/741018

44. Duirk SE, Lindell C, Cornelison CC, Kormos J, Ternes TA, Attene-Ramos M, et al. Formation of toxic iodinated disinfection by-products from compounds used in medical imaging. *Environ Sci Technol*. (2011) 45:6845–54. doi: 10.1021/es200983f

45. Sengar A, Vijayanandan A. Comprehensive review on iodinated X-ray contrast media: complete fate, occurrence, and formation of disinfection byproducts. *Sci Total Environ*. (2021) 769:144846. doi: 10.1016/j.scitotenv.2020.144846

46. Dekker HM, Stroomberg GJ, Prokop M. Tackling the increasing contamination of the water supply by iodinated contrast media. *Insights Imaging*. (2022) 13:30. doi: 10.1186/s13244-022-01175-x

47. Tatar G, Cermik TF, Karagoz Y, Gundogan C, Karacetin D, Yildiz E, et al. The value of whole-body contrast-enhanced 18F-FDG PET/CT imaging in the diagnosis and staging of patients with laryngeal carcinoma. *Nucl Med Commun*. (2018) 39:334–42. doi: 10.1097/MNM.0000000000000809

48. Sheikhbahaei S, Taghipour M, Ahmad R, Fakhry C, Kiess AP, Chung CH, et al. Diagnostic accuracy of follow-up FDG PET or PET/CT in patients with head and neck Cancer after definitive treatment: a systematic review and Meta-analysis. *AJR Am J Roentgenol*. (2015) 205:629–39. doi: 10.2214/AJR.14.14166

49. Kyzas PA, Evangelou E, Denaxa-Kyza D, Ioannidis JP. 18F-fluorodeoxyglucose positron emission tomography to evaluate cervical node metastases in patients with head and neck squamous cell carcinoma: a meta-analysis. *J Natl Cancer Inst*. (2008) 100:712–20. doi: 10.1093/jnci/djn125

50. Rusthoven KE, Koshy M, Paulino AC. The role of fluorodeoxyglucose positron emission tomography in cervical lymph node metastases from an unknown primary tumor. *Cancer*. (2004) 101:2641–9. doi: 10.1002/cncr.20687

51. Lassen P, Primdahl H, Johansen J, Kristensen CA, Andersen E, Andersen LJ, et al. Impact of HPV-associated p16-expression on radiotherapy outcome in advanced oropharynx and non-oropharynx cancer. *Radiother Oncol*. (2014) 113:310–6. doi: 10.1016/j.radonc.2014.11.032

52. Economopoulou P, de Bree R, Kotsantis I, Psyrri A. Diagnostic tumor markers in head and neck squamous cell carcinoma (HNSCC) in the clinical setting. *Front Oncol*. (2019) 9:827. doi: 10.3389/fonc.2019.00827

53. Sakso M, Mortensen LS, Primdahl H, Johansen J, Kallehauge J, Hansen CR, et al. Influence of FAZA PET hypoxia and HPV-status for the outcome of head and neck squamous cell carcinoma (HNSCC) treated with radiotherapy: long-term results from the DAHANCA 24 trial (NCT01017224). *Radiother Oncol*. (2020) 151:126–33. doi: 10.1016/j.radonc.2020.08.006

54. Nesteruk M, Lang S, Veit-Haibach P, Studer G, Stieb S, Glatz S, et al. Tumor stage, tumor site and HPV dependent correlation of perfusion CT parameters and [18F]-FDG uptake in head and neck squamous cell carcinoma. *Radiother Oncol*. (2015) 117:125–31. doi: 10.1016/j.radonc.2015.09.026

55. Suenaga Y, Kitajima K, Ishihara T, Sasaki R, Otsuki N, Nibu K, et al. FDG-PET/contrast-enhanced CT as a post-treatment tool in head and neck squamous cell carcinoma: comparison with FDG-PET/non-contrast-enhanced CT and contrast-enhanced CT. *Eur Radiol*. (2016) 26:1018–30. doi: 10.1007/s00330-015-3902-1

56. Brendle CB, Aschoff P, Kratt T, Schraml C, Reimold M, Claussen CD, et al. Is there any additional benefit of contrast-enhanced CT as part of routine PET/CT protocols for the differentiation of suspicious incidental gastrointestinal 2-deoxy-(18)F-FDG uptake? *Korean J Radiol*. (2013) 14:951–9. doi: 10.3348/kjr.2013.14.6.951

57. Jimenez Londono GA, Garcia Vicente AM, Sanchez Perez V, Jimenez Aragon F, Leon Martin A, Cano Cano JM, et al. (1)(8)F-FDG PET/contrast enhanced CT in the standard surveillance of high risk colorectal cancer patients. *Eur J Radiol*. (2014) 83:2224–30. doi: 10.1016/j.ejrad.2014.08.016

58. Tateishi U, Maeda T, Morimoto T, Miyake M, Arai Y, Kim EE. Non-enhanced CT versus contrast-enhanced CT in integrated PET/CT studies for nodal staging of rectal cancer. *Eur J Nucl Med Mol Imaging*. (2007) 34:1627–34. doi: 10.1007/s00259-007-0455-9

59. Zhang J, Zuo CJ, Jia NY, Wang JH, Hu SP, Yu ZF, et al. Cross-modality PET/CT and contrast-enhanced CT imaging for pancreatic cancer. *World J Gastroenterol*. (2015) 21:2988–96. doi: 10.3748/wjg.v21.i10.2988

60. Apitzsch J, Verburg FA, Mottaghy F, Heinzel A. Use of full-dose contrast-enhanced CT for extrahepatic staging using Gallium-68-DOTATATE PET/CT in patients with neuroendocrine tumors. *Diagn Interv Radiol*. (2021) 27:573–9. doi: 10.5152/dir.2021.19424

61. Cronin CG, Prakash P, Blake MA. Oral and IV contrast agents for the CT portion of PET/CT. *AJR Am J Roentgenol*. (2010) 195:W5–w13. doi: 10.2214/AJR.09.3844

62. Blake MA, Setty BN, Cronin CG, Kalra M, Holalkere NS, Fischman AJ, et al. Evaluation of the effects of oral water and low-density barium sulphate suspension on bowel appearance on FDG-PET/CT. *Eur Radiol*. (2010) 20:157–64. doi: 10.1007/s00330-009-1527-y

63. Groves AM, Kayani I, Dickson JC, Townsend C, Croasdale I, Syed R, et al. Oral contrast medium in PET/CT: should you or shouldn't you? *Eur J Nucl Med Mol Imaging*. (2005) 32:1160–6. doi: 10.1007/s00259-005-1833-9

64. Chen YK, Chen JH, Tsui CC, Chou HH, Cheng RH, Chiu JS. Use of laxative-augmented contrast medium in the evaluation of colorectal foci at FDG PET. *Radiology*. (2011) 259:525–33. doi: 10.1148/radiol.11101193

65. Guo L, Shen G. Enterovesical fistula in a lymphoma patient revealed by FDG PET/CT with an Oral contrast agents. *Clin Nucl Med*. (2024) 49:e38–9. doi: 10.1097/RLU.0000000000004954

66. Otsuka H, Graham MM, Kubo A, Nishitani H. The effect of oral contrast on large bowel activity in FDG-PET/CT. *Ann Nucl Med*. (2005) 19:101–8. doi: 10.1007/BF03027388

67. Meyer SA, Gawde S. Utility of negative oral contrast (milk with 4% fat) in PET-CT studies. *Indian J Nucl Med*. (2012) 27:151–5. doi: 10.4103/0972-3919.112719

68. Antoch G, Kuehl H, Kanja J, Lauenstein TC, Schneemann H, Hauth E, et al. Dual-modality PET/CT scanning with negative oral contrast agent to avoid artifacts: introduction and evaluation. *Radiology*. (2004) 230:879–85. doi: 10.1148/radiol.2303021287

69. Sun XG, Huang G, Liu JJ, Wan LR. Comparison of the effect of positive and negative oral contrast agents on (18)F-FDG PET/CT scan. *Hell J Nucl Med*. (2009) 12:115–8.

70. Otero HJ, Yap JT, Patak MA, Erturk SM, Israel DA, Johnston CJ, et al. Evaluation of low-density neutral oral contrast material in PET/CT for tumor imaging: results of a randomized clinical trial. *AJR Am J Roentgenol*. (2009) 193:326–32. doi: 10.2214/AJR.08.1565

71. Tawakol A, Abdelhafez YG, Osama A, Hamada E, El Refaei S. Diagnostic performance of 18F-FDG PET/contrast-enhanced CT versus contrast-enhanced CT alone for post-treatment detection of ovarian malignancy. *Nucl Med Commun*. (2016) 37:453–60. doi: 10.1097/MNM.0000000000000477

72. Kitajima K, Murakami K, Yamasaki E, Kaji Y, Fukasawa I, Inaba N, et al. Diagnostic accuracy of integrated FDG-PET/contrast-enhanced CT in staging ovarian cancer: comparison with enhanced CT. *Eur J Nucl Med Mol Imaging*. (2008) 35:1912–20. doi: 10.1007/s00259-008-0890-2

73. Kitajima K, Ueno Y, Suzuki K, Kita M, Ebina Y, Yamada H, et al. Low-dose non-enhanced CT versus full-dose contrast-enhanced CT in integrated PET/CT scans for diagnosing ovarian cancer recurrence. *Eur J Radiol*. (2012) 81:3557–62. doi: 10.1016/j.ejrad.2012.03.020

74. Massollo M, Fiz F, Bottoni G, Ugolini M, Paparo F, Puppo C, et al. To enhance or not to enhance? The role of contrast medium (18)F-FDG PET/CT in recurrent ovarian carcinomas. *Medicina (Kaunas)*. (2021) 57:561. doi: 10.3390/medicina57060561

75. Kitajima K, Murakami K, Yamasaki E, Domeki Y, Kaji Y, Fukasawa I, et al. Performance of integrated FDG-PET/contrast-enhanced CT in the diagnosis of recurrent ovarian cancer: comparison with integrated FDG-PET/non-contrast-enhanced CT and enhanced CT. *Eur J Nucl Med Mol Imaging*. (2008) 35:1439–48. doi: 10.1007/s00259-008-0776-3

76. Kitajima K, Suzuki K, Senda M, Kita M, Nakamoto Y, Sakamoto S, et al. Preoperative nodal staging of uterine cancer: is contrast-enhanced PET/CT more accurate than non-enhanced PET/CT or enhanced CT alone? *Ann Nucl Med*. (2011) 25:511–9. doi: 10.1007/s12149-011-0496-9

77. Kitajima K, Suzuki K, Nakamoto Y, Onishi Y, Sakamoto S, Senda M, et al. Low-dose non-enhanced CT versus full-dose contrast-enhanced CT in integrated PET/CT studies for the diagnosis of uterine cancer recurrence. *Eur J Nucl Med Mol Imaging*. (2010) 37:1490–8. doi: 10.1007/s00259-010-1440-2

78. Kitajima K, Murakami K, Yamasaki E, Domeki Y, Kaji Y, Morita S, et al. Performance of integrated FDG-PET/contrast-enhanced CT in the diagnosis of recurrent uterine cancer: comparison with PET and enhanced CT. *Eur J Nucl Med Mol Imaging*. (2009) 36:362–72. doi: 10.1007/s00259-008-0956-1

79. Pfluger T, Melzer HI, Schneider V, La Fougere C, Coppenrath E, Berking C, et al. PET/CT in malignant melanoma: contrast-enhanced CT versus plain low-dose CT. *Eur J Nucl Med Mol Imaging*. (2011) 38:822–31. doi: 10.1007/s00259-010-1702-z

80. Morimoto T, Tateishi U, Maeda T, Arai Y, Nakajima Y, Edmund KE. Nodal status of malignant lymphoma in pelvic and retroperitoneal lymphatic pathways: comparison of integrated PET/CT with or without contrast enhancement. *Eur J Radiol*. (2008) 67:508–13. doi: 10.1016/j.ejrad.2007.08.017

81. Chiaravalloti A, Danieli R, Caracciolo CR, Travascio L, Cantonetti M, Gallamini A, et al. Initial staging of Hodgkin's disease: role of contrast-enhanced 18F FDG PET/CT. *Medicine (Baltimore)*. (2014) 93:e50. doi: 10.1097/MD.0000000000000050

82. Paone G, Raditchkova-Sarnelli M, Ruberto-Macchi T, Cuzzocrea M, Zucca E, Ceriani L, et al. Limited benefit of additional contrast-enhanced CT to end-of-treatment PET/CT evaluation in patients with follicular lymphoma. *Sci Rep*. (2021) 11:18496. doi: 10.1038/s41598-021-98081-x

83. Milgrom SA, Rechner L, Berthelsen A. The optimal use of PET/CT in the management of lymphoma patients. *Br J Radiol*. (2021) 94:20210470. doi: 10.1259/bjr.20210470

84. Qi Z, Gates EL, O'Brien MM, Trout AT. Radiation dose reduction through combining positron emission tomography/computed tomography (PET/CT) and diagnostic CT in children and young adults with lymphoma. *Pediatr Radiol*. (2018) 48:196–203. doi: 10.1007/s00247-017-4019-2

85. Gundogan C, Cermik TF, Erkan E, Yardimci AH, Behzatoglu K, Tatar G, et al. Role of contrast-enhanced 18F-FDG PET/CT imaging in the diagnosis and staging of renal tumors. *Nucl Med Commun*. (2018) 39:1174–82. doi: 10.1097/MNM.0000000000000915

86. Jain A, Srivastava MK, Pawaskar AS, Shelley S, Elangovan I, Jain H, et al. Contrast-enhanced [18F] fluorodeoxyglucose-positron emission tomography-computed tomography as an initial imaging modality in patients presenting with metastatic malignancy of undefined primary origin. *Indian J Nucl Med*. (2015) 30:213–20. doi: 10.4103/0972-3919.158529

87. Husmann L, Huellner MW, Ledergerber B, Eberhard N, Kaelin MB, Anagnostopoulos A, et al. Diagnostic accuracy of PET/CT and contrast enhanced CT in patients with suspected infected aortic aneurysms. *Eur J Vasc Endovasc Surg*. (2020) 59:972–81. doi: 10.1016/j.ejvs.2020.01.032

88. Writing Group, Reviewer Group, Members of EANM Cardiovascular, Members of EANM Infection & Inflammation, Members of Committees, SNMMI Cardiovascular, Members of Council, PET Interest Group, Members of ASNC, EANM Committee CoordinatorSlart RHJA. FDG-PET/CT(a) imaging in large vessel vasculitis and polymyalgia rheumatica: joint procedural recommendation of the EANM, SNMMI, and the PET interest group (PIG), and endorsed by the ASNC. *Eur J Nucl Med Mol Imaging*. (2018) 45:1250–69. doi: 10.1007/s00259-018-3973-8

89. Delgado V, Ajmone Marsan N, de Waha S, Bonaros N, Brida M, Burri H, et al. 2023 ESC guidelines for the management of endocarditis. *Eur Heart J*. (2023) 44:3948–4042. doi: 10.1093/eurheartj/ehad193

90. Lubetsky A. Pulmonary embolism in Cancer patients: a review. *Isr Med Assoc J*. (2022) 24:179–82.

91. Piccardo A, Bottoni G, Boccalatte LA, Camponovo C, Musumeci M, Bacigalupo L, et al. Head-to-head comparison among (18)F-choline PET/CT, 4D contrast-enhanced CT, and (18)F-choline PET/4D contrast-enhanced CT in the detection of hyperfunctioning parathyroid glands: a systematic review and meta-analysis. *Endocrine*. (2021) 74:404–12. doi: 10.1007/s12020-021-02798-8

92. Piccardo A, Trimboli P, Rutigliani M, Puntoni M, Foppiani L, Bacigalupo L, et al. Additional value of integrated (18)F-choline PET/4D contrast-enhanced CT in the localization of hyperfunctioning parathyroid glands and correlation with molecular profile. *Eur J Nucl Med Mol Imaging*. (2019) 46:766–75. doi: 10.1007/s00259-018-4147-4

93. Mayerhoefer ME, Schuetz M, Magnaldi S, Weber M, Trattnig S, Karanikas G. Are contrast media required for (68)Ga-DOTATOC PET/CT in patients with neuroendocrine tumours of the abdomen? *Eur Radiol*. (2012) 22:938–46. doi: 10.1007/s00330-011-2328-7

94. Ruf J, Heuck F, Schiefer J, Denecke T, Elgeti F, Pascher A, et al. Impact of multiphase 68Ga-DOTATOC-PET/CT on therapy management in patients with neuroendocrine tumors. *Neuroendocrinology*. (2010) 91:101–9. doi: 10.1159/000265561

95. Ruf J, Schiefer J, Furth C, Kosiek O, Kropf S, Heuck F, et al. 68Ga-DOTATOC PET/CT of neuroendocrine tumors: spotlight on the CT phases of a triple-phase protocol. *J Nucl Med*. (2011) 52:697–704. doi: 10.2967/jnumed.110.083741

96. Winiger A, Pérez Lago MDS, Lehnick D, Roos JE, Strobel K. The value of intravenous contrast medium in PSMA PET/CT imaging in patients with biochemical recurrence of prostate cancer. *Nucl Med Commun*. (2021) 42:1239–46. doi: 10.1097/MNM.0000000000001453

97. Iravani A, Hofman MS, Mulcahy T, Williams S, Murphy D, Parameswaran BK, et al. (68)Ga PSMA-11 PET with CT urography protocol in the initial staging and biochemical relapse of prostate cancer. *Cancer Imaging*. (2017) 17:31. doi: 10.1186/s40644-017-0133-5

98. Rosar F, Hügle MJ, Ries M, Bartholomä M, Maus S, Fries P, et al. Benefit of including CT urography in [68Ga]PSMA-11 PET/CT with low-dose CT: first results from a larger prostate cancer cohort analysis. *Q J Nucl Med Mol Imaging*. (2022) 66:280–9. doi: 10.23736/S1824-4785.20.03224-0

99. Tulipan AJ, Guzman AJ, Haslerud TM, Foldnes K, Kvernenes OH, Honoré A, et al. Enhancing PSMA-PET/CT with intravenous contrast: improved tracer clearance in the prostate bed. *Nuklearmedizin*. (2022) 61:394–401. doi: 10.1055/a-1821-8112

100. Blodgett TM, McCook BM, Federle MP. Positron emission tomography/computed tomography: protocol issues and options. *Semin Nucl Med*. (2006) 36:157–68. doi: 10.1053/j.semnuclmed.2005.12.004

frontiers | Frontiers in Medicine

TYPE Brief Research Report
PUBLISHED 20 March 2024
DOI 10.3389/fmed.2024.1384533

OPEN ACCESS

EDITED BY
Nataliya Lutay,
Skåne University Hospital, Sweden

REVIEWED BY
Riemer Slart,
University Medical Center Groningen, Netherlands
Ayaz Aghayev,
Brigham and Women's Hospital and Harvard Medical School, United States
Kornelis van der Geest,
University Medical Center Groningen, Netherlands

*CORRESPONDENCE
Daniel Blockmans
✉ Daniel.Blockmans@uzleuven.be

RECEIVED 09 February 2024
ACCEPTED 01 March 2024
PUBLISHED 20 March 2024

CITATION
Blockmans D, Moreel L, Betrains A, Vanderschueren S, Coudyzer W, Boeckxstaens L and Van Laere K (2024) Association between vascular FDG uptake during follow-up and the development of thoracic aortic aneurysms in giant cell arteritis.
Front. Med. 11:1384533.
doi: 10.3389/fmed.2024.1384533

Association between vascular FDG uptake during follow-up and the development of thoracic aortic aneurysms in giant cell arteritis

Daniel Blockmans[1,2,3]*, Lien Moreel [1,2], Albrecht Betrains[1,2], Steven Vanderschueren[1,2,3], Walter Coudyzer[4], Lennert Boeckxstaens[5,6] and Koen Van Laere[5,6]

[1]Department of General Internal Medicine, University Hospitals Leuven, Leuven, Belgium, [2]Department of Microbiology, Immunology and Transplantation, KU Leuven, Leuven, Belgium, [3]European Reference Network for Immunodeficiency, Autoinflammatory, Autoimmune and Pediatric Rheumatic Disease (ERN-RITA), Utrecht, Netherlands, [4]Department of Radiology, University Hospitals Leuven, Leuven, Belgium, [5]Division of Nuclear Medicine, University Hospitals Leuven, Leuven, Belgium, [6]Department of Imaging and Pathology, Nuclear Medicine and Molecular Imaging, KU Leuven, Leuven, Belgium

Background: A positive PET scan at diagnosis was associated with a greater yearly increase in ascending and descending aortic diameter and thoracic aortic volume in patients with giant cell arteritis (GCA). Radiologic and histopathologic vascular abnormalities persist in a subset of treated patients despite clinical remission. The aim of this study was to evaluate the association between vascular FDG uptake during follow-up and the development of thoracic aortic aneurysms.

Methods: We recently performed a prospective cohort study of 106 GCA patients, who underwent FDG PET and CT imaging at diagnosis and CT imaging yearly for a maximum of 10 years. In this *post hoc* analysis, GCA patients who also have had FDG PET imaging during follow-up were included. PET scans were visually scored (0–3) at 7 vascular areas. PET scans were considered positive in case of FDG uptake ≥grade 2 in any large vessel.

Results: Eighty-eight repeat PET scans were performed in 52 out of 106 GCA patients, who were included in the original prospective cohort. Fifty-five (63%) PET scans were done at the time of a relapse and 33 (38%) were done while in remission. Nine out of ten patients with an incident thoracic aortic aneurysm had both a positive PET scan at diagnosis and during follow-up.

Conclusion: In addition to the intensity and extent of the initial vascular inflammation, ongoing aortic inflammation may contribute to the development of thoracic aortic aneurysms in GCA. However, this hypothesis should be confirmed in a large prospective trial with repeat PET scans at predefined time points during follow-up.

KEYWORDS

giant cell arteritis (GCA), PET, aorta, aneurysm, vasculitis

Introduction

Recently, we reported our results of a prospective study investigating the association between vascular ^{18}F-fluorodeoxyglucose (FDG) uptake at diagnosis and changes in aortic dimensions in 106 giant cell arteritis (GCA) patients (1). We found that GCA patients with a positive FDG positron emission tomography (PET) scan at diagnosis (defined as a scan with FDG uptake grade 2 or higher in any large vessel) had a greater increase in ascending and descending aortic diameter and thoracic aortic volume compared to those with a negative scan. There were no differences in abdominal aortic dimensions. In addition, higher total vascular score (defined as the sum of vascular scoring 0–3 in 7 vascular areas) was associated with a greater yearly increase in thoracic aortic diameters and volume. During follow-up, 15 patients developed a new thoracic aortic aneurysm, most frequently in the descending aorta. Fourteen of these 15 thoracic aortic aneurysms were seen in patients who were PET positive at diagnosis and 87% of the patients had thoracic aortic dilatation in a region with elevated FDG uptake at diagnosis. There was no association between the development of a thoracic aortic aneurysm and the duration of glucocorticoid treatment, the cumulative glucocorticoid dose during the first two years after diagnosis, the use of glucocorticoid-sparing agents or the relapse rate. Hence, we concluded that the intensity and extent of the initial inflammation determines the risk for subsequent aortic dilatation.

However, initial aortic wall inflammation may not be the only determining factor in aneurysm formation. Radiologic vascular abnormalities persist in a subset of treated GCA patients despite clinical remission (2–5). It is unclear whether this represents active inflammation or vascular remodeling. In a recent study, histopathological evaluation of aortic surgical specimens after aortic repair showed active aortitis in most GCA patients, who were treated and were in clinical remission (6). This finding suggests that steroid-resistant, smoldering aortic inflammation possibly contributes to the development of thoracic aortic aneurysms in GCA.

In order to test this hypothesis, we wanted to evaluate if there was an association between persistent vascular FDG uptake and the development of thoracic aortic aneurysms as an exploratory *post hoc* analysis of the previously published prospective cohort of GCA patients (1).

Methods

This study was a *post hoc* analysis of the observational prospective study investigating the association between vascular FDG uptake at diagnosis and change in aortic dimensions in 106 GCA patients. Details on the study protocol and outcomes have been recently published (1). Briefly, we included GCA patients, who were evaluated in the department of General Internal Medicine of the University Hospitals Leuven between 2012 and 2020 and who had undergone FDG PET imaging at diagnosis within 3 days after the initiation of glucocorticoids. Patients with a previous diagnosis of GCA, in whom a PET scan and yearly computed tomography (CT) of the aorta were available, were also included. In this *post hoc* analysis, only patients who also had undergone FDG PET imaging during follow-up, were included. PET scans during follow-up were not part of the initial protocol, but were done at the discretion of the treating physician as judged necessary in real life, for instance when the treating physician was in doubt whether there was a relapse or not.

Patients underwent a CT scan of the thorax and abdomen at diagnosis and yearly thereafter for a maximum of 10 years. The aortic diameter was measured perpendicular to the axis of blood flow at 6 different levels (ascending aorta, aortic arch, descending thoracic aorta, suprarenal, juxtarenal and infrarenal aorta) and the thoracic and abdominal aortic volumes were measured. The ascending aorta was considered aneurysmatic when the diameter was ≥45 mm, the aortic arch ≥40 mm and the descending aorta ≥35 mm (7, 8).

The study was conducted in accordance with the Declaration of Helsinki and approved by the ethical committee of the University Hospitals Leuven.

PET imaging and analysis

Patients were required to fast for at least 6 h before intravenous injection of 4–5 MBq/kg of ^{18}F-FDG, and glycemia levels were determined in all patients (as per procedure, should be <140 mg/dl). A whole-body PET scan was performed 60 min after tracer administration. PET scans were performed between 2003 and 2020, consecutively acquired on four different PET cameras (ECAT HR + PET, Hirez Biograph 16 PET/CT, Truepoint Biograph 40 PET/CT [Siemens, Knoxville, TN, USA] or Discovery MI-4 PET/CT [GE, Milwaukee, WI, USA]). Since gamma rays from the positron annihilation in PET are absorbed by the body, a correction for this attenuation allows quantitatively accurate judgment of internal regions in the body. On the PET/CT systems, either a low-dose CT scan or a diagnostic, high-dose CT scan was performed immediately before PET acquisition. The CT scan was used for attenuation correction and for anatomical localization. For the older HR + acquisitions, no attenuation correction was performed. Attenuation-corrected PET images were thus only available for the scans performed on a PET/CT system ($n = 71$, 81%). PET data were corrected for scatter and randoms. Data were reconstructed using iterative OSEM reconstruction, with image quality parameters improving over the years.

Reconstructed PET images were re-evaluated visually by 1 specialist in nuclear medicine (LB), who was blinded to all other patient information. FDG PET uptake was scored visually at 7 vascular regions (thoracic and abdominal aorta, subclavian, axillary, carotid, iliac, and femoral arteries) as 0 (no FDG uptake), 1 (minimal but not negligible FDG uptake), 2 (clearly increased FDG uptake), or 3 (very marked FDG uptake). PET scans were considered positive in case of FDG uptake ≥grade 2 in any large vessel. If a patient had multiple PET scans during follow-up, the patient was considered to be PET positive during follow-up when one of the PET scans was positive.

Statistical analysis

Categorical and continuous variables were expressed as count (percentage) and as median ± interquartile range (IQR) and range

TABLE 1 Comparison between patients with (included in this *post hoc* analysis) and without (excluded) repeat PET scan during follow-up.

Characteristics	Total (*n* = 106)	Included in *post hoc* analysis (*n* = 52)	Excluded from *post hoc* analysis (*n* = 54)
Age at inclusion, years, mean (SD)	70 (8)	70 (8)	70 (8)
Sex, no. of females, *n* (%)	70 (66%)	33 (63%)	37 (69%)
Symptom duration until diagnosis, week, median (IQR)	6 (3–14)[11]	7 (4–17)[7]	4 (2–9)[4]
Cardiovascular risk factors/events at diagnosis			
○ Active or past tobacco use, *n* (%)	48 (48%)[7]	26 (51%)[1]	22 (46%)[6]
○ Antihypertensive medication, *n* (%)	51 (48%)	24 (46%)	27 (50%)
○ Statin use, *n* (%)	33 (31%)	12 (23%)	21 (39%)
○ Diabetes mellitus, *n* (%)	5 (5%)	1 (2%)	4 (7%)
○ History of stroke, *n* (%)	5 (5%)	2 (4%)	3 (6%)
○ History of myocardial infarction or angina, *n* (%)	2 (2%)	0 (0%)	2 (4%)
○ History of peripheral vascular, disease, *n* (%)	2 (2%)	1 (2%)	1 (2%)
○ Betablocker at diagnosis, *n* (%)	39 (37%)	16 (31%)	23 (43%)
○ Betablocker during follow-up, *n* (%)	54 (51%)	25 (48%)	29 (54%)
AORTA score, median (IQR)	3.09 (2.97–3.22)	3.05 (2.94–3.21)	3.10 (2.98–3.22)
Symptoms at diagnosis			
○ Cranial symptoms, *n* (%)	80 (75%)	39 (75%)	41 (76%)
○ PMR, n (%)	39 (37%)	19 (37%)	20 (37%)
○ Constitutional symptoms, *n* (%)	93 (88%)	45 (87%)	48 (89%)
○ Limb claudication, *n* (%)	4 (4%)	3 (6%)	1 (2%)
Laboratory tests at diagnosis			
○ ESR, mm/h, median (IQR)	68 (48–105)[16]	93 (57–110)[3]	57 (45–70)[13]
○ CRP, mg/l, median (IQR)	89 (48–135)	105 (46–157)	81 (48–129)
Positive temporal artery biopsy at diagnosis, *n* (%)	54 (64%)[22]	25 (60%)[10]	29 (69%)[12]
PET results at diagnosis			
○ Positive PET, *n* (%)	75 (71%)	37 (71%)	38 (70%)
○ Positive PET in thoracic aorta, *n* (%)	61 (58%)	32 (62%)	29 (54%)
○ TVS, median (IQR)	7 (1–14)	8 (1–16)	6 (2–14)
○ Number of vessels with FDG uptake ≥grade 2, median (IQR)	3 (0–5)	3 (0–5)	2 (0–5)
○ Intensity of FDG uptake in affected vessels, median (IQR)°	2.8 (0.0–3.0)	2.8 (0.0–3.0)	2.7 (0.0–3.0)
Treatment			
○ Duration of GC treatment, months, median (IQR)	33 (21–64)[3]	60 (33–96)[2]	24 (17–34)
○ Cumulative GC dose in first 2 years after diagnosis, g methylprednisolone, mean (SD)	4.5 (3.7–5.4)[6]	5.3 (3.9–6.4)[4]	4.1 (3.6–4.8)[2]
○ Use of glucocorticoid-sparing agents during follow-up, *n* (%)	32 (31%)[2]	23 (46%)[2]	9 (17%)
○Duration of follow-up, months, median (IQR)	78 (40–110)	94 (64–120)	55 (29–95)
○Relapse, *n* (%)	69 (65%)	48 (92%)	21 (39%)
Cardiovascular event during follow-up			
○ Aortic dissection, *n* (%)	0 (0)	0 (0)	0 (0)
○ Vascular stenosis, *n* (%)	14 (13%)	10 (19%)	4 (7%)
○ Vascular surgery, *n* (%)	7 (7%)	6 (12%)	1 (2%)
○ Myocardial infarction, *n* (%)	3 (3%)	2 (4%)	1 (2%)
○ Stroke, *n* (%)	11 (10%)	6 (12%)	5 (9%)
○ AION, *n* (%)	2 (2%)	1 (2%)	1 (2%)
Mortality, *n* (%)	15 (14%)	7 (13%)	8 (15%)

AION, anterior ischemic optic neuropathy; CRP, C-reactive protein; ESR, erythrocyte sedimentation rate; FDG, fluorodeoxyglucose; GC, glucocorticoids; IQR, interquartile range; no., number; PET, positron emission tomography; PMR, polymyalgia rheumatica; SD, standard deviation; TVS, total vascular score. Number of missing values are reported in superscript. °Calculated as total vascular score divided by the number of vessels with FDG uptake ≥grade 2.

TABLE 2 Reasons for repeat PET imaging stratified by disease activity.

N (%)	Total (*n* = 88)	Relapse (*n* = 55)	Remission (*n* = 33)
Suspected relapse	76 (86%)	55 (100%)	21 (64%)
Other disorders	5 (6%)	0 (0%)	5 (15%)
PET/CT scan performed instead of standalone CT scan	5 (6%)	0 (0%)	5 (15%)
Simultaneous participation to another study protocol	2 (%)	0 (0%)	2 (6%)

as appropriate. Given the expected bias and small patient number due to the fact that PET scans during follow-up were not part of the initial protocol, we only performed a descriptive analysis and did not perform statistical comparisons.

Results

Eighty-eight repeat PET scans were performed in 52 out of 106 GCA patients, who were included in the original prospective cohort. Compared to patients without repeat PET scan during follow-up, GCA patients with a PET scan during follow-up included in this *post hoc* analysis had a longer symptom duration until diagnosis (7 vs 4 weeks), more frequently experienced relapse (92% vs 39%) and were treated longer (60 vs 24 months) with a higher cumulative glucocorticoid dose in the first 2 years (5.3 vs 4.1 g methylprednisolone) and more frequently with a glucocorticoid-sparing agent (46 vs 17%) (Table 1). There were no differences in age, sex, cardiovascular risk factors, symptoms, PET results, and temporal artery biopsy result at diagnosis and cardiovascular events during follow-up. Median time between PET scan at diagnosis and PET scans during follow-up was 28 months (IQR 17–56 months, range 2–109 months). Median daily methylprednisolone dose at time of repeat PET scan was 1 mg (IQR 0–4 mg, range 0–16 mg). Reasons for repeat PET imaging were described in Table 2. After interpreting all data (clinical signs and symptoms, acute phase response and PET results), 55 (63%) PET scans were done at the time of a relapse and 33 (38%) were done while the patient was in remission. At the time of relapse, 43 (78%) patients had PMR symptoms, 27 (49%) cranial symptoms, 35 (64%) constitutional symptoms and 3 (5%) patients had limb claudication. Among the patients with a positive PET scan at diagnosis ($n = 37$), 31 (84%) were persistently positive and 6 (16%) were negative during follow-up. Among the patients with a negative PET scan at diagnosis ($n = 15$), 12 (80%) remained negative and 3 (20%) were positive during follow-up.

Four out of 52 (8%) patients had a thoracic aortic aneurysm on the first CT scan, who all had both a positive PET scan at diagnosis and during follow-up. Ten (19%) out of 52 patients developed a thoracic aortic aneurysm during follow-up at a median time since diagnosis of 60 months (IQR 34–75), of which 9 patients had both a positive PET scan at diagnosis and during follow-up and 1 patient twice had a negative PET scan. Of the 9 patients with an incident thoracic aortic aneurysm and both a positive PET scan at diagnosis and during follow-up, 7 patients had twice a positive PET scan in the thoracic aorta, one patient had a positive PET scan in the thoracic aorta at diagnosis, but not during follow-up and one patient had twice a negative PET scan in the thoracic aorta. Figure 1 shows the Kaplan-Meier curve of the proportion of patients with an incident thoracic aortic aneurysm stratified according to PET positivity in any large vessel (Figure 1A) and PET positivity in the thoracic aorta (Figure 1B).

Considering all 88 PET scans performed in these 52 patients, 14/17 (82%) PET scans performed during relapse were positive in patients with an incident thoracic aortic aneurysm compared to 26/38 (68%) PET scans in those without an incident thoracic aortic aneurysm (Figure 2). Of the PET scans performed while the patient was in remission, 2/3 (67%) PET scans were positive in patients with an incident thoracic aortic aneurysm compared to 8/30 (27%) PET scans in those without.

Discussion

In our recently published prospective cohort study, we found that total vascular score at diagnosis was associated with a greater yearly increase in thoracic aortic diameters and volume (1). There was no association between the development of a thoracic aortic aneurysm and the treatment regimen or relapse rate. Hence, we concluded that the intensity and extent of the initial inflammation determines the risk for subsequent aortic dilatation.

However, in this *post hoc* analysis we found that nine out of ten incident thoracic aortic aneurysms occurred in GCA patients with both a positive PET scan at diagnosis and during follow-up. This suggests that ongoing aortic inflammation also may contribute to the development of thoracic aortic aneurysms in GCA. Since the majority of repeat PET scans in patients with an incident thoracic aortic aneurysm were performed at the time of a relapse, it is not possible to draw conclusions about FDG uptake in remission in these patients. However, our group earlier described the persistence of FDG uptake in a subset of treated asymptomatic GCA patients (3). In addition, recent reports of the group of Cornelia Weyand on the histopathological evaluation of repeat temporal biopsies (9) and aortic surgical specimens after aortic repair (6) showed ongoing vascular inflammation despite treatment and lack of clinical signs. This smoldering aortic inflammation may be caused by IFN-γ producing Th1 lymphocytes, which are more resistant to glucocorticoids in contrast to Th17 lymphocytes (10). Targeted therapies against Th1 cells may be necessary in addition to glucocorticoids to control chronic, smoldering vasculitis and to prevent the development of thoracic aortic aneurysms.

Four thoracic aortic aneurysms were already present on the first CT scan. These aneurysms may also be caused by smoldering vascular inflammation, which may have been already present prior to the development of symptomatic GCA.

The hypothesis that ongoing aortic inflammation may contribute to the development of thoracic aortic aneurysms in

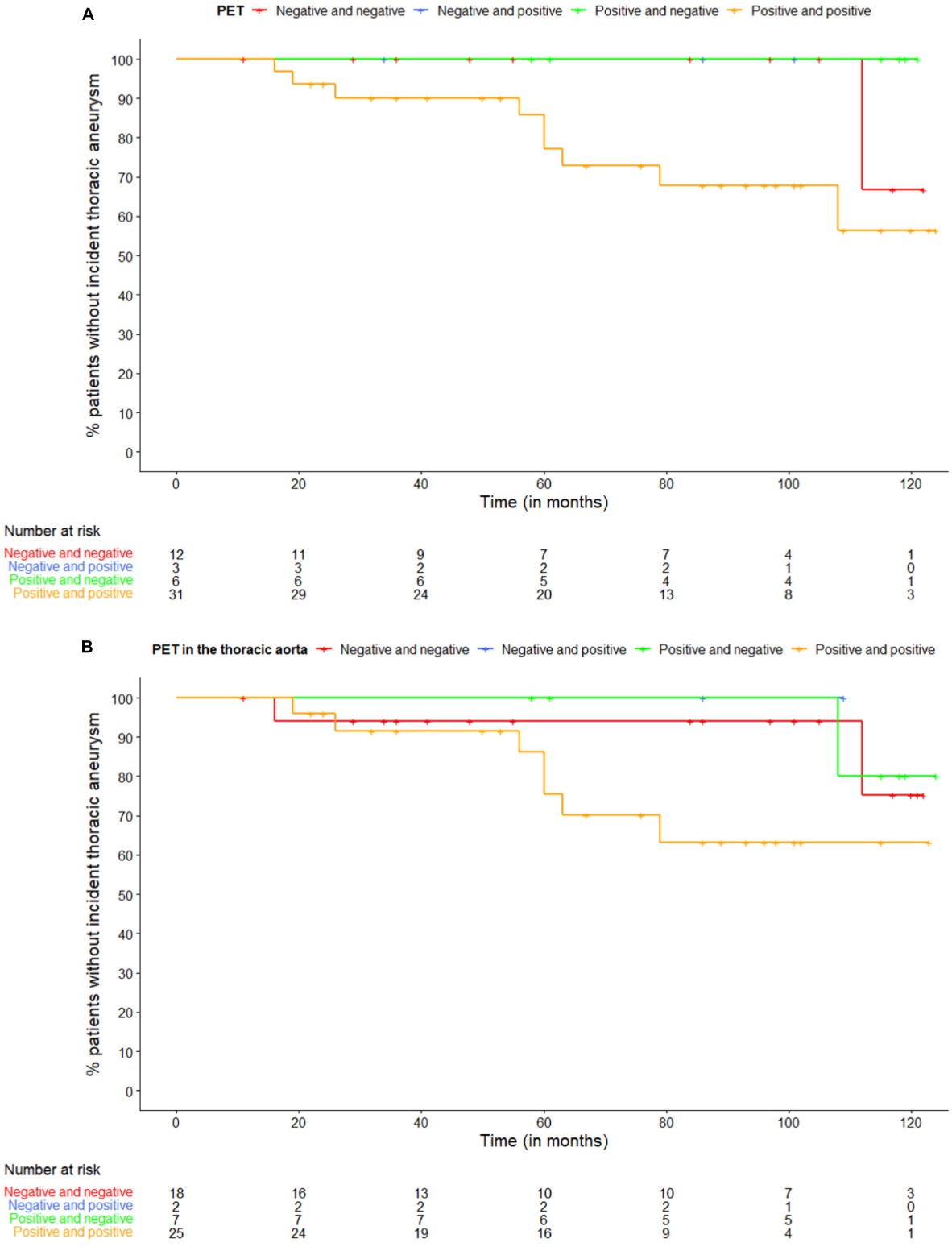

FIGURE 1
Kaplan-Meier curve of the proportion of patients with an incident thoracic aneurysm stratified according to panel **(A)** PET positivity in any large vessel and **(B)** PET positivity in the thoracic aorta. The first PET scan is at diagnosis, the second during follow-up.

GCA is in contrast with the lack of association between occurrence of thoracic aortic aneurysms and treatment regimen or relapse rate. This may be explained by a difference in the number of relapses with large vessel vasculitis and relapses without large vessel vasculitis (e.g., isolated PMR or isolated cranial relapses). However, since there are no specific symptoms of large vessel vasculitis and since we did not routinely perform imaging at time of relapse, we could not prove this hypothesis.

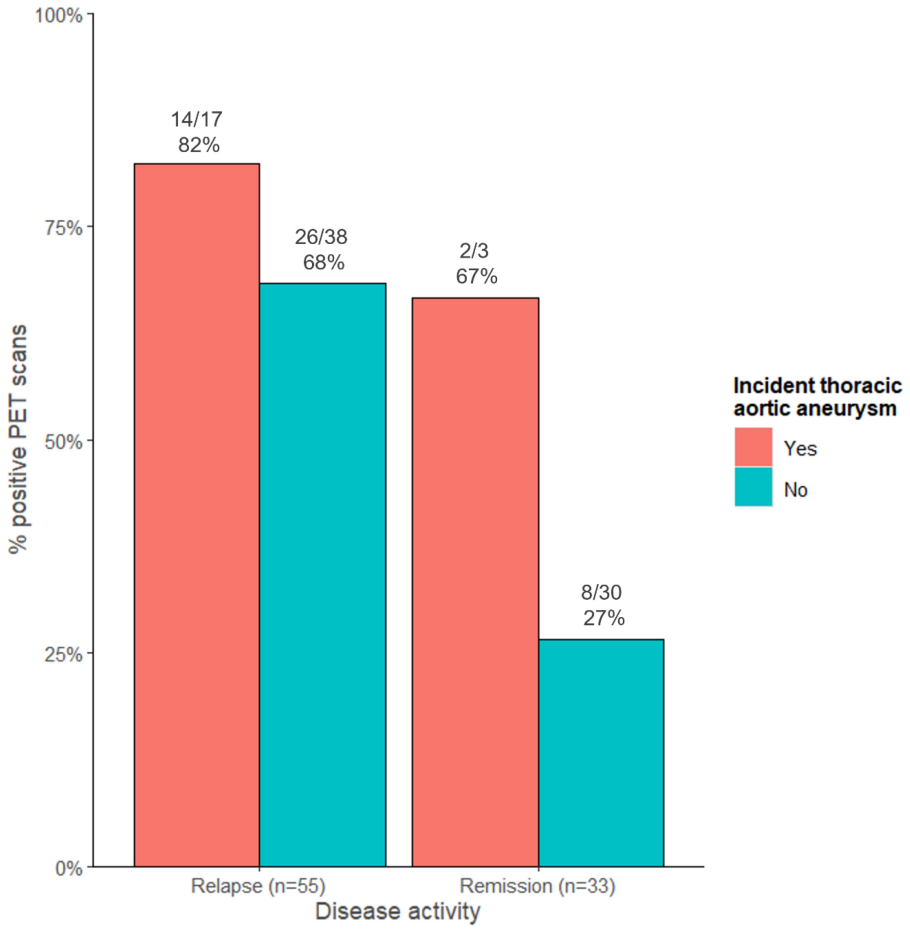

FIGURE 2
Proportion of positive PET scans stratified according to disease activity and to the presence of an incident thoracic aortic aneurysm.

Besides the limitations already mentioned in the original study (PET scans performed over a long time with increasing device quality, part of CT scans performed with contrast or on a PET/CT system, missing CT scans, single-center study and treatment at the discretion of the physician), this study has a major additional limitation. Repeat PET scans at predefined time points during follow-up were not included in the study protocol of the original prospective cohort study. The repeat PET scans during follow-up in this study were performed as driven by clinical practice, most frequently when a relapse was suspected. As a result, there is an important selection bias and the number of patients included is too small to draw solid conclusions. In addition, the data are very heterogeneous, both in terms of disease activity, disease duration since diagnosis and dose of glucocorticoids at the time of the repeat PET scan. Given these important limitations, we only performed a descriptive analysis and did not perform statistical comparisons.

In conclusion, nine out of ten patients with an incident thoracic aortic aneurysm, were PET positive at diagnosis and remained PET positive during follow-up. This finding suggests that in addition to the intensity and extent of the initial inflammation, ongoing aortic inflammation may contribute to the development of thoracic aortic aneurysms in GCA. However, this should be confirmed in a large prospective trial with repeat PET scans at predefined time points during follow-up.

Data availability statement

The original contributions presented in this study are included in this article/supplementary material, further inquiries can be directed to the corresponding author.

Ethics statement

The studies involving humans were approved by the Ethical Committee of the University Hospitals Leuven. The studies were conducted in accordance with the local legislation and institutional requirements. The ethics committee/institutional review board waived the requirement of written informed consent for participation from the participants or the participants' legal guardians/next of kin because this was a purely retrospective study.

Author contributions

DB: Writing – review and editing, Writing – original draft, Supervision, Methodology, Investigation, Formal Analysis, Data curation, Conceptualization. LM: Writing – review and editing,

Writing – original draft, Visualization, Methodology, Investigation, Formal Analysis, Data curation. AB: Writing – review and editing, Writing – original draft, Visualization, Methodology, Formal Analysis, Data curation. SV: Writing – review and editing, Writing – original draft. WC: Writing – review and editing, Writing – original draft, Methodology, Investigation. LB: Writing – review and editing, Writing – original draft, Investigation, Formal Analysis. KL: Writing – review and editing, Writing – original draft.

Funding

The author(s) declare that no financial support was received for the research, authorship, and/or publication of this article.

Conflict of interest

The authors declare that the research was conducted in the absence of any commercial or financial relationships that could be construed as a potential conflict of interest.

Publisher's note

References

1. Moreel L, Coudyzer W, Boeckxstaens L, Betrains A, Molenberghs G, Vanderschueren S, et al. Association between vascular 18F-fluorodeoxyglucose uptake at diagnosis and change in aortic dimensions in giant cell arteritis. *Ann Intern Med.* (2023) 176:1321–9. doi: 10.7326/M23-0679

2. Reichenbach S, Adler S, Bonel H, Cullmann JL, Kuchen S, Bütikofer L, et al. Magnetic resonance angiography in giant cell arteritis: results of a randomized controlled trial of tocilizumab in giant cell arteritis. *Rheumatology.* (2018) 57:982–6. doi: 10.1093/rheumatology/key015

3. Blockmans D, Ceuninck L, Vanderschueren S, Knockaert D, Mortelmans L, Bobbaers H. Repetitive 18F-fluorodeoxyglucose positron emission tomography in giant cell arteritis: a prospective study of 35 patients. *Arthritis Care Res (Hoboken).* (2006) 55:131–7. doi: 10.1002/art.21699

4. Nielsen BD, Therkildsen P, Keller KK, Gormsen LC, Hansen IT, Hauge EM. Ultrasonography in the assessment of disease activity in cranial and large-vessel giant cell arteritis: a prospective follow-up study. *Rheumatology.* (2023) 62:3084–94. doi: 10.1093/rheumatology/kead028

5. Prieto-González S, García-Martínez A, Tavera-Bahillo I, Hernández-Rodríguez J, Gutiérrez-Chacoff J, Alba MA, et al. Effect of glucocorticoid treatment on computed tomography angiography detected large-vessel inflammation in giant-cell arteritis. A prospective, longitudinal study. *Medicine (Baltimore).* (2015) 94:e486. doi: 10.1097/MD.0000000000000486

6. Kaymakci MS, Boire NA, Bois MC, Elfishawi MM, Langenfeld HE, Hanson AC, et al. Persistent aortic inflammation in patients with giant cell arteritis. *Autoimmun Rev.* (2023) 22:103411. doi: 10.1016/j.autrev.2023.103411

7. De Boysson H, Liozon E, Lambert M, Parienti JJ, Artigues N, Geffray L, et al. 18 F-fluorodeoxyglucose positron emission tomography and the risk of subsequent aortic complications in giant-cell arteritis. *Medicine (Baltimore).* (2016) 95:e3851. doi: 10.1097/MD.0000000000003851

8. de Boysson H, Daumas A, Vautier M, Parienti JJ, Liozon E, Lambert M, et al. Large-vessel involvement and aortic dilation in giant-cell arteritis. A multicenter study of 549 patients. *Autoimmun Rev.* (2018) 17:391–8. doi: 10.1016/j.autrev.2017.11.029

9. Maleszewski JJ, Younge BR, Fritzlen JT, Hunder GG, Goronzy JJ, Warrington KJ, et al. Clinical and pathological evolution of giant cell arteritis: a prospective study of follow-up temporal artery biopsies in 40 treated patients. *Mod Pathol.* (2017) 30:788–96. doi: 10.1038/modpathol.2017.10.Clinical

10. Deng J, Younge BR, Olshen RA, Goronzy JJ, Weyand CM. Th17 and th1 T-cell responses in giant cell arteritis. *Circulation.* (2010) 121:906–15. doi: 10.1161/CIRCULATIONAHA.109.872903

frontiers | Frontiers in Medicine

TYPE Systematic Review
PUBLISHED 25 March 2024
DOI 10.3389/fmed.2024.1381863

OPEN ACCESS

EDITED BY
Ronan Abgral,
Centre Hospitalier Regional Universitaire (CHU) de Brest, France

REVIEWED BY
Natale Quartuccio,
Azienda Ospedaliera Ospedali Riuniti Villa Sofia Cervello, Italy
Riccardo Laudicella,
Università degli Studi di Messina, Italy

*CORRESPONDENCE
Giorgio Treglia
✉ giorgio.treglia@eoc.ch

RECEIVED 04 February 2024
ACCEPTED 27 February 2024
PUBLISHED 25 March 2024

CITATION
Rizzo A, Albano D, Dondi F, Cioffi M, Muoio B, Annunziata S, Racca M, Bertagna F, Piccardo A and Treglia G (2024) Diagnostic yield of FAP-guided positron emission tomography in thyroid cancer: a systematic review.
Front. Med. 11:1381863.
doi: 10.3389/fmed.2024.1381863

Diagnostic yield of FAP-guided positron emission tomography in thyroid cancer: a systematic review

Alessio Rizzo[1], Domenico Albano[2], Francesco Dondi[2], Martina Cioffi[3], Barbara Muoio[4], Salvatore Annunziata[5], Manuela Racca[1], Francesco Bertagna[2], Arnoldo Piccardo[6] and Giorgio Treglia[7,8,9]*

[1]Department of Nuclear Medicine, Candiolo Cancer Institute, FPO – IRCCS, Turin, Italy, [2]Division of Nuclear Medicine, Università degli Studi di Brescia and ASST Spedali Civili di Brescia, Brescia, Italy, [3]Nuclear Medicine Unit, Department of Medical Sciences, AOU Città della Salute e della Scienza, University of Turin, Turin, Italy, [4]Clinic of Medical Oncology, Oncology Institute of Southern Switzerland, Ente Ospedaliero Cantonale, Bellinzona, Switzerland, [5]Unità di Medicina Nucleare, GSTeP Radiopharmacy - TracerGLab, Dipartimento di Diagnostica per Immagini, Radioterapia Oncologica ed Ematologia, Fondazione Policlinico Universitario A. Gemelli, IRCCS, Rome, Italy, [6]Department of Nuclear Medicine, E.O. "Ospedali Galliera," Genoa, Italy, [7]Clinic of Nuclear Medicine, Imaging Institute of Southern Switzerland, Ente Ospedaliero Cantonale, Bellinzona, Switzerland, [8]Faculty of Biology and Medicine, University of Lausanne, Lausanne, Switzerland, [9]Faculty of Biomedical Sciences, Università della Svizzera Italiana, Lugano, Switzerland

Background: Several recent studies have proposed the possible application of positron emission tomography/computed tomography (PET/CT) administering radiolabelled fibroblast-activation protein (FAP) inhibitors for various forms of thyroid cancer (TC), including differentiated TC (DTC), and medullary TC (MTC).

Methods: The authors conducted an extensive literature search of original studies examining the effectiveness of FAP-guided PET/CT in patients with TC. The papers included were original publications exploring the use of FAP-targeted molecular imaging in restaging metastatic DTC and MTC patients.

Results: A total of 6 studies concerning the diagnostic yield of FAP-targeted PET/CT in TC (274 patients, of which 247 DTC and 27 MTC) were included in this systematic review. The included articles reported high values of FAP-targeted PET/CT detection rates in TC, ranging from 81 to 100% in different anatomical sites and overall superior to the comparative imaging method.

Conclusion: Although there are promising results, the existing literature on the diagnostic accuracy of FAP-guided PET in this context is still quite limited. To thoroughly evaluate its potential significance in TC patients, it is needed to conduct prospective randomized multicentric trials.

KEYWORDS

thyroid cancer, FAPI, PET, nuclear medicine, oncology, systematic review

1 Introduction

Differentiated thyroid cancer (DTC) is the leading malignant tumour affecting the endocrine system, and its global occurrence continues to increase annually due to the implementation of enhanced screening methods, such as neck ultrasonography and fine needle aspiration biopsy in everyday clinical practice, for detecting and characterising small thyroid nodules (1). Most of these TCs encompass small and asymptomatic papillary TCs (PTCs) belonging to a significant subclinical group of slow-growing tumours (2) and high-risk DTCs in a lower percentage (3). Adjuvant post-surgical Radioiodine (RAI) therapy and relative post-therapeutic whole-body scan performed after RAI administration have traditionally been crucial in assessing the extent of tumour burden in high-risk DTC and the ability of residual or recurrent illness to concentrate RAI (3). Regrettably, only around two-thirds of patients with metastatic DTC exhibit uptake of RAI in their lesions. Conversely, the remainder of patients either develop metastases that do not exhibit significant RAI uptake on post-therapeutic whole-body scan (or lose the ability to concentrate it) or experience disease progression after RAI treatment (3, 4). As a result of this statement, the concept of RAI-refractoriness (RAI-R) was introduced in the literature. According to the latest American and European Thyroid and Nuclear Medicine Societies, RAI-R is defined as follows: patients with abnormal thyroglobulin (Tg) levels or evidence of disease in other diagnostic examinations without RAI concentration on a diagnostic or post-therapeutic RI scan; tumour foci that show RAI uptake while others do not; progressive disease despite evidence of RAI uptake in DTC lesions (3).

Concerning the diagnostic instrumental investigations currently employed to manage RAI-R DTC patients, whole-body contrast-enhanced computed tomography (CT) is the most diffused examination due to its ability to assess the development of locally recurrent invasive disease, lymph node and distant metastases as well as its worldwide availability and cost-effectiveness (5). However, several authors have observed how fluorine-18 fluorodeoxyglucose ([^{18}F]FDG) positron emission tomography (PET)/CT may play a role in the management of these patients, particularly as a prognosis predictor, despite its variable accuracy, which is usually affected by different pathology features such as tumour dedifferentiation and burden (3, 6, 7).

Among the variety of tumours which can onset in the context of thyroid gland, it does worth mention the medullary thyroid cancer (MTC), which is a rare neuroendocrine neoplasm originating from the para-follicular C-cells of the thyroid and encompasses for 3 to 10% of all TCs (8–10). Calcitonin is the most commonly used serum marker for screening and monitoring patients diagnosed with MTC (11). When MTC is detected, the metastatic spread to the cervical lymph nodes is a frequent condition (12). Regarding MTC, CT is the primary cross-sectional imaging technique used to evaluate the severity of the disease in individuals with elevated calcitonin levels, particularly for lymph nodes and liver metastases (although magnetic resonance imaging is more effective in detecting bone lesions) (13, 14). Regarding the molecular imaging of MTC, PET/CT is a highly beneficial nuclear medicine technology in comparison to conventional scintigraphic techniques. The PET radiopharmaceuticals most typically utilized in MTC restaging (when blood tumour marker levels rise) are [^{18}F] dihydroxyphenylalanine ([^{18}F]DOPA), [^{18}F]FDG and [^{68}Ga]Ga-labelled somatostatin analogs and, among them, [^{18}F]DOPA has the best detection rate (15, 16).

Overall, there is an urgent need of more accurate molecular imaging methods focused on new targets for evaluating RAI-R DTC and MTC.

For several decades, carcinomas were thought to be made up of altered cells with cell-autonomous hyper-proliferative and invasive survival features. Nevertheless, the tumour microenvironment (TME), which includes tumour-associated stromal cells and the extracellular matrix, is also crucial in tumour invasion and metastases onset, promoting cell migration (17–19); for example, cancer-associated fibroblasts (CAFs) are a significant component of the tumour stroma. CAFs, also known as reactive fibroblasts or myofibroblasts, are found in a variety of malignant tumours, including head and neck malignancies other than TC (20, 21). FAP expression may also variate according to the solid tumours' grading, such as in prostate cancer (22, 23). Despite CAFs being stromal cells, which are part and parcel of neoplastic lesions, they do not express epithelial, endothelial, or leukocyte markers and are notably devoid of oncogene mutations (24). Finally, CAFs have been found to express a variety of receptors on their cell membrane, including alpha-smooth muscle actin and fibroblast-activating protein (FAP) (25). FAP expression is typically slight in physiologic adult tissues but significantly higher in sites undergoing tissue remodelling, such as malignancies (26). According to these findings, FAP became an attractive target for molecular imaging of various cancers and non-oncological disorders. Subsequently, different radiolabelled FAP inhibitors (FAPi) have been synthesised in order to assess the *in vivo* expression of FAP by PET imaging in various malignancies, including TC (27). The purpose of this systematic is to thoroughly evaluate the diagnostic performance of FAP-guided PET imaging in detecting TC lesions in different clinical scenarios.

2 Materials and methods

2.1 Protocol and review question

A preconceived protocol guided the development of the current systematic review (28). Namely, it was based on the "Preferred Reporting Items for a Systematic Review and Meta-Analysis" (PRISMA 2020 statement) for its put in writing (29). **Supplementary Table 1** reports the thorough PRISMA checklist. The present systematic review was not registered in any comprehensive listing of systematic review protocols (e.g., PROSPERO).

The first step was defining a review question according to the PICO (Population, Intervention, Comparator, Outcomes) framework: which is the diagnostic yield (outcome) of FAP-guided PET imaging (intervention) in patients with TC (patient) compared with other imaging methods (comparator)? This predefined review question has guided the choice of eligibility criteria for the inclusion of pertinent studies in the systematic review.

The comprehensive literature search, study selection, quality assessment and data extraction were all performed by two reviewers

(AR and GT) independently. Any disagreements among the reviewers were resolved through a discussion with a third reviewer.

2.2 Literature search strategy and information sources

As stated, the authors searched for articles concerning the employment of FAP guided PET in the management of TC using two distinct electronic bibliographic databases (Cochrane Library and PubMed/MEDLINE).

Taking into account the predefined review question, a search algorithm was created based on a combination of the following terms: (A) "FAP" OR "FAPi" AND (B) "thyroid." Terms such as "PET," "positron," and "cancer" were deliberately excluded from the search algorithm since the authors agreed on opting for a more sensitive research string than for a specific one, trying to collect all the articles concerning the preconceived topic.

No restrictions were applied regarding the articles' language or publication year. Moreover, reviewers screened included studies' references, searching for additional eligible articles considering the review question. The literature search was last updated on 06 December 2023.

2.3 Eligibility criteria

This systematic review deemed clinical trials reporting data on the diagnostic yield of FAP-guided PET imaging in TC patients appropriate for inclusion. Editorials, letters, reviews, comments, case reports, minor case series, and original investigations on different topics than the preconceived one (including pre-clinical studies) were excluded. Moreover, since the present review had the aim to assess the potential role of FAP-guided PET in TC diagnostics, studies concerning the role of FAP-targeting radiopharmaceuticals as radioligand therapy agents were not considered as papers in the field of interest.

2.4 Selection process

At least two review authors (AR and GT) separately examined the titles and abstracts from the list of records generated using the search string in the selected bibliographic databases. They chose the studies eligible for the systematic review based on the stated inclusion and exclusion criteria, explaining their reasoning for each selection.

2.5 Data collection process and data extraction

The reviewers (AR and GT) gathered data from all of the included studies, taking advantage of full-text, tables, and figures regarding general study information (authors, publication year, country, study design, funding sources); patients' characteristics (sample size, age, sex ratio, clinical setting, histological TC subtypes, serum markers levels); and index text characteristics (employed radiopharmaceuticals, hybrid imaging protocol, administered radiopharmaceutical activity, uptake time).

2.6 Quality assessment (risk of bias assessment)

QUADAS-2, a methodology for evaluating quality in diagnostic test accuracy studies, was chosen to analyse the risk of bias in individual studies and their applicability to the review question (28). Two authors (AR and GT) graded the research in the systematic review based on the potential for bias in four areas (patient selection, index test, reference standard, and flow and timing) and applicability in three categories (patient selection, index test, and reference standard).

3 Results

3.1 Literature search and study selection

The literature search was updated on 06 December 2023 and yielded 244 records. Subsequently, 238 publications were excluded based on the previously stated selection criteria. Of these, 217 were deemed irrelevant to the field of interest, five were reviews, editorials, book chapters, or letters related to the analysed topic, and 16 were case reports within the field of interest. At the end, six publications were judged as eligible by the review authors and they were included in the qualitative synthesis based on the preconceived inclusion criteria (30–35). Reviewers were unable to locate any further appropriate publications by examining the references of these articles. **Figure 1** provides a concise overview of the approach used to select the studies for this analysis.

3.2 Study characteristics

The present systematic review includes six studies satisfying the inclusion criteria. These studies involve 247 TC patients and are comprehensively analysed in **Tables 1–3** (30–35). The chosen studies were published by Chinese (3/6), Indian (2/6), and Turkish (1/6) groups during the years 2022 and 2023. Half of the studies reported in the analysis utilized a prospective design, while the remaining half conducted a retrospective analysis of their case studies. Each trial included in the review was performed in a single Institution. Additionally, two studies mentioned the sources of funding in their text.

Table 2 provides details regarding the TC patients included across the different studies. The number of individuals involved ranged from 24 to 117, with an average age of 42.4 to 53.2 years. The proportion of male participants varied from 24 to 51%. The index test was only employed for restaging RAI-R DTC patients in two papers (29, 32). In three research, it was utilized for restaging DTC patients regardless of their refractoriness to RAI (31–33). The last study focused on employing the index test for both staging and restaging MTC patients (35). Regarding histologic subtypes,

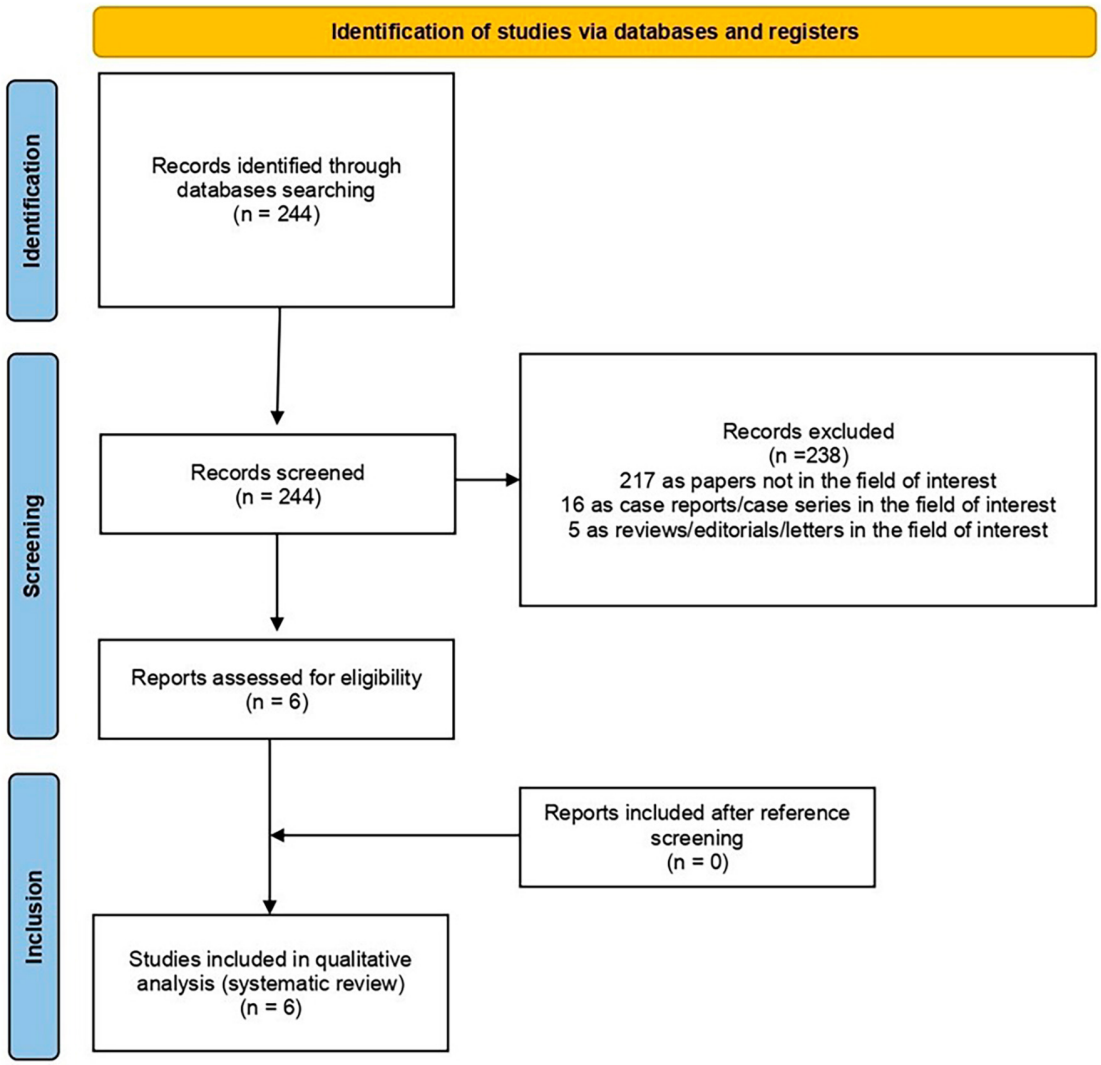

FIGURE 1
Comprehensive overview of the study selection process for the systematic review.

TABLE 1 General study information.

References	Country	Study design/number of involved centres	Funding sources
Chen et al. (30)	China	Prospective/single centre	National Natural Science Foundation of China; Natural Science Foundation of Fujian; Fujian Provincial Health Commission Science and Technology and Programme.
Fu et al. (31)	China	Prospective/single centre	None declared
Mu et al. (32)	China	Prospective/single centre	Guangxi Health Commission; Key Laboratory of Nanomedical Technology (Education Department of Fujian Province); School of Pharmacy, Nano Medical Technology Research Institute, Fujian Medical University; Key Laboratory for Endocrine-Related Cancer Precision Medicine of Xiamen.
Sayiner et al. (33)	Türkiye	Retrospective/Single centre	None declared
Ballal et al. (34)	India	Retrospective/single centre	None declared
Ballal et al. (35)	India	Retrospective/Single centre	None declared

five studies included individuals with DTC, with the most common variant being papillary thyroid cancer (PTC) with 184 patients (30–34). The remaining research specifically targeted patients who had been diagnosed with MTC (33). Regarding the five investigations dealing with DTC, the average value of Tg varied from 60 to 1552 ng/mL (30–34). Conversely, the only study including patients diagnosed with MTC revealed a central value of calcitonin at 666.5 pg/mL (35). Ultimately, tree research studies compared

TABLE 2 Patient key characteristics and clinical settings.

References	Sample size	Mean/median age (years)	Gender (male %)	Clinical setting (no. patients)	Histopathological TC subtypes (no. patients)	Mean/Median Tg / calcitonin	Comparative imaging
Chen et al. (30)	24	Mean: 49.6 ± 10.5	29%	RAI-R DTC	22 PTC 2 n.a.	Mean Tg: 791.7 ng/mL	CT
Fu et al. (31)	35	Median: 44	51%	Restaging DTC	32 PTC 2 FTC 1 Hürthle TC	Median Tg: 60.2 ng/mL	[^{18}F] FDG PET/CT
Mu et al. (32)*	42	Median: 45	38%	Relapsing DTC	36 PTC 5 FTC 1 Hürthle TC	Tg < 10 ng/mL in 24 patients Tg > 10 ng/mL in 18 patients	TxWBS, [^{18}F] FDG PET/CT
Sayiner et al. (33)	29	Mean: 45.8 ± 16.4	24%	Relapsing DTC	25 PTC 4 PDTC	Mean Tg: 1552.9	[^{18}F] FDG PET/CT
Ballal et al. (34)	117	Mean: 53.2 ± 11.7	42%	RAIR-R DTC	69 PTC 17 FTC PDTC	Median Tg: 183 ng/mL	[^{18}F] FDG PET/CT
Ballal et al. (35)	27	Mean: 42.4 ± 13.2	78%	Staging and restating MTC	27 MTC	Median calcitonin: 666.5 pg/mL	[^{68}Ga]Ga-DOTANOC

CT, computed tomography; DTC, differentiated thyroid cancer; FDG, fluorodeoxyglucose; FTC, follicular thyroid cancer; MTC, medullary thyroid cancer; n.a., not available; PET, positron emission tomography; PDTC, poorly differentiated thyroid cancer; PTC, papillary thyroid cancer; RAI-R, radioiodine refractory; TC, thyroid cancer; Tg, thyroglobulin; TxWBS, post-therapeutic radioiodine whole-body scan.
*Only a part of the included patients underwent comparative imaging (13 patients and 11 patients were submitted to TxWBS and [^{18}F] FDG PET/CT).

TABLE 3 Index test key characteristics.

References	Tracer	Hybrid imaging	Tomograph	Administered activity	Uptake time (minutes)	Image analysis
Chen et al. (30)	[^{68}Ga]Ga-DOTA-FAPi-04	Analogic PET/CT	Biograph mCT 64 (Siemens®)	1.85–2.22 MBq/Kg	30	Qualitative, semiquantitative (SUV_{max}, SUV_{mean}, TBR)
Fu et al. (31)	[^{68}Ga]Ga-DOTA-FAPi-04	Digital PET/CT	Discovery MI (GE®)	1.8–2.2 MBq/Kg	60	Qualitative, semiquantitative (SUV_{max})
Mu et al. (32)	[^{18}F]FAPi-42	AnalogicPET/CT	Ingenuity TF (Philips®)	215 MBq	60	Qualitative, semiquantitative (SUV_{max}, TBR)
Sayiner et al. (33)	[^{68}Ga]Ga-DOTA-FAPi-04	Digital PET/CT	Discovery IQ (GE®)	185–222 MBq	30	Qualitative, semiquantitative (SUV_{max})
Ballal et al. (34)	[^{68}Ga]Ga-DOTA.SA.FAPi	Analogic PET/CT	Discovery 710 (GE®)	180 MBq	60	Qualitative, semiquantitative (SUV_{max}, SUL_{peak})
Ballal et al. (35)	[^{68}Ga]Ga-DOTA.SA.FAPi	Analogic PET/CT	Discovery 710 (GE®)	185 MBq	60	Qualitative, semiquantitative (SUV_{max}, SUL_{peak})

CT, computed tomography; FAPi, fibroblast activation protein inhibitor; MBq, MegaBecquerel; PET, positron emission tomography; SUL, standard uptake value corrected for lean body mass; SUV, standardized uptake value; TBR, target-to-background ratio.

10.3389/fmed.2024.1381863

the results obtained from the index test using only [^{18}F]FDG PET/CT (31, 33, 34); another publication compared the index test to [^{18}F]FDG PET/CT and post-therapeutic RAI whole-body scan (32); one paper utilised contrast-enhanced CT as a comparator (30), while the last paper employed [^{68}Ga]Ga-DOTANOC PET/CT (35).

The index test features exhibited substantial variation among the studies taken into account, as seen in **Table 3** of the present review. Three experiments utilised [^{68}Ga]Ga-DOTA-FAPi-04 (30, 31, 33), two studies employed [^{68}Ga]Ga-DOTA-SA-FAPi (34, 35), and one utilised [^{18}F]FAPi-42 (32). The administered activity varied between 180 and 222 MBq when measured using absolute values and between 1.8 and 2.22 MBq/Kg when measured using relative values. Furthermore, there was a time interval of 30 to 60 min between the administration of the experimented radiopharmaceutical and the PET imaging procedure. All the experiments utilised PET/CT as a hybrid imaging technique. PET scans in all the included studies were analysed using qualitative and semiquantitative techniques (30–35). The PET metrics assessed in the included publications were the target-to-background uptake ratio (TBR), as well as the maximal and mean standardised uptake values (SUVmax and SUVmean) of the pathological findings under examination. Regarding the PET metrics documented in the research, two articles authored by the same group presented the standardised uptake value adjusted for the lean body mass of the analysed lesions (SULpeak) (34, 35).

3.3 Risk of bias and applicability

The authors assessed the risk of bias and the relevance of the included publications using the QUADAS-2 tool, extracting the information presented in each investigation. **Figure 2** presents the findings concerning the quality evaluation as well as the concerns regarding the applicability of the included research.

3.4 Results of individual studies (qualitative synthesis)

None of the reports included in the analysis revealed any negative effects following the injection of FAP-targeting radiopharmaceuticals (30). None of the included papers evaluated the inter-reader agreement of FAP-targeted PET images in assessing thyroid malignancies. All the studies dealing with DTC evaluated the uptake of FAP-targeting radiopharmaceuticals in both regional and metastatic sites: in the majority of reports, the tumour uptake was reported to be higher than the surrounding background. Concerning the semiquantitative metrics, average SUVmax reported values ranged from 4.2 and 12.6 for local recurrences and varied between 4.1 and 9.1 for metastatic lesions, including neck lymph nodes and distant metastases in lung, bone, liver and pleura. The high heterogeneity observed among the included studies may be explained by differences in the administered FAP-targeting radiopharmaceutical forms, radiolabelled with different positron-emitters radionuclides, in the PET devices employed and in the uptake times (30–35).

Among the studies exploring the role of FAP-targeted PET in DTC patients, one expressed the uptake of the lesions using standardized uptake value corrected for lean body mass (SULpeak) as the unit of measurement; subsequently, it was not feasible to compare its results to the other included studies. Among the included papers, four assessed the FAP-guided PET diagnostic yield in the detection of local recurrences as well as of distant metastases in DTC based on a per-patient analysis: two of them reported an overall value of detection rate (DR) of approximately 85%, one reported an overall sensitivity and specificity of 96 and 50%, respectively, and one assessed a DR for lymph node metastases of 86%, for lung lesions of 81.7% and bone secondaries of 100%. Conversely, only two of the included studies performed a per lesion analysis, with one paper reporting a sensitivity and specificity for neck lesions of 83 and 42%, respectively, and a DR for distant metastases of 79%, and the other reporting a DR for lymph node metastases of 95.4% (30–34).

When compared to [^{18}F]FDG PET, the index test overall showed a superior diagnostic performance; FAP-guided PET was indeed able to reveal a higher number of lesions both in lymph nodes as well as in lung, bone, and liver; however, its superiority was not statistically relevant in most of the cases. The results of the included papers dealing with DTC, including semiquantitative metrics, sites of the lesions, and diagnostic yield of the index test, are reported in **Table 4** (30–34).

Only one of the included papers focused on patients diagnosed with MTC, enrolling subjects both in a staging and restaging setting. A comprehensive overview of the FAP-guided PET metrics and diagnostic accuracy reported in the paper are presented in **Table 4**. Concerning the diagnostic performance of the index test when compared to [^{68}Ga]Ga-DOTANOC PET/CT, it showed higher accuracy in detecting both local recurrences and distant metastases (35).

With regard to FAP-guided PET imaging accuracy in different TC histopathologic subtypes, none of the included studies made a statistical analysis to assess differences in uptake values among the explored histopathologic variants. Moreover, it is worth noting that none of the included studies incorporated an immunohistochemistry (IHC) analysis in its design to assess the immunostaining of FAP in biopsy samples; in this setting, only one of the included papers performed an IHC analysis to evaluate the expression of FAP in the TME only on one pleural lesion.

Since each study explored the diagnostic yield of FAP-guided PET using a single radiopharmaceutical form, no reports are available concerning the differences in the accuracy of the different FAP-targeting radiopharmaceuticals available in this clinical setting.

4 Discussion

The upregulation of FAP on the cell membrane of stromal cells in the TME offers a promising opportunity for molecular imaging and potentially radioligand therapy (35). In the past few years, there has been a consistent increase in clinical research investigating the application of PET imaging using radiolabelled FAPi in several contexts, mainly in oncology. This emerging research provides crucial insights into the potential applications of this innovative diagnostic approach. Moreover, recent investigations have demonstrated that FAP-guided PET has displayed remarkable

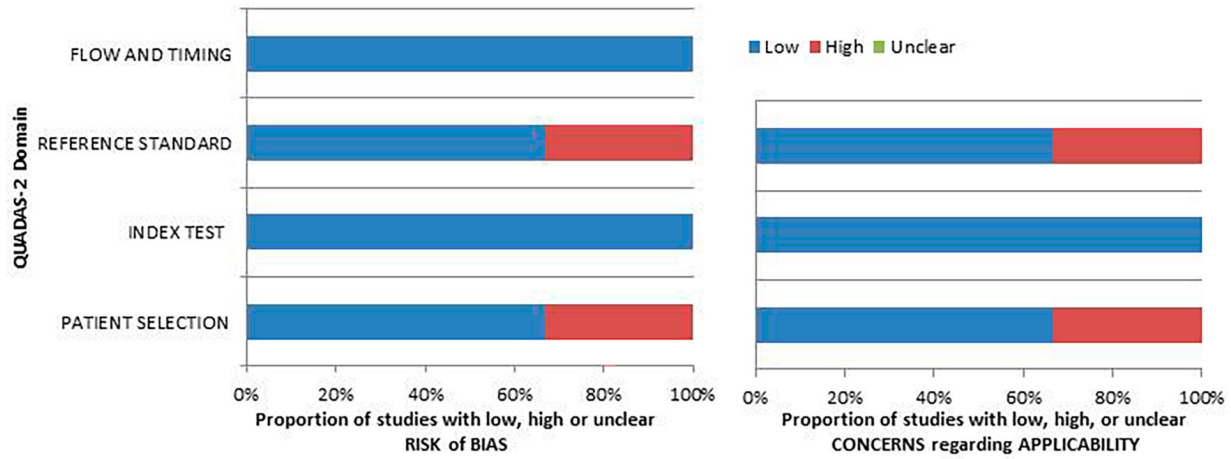

FIGURE 2
An iconographic summary of the quality assessment carried out with the QUADAS-2 tool. The researchers classified the papers included in the qualitative synthesis according to their degree of bias or applicability concerns for specific areas indicated on the ordinate axis. By contrast, the abscissa axis displays the percentage of studies. Based on the graph, about the 40% of the assessed studies demonstrate a notable risk of bias in the "patient selection" and "reference standard" domains.

TABLE 4 Main results of the included studies.

References	Lesions' PET metrics	Lesions site	Diagnostic performance		Outcome
			Per patient	Per lesion	
Chen et al. (30)	Mean SUV_{max} Lymph node: 7.06 ± 0.39 Lung: 6.39 ± 0.91 Bone: 4.01 ± 0.48	Lymph node Lung Bone Pleura	DR: 87.5%	n.a.	DTC lesions showed intermediate-to-high uptake on FAP-guided PET images.
Fu et al. (31)	Median SUV_{max} Local recurrence: 12.6 Lymph node: ranging from 6.0 to 9.1 depending on the region Lung: 1.7 Bone: 6.0	Local recurrence Lymph node Lung Bone Liver	Sensitivity: 96% Specificity: 50%	Neck lesions sensitivity: 83% specificity: 42% Distant metastases DR: 79%	FAP-guided PET has superior diagnostic performance over FDG PET in a per-lesion analysis.
Mu et al. (32)	Median SUV_{max} Local recurrence: 4.2 Lymph node: 3.9 Lung: 1.3	Local recurrence Lymph node Lung Bone	n.a.	n.a.	FAP-guided PET had comparable performance to FDG PET.
Sayiner et al. (33)	Mean SUV_{max} All lesions: 7.5 ± 3.41	n.a.	DR: 86.2%	n.a.	FAP-guided PET was able to individuate more positive patients than FDG PET.
Ballal et al. (34)	Median SUL_{peak} Lymph node: 6.86 Lung: 5.64 Bone: 8.24	Primary tumour Local recurrence Lymph node Lung Pleura Bone Liver Brain	Lymph node DR: 86% Lung DR: 81.7% Bone DR: 100%	Lymph node DR: 95.4%	FAP-targeted PET revealed fewer false-positive and false-negative findings than FDG PET.
Ballal et al. (35)	Median SUL_{peak} Local recurrence: 6.5 Lymph node: 6.9 Lung: 4.6 Bone: 5.8 Liver: 6.0	Primary tumour Lymph nodes Lung Pleura Bone Liver Brain	Primary tumour DR: 100% Lymph node DR: 100% Lung DR: 81.3% Bone DR: 91.6%	Lymph node DR: 98.3% Lung DR: 93.5% Bone DR: 92.4%	FAP-guided PET exhibited a superior accuracy than DOTA-NOC PET in detecting both local recurrence and distant metastases.

DR, detection rate; FAP, fibroblast activation protein; FAPi, fibroblast activation protein inhibitors; n.a., not available; PET, positron emission tomography; SUL_{peak}, standardized uptake value corrected for lean body mass; SUV_{max}, maximum standardized uptake value.

results in identifying various malignancies, including tumours frequently associated with limited or insignificant [^{18}F]FDG uptake (36–38). FAP-targeted PET imaging offers several advantages, since it exhibits relatively lower levels of background activity in muscle and blood pool compared to other tracers (39).

Over the past 2 years, various clinical studies have attempted to assess the diagnostic yield of PET imaging using radiolabelled FAPi in TCs. The research aimed to determine the accuracy of FAPi in various clinical scenarios and to identify its conceivable applications for individuals diagnosed with DTC and MTC (30–35). These research papers have included newly diagnosed individuals and those who previously had surgical procedures or systemic treatments, including RAI therapy. The objective of this systematic review was to collect the existing data, analyse variations among the included studies, and advocate for future research perspectives to ultimately establish a more accurate assessment of the effectiveness of FAP-guided PET.

One of the main issues concerning the regular employment of FAP-targeting radiopharmaceuticals, both as a diagnostic probe or as a theragnostic compound, is the radiopharmaceutical retention in the target cells, especially in monomeric pharmaceutical forms, irrespectively of the radionuclide it is radiolabelled with (36). This statement opens a debate on the best uptake time to acquire emissive images. In the studies gathered in this systematic review, the uptake time ranged between 30 and 60 min, and none of them included a dynamic acquisition in their design. Theoretically, using a shorter uptake time should forestall the radiopharmaceutical excretion; however, dynamic studies of biodistribution in different neoplasms are warranted to assess the best uptake time and advocate for univocal procedure guidelines.

Concerning the diagnostic performance of FAP-targeted PET in DTC, despite most of the studies gathered in this systematic review where proof of concept trials enrolling a constrained number of DTC patients, the evidence is relatively homogeneous (30–34). Indeed, the four studies assessing the DR of this novel instrumental examination observed optimal values in neck lesions (expressed as local recurrence and lymph node metastases) as well as distant metastases in typical and atypical anatomic sites, including lung, liver, bone, and pleura. Interestingly, when compared to [^{18}F]FDG PET, FAP-targeted PET imaging showed more true positive findings and fewer false negative results (30, 31, 33, 34). Despite these differences in terms of number of lesions were not statistically significant in any of the included papers, more studies are needed to assess if the increased DR of this novel imaging technique might be able to change DTC patients' stage and, subsequently, management. The difference in terms of DR of these two instrumental examinations might underlie the variable diagnostic accuracy of [^{18}F]FDG PET in DTC, which is affected by several different clinical and histological features (40–42); however, since none of the included studies assessed the differences in diagnostic accuracy of both examinations based on histologic variants and clinical features; it is not feasible to validate this hypothesis. In this setting, it is noteworthy that [^{18}F]FDG has a valuable diagnostic performance in DTC patients with hematogenous metastases, as stated in a recent meta-analysis of literature (43); unfortunately, it is currently not feasible to make an indirect comparison of these two imaging techniques since the data gathered in this systematic review does not allow to pool the diagnostic accuracies reported in the included studies. More studies are needed in this setting to assess which patients might benefit from FAP-targeted imaging rather than [^{18}F]FDG PET. Furthermore, given the recent technologic developments in PET devices, which allow dual-tracer acquisition protocols, future research should explore the potential impact of an imaging technique assessing two metabolic pathways (related on glucose metabolism and fibroblastic tissue remodelling, respectively) in DTC patients (44, 45).

Regarding the diagnostics of DTC, recent IHC and molecular imaging studies explored the *in vitro* and *in vivo* expression of prostate-specific membrane antigen (PSMA, also known as carboxypeptidase type II), reporting a variable expression of this transmembrane protein on the surface of neo endothelial cells within tumour's neo angiogenesis and conflicting results concerning the potential employment of PSMA-targeted PET in DTC patients (46–48). Given the lack of existing literature comparing these two tracers in DTC patients and the recent development of bispecific radiopharmaceuticals designed to target both FAP and PSMA, it is necessary to conduct prospective studies encompassing both diagnostic methods in order to assess which instrumental examination is more dependable for this type of malignancy (49).

Only one of the included studies explored the diagnostic accuracy of FAP-targeted PET in MTC, reporting an optimal DR in the detection of neck lesions as well as distant metastases, superior to [^{68}Ga]Ga-DOTA-NOC PET (35). In recent literature, it is reported that FAP is highly expressed in peritumoral and intratumoral stromal compartments of MTC and that the expression of AP positively correlates with the level of desmoplasia determined in the histological analysis (50–52). Moreover, it has been reported that desmoplasia is associated with a higher incidence of lymph node metastases in both PTC and MTC. The high uptake of radiolabelled FAPi in MTC lesions is likely explained by the stromal development and the abundant stromal components found even at the early stages of MTC onset (52). As well known, neuroendocrine neoplasms accumulate amine precursors and amino acids, including dihydroxyphenylalanine (DOPA). This molecule, labelled with [^{18}F]F, has been successfully used as an imaging compound for PET/CT investigations in neuroendocrine tumours and is currently considered the best choice for imaging MTC patients in various clinical settings (53, 54). In order to assess the actual advantage of using FAP-targeting radiopharmaceuticals rather than currently available tracers in MTC and advocate for their regular employment in clinical practice, it is necessary to develop clinical trials comparing FAP-targeted imaging to [^{18}F]DOPA PET in patients diagnosed with this malignancy.

So far, RAI has been the most often used additional treatment for patients with intermediate- or high-risk of disease recurrence or metastatic DTC (55). However, patients with advanced DTC either have inherent resistance or develop resistance to this treatment (56). Additionally, MTC and anaplastic TC do not exhibit a valuable response to RAI therapy due to their inability to metabolize iodine. Despite significant advancements in Tyrosine Kinase inhibitor treatments for RAI-R TC in recent years, the presence of drug resistance continues to pose a significant challenge in enhancing prognosis (57). To date, there are no alternative therapies accessible to individuals with progressive tumours who have either completed or declined traditional treatment choices (58). Based on these statements, FAP-targeted therapy with radiolabelled FAPI might provide a potential therapeutic option for

TABLE 5 Synthesis of papers dealing with FAP-targeted radioligand therapy.

References	No. patients	Histopathological TC subtypes (no. patients)	Radiopharmaceutical	Main results
Ballal et al. (59)	1	1 MTC	[^{177}Lu] Lu-DOTAGA.(SA.FAPi)2	Significative reduction of the tumour burden with significant improvement in the quality of life of the patient.
Ballal et al. (60)	15	15 RAI-R DTC	[^{177}Lu]-DOTAGA.(SA.FAPi)2	About half of the enrolled patients had partial response to treatment or stable disease. None of the patients experienced grade III/IV hematological, renal, or hepatotoxicity.
Fu et al. (61)	1	RAI-R DTC	[^{177}Lu] Lu-FAPi-46	The patient had stable disease after a four-cycles treatment.
Fu et al. (62)	12	RAI-R DTC	[^{177}Lu] Lu-EB-FAPi	Overall, the radiopharmaceutical was well tolerated by all patients with high radiation doses delivered to mRAIR-TC lesions.
Martin et al. (63)	1	MTC	[^{177}Lu] Lu-DOTAGA.Glu.(FAPi)$_2$	The employed radiopharmaceutical showed longer retention than other pharmaceutical forms.

FAPi, fibroblast activation protein inhibitors; MTC, medullary thyroid cancer; RAI-R, radioiodine refractory; DTC, differentiated thyroid cancer.

RAI-R TC patients. In this setting, several [^{177}Lu]Lu-radiolabelled FAP-targeting compounds were tested to assess their safety; as a result, these pharmaceuticals were well tolerated by RAI-R TC patients. Moreover, the preliminary data on the efficacy of these novel radiopharmaceuticals encourage further research to assess if they can significantly prolong survival in this clinical scenario (59–63). **Table 5** synthesizes the main results of these trials.

This systematic review represents the first thorough literature examination concerning the use of FAP-targeting PET radiopharmaceuticals in patients with thyroid malignancies. However, it is worth noting that it accounts for significant limitations, including the limited number of studies in the field of interest with constrained sample sizes and their heterogeneity, which hampered the possibility of drawing up a quantitative analysis of the retrieved data. Furthermore, potential sources of bias about patient selection and comparative imaging domains were found in the included studies.

5 Conclusion

The presented systematic review has furnished qualitative data underscoring the potential role of FAP-targeted radiopharmaceuticals in the diagnostics of different forms of TC, and potentially in its employment as theragnostic agent.

Data availability statement

The original contributions presented in the study are included in the article/**Supplementary material**, further inquiries can be directed to the corresponding author.

Author contributions

AR: Writing – review and editing, Writing – original draft. DA: Writing – review and editing. FD: Writing – review and editing. MC: Writing – review and editing. BM: Writing – review and editing. SA: Writing – review and editing. MR: Writing – review and editing. FB: Writing – review and editing. AP: Writing – review and editing. GT: Writing – review and editing, Writing – original draft.

Funding

The author(s) declare that no financial support was received for the research, authorship, and/or publication of this article.

Conflict of interest

The authors declare that the research was conducted in the absence of any commercial or financial relationships that could be construed as a potential conflict of interest.

The author(s) declared that they were an editorial board member of Frontiers, at the time of submission. This had no impact on the peer review process and the final decision.

Publisher's note

Supplementary material

The Supplementary Material for this article can be found online at: https://www.frontiersin.org/articles/10.3389/fmed.2024.1381863/full#supplementary-material

References

1. McLeod D, Zhang L, Durante C, Cooper D. Contemporary debates in adult papillary thyroid cancer management. *Endocr Rev.* (2019) 40:1481–99. doi: 10.1210/er.2019-00085

2. Enewold L, Zhu K, Ron E, Marrogi A, Stojadinovic A, Peoples G, et al. Rising thyroid cancer incidence in the United States by demographic and tumor characteristics, 1980–2005. *Cancer Epidemiol Biomark Prev.* (2009) 18:784–91. doi: 10.1158/1055-9965.EPI-08-0960

3. Haugen B, Alexander E, Bible K, Doherty G, Mandel S, Nikiforov Y, et al. 2015 American thyroid association management guidelines for adult patients with thyroid nodules and differentiated thyroid cancer: The American thyroid association guidelines task force on thyroid nodules and differentiated thyroid cancer. *Thyroid.* (2016) 26:1–133. doi: 10.1089/thy.2015.0020

4. Fugazzola L, Elisei R, Fuhrer D, Jarzab B, Leboulleux S, Newbold K, et al. 2019 European thyroid association guidelines for the treatment and follow-up of advanced radioiodine-refractory thyroid cancer. *Eur Thyroid J.* (2019) 8:227–45. doi: 10.1159/000502229

5. Yoon D, Hwang H, Chang S, Rho Y, Ahn H, Kim J, et al. CT, MR, U,18F-FDG PET/CT, and their combined use for the assessment of cervical lymph node metastases in squamous cell carcinoma of the head and neck. *Eur Radiol.* (2009) 19:634–42. doi: 10.1007/s00330-008-1192-6

6. Rizzo A, Perotti G, Zagaria L, Lanni V, Racca M, Palestini N, et al. 18F-FDG PET/CT concurrent with first radioiodine post-therapeutic scan in high risk differentiated thyroid cancer: A useful tool or just an expensive diversion? *Q J Nucl Med Mol Imaging.* (2023) 67:158–66. doi: 10.23736/S1824-4785.22.03364-7

7. Leboulleux S, Schroeder P, Busaidy N, Auperin A, Corone C, Jacene H, et al. Assessment of the incremental value of recombinant thyrotropin stimulation before 2-[18F]-Fluoro-2-deoxy-D-glucose positron emission tomography/computed tomography imaging to localize residual differentiated thyroid cancer. *J Clin Endocrinol Metab.* (2009) 94:1310–6. doi: 10.1210/jc.2008-1747

8. Imperiale A, Berti V, Burgy M, Cazzato R, Piccardo A, Treglia G. Molecular imaging and related therapeutic options for medullary thyroid carcinoma: State of the art and future opportunities. *Rev Endocr Metab Disord.* (2023) 25:187–202. doi: 10.1007/s11154-023-09836-y

9. Costante G, Meringolo D, Durante C, Bianchi D, Nocera M, Tumino S, et al. Predictive value of serum calcitonin levels for preoperative diagnosis of medullary thyroid carcinoma in a cohort of 5817 consecutive patients with thyroid nodules. *J Clin Endocrinol Metab.* (2007) 92:450–5. doi: 10.1210/jc.2006-1590

10. Essig G, Porter K, Schneider D, Arpaia D, Lindsey S, Busonero G, et al. Multifocality in sporadic medullary thyroid carcinoma: An international multicenter study. *Thyroid.* (2016) 26:1563–72. doi: 10.1089/thy.2016.0255

11. Machens A, Dralle H. Biological relevance of medullary thyroid microcarcinoma. *J Clin Endocrinol Metab.* (2012) 97:1547–53. doi: 10.1210/jc.2011-2534

12. Moley J. Medullary thyroid carcinoma: Management of lymph node metastases. *J Natl Compr Canc Netw.* (2010) 8:549–56. doi: 10.6004/jnccn.2010.0042

13. Machens A, Dralle H. Biomarker-based risk stratification for previously untreated medullary thyroid cancer. *J Clin Endocrinol Metab.* (2010) 95:2655–63. doi: 10.1210/jc.2009-2368

14. Klain M, Hadoux J, Nappi C, Finessi M, Ambrosio R, Schlumberger M, et al. Imaging medullary thyroid cancer patients with detectable serum markers: State of the art and future perspectives. *Endocrine.* (2022) 75:330–7. doi: 10.1007/s12020-021-02930-8

15. Castinetti F, Taïeb D. Positron emission tomography imaging in medullary thyroid carcinoma: Time for reappraisal? *Thyroid.* (2021) 31:151–5. doi: 10.1089/thy.2020.0674

16. Treglia G, Sadeghi R, Giovinazzo F, Galiandro F, Annunziata S, Muoio B, et al. PET with different radiopharmaceuticals in neuroendocrine neoplasms: An umbrella review of published meta-analyses. *Cancers (Basel).* (2021) 13:5172. doi: 10.3390/cancers13205172

17. Yang X, Lin Y, Shi Y, Li B, Liu W, Yin W, et al. FAP promotes immunosuppression by cancer-associated fibroblasts in the tumor microenvironment via STAT3-CCL2 signaling. *Cancer Res.* (2016) 76:4124–35. doi: 10.1158/0008-5472.CAN-15-2973

18. Jiang K, Xu L, Ning J, Cheng F. FAP promotes clear cell renal cell carcinoma progression via activating the PI3K/AKT/mTOR signaling pathway. *Cancer Cell Int.* (2023) 23:217. doi: 10.1186/s12935-023-03073-8

19. Cho J, Byeon H, Oh K, Baek S, Kwon S, Jung K, et al. Clinicopathological significance of cancer-associated fibroblasts in papillary thyroid carcinoma: A predictive marker of cervical lymph node metastasis. *Eur Arch Otorhinolaryngol.* (2018) 275:2355–61. doi: 10.1007/s00405-018-5061-x

20. Rizzo A, Miceli A, Racca M, Bauckneht M, Morbelli S, Albano D, et al. Diagnostic accuracy of [^{68}Ga]Ga labeled fibroblast-activation protein inhibitors in detecting head and neck cancer lesions using positron emission tomography: A systematic review and a meta-analysis. *Pharmaceuticals.* (2023) 16:1664. doi: 10.3390/ph16121664

21. Treglia G, Muoio B, Roustaei H, Kiamanesh Z, Aryana K, Sadeghi R. Head-to-head comparison of fibroblast activation protein inhibitors (FAPI) radiotracers versus [^{18}F]F-FDG in oncology: A systematic review. *Int J Mol Sci.* (2021) 22:11192. doi: 10.3390/ijms222011192

22. Laudicella R, Spataro A, Crocè L, Giacoppo G, Romano D, Davì V, et al. Preliminary findings of the role of FAPi in prostate cancer theranostics. *Diagnostics (Basel).* (2023) 13:1175. doi: 10.3390/diagnostics13061175

23. Giesel F, Kratochwil C, Lindner T, Marschalek M, Loktev A, Lehnert W, et al. ^{68}Ga-FAPI PET/CT: Biodistribution and preliminary dosimetry estimate of 2 DOTA-containing FAP-targeting agents in patients with various cancers. *J Nucl Med.* (2019) 60:386–92.

24. Sahai E, Astsaturov I, Cukierman E, DeNardo D, Egeblad M, Evans R, et al. A framework for advancing our understanding of cancer-associated fibroblasts. *Nat Rev Cancer.* (2020) 20:174–86. doi: 10.1038/s41568-019-0238-1

25. Peltier A, Seban R, Buvat I, Bidard F, Mechta-Grigoriou F. Fibroblast heterogeneity in solid tumors: From single cell analysis to whole-body imaging. *Semin Cancer Biol.* (2022) 86:262–72. doi: 10.1016/j.semcancer.2022.04.008

26. Mousavi M, Farhadi E, Vodjgani M, Karami J, Tahmasebi M, Sharafat Vaziri A, et al. Role of fibroblast activation protein alpha in fibroblast-like synoviocytes of rheumatoid arthritis. *Iran J Allergy Asthma Immunol.* (2021) 20:338–49. doi: 10.18502/ijaai.v20i3.6335

27. Mona C, Benz M, Hikmat F, Grogan T, Lueckerath K, Razmaria A, et al. Correlation of ^{68}Ga-FAPi-46 PET biodistribution with FAP expression by immunohistochemistry in patients with solid cancers: Interim analysis of a prospective translational exploratory study. *J Nucl Med.* (2022) 63:1021–6. doi: 10.2967/jnumed.121.262426

28. Sadeghi R, Treglia G. Systematic reviews and meta-analyses of diagnostic studies: A practical guideline. *Clin Transl Imaging.* (2017) 5:83–7. doi: 10.1007/s40336-016-0219-2

29. Page M, McKenzie J, Bossuyt P, Boutron I, Hoffmann T, Mulrow C, et al. The PRISMA 2020 statement: An updated guideline for reporting systematic reviews. *BMJ.* (2021) 372:n71. doi: 10.1136/bmj.n71

30. Chen Y, Zheng S, Zhang J, Yao S, Miao W. ^{68}Ga-DOTA-FAPI-04 PET/CT imaging in radioiodine-refractory differentiated thyroid cancer (RR-DTC) patients. *Ann Nucl Med.* (2022) 36:610–22. doi: 10.1007/s12149-022-01742-8

31. Fu H, Wu J, Huang J, Sun L, Wu H, Guo W, et al. ^{68}Ga fibroblast activation protein inhibitor PET/CT in the detection of metastatic thyroid cancer: Comparison with 18F-FDG PET/CT. *Radiology.* (2022) 304:397–405. doi: 10.1148/radiol.212430

32. Mu X, Huang X, Jiang Z, Li M, Jia L, Lv Z, et al. [^{18}F]FAPI-42 PET/CT in differentiated thyroid cancer: Diagnostic performance, uptake values, and comparison with 2-[^{18}F]FDG PET/CT. *Eur J Nucl Med Mol Imaging.* (2023) 50:1205–15. doi: 10.1007/s00259-022-06067-2

33. Sayiner Z, Elboğa U, Sahin E, Ozturk S, Cayirli Y, Celen Y, et al. Comparison of ^{68}Ga-FAPI-04 and ^{18}F-FDG PET/CT for diagnosis of metastatic lesions in patients with recurrent papillary thyroid carcinoma. *Hell J Nucl Med.* (2023) 26:41–6. doi: 10.1967/s002449912560

34. Ballal S, Yadav M, Roesch F, Satapathy S, Moon E, Martin M, et al. Head-to-head comparison of [^{68}Ga]Ga-DOTA.SA.FAPi with [^{18}F]F-FDG PET/CT in radioiodine-resistant follicular-cell derived thyroid cancers. *Eur J Nucl Med Mol Imaging.* (2023) 51:233–44. doi: 10.1007/s00259-023-06404-z

35. Ballal S, Yadav M, Roesch F, Raju S, Satapathy S, Sheokand P, et al. Head-to-head comparison of [^{68}Ga]Ga-DOTA.SA.FAPi and [^{68}Ga]Ga-DOTANOC positron emission tomography/computed tomography imaging for the follow-up surveillance of patients with medullary thyroid cancer. *Thyroid.* (2023) 33:974–82. doi: 10.1089/thy.2023.0008

36. Gilardi L, Airò Farulla L, Demirci E, Clerici I, Omodeo Salè E, Ceci F. Imaging cancer-associated fibroblasts (CAFs) with FAPi PET. *Biomedicines.* (2022) 10:523. doi: 10.3390/biomedicines10030523

37. Kratochwil C, Flechsig P, Lindner T, Abderrahim L, Altmann A, Mier W, et al. ^{68}Ga-FAPI PET/CT: Tracer uptake in 28 different kinds of cancer. *J Nucl Med.* (2019) 60:801–5. doi: 10.2967/jnumed.119.227967

38. Chen H, Zhao L, Ruan D, Pang Y, Hao B, Dai Y, et al. Usefulness of [^{68}Ga]Ga-DOTA-FAPI-04 PET/CT in patients presenting with inconclusive [^{18}F]FDG PET/CT findings. *Eur J Nucl Med Mol Imaging.* (2021) 48:73–86. doi: 10.1007/s00259-020-04940-6

39. Meyer C, Dahlbom M, Lindner T, Vauclin S, Mona C, Slavik R, et al. Radiation dosimetry and biodistribution of ^{68}Ga-FAPI-46 PET imaging in cancer patients. *J Nucl Med.* (2020) 61:1171–7. doi: 10.2967/jnumed.119.236786

40. Salvatori M, Biondi B, Rufini V. Imaging in endocrinology: 2-[18F]-fluoro-2-deoxy-D-glucose positron emission tomography/computed tomography in differentiated thyroid carcinoma: Clinical indications and controversies in diagnosis and follow-up. *Eur J Endocrinol.* (2015) 173:R115–30. doi: 10.1530/EJE-15-0066

41. Santhanam P, Khthir R, Solnes L, Ladenson P. THE RELATIONSHIP OF BRAF^{V600E} MUTATION STATUS TO FDG PET/CT AVIDITY IN THYROID CANCER: A REVIEW AND META-ANALYSIS. *Endocr Pract.* (2018) 24:21–6. doi: 10.4158/EP-2017-0080

42. Sonavane S, Basu S. Role of PET/computed tomography in elderly thyroid cancer: Tumor biology and clinical management. *PET Clin.* (2023) 18:81–101. doi: 10.1016/j.cpet.2022.09.005

43. Quartuccio N, Rubello D. Role of ^{18}F-FDG PET/CT in detection of hematogenous metastases of advanced differentiated thyroid carcinoma: A systematic review and meta-analysis. *J Cancer Metastasis Treat.* (2021) 7:14. doi: 10.20517/2394-4722.2020.118

44. Filippi L, Dimitrakopoulou-Strauss A, Evangelista L, Schillaci O. Long axial field-of-view PET/CT devices: Are we ready for the technological revolution? *Expert Rev Med Devices.* (2022) 19:739–43. doi: 10.1080/17434440.2022.2141111

45. Roth K, Voltin C, van Heek L, Wegen S, Schomäcker K, Fischer T, et al. Dual-tracer PET/CT protocol with [^{18}F]-FDG and [^{68}Ga]Ga-FAPI-46 for cancer imaging: A proof of concept. *J Nucl Med.* (2022) 63:1683–6. doi: 10.2967/jnumed.122.263835

46. Rizzo A, Racca M, Dall'Armellina S, Delgado Bolton R, Albano D, Dondi F, et al. Potential role of PSMA-targeted PET in thyroid malignant disease: A systematic review. *Diagnostics (Basel).* (2023) 13:564. doi: 10.3390/diagnostics13030564

47. Sollini M, di Tommaso L, Kirienko M, Piombo C, Erreni M, Lania A, et al. PSMA expression level predicts differentiated thyroid cancer aggressiveness and patient outcome. *EJNMMI Res.* (2019) 9:93. doi: 10.1186/s13550-019-0559-9

48. Feng, Y, Shi Y, Xia Z, Xu L, Li W, Pang H, et al. The clinical signification and application value of [^{68}Ga]Ga-PSMA imaging in thyroid malignancy. *Endocrine.* (2023). doi: 10.1007/s12020-023-03599-x [Epub ahead of print].

49. Verena A, Zhang Z, Kuo H, Merkens H, Zeisler J, Wilson R, et al. Synthesis and preclinical evaluation of three novel ^{68}Ga-labeled bispecific PSMA/FAP-targeting tracers for prostate cancer imaging. *Molecules.* (2023) 28:1088. doi: 10.3390/molecules28031088

50. Prete A, Borges de Souza P, Censi S, Muzza M, Nucci N, Sponziello M. Update on fundamental mechanisms of thyroid cancer. *Front Endocrinol (Lausanne).* (2020) 11:102. doi: 10.3389/fendo.2020.00102

51. Arcucci A, Ruocco M, Granato G, Sacco A, Montagnani S. Cancer: An oxidative crosstalk between solid tumor cells and cancer associated fibroblasts. *Biomed Res Int.* (2016) 2016:4502846. doi: 10.1155/2016/4502846

52. Koperek O, Scheuba C, Puri C, Birner P, Haslinger C, Rettig W, et al. Molecular characterization of the desmoplastic tumor stroma in medullary thyroid carcinoma. *Int J Oncol.* (2007) 31:59–67.

53. Treglia G, Rufini V, Piccardo A, Imperiale A. Update on management of medullary thyroid carcinoma: Focus on nuclear medicine. *Semin Nucl Med.* (2023) 53:481–9. doi: 10.1053/j.semnuclmed.2023.01.003

54. Araz M, Soydal Ç, Demir Ö, Gökcan M, Küçük N. The Role of ^{18}F-FDOPA PET/CT in recurrent medullary thyroid cancer patients with elevated serum calcitonin levels. *Mol Imaging Radionucl Ther.* (2023) 32:1–7. doi: 10.4274/mirt.galenos.2022.81904

55. Luster M, Pfestroff A, Hänscheid H, Verburg F. Radioiodine therapy. *Semin Nucl Med.* (2017) 47:126–34. doi: 10.1053/j.semnuclmed.2016.10.002

56. Chan W, Chan S, Kwong D. Radioiodine refractory differentiated thyroid cancer. *Methods Mol Biol.* (2022) 2534:243–57. doi: 10.1007/978-1-0716-2505-7_17

57. Schlumberger M, Tahara M, Wirth L, Robinson B, Brose M, Elisei R, et al. Lenvatinib versus placebo in radioiodine-refractory thyroid cancer. *N Engl J Med.* (2015) 372:621–30. doi: 10.1056/NEJMoa1406470

58. Ancker O, Krüger M, Wehland M, Infanger M, Grimm D. Multikinase inhibitor treatment in thyroid cancer. *Int J Mol Sci.* (2019) 21:10. doi: 10.3390/ijms21010010

59. Ballal S, Yadav M, Moon E, Rösch F, ArunRaj S, Agarwal S, et al. First-in-human experience with 177Lu-DOTAGA.(SA.FAPi)2 therapy in an uncommon case of aggressive medullary thyroid carcinoma clinically mimicking as anaplastic thyroid cancer. *Clin Nucl Med.* (2022) 47:e444–5. doi: 10.1097/RLU.0000000000004164

60. Ballal S, Yadav M, Moon E, Roesch F, Kumari S, Agarwal S, et al. Novel fibroblast activation protein inhibitor-based targeted theranostics for radioiodine-refractory differentiated thyroid cancer patients: A pilot study. *Thyroid.* (2022) 32:65–77. doi: 10.1089/thy.2021.0412

61. Fu H, Huang J, Sun L, Wu H, Chen H. FAP-targeted radionuclide therapy of advanced radioiodine-refractory differentiated thyroid cancer with multiple cycles of 177 Lu-FAPI-46. *Clin Nucl Med.* (2022) 47:906–7. doi: 10.1097/RLU.0000000000004260

62. Fu H, Huang J, Zhao T, Wang H, Chen Y, Xu W, et al. Fibroblast activation protein-targeted radioligand therapy with 177Lu-EB-FAPI for metastatic radioiodine-refractory thyroid cancer: First-in-human, dose-escalation study. *Clin Cancer Res.* (2023) 29:4740–50. doi: 10.1158/1078-0432.CCR-23-1983

63. Martin M, Ballal S, Yadav M, Bal C, Van Rymenant Y, De Loose J, et al. Novel generation of FAP inhibitor-based homodimers for improved application in radiotheranostics. *Cancers (Basel).* (2023) 15:1889. doi: 10.3390/cancers15061889

frontiers | Frontiers in Medicine

TYPE Brief Research Report
PUBLISHED 15 May 2024
DOI 10.3389/fmed.2024.1414415

OPEN ACCESS

EDITED BY
Giorgio Treglia,
Ente Ospedaliero Cantonale (EOC), Switzerland

REVIEWED BY
Alessio Rizzo,
IRCCS Candiolo Cancer Institute, Italy
Domenico Albano,
University of Brescia, Italy

*CORRESPONDENCE
Erik H. J. G. Aarntzen
✉ erik.aarntzen@radboudumc.nl

RECEIVED 08 April 2024
ACCEPTED 29 April 2024
PUBLISHED 15 May 2024

CITATION
Koenen HJPM, Kouijzer IJE, de Groot M, Peters S, Lobeek D, van Genugten EAJ, Diavatopoulos DA, van Oosten N, Gianotten S, Prokop MM, Netea MG, van de Veerdonk FL and Aarntzen EHJG (2024) Preliminary evidence of localizing CD8+ T-cell responses in COVID-19 patients with PET imaging.
Front. Med. 11:1414415.
doi: 10.3389/fmed.2024.1414415

Preliminary evidence of localizing CD8+ T-cell responses in COVID-19 patients with PET imaging

Hans J. P. M. Koenen[1], Ilse J. E. Kouijzer[2], Michel de Groot[3], Steffie Peters[3], Daphne Lobeek[3], Evelien A. J. van Genugten[3], Dimitri A. Diavatopoulos[1], Nienke van Oosten[2], Sanne Gianotten[2], Mathias M. Prokop[3], Mihai G. Netea[2], Frank L. van de Veerdonk[2] and Erik H. J. G. Aarntzen[1]*

[1]Department of Laboratory Medicine, Radboud University Medical Center, Nijmegen, Netherlands, [2]Department of Internal Medicine and Radboud Center for Infectious Diseases, Radboud University Medical Center, Nijmegen, Netherlands, [3]Department of Medical Imaging, Radboud University Medical Center, Nijmegen, Netherlands

The upper respiratory tract (URT) is the entry site for severe acute respiratory syndrome-coronavirus-2 (SARS-CoV-2), from where it further disseminates. Early and effective adaptive immune responses are crucial to restrict viral replication and limit symptom development and transmission. Current vaccines increasingly incorporate strategies to boost mucosal immunity in the respiratory tract. Positron emission tomography (PET) is a non-invasive technology that measures cellular responses at a whole-body level. In this case series, we explored the feasibility of [^{89}Zr]Zr-crefmirlimab berdoxam PET to assess CD8+ T-cell localization during active COVID-19. Our results suggest that CD8+ T-cell distributions assessed by PET imaging reflect their differentiation and functional state in blood. Therefore, PET imaging may represent a novel tool to visualize and quantify cellular immune responses during infections at a whole-body level.

KEYWORDS

SARS-CoV2, PET imaging, mucosal immunity, CD8+ T-cells, trafficking

Introduction

The upper respiratory tract (URT) represents the site of entry for severe acute respiratory syndrome coronavirus 2 (SARS-CoV-2) (1). In the absence of an adequate mucosal immune response, including T-cells (2), it may replicate and spread to the lower respiratory tract (LRT) and eventually distant organ sites (3). Mucosal T-cells help control the viral load (4) and limit the (progression of) disease, thus reducing viral spread in the population (5). CD8+ T-cells are major effector cells of these local cytotoxic responses to viral infection and are rapidly recruited to the nasopharynx following a controlled challenge of volunteers with SARS-CoV-2 (6). Although CD8+ T-cells are important for the clearance of infected cells, delayed and persistent bystander activation of CD8+ T-cells in hospitalized patients suggests that they may also contribute to lung pathology (7, 8).

Little is known about the spatial distributions of CD8+ lymphocytes at a whole-body level (9) during acute coronavirus disease 2019 (COVID-19). This case series describes the *in vivo*

distribution of CD8+ T-cells in hospitalized patients during active SARS-CoV-2 infection using positron emission tomography (PET) imaging and functional characterization of circulating lymphocytes using flow cytometry.

Methods

Study design

A prospective observational, open-label, non-randomized pilot study was performed on patients admitted to the hospital with active SARS-CoV-2 infection. Eligibility criteria included age > 50 years and PCR-confirmed SARS-CoV-2 infection. Patients underwent a [^{89}Zr]Zr-crefmirlimab berdoxam PET/CT scan; 20 mL EDTA blood and 10 mL EDTA plasma were collected immediately before tracer injection. Patients were monitored, and vital signs were measured every 6 h during admission. The protocol was approved by the Institutional Review Board, and all patients provided written informed consent (ClinicalTrials.gov identifier NCT04874818). In total, 6 patients were counseled for this study, 4 were eligible, and three patients underwent scanning. One patient did provide informed consent but was not scanned as a tracer dose was not available. Two patients did not provide informed consent due to claustrophobia ($n = 1$) and radiation dose ($n = 1$). As the SARS-CoV-2 pandemic resided, further enrollment was halted, and the data were preliminarily analyzed.

Positron emission tomography imaging

[^{89}Zr]Zr-crefmirlimab berdoxam is a 79,946 Da minibody (Mb) directed to the CD8 antigen, conjugated with deferoxamine (Df) and radiolabeled with ^{89}Zr for imaging CD8+ cells in humans. The total molecular weight of the [^{89}Zr]Zr-crefmirlimab berdoxam imaging agent is 81,453.8 Da. It binds to both CD8αα and CD8αβ, thus binding to mature T-cells, developing thymocytes, TCRαβ-expressing gut intra-epithelial T-cells, some γδT-cells, and some natural killer and dendritic cell subsets. The lack of Fc-receptor interaction domains makes it pharmacologically inert with respect to Fcγ-receptor-mediated effector functions. [^{89}Zr]Zr-crefmirlimab berdoxam was produced according to Good Manufacturing Practice as described previously (10, 11) and obtained from ImaginAb Inc. A single dose of 37 MBq ± 10% (range 37 to 39.3 MBq) of [^{89}Zr]Zr-crefmirlimab berdoxam (total minibody mass of 1.5 mg) was administered as a slow bolus intravenously over 5 min. No premedication was administered. At 21–27 h post-injection, PET acquisitions were performed from the skull to the greater trochanter on a Siemens Biograph mCT (Siemens Healthineers, Knoxville, United States), using 5 min per bed position for the chest and 3 min per bed position for the remainder. Images were reconstructed into a 200 × 200 matrix TrueX+TOF (21 subsets; 3 iterations). A low-dose CT scan without iodinated contrast was used for anatomical reference and attenuation correction. Volumes of interest were drawn manually to compute maximum and mean standardized uptake values (SUV_{max} and SUV_{mean}, respectively). For the individual organ sites, tracer uptake values are expressed as tissue-to-blood ratio (TBR) calculated as the SUVmean of the tissue divided by the SUVmean of the blood pool, measured in a spherical volume-of-interest of at least 10 mm diameter in the descending aorta.

Flow cytometry

A 10-color flow cytometry of freshly drawn blood samples was performed and analyzed as described previously (12). The following monoclonal antibodies were used: CD57-FITC, CD45RA-ECD, CD8APC-AF750, CD45-KO (Beckman Coulter), CD196-PE, CD194-PC7, CD199-AF488, CD25-APC (BD Biosciences) CD183-PerCpCy5.5, CD197-BV421, KLRG1-PerCpCy5.5 (Biolegend), CD4-AF700, CD279-PC7 (eBioscience), and CD28-PE (Dako). Two 10-color panels were used; panel 1 included CD45RA, CD196, CD8, CD183, CD194, CD25, CD4, CD199, CD197, and CD45 and panel 2 included CD57, CD28, CD45RA, KLRG1, CD279, CD25, CD4, CD8, CD197, and CD45.

Staining

All cells were surface stained in 25 µL of surface staining master mix at RT for 20 min. The cells were washed twice by adding PBS + 0.2% bovine serum albumin (BSA) and centrifuged at 250 x*g* for 2.5 min. The buffer was removed by flicking the plates. Before acquisition, whole blood-derived cells were resuspended in 100 µL PBS + 0.2% BSA.

For intracellular staining, the surface-stained peripheral blood mononuclear cells (PBMC) were fixed and permeabilized using the Fix/Perm solution (eBioscience, Vienna, Austria). After 30 min at 4°C, protected from light, the cells were washed and centrifuged at 250 xg for 2.5 min twice using a permeabilization buffer (eBioscience, Vienna, Austria). Then, 25 µL of the intracellular staining master mix was applied, and the samples were incubated for 30 min at 4°C, protected from light. After a second washing step using permeabilization buffer, the cells were resuspended in 100 µL PBS + 0.2% BSA for data acquisition.

Gating strategy

Each sample was analyzed by two multi-color antibody panels, as described previously. For each panel, the single cells, identified by plotting the FS Time Of Flight (FS TOF) against FS, within the leukocyte (CD45+) population were first gated, and then the lymphoid cells were gated.

In both panels, the lymphocytes were discriminated by forward scatter and side scatter. Within the CD8 + CD4- cells, maturation stages were defined based on CD45RA and CCR7 expression, namely, CD45RA+/CD197+ naïve cells, CD45RA-/CD197+ central memory (CM) cells, CD45RA-/CD197 effector memory (EM) cells, and CD45+/CD197- terminally differentiated effector memory (TEMRA) cells. Within these T-cell maturation stages, the percentage of CD196, CD183, CD194, and CD199 (panel1) and CD57, CD28, KLRG1, CD279, and CD25 (panel 2) expressing cells was determined.

Flow cytometry measurements and data analysis

Data were acquired using a Navios Flow Cytometer, as described above. Each sample suspended in 100 µL was measured for 60 s, representing 75% of the sample volume. This prevented the intake of air, leading to a non-specific signal at the end of the measurement. For the flow cytometry analysis, a manual gating strategy was conducted.

Each analysis was verified by two independent specialists to prevent gating errors. Analyzed data were stored batch-wise per 20 samples each. The statistics were exported batch-wise for further analysis.

Results

Patient characteristics

The study was performed in an acute clinical setting where patients were admitted with respiratory symptoms and PCR-test positive for SARS-CoV-2. During the period of subject enrollment in February and March 2022, the SARS-CoV-2 delta-variant BA.1 and BA.2 were dominant in The Netherlands.[1] However, the determination of virus variants and exact viral load was not routinely performed and is not available for this cohort.

Case 1 was a 79-year-old man with chronic obstructive pulmonary disease (COPD) who was admitted to the hospital with respiratory stress 4 days after the onset of COVID-19 symptoms. He had not been previously vaccinated. PCR testing of the nasopharyngeal swab for SARS-CoV-2 on admission was positive, with a cycle threshold of 16. The oxygen saturation level was 94% without additional oxygen needed. Laboratory evaluation showed lymphopenia (0.44×10^9/L, normal values $1.00–3.50 \times 10^9$/L) and a C-reactive protein level of 17 mg/L (normal values <5 mg/L). Treatment with prednisone 30 mg once daily was initiated under suspicion of exacerbation of COPD triggered by SARS-CoV-2 infection. PET/CT imaging was performed on day 7 after the onset of symptoms, and the patient was discharged from the hospital 6 days after admission.

Case 2 was an 83-year-old man with type 2 diabetes, hypertension, and chronic idiopathic thrombocytopenic purpura admitted to the hospital with respiratory stress and worsening of known late-onset cerebellar ataxia 2 days after the onset of symptoms. He was vaccinated twice against SARS-CoV-2 with BNT162b2 (Tozinameran) and received a booster vaccination with the same vaccine before admission. On admission, PCR testing of the nasopharyngeal swab for SARS-CoV-2 was positive, with a cycle threshold of 20. The oxygen saturation level was 96% without additional oxygen needed. Laboratory evaluation showed normal lymphocyte counts (1.34×10^9/L, normal values $1.00–3.50 \times 10^9$/L) and a C-reactive protein level of 70 mg/L. Treatment with intravenous immunoglobulin and donor-platelet infusion was initiated because of thrombocytopenia. PET/CT imaging was performed on day 5 after the onset of symptoms, and the patient was discharged from the hospital 8 days after admission.

Case 3 was an 89-year-old man with COPD and cardiovascular disease admitted to the hospital with respiratory stress 10 days after the onset of symptoms. He was vaccinated with BNT162b2 (Tozinameran) and had received a booster vaccination with the same vaccine prior to admission. PCR testing of the nasal swab for SARS-CoV-2 was positive, with a cycle threshold of 23. Oxygen saturation was 90% with 4 L/min oxygen. Laboratory evaluation showed lymphopenia (0.22×10^9/L, normal values $1.00–3.50 \times 10^9$/L) and a C-reactive protein level of 81 mg/L. Treatment with dexamethasone 6 mg once daily was initiated. PET/CT imaging was performed on day 13 after the onset of symptoms, and the patient was discharged 22 days after admission.

Visualizing CD8+ T-cells during early and late stages of COVID-19

High tracer accumulation is commonly observed in CD8+ T-cell-rich organs, such as the spleen and bone marrow, as well as activity in the excretory organs, such as the hepatobiliary tract, which subsequently results in bowel activity (10, 11). Patients 1 and 2 were imaged at early time points after the onset of symptoms, on days 7 and 5, respectively. Both patients presented with mild symptoms and were discharged soon after imaging. PET/CT imaging showed an increased presence of CD8+ T-cells in the nasal mucosa in these patients, compared to patient 3 (TBR 6.8 and 4.3 vs. TBR 1.4, respectively) (Figures 1, 2). A similar pattern was observed in the URT-associated lymphoid tissue, e.g., tonsils (TBR 7.4 and 5.3 vs. TBR 1.4) and cervical lymph nodes (TBR 13.4 and 3.1 vs. TBR 3.9). No tracer uptake was observed in the lower respiratory tract in patients 1 and 2 (Figures 1, 2).

Patient 3 presented with dyspnea and increased oxygen demand, suggesting involvement of the lower respiratory tract. This patient was imaged on day 10, and no tracer uptake in the URT was observed (Figure 1). Although absolute tracer uptake in the affected lung parenchyma was increased (SUV_{max} 6.6) as compared to patients 1 and 2 (SUV_{max} 3.4 and 2.2), TBR was in the same range (TBR 2.4 vs. 4.2 and 1.1) (Figure 2), indicating the mere presence of tracer in the increased blood volume in the affected parenchyma, rather than trans-endothelial migration of CD8+ T-cells into the interstitial space.

In addition to the distribution patterns in the respiratory tract, patient 1 also showed markedly increased presence of CD8+ T-cells across primary (bone marrow and spleen) and distant secondary (inguinal and mediastinal lymph nodes) lymphoid organs, as well as other organ sites, including the liver, kidney, and gluteal muscle.

PET-based distribution patterns correspond to CD8+ T-cell phenotype

The increased TBR in the URT in patients 1 and 2 coincided with higher expression of C-C chemokine receptor type 6 (CCR6/CD196) on the peripheral blood total CD8+ cells, in comparison to patient 3 (8.1 and 7.1% vs. 4.3%) (Figure 3).

Patient 2 showed increased TBR in primary, distant secondary lymphoid organs, and non-lymphoid organs, suggestive of rapid in- and efflux of CD8+ T-cells from the circulation. In this patient, the fraction of C-X-C motif chemokine receptor 3 (CXCR3/CD183) positive lymphocytes among the total CD8+ population was higher than in patients 1 and 3 (Figure 3).

In both patients 1 and 2 imaged earlier after the onset of symptoms, the CD8+ T-cell population was dominated by an abundance of CD45RA-/CD197+ effector memory (Tem) and CD45RA+/CD197- terminally differentiated effector memory (Temra) phenotypes, indicative of recent priming (Figure 4). At a later stage of infection in patient 3, the CD8+ T-cell population was characterized by an increase in Temra phenotypes, as well as

1 https://www.rivm.nl/en/coronavirus-covid-19/current/variants

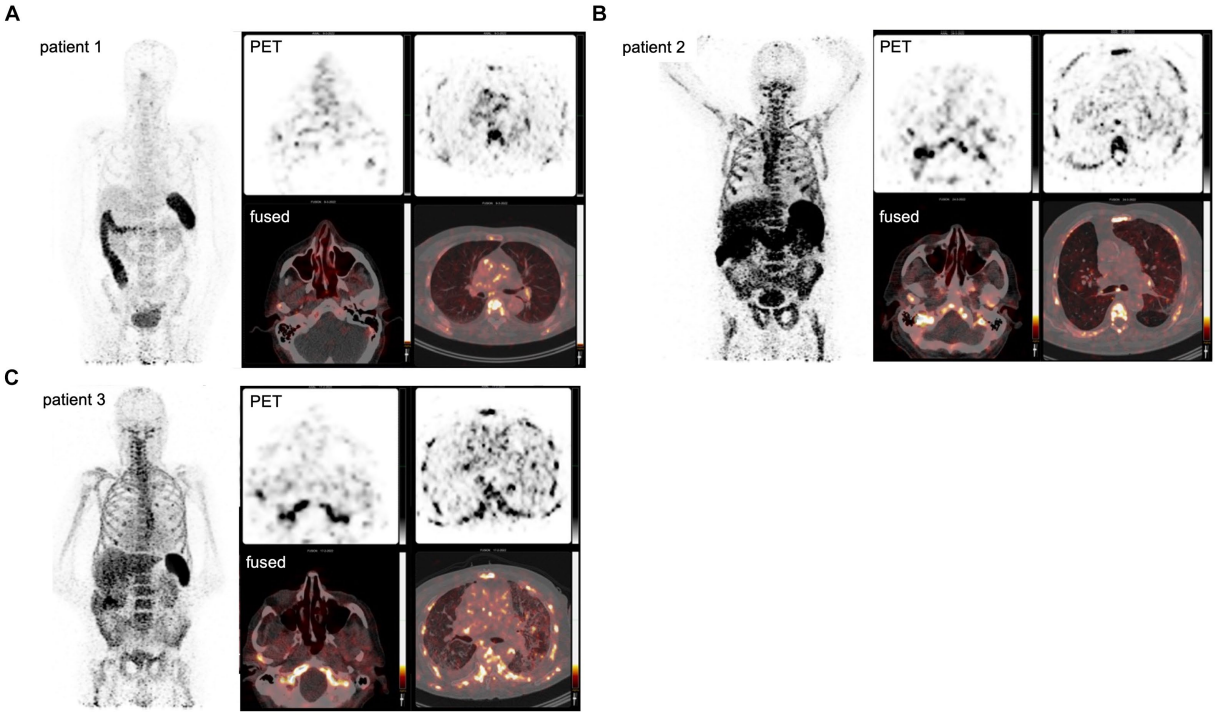

FIGURE 1
PET imaging visualizes the *in vivo* distribution of CD8+ T-cells in acute COVID-19. Using a Zirconium-89-labeled CD8α chain targeting minibody for PET/CT images, the *in vivo* distribution of CD8+ T-cell was visualized at a whole-body level in three subjects with acute COVID-19 **(A–C)**. The left-upper panel displays the maximum intensity projections (MIP), the right panels display the PET-only transversal view of the upper respiratory tract (upper-middle panel) and lower respiratory tract (upper-right panel), and PET/CT fused transversal view (lower panels). CD8+ T-cell-rich organs, e.g., spleen and bone marrow, show the highest uptake and activity in the excretory organs, such as the hepatobiliary tract, resulting in bowel activity. In patients 1 and 2, the uptake in the nasal mucosa is markedly increased (arrows).

CD45RA+/CD197+ naïve T-cells (Figure 4), suggestive of prolonged antigen stimulation and a replenished CD8+ T-cell reservoir. In addition to the evidence of evolving CD8+ T-cell differentiation, patient 3 also had higher frequencies of senescent/exhausted CD8+ T-cells as indicated by the loss of expression of CD28 (35.9% vs. 62.5 and 72.0%) and reduced programmed death receptor-1 (CD297) expression (6.9% vs. 31.4 and 23.0%) among the total CD8+ population (Figure 3).

Discussion

Cellular immune responses are important for viral clearance and limitation of disease severity of SARS-CoV-2 infection. CD8+ T cells can help restrict viral replication, disease, and transmission (2, 13) but may also contribute to pathology (7, 8). An early and balanced recruitment and activation of CD8+ T cells in the mucosa and their expansion in secondary lymph nodes is a complex process that involves a concerted response of multiple immune cell populations and inflammatory mediators (13, 14). Previous studies highlighted that T-cell migration in response to inflammatory stimuli is governed by cell-intrinsic and cell-extrinsic factors, which vary throughout stages of differentiation and organ sites (15). This results in a spatial and temporal compartmentalization of T-cell subsets (16), which is difficult to infer from peripheral blood samples, which contain only a fraction of the total T-cell population (17). This study responds to the need for technologies that allow evaluation of the presence and dynamics of T-cells on a whole-body scale. PET imaging meets these prerequisites as it provides quantitative data in a non-invasive fashion and is feasible in clinical studies. We employed a radiolabeled minibody targeting the human CD8α subunit (10, 11) to interrogate the *in vivo* distribution of CD8 T-cells in patients admitted to the hospital with COVID-19.

Albeit in a small series of patients, PET imaging demonstrated the differential distribution of CD8+ T-cells in the mucosa and associated lymphoid organs of the URT during early and later stages of SARS-CoV-2 infection, underscoring the concept of spatial and temporal compartmentalization of CD8+ T-cell responses to respiratory viral infection. Furthermore, the observed differences in patterns of CD8+ T-cell distribution across mucosa, primary and secondary lymphoid organs, blood pool, and peripheral tissues can be correlated with changes in CD8+ T-cell functional phenotypes. The chemokine receptor CXCR3 generally regulates leukocyte trafficking, promoting T-helper 1 recruitment and maturation (18). CXCR3 expression was the highest in patient 3, coinciding with the highest tracer uptake values across both lymphoid and non-lymphoid organs, suggesting increased trafficking of CD8+ T-cells from the circulation into peripheral tissues. Furthermore, the expression levels of the chemokine receptor CCR6, which directs T-cells to mucosal tissues in response to its ligand macrophage inflammatory protein 3 alpha (MIP-3α/CCL20) (18), were the highest in the two patients scanned earlier during their course of the disease and were associated with the

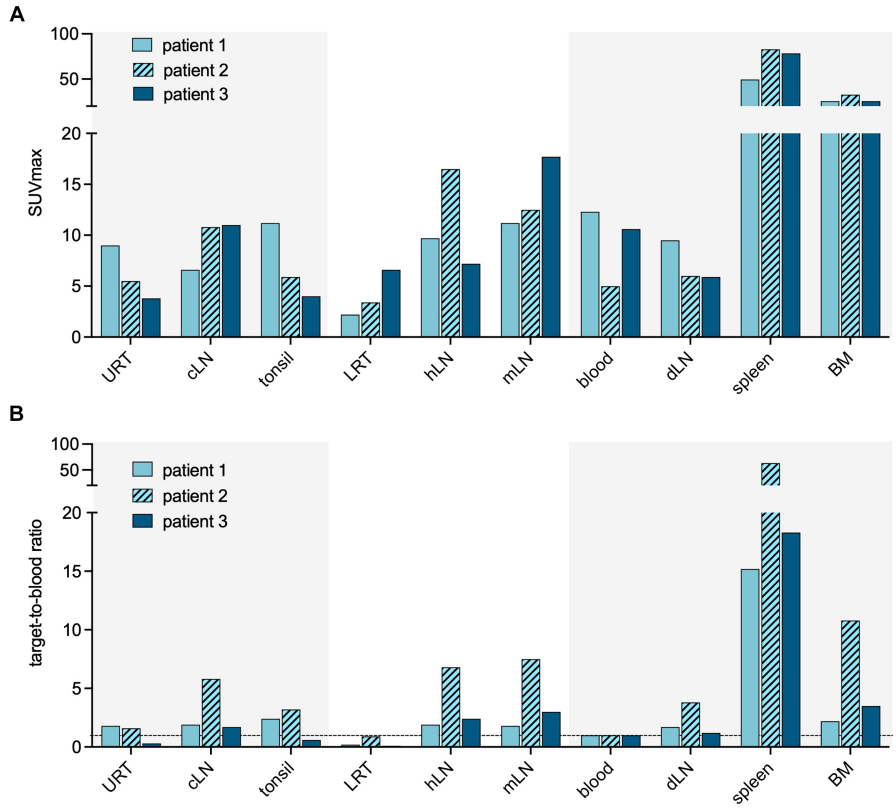

FIGURE 2
Quantification of CD8 targeting PET signal in acute COVID-19. Quantification of the PET signal in either maximum standardized uptake value (SUV_{max}) **(A)** or target-to-blood ratios **(B)** for the upper respiratory tract (URT), cervical lymph nodes (cLN), tonsils, lower respiratory tract (LRT), hilar lymph nodes (hLN), mediastinal lymph nodes (mLN), spleen, and bone marrow (BM).

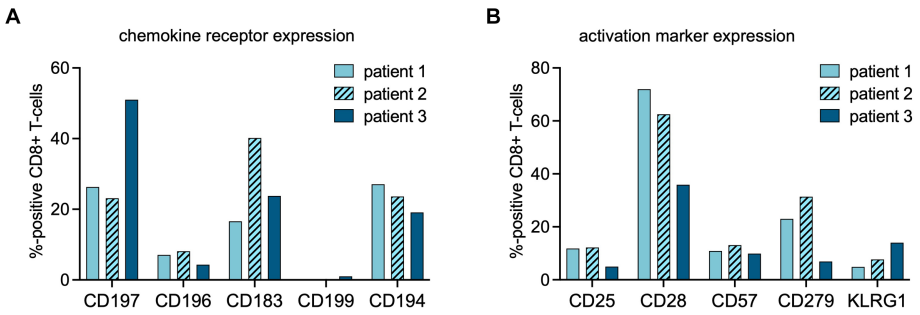

FIGURE 3
Flow cytometric analysis of CD8+ cells at time point of PET imaging. The percentages of CD8+ cells expressing chemokine receptors **(A)** or activation markers **(B)** at the time point of PET imaging were assessed using multipanel flow cytometry (chemokine receptor profiles: CD197 = CCR7, homing to secondary lymphoid organs; CD196 = CCR6, homing to mucosal tissues; CD183 = CXCR3, a general leukocyte trafficking receptor; CD199 = CCR9, homing to gastrointestinal organs, CD194 = CCR4, Th2 T-cell trafficking). (activation marker profiles: CD25 = interleukin (IL)-2 receptor; CD57 = human natural killer-1 (HNK1), marker of immune aging; CD279 = programmed death receptor (PD)-1; CD28 = co-stimulatory receptor, KLRG-1 = Killer cell lectin-like receptor subfamily G member 1, a co-inhibitory receptor on late-differentiated T-cells).

highest tracer uptake values in the nasal mucosa. Finally, in the patient with a prolonged course of disease and features of exhaustion and senescence, predominantly in the circulating terminally differentiated CD8+ lymphocyte compartment, the lowest tissue-to-blood ratios were observed. This finding is consistent with the limited capacity of exhausted CD8+ T-cells to infiltrate into tissues (19). These observations hint at the potential of PET/CT imaging to develop quantitative parameters inferred from the spatial and dynamic substrates of CD8+ T-cell behavior.

It is important to note that these cases provide anecdotal observations and warrant further studies that include translational data linking functional or phenotypic characterization of CD8+ T-cells to tracer distribution patterns observed on PET imaging. In general terms, CD8+ T-cell responses in elderly patients, as in this case

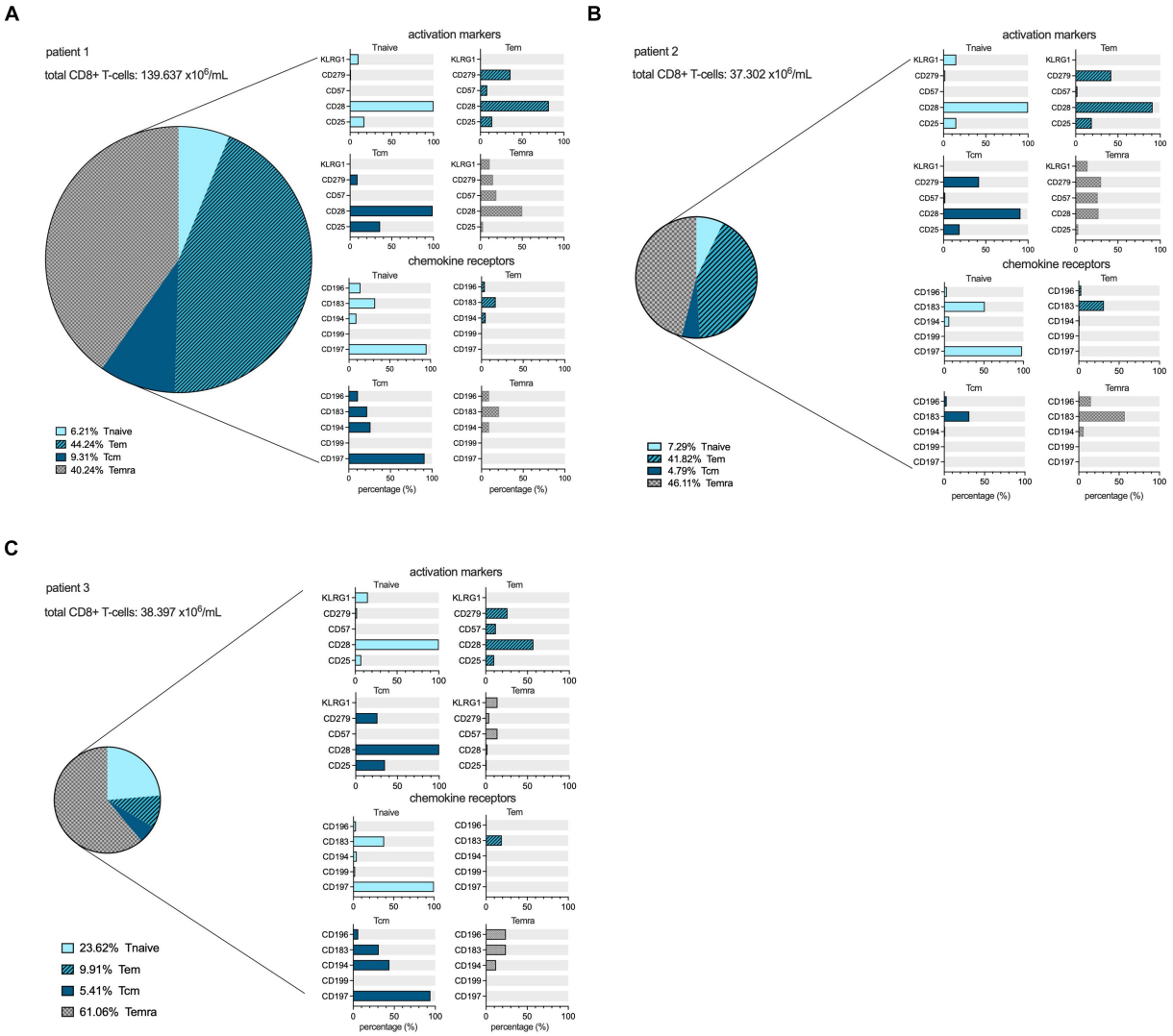

FIGURE 4
CD8+ cell maturation stages and flowcytometric subtyping. Distribution of different maturation stages, based on differential expression of CD45RA and CD197, within the CD8+ lymphocyte compartment in the peripheral blood at the time point of scanning for each patient in percentages, as well as the expression profiles of activation markers and chemokine receptors among the T_{naive} (light blue), $T_{effector\ memory}$ (dark blue, hatched), $T_{central\ memory}$ (dark blue filled), and T_{emra} (grey hatched) populations within CD8+ T-cells. The size of the pie chart corresponds to the absolute number of CD8+ T-cells (in $\times 10^6$/mL) for each subject **(A–C)**.

series, may be impaired by reduced clonal diversity (20) and proliferative capacity (21) and increased exhaustion (22), also shown to be relevant in SARS-CoV2 infection. It is yet unknown how these aspects of CD8+ T-cell behavior *in vivo* affect the distribution and quantification of [^{89}Zr]Zr-crefmirlimab berdoxam. The limited number of subjects in this study, sharing general characteristics such as age, gender, and SARS-CoV2 variant, preclude assumptions of a direct correlation with PET imaging findings. In this respect, studies using this tracer in healthy volunteers under steady-state conditions are not available as references. Such studies are currently only feasible on ultra-sensitive PET systems (23) that allow for reducing the administered dose of Zirconium-89 to match the ICRP62 risk category IIIa, balancing the acquisition of knowledge regarding serious disease with additional effective doses by study-related radiological procedures. Furthermore, a robust analytical framework for interpretation that allows for quantitative correlation between the high-dimensional data from flow cytometry on a selected fraction of CD8+ T-cells from the blood compartment and the spatial information described by PET parameters is to be developed. The simple linear associations presented in this article should be interpreted as illustrative, aiming to stimulate researchers in immunological domains to embrace imaging technology in addition to established assays.

However, acknowledging the importance of early and local control of respiratory viruses by the adaptive immune system, a key objective of new vaccines is to develop strategies that induce robust mucosal cellular responses (24, 25). Biomarker technologies that allow early and quantitative assessment of changes in CD8+ T-cell distributions, e.g., from lymphoid compartments to mucosal linings, may provide alternative endpoints that can accelerate the development of effective vaccination approaches. Similarly, novel treatment strategies in immune-mediated inflammatory conditions that are dominated by

CD8+ T-cells (26) or in which CD8+ T-cells are therapeutically targeted may benefit from non-invasive imaging approaches. The observations made in this case series highlight PET imaging with immune cell-specific tracers as an imaging biomarker that may complement current immunological assays with information on the spatiotemporal distributions of CD8+ T-cells on a whole-body scale, assessing yet another aspect of CD8+ T-cell biology (9).

In conclusion, PET/CT imaging with a radiolabeled minibody targeting CD8α on T-cells allows the localization of CD8+ T-cell responses *in vivo* in COVID-19 patients.

Data availability statement

The original contributions presented in the study are included in the article/supplementary material, further inquiries can be directed to the corresponding author.

Ethics statement

The studies involving humans were approved by Medisch Ethische Commissie Arnhem en Nijmegen. The studies were conducted in accordance with the local legislation and institutional requirements. The participants provided their written informed consent to participate in this study.

Author contributions

HK: Conceptualization, Formal analysis, Writing – review & editing, Validation. IK: Writing – review & editing, Investigation. MG: Writing – review & editing, Project administration, Resources. SP: Project administration, Writing – review & editing, Methodology. DL: Methodology, Project administration, Writing – review & editing. EG: Methodology, Writing – review & editing, Formal analysis. DD: Formal analysis, Writing – review & editing, Conceptualization. NO: Writing – review & editing, Project administration, Resources. SG: Writing – review & editing, Investigation. MP: Writing – review & editing, Methodology. MN: Writing – review & editing, Formal analysis. FV: Formal analysis, Writing – review & editing. EA: Formal analysis, Writing – review & editing, Conceptualization, Writing – original draft.

Funding

The author(s) declare financial support was received for the research, authorship, and/or publication of this article. This study is sponsored and initiated by the Radboud University Medical Center. The tracer was provided by ImaginAb Inc. at no cost.

Acknowledgments

The authors would like to thank the nursery staff and heads of the involved departments for facilitating this study.

Conflict of interest

The authors declare that the research was conducted in the absence of any commercial or financial relationships that could be construed as a potential conflict of interest.

The author(s) declared that they were an editorial board member of Frontiers, at the time of submission. This had no impact on the peer review process and the final decision.

Publisher's note

References

1. Zou L, Ruan F, Huang M, Liang L, Huang H, Hong Z, et al. SARS-CoV-2 viral load in upper respiratory specimens of infected patients. *N Engl J Med*. (2020) 382:1177–9. doi: 10.1056/NEJMc2001737

2. Chen Z, John WE. T cell responses in patients with COVID-19. *Nat Rev Immunol*. (2020) 20:529–36. doi: 10.1038/s41577-020-0402-6

3. Gupta A, Madhavan MV, Sehgal K, Nair N, Mahajan S, Sehrawat TS, et al. Extrapulmonary manifestations of COVID-19. *Nat Med*. (2020) 26:1017–32. doi: 10.1038/s41591-020-0968-3

4. Roukens AHE, Pothast CR, Konig M, Huisman W, Dalebout T, Tak T, et al. Prolonged activation of nasal immune cell populations and development of tissue-resident SARS-CoV-2-specific CD8(+) T cell responses following COVID-19. *Nat Immunol*. (2022) 23:23–32. doi: 10.1038/s41590-021-01095-w

5. Melms JC, Biermann J, Huang H, Wang Y, Nair A, Tagore S, et al. A molecular single-cell lung atlas of lethal COVID-19. *Nature*. (2021) 595:114–9. doi: 10.1038/s41586-021-03569-1

6. Lindeboom RG, Worlock KB. Human SARS-CoV-2 challenge resolves local and systemic response dynamics. *Med Rxiv*. (2023). [Epub ahead of preprint] doi: 10.1101/2023.04.13.23288227

7. Bergamaschi L, Mescia F, Turner L, Hanson AL, Kotagiri P, Dunmore BJ, et al. Longitudinal analysis reveals that delayed bystander CD8+ T cell activation and early immune pathology distinguish severe COVID-19 from mild disease. *Immunity*. (2021) 54:1257–1275.e8. doi: 10.1016/j.immuni.2021.05.010

8. Kent SJ, Khoury DS, Reynaldi A, Juno JA, Wheatley AK, Stadler E, et al. Disentangling the relative importance of T cell responses in COVID-19: leading actors or supporting cast? *Nat Rev Immunol*. (2022) 22:387–97. doi: 10.1038/s41577-022-00716-1

9. Schenkel JM, Pauken KE. Localization, tissue biology and T cell state - implications for cancer immunotherapy. *Nat Rev Immunol*. (2023) 23:807–23. doi: 10.1038/s41577-023-00884-8

10. Farwell MD, Gamache RF, Babazada H, Hellmann MD, Harding JJ, Korn R, et al. CD8-targeted PET imaging of tumor-infiltrating T cells in patients with Cancer: a phase I first-in-humans study of (89) Zr-Df-IAB22M2C, a radiolabeled anti-CD8 Minibody. *J Nucl Med*. (2022) 63:720–6. doi: 10.2967/jnumed.121.262485

11. Pandit-Taskar N, Postow M, Hellmann M, Harding J, Barker C, O'Donoghue J, et al. First-in-human imaging with (89) Zr-Df-IAB22M2C anti-CD8 minibody in patients with solid malignancies: preliminary pharmacokinetics, biodistribution, and lesion targeting. *J Nucl Med*. (2020) 61:512–9. doi: 10.2967/jnumed.119.229781

12. Aguirre-Gamboa R, Joosten I, Urbano PCM, van der Molen RG, van Rijssen E, van Cranenbroek B, et al. Differential effects of environmental and genetic factors on T and B cell immune traits. *Cell Rep*. (2016) 17:2474–87. doi: 10.1016/j.celrep.2016.10.053

13. Mettelman RC, Allen EK, Thomas PG. Mucosal immune responses to infection and vaccination in the respiratory tract. *Immunity*. (2022) 55:749–80. doi: 10.1016/j.immuni.2022.04.013

14. Lee M, Mandl JN, Germain RN, Yates AJ. The race for the prize: T-cell trafficking strategies for optimal surveillance. *Blood*. (2012) 120:1432–8. doi: 10.1182/blood-2012-04-424655

15. Weninger W, Biro M, Jain R. Leukocyte migration in the interstitial space of non-lymphoid organs. *Nat Rev Immunol*. (2014) 14:232–46. doi: 10.1038/nri3641

16. Thome JJ, Yudanin N, Ohmura Y, Kubota M, Grinshpun B, Sathaliyawala T, et al. Spatial map of human T cell compartmentalization and maintenance over decades of life. *Cell*. (2014) 159:814–28. doi: 10.1016/j.cell.2014.10.026

17. Ganusov VV, De Boer RJ. Do most lymphocytes in humans really reside in the gut? *Trends Immunol*. (2007) 28:514–8. doi: 10.1016/j.it.2007.08.009

18. Fowell DJ, Kim M. The spatio-temporal control of effector T cell migration. *Nat Rev Immunol*. (2021) 21:582–96. doi: 10.1038/s41577-021-00507-0

19. Boussiotis VA. Molecular and biochemical aspects of the PD-1 checkpoint pathway. *N Engl J Med*. (2016) 375:1767–78. doi: 10.1056/NEJMra1514296

20. Britanova OV, Putintseva EV, Shugay M, Merzlyak EM, Turchaninova MA, Staroverov DB, et al. Age-related decrease in TCR repertoire diversity measured with deep and normalized sequence profiling. *J Immunol*. (2014) 192:2689–98. doi: 10.4049/jimmunol.1302064

21. Gruver AL, Hudson LL, Sempowski GD. Immunosenescence of ageing. *J Pathol*. (2007) 211:144–56. doi: 10.1002/path.2104

22. Rydyznski Moderbacher C, Ramirez SI, Dan JM, Grifoni A, Hastie KM, Weiskopf D, et al. Antigen-specific adaptive immunity to SARS-CoV-2 in acute COVID-19 and associations with age and disease severity. *Cell*. (2020) 183:996–1012.e19. doi: 10.1016/j.cell.2020.09.038

23. Omidvari N, Jones T, Price PM, Ferre AL, Lu J, Abdelhafez YG, et al. First-in-human immunoPET imaging of COVID-19 convalescent patients using dynamic total-body PET and a CD8-targeted minibody. *Sci Adv*. (2023) 9:41. doi: 10.1126/sciadv.adh7968

24. Alu A, Chen L, Lei H, Wei Y, Tian X, Wei X. Intranasal COVID-19 vaccines: from bench to bed. *EBioMedicine*. (2022) 76:103841. doi: 10.1016/j.ebiom.2022.103841

25. Hameed SA, Paul S, Dellosa GKY, Jaraquemada D, Bello MB. Towards the future exploration of mucosal mRNA vaccines against emerging viral diseases; lessons from existing next-generation mucosal vaccine strategies. *NPJ Vaccines*. (2022) 7:71. doi: 10.1038/s41541-022-00485-x

26. Quinn C, Moulton K, Farwell M, Le W, Wilson I, Goel N, et al. Imaging with PET/CT of diffuse CD8 T-cell infiltration of skeletal muscle in patients with inclusion body myositis. *Neurology*. (2023) 101:e1158–66. doi: 10.1212/WNL.0000000000207596

frontiers | Frontiers in Medicine

TYPE Case Report
PUBLISHED 16 May 2024
DOI 10.3389/fmed.2024.1408967

OPEN ACCESS

EDITED BY
Nataliya Lutay,
Skåne University Hospital, Sweden

REVIEWED BY
Francisco Torres Hoyos,
University of Córdoba, Colombia
Roberto Cannella,
University of Palermo, Italy
Tingfan Wu,
Shanghai United Imaging Medical Technology Co., Ltd, China
Cheng Xue,
Second Military Medical University, China
Darine Daher,
University of Texas Southwestern Medical Center, United States

*CORRESPONDENCE
Pan Wang
1298178828@qq.com
Jiong Cai
jiong_cai@163.com

†These authors have contributed equally to this work

RECEIVED 29 March 2024
ACCEPTED 06 May 2024
PUBLISHED 16 May 2024

CITATION
Hu X, Li X, Zhao W, Cai J and Wang P (2024) Multimodal imaging findings of primary liver clear cell carcinoma: a case presentation. *Front. Med.* 11:1408967. doi: 10.3389/fmed.2024.1408967

Multimodal imaging findings of primary liver clear cell carcinoma: a case presentation

Xianwen Hu[1†], Xiaotian Li[1†], Wei Zhao[2], Jiong Cai[1*] and Pan Wang[1*]

[1]Department of Nuclear Medicine, Affiliated Hospital of Zunyi Medical University, Zunyi, China, [2]Department of Pathology, Affiliated Hospital of Zunyi Medical University, Zunyi, China

Primary clear cell carcinoma of liver (PCCCL) is a special and relatively rare subtype of hepatocellular carcinoma (HCC), which is more common in people over 50 years of age, with a preference for men and a history of hepatitis B or C and/or cirrhosis. Herein, we present a case of a 60-year-old woman who came to our hospital for medical help with right upper abdominal pain. The imaging examination showed a low-density mass in the right lobe of his liver. In contrast enhanced computed tomography (CT) or T1-weighted imaging, significant enhancement can appear around the tumor during the arterial phase, and over time, the degree of enhancement of the tumor gradually decreases. The lesion showed obviously increased fluorine-18 fluorodeoxyglucose (^{18}F-FDG) uptake on positron emission tomography/CT. These imaging findings contribute to the diagnosis of PCCCL and differentiate it from other types of liver tumors.

KEYWORDS

liver, clear cell carcinoma, imaging findings, MRI, PET/CT

Introduction

Primary clear cell carcinoma of liver (PCCCL) is a relatively rare subtype of hepatocellular carcinoma (HCC) in histology, with clear cells accounting for 50% or more of the tumor and an incidence rate of approximately 0.9 to 8.8% of liver cancer (1, 2). The pathogenesis of PCCCL is not well understood. One study believed that its pathogenesis may be caused by the decrease of blood supply to the portal static vein, relative ischemia of the tumor, and the subsequent lipid and glycogen turbulence, and the organelles in the cytoplasm are replaced by glycogen and lipids, making the tumor cells appear clear or vacuolar (3). It is more common in more than 50 years of age, preferring men, most of them have a history of hepatitis B or C and/or cirrhosis, the patient has no characteristic clinical symptoms, mostly due to right upper abdominal pain or physical examination found liver occupation (4). PCCCL is a low-grade malignant tumor, mostly well differentiated, and often has a pseudocapsule, making it easier to undergo complete surgical resection. Its prognosis and survival rate are superior to other types of liver carcinoma, so obtaining a correct diagnosis before surgery is crucial (5). Herein, we present the diagnosis and treatment of a patient with primary PCCCL, focusing on its multimodal imaging features including computed tomorgraphy (CT), magnetic resonance imaging (MRI), and positron emission tomography (PET)/CT, with a view to increasing awareness of this rare disease.

Case presentation

A 60-year-old woman had dull pain in the right upper abdomen without obvious reasons a month ago, no radiating pain in the shoulder and back, each pain lasting from 30 min to 1 h, 1–2 times a day, and the frequency increased in the past week, during which no treatment was performed. Ultrasound from an external hospital indicates a liver occupying lesion, and the patient came to our hospital for further diagnosis and treatment on February 3, 2024. Physical examination revealed tenderness in the right upper abdomen without significant rebound pain or other positive signs. The patient denied any history of hepatitis or other liver problems, and she and her family denied any history of cancer or genetic problems. The results of laboratory examination indicated that the liver function was impaired (the parameters of abnormal liver function are shown in Table 1) while the renal function index was within the normal reference value range. The results of serum tumor markers revealed an increase in carbohydrate antigen-199 (Ca-199) and alpha fetoprotein (AFP), with values of 541 U/mL (normal: 0–30 U/mL) and 66.9 g/L (normal: 0–20 ug/L), respectively. The values of other gastrointestinal tumor markers were within the normal range.

The upper abdominal CT scan (CT examination was performed using 16-detector-row scanners [Siemens, Germany] from the top of the liver to the lower pole of the kidney; The contrast-enhanced scan was performed with iohexol [300 mg I/mL]1.5 mL/kg, and a single phase injection at a rate of 3.0 mL/s was performed with a high pressure syringe) showed a circular low-density lession near the gallbladder fossa in the right lobe of the liver, with uneven mild enhancement on contrast-enhanced scanning (as shown in Figure 1); Moreover, CT showed that the left and right lobes of the liver were disproportioned, the left lobe was enlarged, and the liver fissure was widened, suggesting possible cirrhosis. The MRI (GE 3.0 T Signa HDxt superconducting magnetic resonance instrument, with abdominal coil; Conventional T1WI and T2WI sequence plain scan and contrast-enhanced scan were performed; and the contrast-enhanced scan was intravenously injected with 0.1mmoL/kg meglumine gadopenate, and the injection flow rate was 3.0 mL/s) of the upper abdomen showed that the lesion presented equal signal on T1WI and slightly uneven high signal on T2WI (Figure 2). Based on these imaging findings, the patient was initially suspected to have intrahepatic cholangiocarcinoma. In order to further evaluate the nature of the tumor and determine the optimal treatment plan for the patient, she underwent fluorine-18 fluorodeoxyglucose (^{18}F-FDG) PET/CT examination (Biograph mCT, Siemens, Germany; The injection dose of ^{18}F-FDG was 9.0 mCi [0.15 mCi/kg]), and the results revealed increased ^{18}F-FDG uptake in the lesion, while no other increased radioactive uptake lessions were observed in the rest of body (Figure 3). After a thorough evaluation of the patient's condition by the clinician, she underwent "total hepatectomy and allogeneic orthotopic liver transplantation" under general anesthesia on February 13, 2024. Postoperatively, the excised liver tissue will be sent for pathological examination. Under the microscope, the surface of the liver was miliary nodules, and a mass was found in the right lobe of the liver near the gallbladder, about 55 × 30 × 20 mm. The section was grayish-yellow solid, medium in quality, and the boundary between the surrounding tissues was clear. Hematoxylin–eosin staining showed that most of the lesions were clear cells with rich and clear cytoplasm, and the nucleus was located in the center, deeply stained and irregular (Figure 4). The immunohistochemical results showed that the tumor cells expressed hepatocyte paraffin 1 (Hep par1), CK, Glypican (GPC3), HSP70 (partially), and Ki67 (about 40%) positively, while AFP, CD10, and CD68 were negatively expressed. Based on these findings, the patient was ultimately diagnosed with PCCCL. After liver transplantation, the patient underwent contrast-enhanced CT scan of the upper abdomen, which showed rich liver blood supply, indicating successful surgery. The patient did not complain of any discomfort during follow-up up to now. A detailed summary of the patient's journey is shown in Table 2.

Discussion

As is well known, the common pathological type of liver cancer is not otherwise specified hepatocellular carcinoma (NOS-HCC), while clear cell carcinoma is a relatively rare subtype of HCC. Like NOS-HCC, PCCCL also tend to prefer middle-aged and elderly people, and most patients have a history of hepatitis B or hepatitis C, cirrhosis, and can be accompanied by increased AFP (2). Our patient was a 60-year-old woman with elevated serum AFP, consistent with the clinical profile of PCCCL. However, she had not been checked for chronic liver disease before, and the imaging examination of this time indicated cirrhosis, revealing that the patient may have long-term chronic liver disease such as hepatitis B or C, but she did not know it.

Imaging examinations play a significant role in the diagnosis and differential diagnosis of liver tumor lesions. In clinical practice, due to the low incidence rate of PCCCL, there are relatively few research reports on its imaging characteristics. On CT, PCCCL mostly presents low-density shadows, and the higher the proportion of transparent

TABLE 1 Abnormal indixes of the patient's liver function.

Indexes	Results	Unit	Annotation	Reference
Alanine aminotransferase	95.0	U/L	up	7–40
Aspartate aminotransferase	41.0	U/L	up	13–35
Glutamyltransferase	186.0	U/L	up	7–45
Total bilirubin	21.1	μmol/L	up	5–21
Direct bilirubin	9.0	μmol/L	up	0–3.4
Albumin	27.8	g/L	down	40–55
Globulin	47.0	g/L	down	20–40
Albumin/Globulin	0.6		down	1.2–2.4

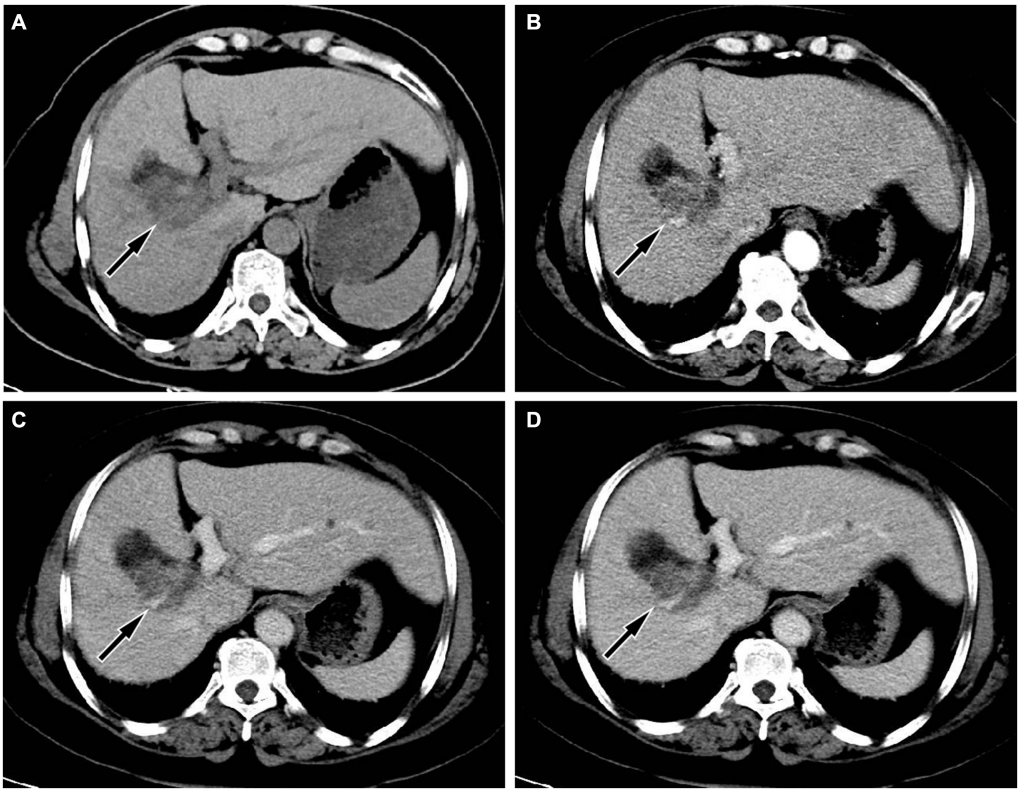

FIGURE 1
(A) Abdominal computed tomography (CT) scan showed a circular low-density shadow near the gallbladder fossa in the right lobe of the liver (arrow); moreover, the volume of the left lobe of the liver increases, the ratio of the left and right lobes is unbalanced, and the widening of the liver cleft can also be seen, suggesting cirrhosis; **(B)** In the arterial phase of contrast-enhanced CT scan, the lesion showed uneven enhancement, mainly with peripheral enhancement of the lesion (arrow); During the portal vein phase **(C)** and delayed phase **(D)**, the degree of enhancement of the lesion gradually declines (arrows).

cells, the lower the density of the tumor (6). On contrast-enhanced scanning, the lesion showed uneven enhancement and mainly peripheral enhancement during the arterial phase, and decreased enhancement in the portal vein stage and delayed stage (7). However, there are also a few cases of rapid reinforcement in the arterial phase, rapid decline in the portal phase of the "fast in and fast out" sign (8). The diversity of enhancement modes may be related to the content of clear cells: the higher the content of clear cells, the more inconsistent the enhancement mode is with NOS-HCC; on the contrary, the lower the content of clear cells, the more inclined the enhancement mode is to the "fast in and fast out" enhancement formula of typical hepatocellular carcinoma (9). On MRI, PCCCL mostly showed equal or slightly lower signals on T1WI sequences, and mixed high or slightly higher signals on T2WI sequences. Compared with CT, MRI is more sensitive to reveal the fat components in tumors, and on T2WI sequences, patchy or nodular signal reduction can be seen in lesions, which is one of its characteristic findings, but the probability of occurrence is low (6, 9). Our case showed a slightly low-density shadow on CT, and the contrast-enhanced scan showed rapid enhancement at the edge of the lesion in the arterial phase. With the passage of time, the enhancement degree of the lesion gradually decreased, which was different from the enhancement pattern of most PCCCL reported in the above literature. As for MRI findings, our case was consistent with literature reports, that is, the lesion showed equal signal on T1WI sequence and uneven slightly higher signal on T2WI sequence. To our knowledge, there have been few studies reported on the PET/CT findings of primary PCCCL. The pathologic properties of PCCCL are the same as those of clear cell carcinoma of kidney, ovary and adrenal gland, so it is presumed that its PET/CT findings are consistent with theirs, and it may also be presented by high uptake of ^{18}F-FDG, which is reflected in our case, but this needs to be verified in a large number of cases in the future.

PCCCL, as a special subtype of HCC, needs to be differntiated from other subtypes of HCC such as NOS-HCC, macrotrabecular massive subtype HCC (MMS-HCC), steatohepatitic subtype HCC (SHS-HCC), and fibrolamellar subtype HCC (FS-HCC). As the most common subtype of HCC, NOS-HCC showed non-rim arterial phase hyperenhancement and rapid regression in the portal venous phase, presenting a "fast in and fast out" enhancement pattern (10). MMS-HCC is more prone to macrovascular invasion and significant elevation of serum AFP, and the volume of the tumor is usually larger, with a length diameter usually greater than 5.0 cm (11, 12). Steatosis occurs in about 80% of SHS-HCC and is typically characterized by low signal on the inverse-phase T1WI of MRI, and the proportion of steatosis is far more than that of PCCCL (11, 13). For FS-HCC, there are no specific imaging features, but it is more common in younger patients and tends to favor women (14). Moreover, PCCCL also needs to be differentiated from other non HCC diseases including intrahepatic cholangiocarcinoma (IHC), hepatic perivascular epithelioid cell tumors, hepatic hemangioma, etc. IHC on contrast-enhanced CT or T1WI presents

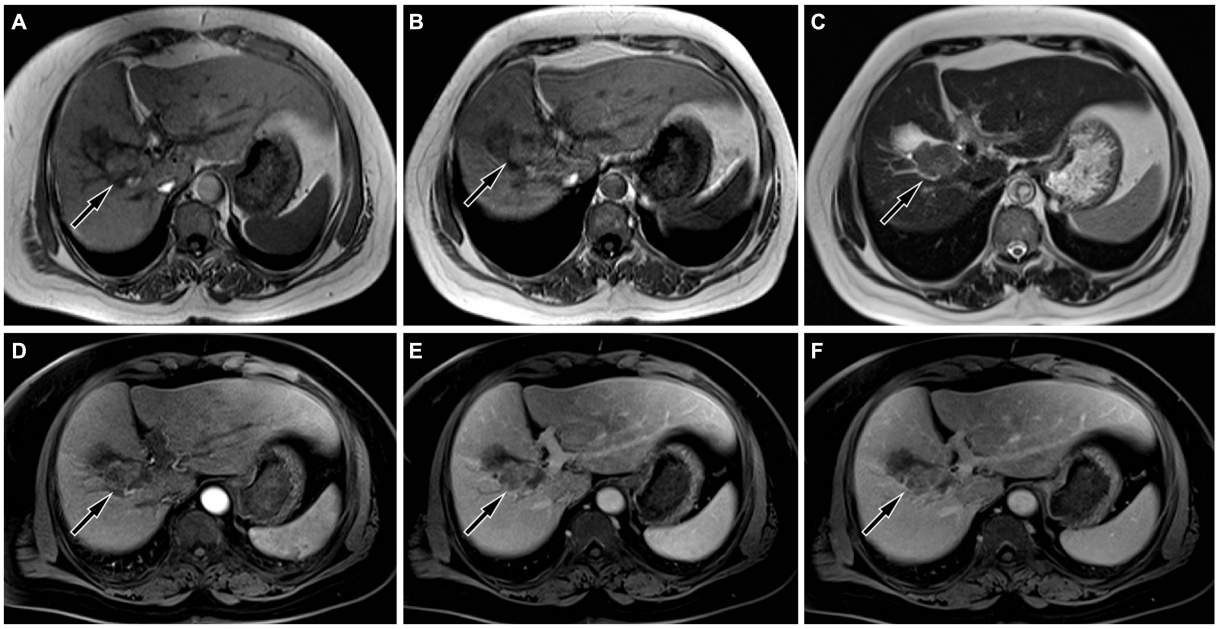

FIGURE 2
On magnetic resonance imaging (MRI), the lesion showed equal signal on both in-phase **(A)** and out-phase **(B)** of T1-weighted imaging (T1WI, arrows), and uneven slightly higher signal on T2WI (**(C)**, arrow). On contrast-enhanced T1WI, the lesion showed mild to moderate enhancement in arterial phase (**(D)**, arrow), portal phase (**(E)**, arrow) and delayed phase (**(F)**, arrow), mainly peripheral enhancement.

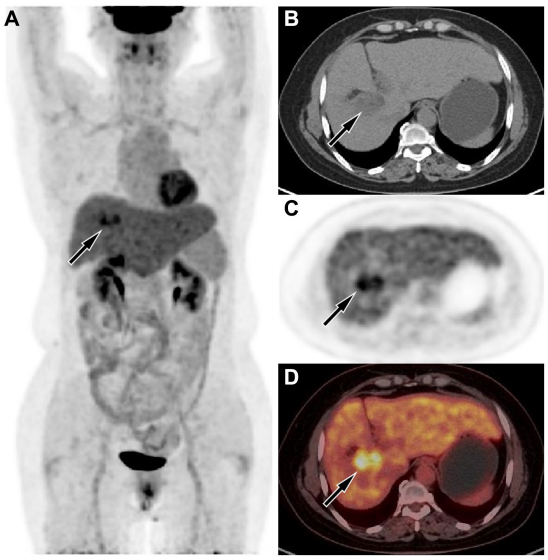

FIGURE 3
(A) The maximum intensity projection of the positron emission tomography (PET)/computed tomography (CT) showed a lesion in the liver region with increased uptake of fluorine-18 fluorodeoxyglucose (^{18}F-FDG), with a maximum standardized uptake value (SUVmax) of 8.5. Axial CT **(B)** showed the lesion in the right lobe of the liver (arrow). Axial PET **(C)** and PET/CT fusion image **(D)** showed obviously increased ^{18}F-FDG uptake of the mass (arrows).

mainly peripheral or compartmented enhancement, similar to the enhancement pattern in our patient, but IHC is usually accompanied by adjacent hepatic capsule atrophy and intrahepatic bile duct dilatation, which is different from PCCCL (15). Most of the perivascular epithelioid cell tumors in the liver are angiomyolipomas. Hepatic angiomyolipoma (HAL) showed uneven density on CT, including solid components of the tumor with equal density to the liver parenchyma and low density fat components. On PET, the solid components of the tumor can also present increased ^{18}F-FDG uptake, but the maximum standard uptake value (SUVmax) is lower than that of PCCCL. Moreover, HAL usually shows a "fast in and fast out" enhancement pattern on contrast-enhanced CT or T1WI (16). Hepatic hemangiomas usually show uniform isodense or slightly low density on CT. On contrast-enhanced CT or T1WI, peripheral nodular enhancement is common in arterial phase, and progressive centripetal filling is common in venous phase and extended phase (17), which can be differentiated from PCCCL.

As with most tumors, the diagnosis of PCCCL is determined by histopathological examination. Under the microscope, most of the tumor tissues were clear cells with abundant and bright cytoplasm, and the nucleus was located in the center, which was deeply stained and irregular. Some of the liver cells around the tumor were lipoid degeneration, showing chronic interstitial hepatitis changes (18). Immunohistochemical examination showed that almost all PCCCL were positive for Hep par1, and most of them were positive for CK, but few were positive for AFP (19, 20). The case we reported showed diffuse distribution of clear cells within the tumor tissue under the microscope, and the tumor cells expressed positive Hep par1 and CK, which met the pathological diagnostic criteria of PCCCL.

Surgical radical resection of tumors is the main treatment method for PCCCL, and surgical intervention can improve the prognosis of patients (21). For PCCCL with a diameter less than 5.0 cm, some researchers believe that radiofrequency ablation treatment can be performed; however, radiotherapy is not effective in improving the prognosis of patients (22, 23). PCCCL has a better prognosis than

TABLE 2 The outline of the patient journey.

Time flow	Affair	Results
02/01/2024	The patient had dull right upper abdominal pain without obvious cause	No processing is performed
01/02/2024	Abdominal ultrasound was performed in an outside hospital	A space-occupying lesion was found in the liver
03/02/2024	He was admitted to the Department of Gastroenterology of our hospital, and underwent laboratory examination of liver and renal function, serum tumor markers and so on	Abnormal liver function, elevated tumor marker alpha-fetoprotein.
04/02/2024	CT examination of the upper abdomen	Space occupying lesion at the junction of the left and right lobes of the liver, suspected malignant tumor
05/02/2024	MRI examination of the upper abdomen	It is suspected that the liver occupying lesion may be cholangiocarcinoma
07/02/2024	Whole body PET/CT examination	Liver malignancy, no obvious signs of metastasis were found in the rest of the body scan.
13/02/2024	The patient underwent "total hepatectomy and allogeneic orthotopic liver transplantation"	Successful surgery
13/02/2024–19/02/2024	Pathological immunohistochemical examination	Clear cell carcinoma of the liver was diagnosed
21/02/2024	CT examination of the upper abdomen	Liver blood flow is abundant, indicating the success of liver transplantation.
22/02/2024	Patient discharge	Patient discharge
26/03/2024	Telephone follow-up	The patient did not report any discomfort

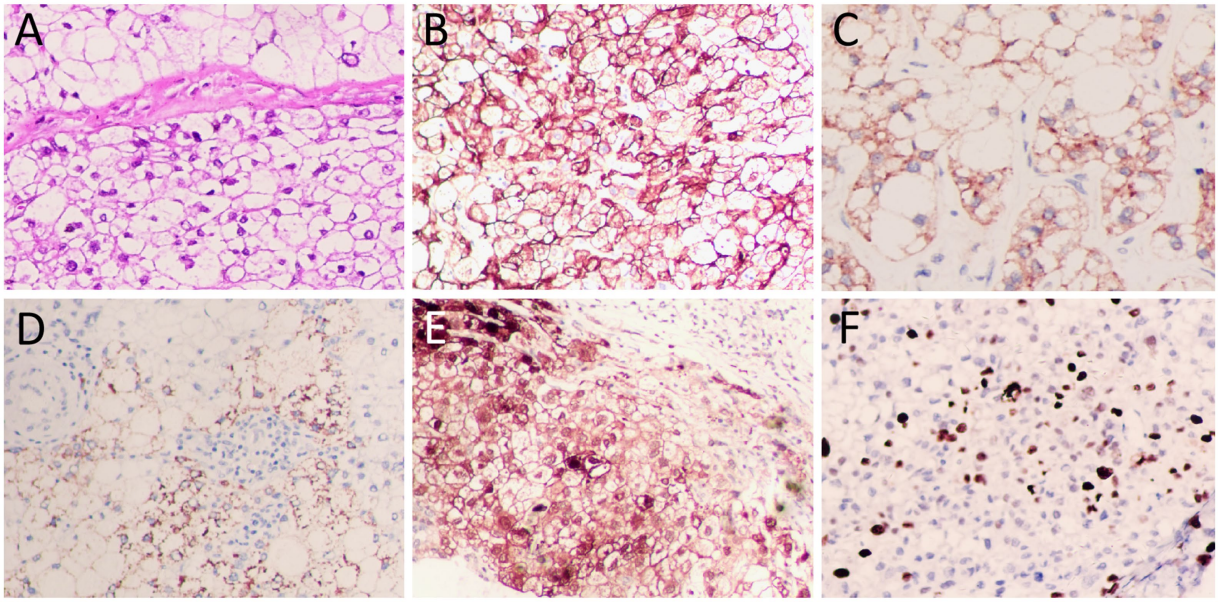

FIGURE 4
(A) Hematoxylin–eosin staining showed diffuse distribution of clear cells with abundant cytoplasm, centrally located nuclei and deep staining. Immunohistochemistry showed positive expression of tumor cells CK **(B)**, Hep par1 **(C)**, and Glypican (GPC3, **(D)**), HSP70 (partially, **(E)**), and Ki67 (about 40%, **(F)**). All images are 200 × magnification.

other types of liver cancer, but the 5-year survival rate is still low, only 28.1% (24). Therefore, understanding the imaging features of PCCCL is helpful to obtain accurate diagnosis and intervention treatment at an early stage, so as to improve its prognosis. Studies revealed that the size of the mass greater than 5.0 cm in diameter and the absence of surgical resection were independent prognostic factors for PCCCL (22–24). Due to the large mass size of the patient we reported, the maximum diameter of which exceeded 5.0 cm, and the combination of cirrhosis, after full consideration by clinicians and communication with the patient, she chose to undergo total hepatectomy and artificial liver transplantation. After the operation, the patient has been followed up so far, and she is still alive with free of disease.

Conclusion

In summary, our case study provides a reference for imaging findings of PCCCL, a relatively rare subtype of HCC. On PET/CT, tumors are usually unevenly low-density, along with increased uptake of ^{18}F-FDG. On contrast-enhanced CT or T1WI, significant enhancement can appear around the tumor during the arterial phase, and over time, the degree of enhancement of the tumor gradually decreases. Moreover, because tumor cells contain more glycogen and lipid components, resluting in the tumor shows equal or slightly higher signal on T1WI, with certain specificity. These imaging features may provide insight into PCCCL, a relatively rare subtype of HCC, and thus improve its preoperative diagnostic accuracy.

Data availability statement

The original contributions presented in the study are included in the article/supplementary material, further inquiries can be directed to the corresponding authors.

Ethics statement

Written informed consent was obtained from the individual(s) for the publication of any potentially identifiable images or data included in this article.

Author contributions

XH: Conceptualization, Data curation, Formal analysis, Funding acquisition, Methodology, Writing – original draft. LX: Investigation, Methodology, Project administration, Writing – original draft. WZ: Data curation, Formal analysis, Investigation, Writing – original draft. JC: Investigation, Resources, Supervision, Validation, Writing – review & editing. PW: Conceptualization, Formal analysis, Supervision, Visualization, Writing – review & editing.

Funding

The author(s) declare that financial support was received for the research, authorship, and/or publication of this article. This study was funded by the Guizhou Province Science and Technology Plan Project (grant numbers: Qiankehe-ZK [2024]-329) and Zunyi Science and Technology Joint Fund (Grant Number: HZ-2023-284).

Conflict of interest

The authors declare that the research was conducted in the absence of any commercial or financial relationships that could be construed as a potential conflict of interest.

Publisher's note

All claims expressed in this article are solely those of the authors and do not necessarily represent those of their affiliated organizations, or those of the publisher, the editors and the reviewers. Any product that may be evaluated in this article, or claim that may be made by its manufacturer, is not guaranteed or endorsed by the publisher.

References

1. Mann SA, Saxena R. Differential diagnosis of epithelioid and clear cell tumors in the liver. *Semin Diagn Pathol.* (2017) 34:183–91. doi: 10.1053/j.semdp.2016.12.014

2. Liu Z, Ma W, Li H, Li Q. Clinicopathological and prognostic features of primary clear cell carcinoma of the liver. *Hepatol Res.* (2008) 38:291–9. doi: 10.1111/j.1872-034X.2007.00264.x

3. Yang SH, Watanabe J, Nakashima O, Kojiro M. Clinicopathologic study on clear cell hepatocellular carcinoma. *Pathol Int.* (1996) 46:503–9. doi: 10.1111/j.1440-1827.1996.tb03645.x

4. Kothadia JP, Kaur N, Arju R, Dakhel M, Giashuddin S. Primary clear cell carcinoma of the non-cirrhotic liver presenting as an acute abdomen: a case report and review of the literature. *J Gastrointest Cancer.* (2017) 48:211–6. doi: 10.1007/s12029-016-9831-7

5. Maharajan K, Hey H, Tham I, Thamboo TP, Wong A, Khan IS, et al. Solitary vertebral metastasis of primary clear cell carcinoma of the liver: a case report and review of literature. *J Spine Surg.* (2017) 3:287–93. doi: 10.21037/jss.2017.06.06

6. Wu J, Lu AD, Zhang LP, Zuo YX, Jia YP. Study of clinical outcome and prognosis in pediatric core binding factor-acute myeloid leukemia. *Zhonghua Xue Ye Xue Za Zhi.* (2019) 40:52–7. doi: 10.3760/cma.j.issn.0253-2727.2019.01.010

7. Kokubo R, Saito K, Shirota N, Wakabayashi Y, Tsuchida A, Nagai T, et al. A case of primary clear cell hepatocellular carcinoma comprised mostly of clear cells. *Radiol Case Rep.* (2019) 14:1377–81. doi: 10.1016/j.radcr.2019.08.021

8. Wang H, Tan B, Zhao B, Gong G, Xu Z. CT findings of primary clear cell carcinoma of liver: with analysis of 19 cases and review of the literature. *Abdom Imaging.* (2014) 39:736–43. doi: 10.1007/s00261-014-0104-2

9. Liu QY, Li HG, Gao M, Lin XF, Li Y, Chen JY. Primary clear cell carcinoma in the liver: CT and MRI findings. *World J Gastroenterol.* (2011) 17:946–52. doi: 10.3748/wjg.v17.i7.946

10. Vande Lune P, Abdel Aal AK, Klimkowski S, Zarzour JG, Gunn AJ. Hepatocellular carcinoma: diagnosis, treatment algorithms, and imaging appearance after Transarterial chemoembolization. *J Clin Transl Hepatol.* (2018) 6:175–88. doi: 10.14218/JCTH.2017.00045

11. Auer TA, Halskov S, Fehrenbach U, Nevermann NF, Pelzer U, Mohr R, et al. Gd-EOB MRI for HCC subtype differentiation in a western population according to the 5(th) edition of the World Health Organization classification. *Eur Radiol.* (2023) 33:6902–15. doi: 10.1007/s00330-023-09669-y

12. Cannella R, Dioguardi Burgio M, Beaufrère A, Trapani L, Paradis V, Hobeika C, et al. Imaging features of histological subtypes of hepatocellular carcinoma: implication for LI-RADS. *JHEP Rep.* (2021) 3:100380. doi: 10.1016/j.jhepr.2021.100380

13. Bannasch P, Ribback S, Su Q, Mayer D. Clear cell hepatocellular carcinoma: origin, metabolic traits and fate of glycogenotic clear and ground glass cells. *Hepatobiliary Pancreat Dis Int.* (2017) 16:570–94. doi: 10.1016/S1499-3872(17)60071-7

14. Eggert T, McGlynn KA, Duffy A, Manns MP, Greten TF, Altekruse SF. Fibrolamellar hepatocellular carcinoma in the USA, 2000-2010: a detailed report on frequency, treatment and outcome based on the surveillance, and End Results database. *United European Gastroenterol J.* (2013) 1:351–7. doi: 10.1177/2050640613501507

15. Saleh M, Virarkar M, Bura V, Valenzuela R, Javadi S, Szklaruk J, et al. Intrahepatic cholangiocarcinoma: pathogenesis, current staging, and radiological findings. *Abdom Radiol.* (2020) 45:3662–80. doi: 10.1007/s00261-020-02559-7

16. Yang W, Sun Q, Shang M, Li S, Hu X, Hu X. Multimodal imaging study of hepatic perivascular epithelioid cell tumors: a case report. *Front Med.* (2023) 10:1322048. doi: 10.3389/fmed.2023.1322048

17. Liu Z, Yi L, Chen J, Li R, Liang K, Chen X, et al. Comparison of the clinical and MRI features of patients with hepatic hemangioma, epithelioid hemangioendothelioma, or angiosarcoma. *BMC Med Imaging*. (2020) 20:71. doi: 10.1186/s12880-020-00465-4

18. Lao XM, Zhang YQ, Jin X, Lin XJ, Guo RP, Li GH, et al. Primary clear cell carcinoma of liver--clinicopathologic features and surgical results of 18 cases. *Hepato-Gastroenterology*. (2006) 53:128–32.

19. Murakata LA, Ishak KG, Nzeako UC. Clear cell carcinoma of the liver: a comparative immunohistochemical study with renal clear cell carcinoma. *Mod Pathol*. (2000) 13:874–81. doi: 10.1038/modpathol.3880156

20. Adamek HE, Spiethoff A, Kaufmann V, Jakobs R, Riemann JF. Primary clear cell carcinoma of noncirrhotic liver: immunohistochemical discrimination of hepatocellular and cholangiocellular origin. *Dig Dis Sci*. (1998) 43:33–8. doi: 10.1023/a:1018859617522

21. Li Z, Wu X, Bi X, Zhang Y, Huang Z, Lu H, et al. Clinicopathological features and surgical outcomes of four rare subtypes of primary liver carcinoma. *Chin J Cancer Res*. (2018) 30:364–72. doi: 10.21147/j.issn.1000-9604.2018.03.08

22. Ji SP, Li Q, Dong H. Therapy and prognostic features of primary clear cell carcinoma of the liver. *World J Gastroenterol*. (2010) 16:764–9. doi: 10.3748/wjg.v16.i6.764

23. Wen J, Yao X, Xue L, Aili A, Wang J. Predictors and survival of primary clear cell carcinoma of liver: a population-based study of an uncommon primary liver tumor. *Transl Cancer Res*. (2021) 10:3326–44. doi: 10.21037/tcr-21-9

24. Chen ZS, Zhu SL, Qi LN, Li LQ. Long-term survival and prognosis for primary clear cell carcinoma of the liver after hepatectomy. *Onco Targets Ther*. (2016) 9:4129–35. doi: 10.2147/OTT.S104827

frontiers | Frontiers in Medicine

TYPE Case Report
PUBLISHED 12 June 2024
DOI 10.3389/fmed.2024.1425112

OPEN ACCESS

EDITED BY
Nataliya Lutay,
Skåne University Hospital, Sweden

REVIEWED BY
Parneet Singh,
All India Institute of Medical Sciences Bhubaneswar, India
Hubing Wu,
Southern Medical University, China
Edel Noriega-Álvarez,
University Hospital of Guadalajara, Spain

*CORRESPONDENCE
Linfeng Hu
✉ 2994642473@qq.com
Fengxiang Liao
✉ 30923363@qq.com

RECEIVED 29 April 2024
ACCEPTED 29 May 2024
PUBLISHED 12 June 2024

CITATION
Qi W, Luo Z, Shao M, Chen M, Liao F and Hu L (2024) Case report: A rare case of isolated sigmoid Rosai-Dorfman disease on contrast-enhanced CT and ^{18}F-FDG PET/CT. *Front. Med.* 11:1425112. doi: 10.3389/fmed.2024.1425112

Case report: A rare case of isolated sigmoid Rosai-Dorfman disease on contrast-enhanced CT and ^{18}F-FDG PET/CT

Wanling Qi[1], Zhehuang Luo[1], Mingyan Shao[1], Min Chen[2], Fengxiang Liao[1]*and Linfeng Hu[3]*

[1]Department of Nuclear Medicine, Jiangxi Provincial People's Hospital, The First Affiliated Hospital of Nanchang Medical College, Nanchang, China, [2]Department of Pathology, Jiangxi Provincial People's Hospital, The First Affiliated Hospital of Nanchang Medical College, Nanchang, China, [3]Department of Pediatrics, Jiangxi Provincial People's Hospital, The First Affiliated Hospital of Nanchang Medical College, Nanchang, China

Rosai-Dorfman disease (RDD) is an uncommon histiocytic disorder that occurs in nodal and/or extranodal sites. Extranodal RDD exhibits a wide range of clinical and radiological presentations, frequently leading to misdiagnoses. Involvement of the gastrointestinal (GI) system is uncommon, accounting for less than 1% of the reported cases. Here we present a case of a 54-year-old male who complained of abdominal distention and was diagnosed with RDD affecting the sigmoid colon, manifesting as a sigmoid mass. The patient had a past medical history of liver transplantation due to hepatocellular carcinoma (HC). This report details the multiphase contrast-enhanced computed tomography (CT) and fluorodeoxyglucose (^{18}F-FDG) positron emission tomography (PET-CT) imaging findings of RDD involving the sigmoid colon without lymphadenopathy, and a review of the relevant literature is provided.

KEYWORDS

Rosai-Dorfman disease, histiocytosis, CT, ^{18}F-FDG, PET/CT

Introduction

Rosai-Dorfman disease (RDD), initially described by Pierre Paul Louis Lucien Destombes in 1965 (1), was later characterized pathologically by Juan Rosai and Ronald Dorfman in 1969 (2), has the potential to affect any tissue or organ. Approximately 25–43% of patients present with extranodal involvement, including the skin, orbits, bones, upper respiratory tract, gastrointestinal (GI) system, genitourinary system, central nervous system, and endocrine glands (3). Although extranodal disease frequently occurs with nodal involvement, isolated extranodal disease is uncommon. This report documents a case of a 54-year-old male with RDD confined to the sigmoid colon. We discuss the imaging findings and diagnosis from multi-phase contrast-enhanced computed tomography (CT) and fluorodeoxyglucose (^{18}F-FDG) positron emission tomography (PET-CT), as well as the patient's treatment and follow-up. While RDD can involve the GI system, such cases are still infrequent in the literature (4–9). To the best of our knowledge, this is the first report of RDD affecting the sigmoid colon, and the utility of PET/CT in such a case has not been previously described.

Case description

A 54-year-old male patient presented with abdominal fullness for 20 days before admission. He denied symptoms of fever, nausea, vomiting, hematemesis, melena, weight loss, night sweats, and lymph node enlargement. Moreover, the patient underwent a liver transplantation eight years ago due to hepatocellular carcinoma (HC) and has since made a good recovery.

After admission, the patient underwent a series of related laboratory tests, a multiphase contrast-enhanced CT, and an ^{18}F-FDG PET/CT. The results of the blood routine tests showed that white blood cell count, red blood cell count, and C-reactive protein levels were all within normal limits. Tumor markers such as carcinoembryonic antigen (CEA), alpha-fetoprotein (AFP), and cancer antigen 19–9 (CA19-9) were within normal ranges. The plain CT scan image (Figure 1A) identified a nodular mass with isodensity in the left lower quadrant of the abdomen, measuring approximately 2.3 × 3.1 cm, with an indistinct border in relation to the sigmoid colon. No enlarged lymph nodes were observed in the surrounding fat spaces or in other areas of the body. The multiphase contrast-enhanced CT scan images (Figures 1B–D) demonstrated the lesion exhibiting mild to moderate enhancement. The CT values recorded for each phase are as follows: non-contrast scan phase 46 HU, arterial phase 57 HU, venous phase 67 HU, and delayed phase P70 HU. Based on these findings, the preliminary CT interpretation favored an inflammatory lesion, with a recommendation for follow-up after antibiotic therapy. Given the patient's history of HC, an PET-CT scan was performed to rule out the possibility of metastasis. The maximum intensity projection (MIP) image (Figure 2A) revealed a focal area of increased FDG uptake in the left lower quadrant of the abdomen. The axial CT and fused axial PET-CT images (Figures 2B,C) revealed an isolated, round, soft-tissue mass with isodensity in the left lower quadrant, showing increased FDG uptake and a maximum standardized uptake value (SUVmax) of 3.6. The corresponding coronal and sagittal CT and fused PET-CT images (Figures 2D–G) demonstrated that the mass had an indistinct margin in relation to the sigmoid colon, suggesting a gastrointestinal stromal tumor (GIST) as a likely diagnosis. The whole-body PET/CT showed the absence of any FDG avid visible lymph node or FDG avid visible disease elsewhere in the regions of the body surveyed.

To further investigate the possibility of the lesion originating from the intestinal tract, a sigmoidal-rectal endoscopic ultrasonography was conducted, which yielded no evidence of abnormality. Experiencing abdominal discomfort and harboring significant concern over the potential for malignancy, the patient underwent laparoscopic resection to obtain a definitive diagnosis. Intraoperative visualization indicated a smooth intestinal mucosa with an ill-defined, tough, off-white area in the serosal layer. Microscopic examination disclosed aggregates of obese histiocytes and plasma cells within the serosal and muscularis propria layers, with lymphocytes present in focal clusters. Peripheral collagenous fibers were observed in a braided, bundled arrangement. The presence of small lymphocytes and plasma cells within the cytoplasm of some histiocytes, a phenomenon known as emperipolesis, was noted (Figures 3A,B). Immunohistochemical analysis confirmed that the histiocytes were positive for CD68 (Figure 3C), S100 (Figure 3D), and CD163, while negative for CK, ALK, CD1a, and Langerin. The pathological findings were consistent with a diagnosis of Rosai-Dorfman disease affecting the serosal surface and deep muscular layer of sigmoid colon. A year post-surgery, routine follow-up examinations have revealed no signs of recurrence.

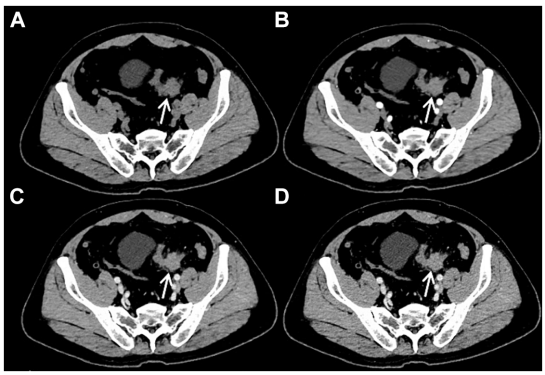

FIGURE 1
Plain CT imaging [**(A)**, arrow ↑] revealed a round soft tissue density lesion in the left lower quadrant abdomen, with the boundary of the lesion with the sigmoid colon not being distinct. On multiphasic contrast-enhanced CT scans [**(B–D)**, arrow ↑], the lesion demonstrated mild to moderate enhancement. The CT values for the non-contrast scan phase, arterial phase, venous phase, and delayed phase were 46 HU, 57 HU, 67 HU, and 70 HU, respectively.

Discussion

Rosai-Dorfman disease (RDD) is currently regarded as a neoplastic condition characterized by the clonal expansion of histiocytes in lymph nodes and/or extranodal sites (10). It is noteworthy that RDD is a rare disorder, with an estimated prevalence of 1 in 200,000 and an annual incidence of approximately 100 cases (11). The precise etiology of RDD remains elusive, but proposed factors include viral infections, such as Epstein–Barr virus and other human herpesviruses, autoimmune dysregulation, genetic mutations, and disruptions in signaling pathways (11–17). Being widely heterogeneous and presenting a variety of clinical manifestations, RDD can range from isolated cases to those associated with other diseases such as autoimmune, hereditary, malignant or IgG4 (18, 19). The GI system is one of the least commonly affected sites. It predominantly affects middle-aged females, presenting with a range of non-specific symptoms that include abdominal pain, diarrhea, rectal bleeding, and weight loss (7–9). This report details a case of RDD confined to the sigmoid colon in a 54-year-old male patient, who presented with abdominal distention. Given that neoplasia-associated RDD refers to RDD that occurs either precedes or arises subsequent to lymphoma or myelodysplastic syndrome (20), the present case, despite having a history of HC, still falls under the category of an isolated form of RDD.

Histopathologically, RDD lesions are distinguished by the infiltration of large histiocytes within the tissue, set against a backdrop of mixed inflammation. These extranodal lesions resemble nodal RDD but tend to exhibit increased fibrosis, sclerosis, a lower density of histiocytes, and less pronounced emperipolesis (21). A panel of immunostains is typically employed to confirm the diagnosis, with

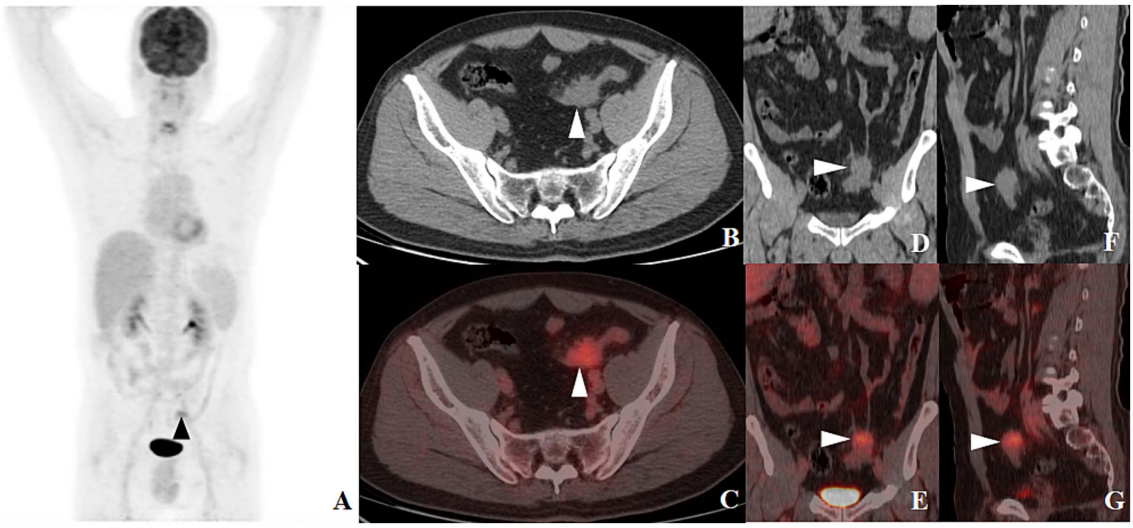

FIGURE 2
^{18}F-FDG PET-CT MIP image [**(A)**, arrow ▲] revealed a lesion with increased FDG uptake in the left lower quadrant of the abdomen. Axial CT [**(B)**, arrow ▲] and fused axial PET-CT [**(C)**, arrow ▲] images depicted an isolated, round soft tissue density mass in the same area, with increased FDG uptake and a SUVmax of 3.6. Coronal and sagittal CT images [**(D,F)**, arrow ▲] and their corresponding fused PET-CT counterparts [**(E,G)**, arrow ▲] revealed an indistinct boundary between the mass and the sigmoid colon.

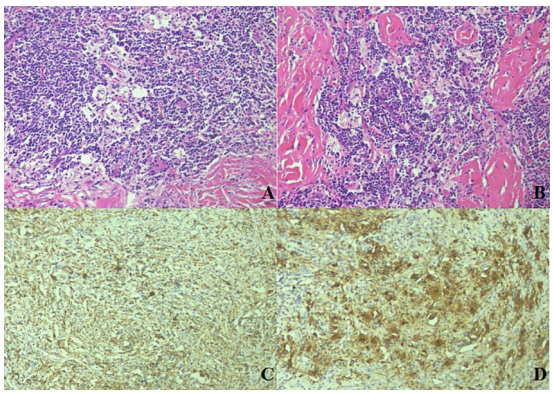

FIGURE 3
Histological and immunohistochemical characteristics of sigmoid RDD. The histological section exhibited clusters of histiocytes amidst lymphocytes and plasmacytes, with a fibrotic background. Emperipolesis, characterized by small lymphocytes and plasmacytes within the cytoplasm of the histiocytes, was evident [**(A,B)**; HE 20×]. The large histiocytes were positive for CD68 [**(C)**; HE 40×] and S100 [**(D)**; HE 40×].

positive markers including S100, CD68, and CD163, and negative markers such as CD1a, ALK, and langerin (22).

The radiological characteristics of extranodal RDD vary depending on the organ involved. On plain CT scans, extranodal RDD typically presents as well-demarcated, single or multiple lesions with isodense or hyperdense masses. Multiphasic contrast-enhanced CT often reveals significant and progressive homogeneous enhancement (20, 23, 24). MRI findings include lesions that are predominantly hypointense to isointense on T1-weighted (T1WI) images and display variable signal intensity on T2-weighted (T2WI) images, which may correspond to the presence of free radicals generated by macrophages during active phagocytosis (23, 25, 26). As most RDD-involved sites are FDG-avid, ^{18}F-FDG PET/CT could identify lesions that were not visible on conventional examinations, which has higher sensitivity and lower false-positive rates (27). The FDG avidity in RDD lesions is due to the high glucose metabolism of the proliferating histiocytes (28). A decrease in FDG uptake can signify effective treatment or spontaneous regression of RDD (27). Thus, the ^{18}F-FDG PET/CT imaging is a whole-body examination that, despite lacking specificity for the diagnosis of RDD, plays a crucial role in assessing disease extent, providing a comprehensive staging of the condition, guiding the biopsy, and monitoring treatment efficacy, considering that RDD can occur in any tissue or organ. In this case, the contrast-enhanced CT scan revealed the lesion with mild to moderate enhancement, and the PET/CT scan displayed correspondingly mild to moderate FDG uptake. Both the intensity of enhancement and the SUVmax values were lower than those reported in previous literature (20, 27, 28). These findings could be related to the proportional composition of the histiocytes, lymphocytes, and fibrosis within the lesion.

RDD in the ileum and colon can be difficult to distinguish from other intestinal pathologies such as Crohn's disease, ulcerative colitis, and colon cancer. GI RDD tends to present with more substantial intestinal wall thickening than Crohn's disease and ulcerative colitis, and it may be accompanied by intestinal obstruction (7). Endoscopic ultrasound-guided fine needle aspiration and cytological examination can provide a qualitative diagnosis (29). In this case, due to the patient's history of HC, it was necessary to differentiate from metastasis. However, the occurrence of HC spreading to the sigmoid colon was uncommon, and the lesion in this region lacked significant enhancement. Furthermore, the patient's AFP levels were normal. Taking all these aspects into account, metastasis was not suspected in the diagnosis. Since the sigmoid mass only invaded the serosal layer and muscularis propria layer of the intestine, endoscopic ultrasonography failed to detect any obvious abnormalities. Generally, GI RDD poses diagnostic challenges and requires a multi-modal approach to identification.

The treatment of RDD remains without a standardized protocol, with diverse management strategies. In general, observation is appropriate for patients with uncomplicated lymphadenopathy and asymptomatic cutaneous lesions. Surgical excision is often curative for patients with solitary extranodal disease (30). Systemic therapies are typically employed for multifocal or treatment-resistant cases (11, 31). Therefore, timely and intuitive assessment of the treatment efficacy through PET/CT is critical for determining effective options when selecting new treatments (27). In this case, the isolated lesion in the sigmoid colon was surgically removed, and the patient's prognosis was positive.

Conclusion

In conclusion, we report a rare case of unifocal extranodal RDD occurring in the sigmoid. CT imaging showed a round, ill-defined isodense mass with mild to moderate enhancement on multiphasic contrast-enhanced scans. Simultaneous PET/CT imaging showed mild to moderate FDG uptake. Given the FDG-avid nature of RDD lesions, PET/CT offers advantages over conventional imaging modalities for initial assessment, treatment strategy adjustment, and efficacy evaluation. Recognizing the imaging characteristics of RDD necessitates the accumulation of more case studies and the synthesis of clinical experience. The ultimate diagnosis of RDD still depends on biopsy or immunohistochemical analysis.

Data availability statement

The original contributions presented in the study are included in the article/supplementary material, further inquiries can be directed to the corresponding authors.

Ethics statement

The studies involving humans were approved by Jiangxi Provincial People's Hospital Medical Ethics Committee. The studies were conducted in accordance with the local legislation and institutional requirements. Written informed consent for participation in this study was provided by the participants' legal guardians/next of kin. Written informed consent was obtained from the individual(s) for the publication of any potentially identifiable images or data included in this article.

Author contributions

WQ: Writing – review & editing, Writing – original draft, Methodology. ZL: Writing – original draft, Formal analysis. MS: Writing – review & editing, Data curation. MC: Writing – review & editing, Investigation. FL: Writing – review & editing, Methodology. LH: Writing – review & editing, Data curation.

Funding

The author(s) declare that no financial support was received for the research, authorship, and/or publication of this article.

Conflict of interest

The authors declare that the research was conducted in the absence of any commercial or financial relationships that could be construed as a potential conflict of interest.

Publisher's note

References

1. Destombes P. Adénites avec surcharge lipidique, de l'enfant ou de l'adulte jeune, observées aux Antilles et au Mali. (Quatre observations) [Adenitis with lipid excess, in children or young adults, seen in the Antilles and in Mali. (4 cases)]. *Bull Soc Pathol Exot Filiales*. (1965) 58:1169–75. French.

2. Rosai J, Dorfman RF. Sinus histiocytosis with massive lymphadenopathy. A newly recognized benign clinicopathological entity. *Arch Pathol*. (1969) 87:63–70.

3. Bruce-Brand C, Schneider JW, Schubert P. Rosai-Dorfman disease: an overview. *J Clin Pathol*. (2020) 73:697–705. doi: 10.1136/jclinpath-2020-206733

4. Alatassi H, Ray MB, Galandiuk S, Sahoo S. Rosai-Dorfman disease of the gastrointestinal tract: report of a case and review of the literature. *Int J Surg Pathol*. (2006) 14:95–9. doi: 10.1177/106689690601400119

5. Noggle E, Ortanca I, Clark I, Yadak N, Glazer ES. Synchronous Colon and Pancreatic Rosai-Dorfman disease. *Am Surg*. (2021) 87:486–91. doi: 10.1177/0003134820950294

6. Nathwani RA, Kenyon L, Kowalski T. Rosai-Dorfman disease of the colon. *Gastrointest Endosc*. (2008) 68:194–6. doi: 10.1016/j.gie.2007.11.007

7. Baran B, Karaca C, Soyer OM, Yonal I, Isiklar AD, Cakmak R, et al. Rosai-Dorfman disease with diffuse gastrointestinal involvement. *Eur J Gastroenterol Hepatol*. (2013) 25:869–74. doi: 10.1097/MEG.0b013e32836019f8

8. Alruwaii ZI, Zhang Y, Larman T, Miller JA, Montgomery EA. Rosai-Dorfman disease of the digestive system-beware vasculopathy: a Clinicopathologic analysis. *Am J Surg Pathol*. (2019) 43:1644–52. doi: 10.1097/PAS.0000000000001343

9. Lauwers GY, Perez-Atayde A, Dorfman RF, Rosai J. The digestive system manifestations of Rosai-Dorfman disease (sinus histiocytosis with massive lymphadenopathy): review of 11 cases. *Hum Pathol*. (2000) 31:380–5. doi: 10.1016/s0046-8177(00)80254-3

10. Ravindran A, Rech KL. How I diagnose Rosai-Dorfman disease. *Am J Clin Pathol*. (2023) 160:1–10. doi: 10.1093/ajcp/aqad047

11. Abla O, Jacobsen E, Picarsic J, Krenova Z, Jaffe R, Emile JF, et al. Consensus recommendations for the diagnosis and clinical management of Rosai-Dorfman-Destombes disease. *Blood*. (2018) 131:2877–90. doi: 10.1182/blood-2018-03-839753

12. Paulli M, Bergamaschi G, Tonon L, Viglio A, Rosso R, Facchetti F, et al. Evidence for a polyclonal nature of the cell infiltrate in sinus histiocytosis with massive lymphadenopathy (Rosai-Dorfman disease). *Br J Haematol*. (1995) 91:415–8. doi: 10.1111/j.1365-2141.1995.tb05313.x

13. Delacrétaz F, Meugé-Moraw C, Anwar D, Borisch B, Chave JP. Sinus histiocytosis with massive lymphadenopathy (Rosai Dorfman disease) in an HIV-positive patient. *Virchows Arch A Pathol Anat Histopathol*. (1991) 419:251–4. doi: 10.1007/BF01626356

14. Chougule A, Bal A, Das A, Singh G. IgG4 related sclerosing mastitis: expanding the morphological spectrum of IgG4 related diseases. *Pathology*. (2015) 47:27–33. doi: 10.1097/PAT.0000000000000187

15. Diamond EL, Durham BH, Haroche J, Yao Z, Ma J, Parikh SA, et al. Diverse and targetable kinase alterations drive histiocytic neoplasms. *Cancer Discov*. (2016) 6:154–65. doi: 10.1158/2159-8290.CD-15-0913

16. Garces S, Medeiros LJ, Patel KP, Li S, Pina-Oviedo S, Li J, et al. Mutually exclusive recurrent KRAS and MAP2K1 mutations in Rosai-Dorfman disease. *Mod Pathol*. (2017) 30:1367–77. doi: 10.1038/modpathol.2017.55

17. Richardson TE, Wachsmann M, Oliver D, Abedin Z, Ye D, Burns DK, et al. BRAF mutation leading to central nervous system rosai-dorfman disease. *Ann Neurol*. (2018) 84:147–52. doi: 10.1002/ana.25281

18. Chen LYC, Slack GW, Carruthers MN. IgG4-related disease and Rosai-Dorfman-Destombes disease. *Lancet*. (2021) 398:1213–4. doi: 10.1016/S0140-6736(21)01812-2

19. Tatit RT, Raffa PEAZ, de Almeida Motta GC, Bocchi AA, Guimaraes JL, Franceschini PR, et al. Rosai-Dorfman disease mimicking images of meningiomas: two case reports and literature review. *Surg Neurol Int*. (2021) 12:292. doi: 10.25259/SNI_918_2020

20. Li H, Li D, Xia J, Huang H, Jiao N, Zheng Z, et al. Radiological features of Rosai-Dorfman disease: case series and review of the literature. *Clin Radiol*. (2022) 77:e799–805. doi: 10.1016/j.crad.2022.07.008

21. McClain KL, Bigenwald C, Collin M, Haroche J, Marsh RA, Merad M, et al. Histiocytic disorders. *Nat Rev Dis Primers*. (2021) 7:313. doi: 10.1038/s41572-021-00307-9

22. Rech KL, He R. Challenges in the histopathologic diagnosis of histiocytic neoplasms. *J Natl Compr Cancer Netw*. (2021) 19:1305–11. doi: 10.6004/jnccn.2021.7098

23. Alimli AG, Oztunali C, Boyunaga OL, Pamukcuoglu S, Okur A, Borcek AO. MRI and CT findings of isolated intracranial Rosai-Dorfman disease in a child. *Neuroradiol J*. (2016) 29:146–9. doi: 10.1177/1971400915628020

24. Rittner RE, Baumann U, Laenger F, Hartung D, Rosenthal H, Hueper K. Whole-body diffusion-weighted MRI in a case of Rosai-Dorfman disease with exclusive multifocal skeletal involvement. *Skeletal Radiol*. (2012) 41:709–13. doi: 10.1007/s00256-011-1328-7

25. Karajgikar J, Grimaldi G, Friedman B, Hines J. Abdominal and pelvic manifestations of Rosai-Dorfman disease: a review of four cases. *Clin Imaging*. (2016) 40:1291–5. doi: 10.1016/j.clinimag.2016.09.006

26. Nguyen PX, Nguyen NV, Le TD. Spinal extranodal Rosai-Dorfman disease: a case report and literature review. *Int J Surg Case Rep*. (2021) 88:106491. doi: 10.1016/j.ijscr.2021.106491

27. Lu X, Wang R, Zhu Z. The value of ^{18}F-FDG PET/CT in the systemic evaluation of patients with Rosai-Dorfman disease: a retrospective study and literature review. *Orphanet J Rare Dis*. (2023) 18:116. doi: 10.1186/s13023-023-02711-8

28. Gupta N, Verma R, Belho ES, Manocha A. Isolated Extranodal Rosai-Dorfman disease on ^{18}F-FDG PET-CT scan. *Indian J Nucl Med*. (2019) 34:319–20. doi: 10.4103/ijnm.IJNM_152_19

29. Ioannidis I, Manolakis C, Laurini JA, Roveda KP, de Melo S, Jr AB, et al. Rectal extranodal Rosai-Dorfman disease diagnosed by EUS-FNA: a case report and review of the literature. *Diagn Cytopathol*. (2015) 43:40–4. doi: 10.1002/dc.23112

30. Zhang GJ, Ma XJ, Zhang YP, Hao LF, Wang L, Zhang JT, et al. Surgical management and outcome of primary intracranial Rosai-Dorfman disease: a single-institute experience and pooled analysis of individual patient data. *Neurosurg Rev*. (2023) 46:76. doi: 10.1007/s10143-023-01983-9

31. Xu H, Zhang H, Li W, Zhang C, Wang H, Wang D. Nasal presentations of Rosai-Dorfman disease: clinical manifestation and treatment outcomes. *Ear Nose Throat J*. (2023):1455613231162226. doi: 10.1177/01455613231162226

frontiers | Frontiers in Medicine

TYPE Systematic Review
PUBLISHED 20 June 2024
DOI 10.3389/fmed.2024.1425134

OPEN ACCESS

EDITED BY
Francesco Dondi,
Universitàdegli Studi di Brescia, Italy

REVIEWED BY
Edel Noriega-Álvarez,
University Hospital of Guadalajara, Spain
Alfred Otoe Ankrah,
Korle Bu Teaching Hospital, Ghana

*CORRESPONDENCE
Yuanrong Wang
✉ 343392994@qq.com

RECEIVED 29 April 2024
ACCEPTED 12 June 2024
PUBLISHED 20 June 2024

CITATION
Wang Y, Jing R, Wang H and Zhao Q (2024) ^{68}Ga-PSMA-11 PET and mpMRI in the diagnosis of initial lymph node staging of prostate cancer: a head-to-head comparative meta-analysis.
Front. Med. 11:1425134.
doi: 10.3389/fmed.2024.1425134

^{68}Ga-PSMA-11 PET and mpMRI in the diagnosis of initial lymph node staging of prostate cancer: a head-to-head comparative meta-analysis

Yuanrong Wang[1]*, Ren Jing[2], Haiyan Wang[1] and Qiuyan Zhao[3]

[1]Department of Geriatric Medical Center, West China Hospital of Sichuan University, Chengdu, China, [2]Department of International Medical Center, West China Hospital of Sichuan University, Chengdu, China, [3]Outpatient Department, West China Hospital of Sichuan University, Chengdu, China

Purpose: This meta-analysis evaluates the comparative diagnostic efficacy of ^{68}Ga-prostate-specific membrane antigen-11 PET (^{68}Ga-PSMA-11 PET) and multiparametric MRI (mpMRI) for the initial lymph node staging of prostate cancer.

Methods: We searched PubMed and Embase databases through October 2023 for studies that provide a head-to-head comparison of ^{68}Ga-PSMA-11 PET and mpMRI, using pelvic lymph node dissection as the gold standard. We assessed sensitivity and specificity using the DerSimonian and Laird method, with variance stabilization via the Freeman-Tukey double inverse sine transformation. The quality of included studies was evaluated using the Quality Assessment of Diagnostic Performance Studies (QUADAS-2) tool.

Results: The meta-analysis incorporated 13 articles, involving a total of 1,527 patients. ^{68}Ga-PSMA-11 PET demonstrated an overall sensitivity of 0.73 (95% CI: 0.51–0.91) and a specificity of 0.94 (95% CI: 0.88–0.99). In comparison, mpMRI showed a sensitivity of 0.49 (95% CI: 0.30–0.68) and a specificity of 0.94 (95% CI: 0.88–0.99). Although ^{68}Ga-PSMA-11 PET appeared to be more sensitive than mpMRI, the differences in sensitivity (p=0.11) and specificity (p=0.47) were not statistically significant.

Conclusion: Our findings indicated that ^{68}Ga-PSMA-11 PET and mpMRI exhibit similar sensitivity and specificity in the diagnosis of initial lymph node staging of prostate cancer. However, given that most included studies were retrospective, further prospective studies with larger sample sizes are essential to validate these results.

Systematic Review Registration: PROSPERO code is CRD42023495266.

KEYWORDS

^{68}Ga-PSMA-PET, mpMRI, lymph node metastases, prostate cancer, meta-analysis

1 Introduction

The 2020 World Cancer Report data indicates that prostate cancer ranks as the 6th most common malignancy in terms of incidence and the 9th in terms of mortality among males (1). In the realm of prostate cancer diagnostics and therapeutics, the evaluation for lymph node metastasis is imperative, given its critical role as a prognostic determinant (2). The

identification of cancer metastasis to lymph nodes aids physicians in gauging the disease's severity, devising more targeted treatment strategies, and estimating patient survival rates and quality of life, thereby underscoring its significance in comprehensive prostate cancer management (3). Given the limitations of pelvic lymph node dissection (PLND) in terms of increased risk of complications and longer hospital stays, there has been a focus on alternative approaches to improve diagnostic accuracy while minimizing adverse effects (3, 4). Conventional imaging techniques such as computed tomography (CT) and magnetic resonance imaging (MRI) have been widely used to assess pelvic lymph nodes. However, their effectiveness is hindered by limitations in sensitivity, specificity, and spatial resolution (5, 6).

In recent years, ^{68}Ga-prostate-specific membrane antigen-11 PET (^{68}Ga-PSMA-11 PET) and multiparametric MRI (mpMRI) have emerged as promising technologies in enhancing the accuracy of initial lymph node staging in prostate cancer (7). These methods have garnered attention for their improved diagnostic precision, yet debates and research continue regarding their relative efficacy, reliability, and accessibility. Several studies present conflicting views on the comparative efficacy of ^{68}Ga-PSMA-11 PET and mpMRI in prostate cancer staging. While some studies highlight the superior sensitivity of ^{68}Ga-PSMA-11 PET, others report comparable diagnostic performance between the two modalities (8–20).

In light of these discrepancies, this meta-analysis aims to systematically evaluate and amalgamate existing research concerning the diagnostic accuracy of ^{68}Ga-PSMA-11 PET and mpMRI in the initial lymph node staging of prostate cancer. To ensure consistency and reduce variability between studies, only those investigations where both modalities were utilized in the same patient cohort have been included.

2 Method

The methodology adhered to the Preferred Reporting Items for a Systematic Review and Meta-analysis of Diagnostic Test Accuracy (PRISMA-DTA) guidelines, ensuring comprehensive and transparent reporting (21). Furthermore, the protocol for this meta-analysis has been registered with PROSPERO (CRD42023495266).

2.1 Search strategy

To gather relevant literature, an extensive search was conducted across databases including PubMed and Embase, covering publications up to October 2023. The search strategy incorporated key terms such as "Positron-Emission Tomography," "Multiparametric Magnetic Resonance Imaging," and "Prostatic Neoplasms," ensuring a focused approach to identifying pertinent studies. For more detailed information regarding the search strategy, refer to Supplementary Table S1.

Additionally, the reference lists of all included studies were manually scrutinized, aiming to uncover any additional relevant articles that may have been missed during the initial database search.

2.2 Inclusion and exclusion criteria

For inclusion in this meta-analysis, studies had to meet specific criteria: population (P): patients undergoing pelvic lymph node staging before radical prostatectomy for prostate cancer; intervention (I): ^{68}Ga-PSMA-11 PET imaging; comparison (C): mpMRI imaging; outcome (O): sensitivity and specificity of each imaging modality in staging pelvic lymph nodes; study design (S): retrospective or prospective design.

Exclusion criteria were applied to maintain study quality and relevance: (1) duplicated articles, abstracts without full texts, editorial comments, letters, case reports, reviews, meta-analyses, irrelevant titles and abstracts, (2) non-English full-text articles were excluded; (3) studies lacking complete or clear data necessary for calculating sensitivity or specificity of the studied imaging modality; (4) patients less than 10; (5) without employing histopathology confirmation from PLND as the reference standard.

The screening process involved two researchers independently evaluating titles and abstracts of retrieved articles. Subsequently, full-text versions of remaining articles were assessed to determine their eligibility for inclusion. Any disagreements between the researchers were resolved through consensus.

2.3 Quality assessment

Two researchers independently assessed the quality and clinical applicability of included studies using the Quality Assessment of Diagnostic Performance Studies (QUADAS-2) tool, which encompasses four critical domains: patient selection, index test, reference standard, and flow and timing. Within each domain, the risk of bias and concerns regarding clinical applicability were categorized as "high risk," "low risk," or "unclear risk." This systematic approach ensured a rigorous evaluation of study quality and provided insights into the practical relevance and applicability of the findings in clinical settings.

2.4 Data extraction

Two researchers independently conducted data extraction from the included articles, covering a range of essential information. This included details about the author, publication year, and the specific imaging test employed in the study. Additionally, data encompassed various study features such as country, design, analysis methods, and duration. Patient characteristics, such as the number of patients or lesions, PSA levels, mean or median age, and Gleason scores, were also extracted. Technical aspects such as scanner modality, ligand dosage, and image analysis techniques were included as well. In instances where discrepancies arose, the researchers engaged in discussions until a consensus was achieved, ensuring the accuracy and reliability of the extracted data.

2.5 Statistical analysis

The DerSimonian and Laird method was employed to assess sensitivity and specificity, which were then transformed using the Freeman–Tukey double inverse sine transformation. To determine the precision of these values, the Jackson method was used to calculate confidence intervals.

Heterogeneity within and between groups was evaluated using the Cochrane Q and I^2 statistics. Significantly differing heterogeneity

($p < 0.10$ or $I^2 > 50\%$) prompted further investigation through meta-regression and sensitivity analysis to identify potential sources.

Publication bias was assessed using both funnel plot analysis and Egger's test, ensuring the examination of potential reporting biases. Statistical significance was set at $p < 0.05$ for all tests conducted. All statistical analyses were performed using R software version 4.3.2.

3 Results

3.1 Study selection

The preliminary search identified 1,473 publications, of which 855 were duplicates and 602 did not meet the eligibility criteria, leading to their exclusion. Subsequently, a comprehensive review of the full texts of the remaining 16 articles was conducted. Among these, three articles were deemed ineligible due to missing data, resulting in their exclusion from the study. Ultimately, 13 articles that evaluated the diagnostic efficacy of ^{68}Ga-PSMA-11 PET and mpMRI met all criteria and were included in the meta-analysis (8–20). The process of article selection of the PRISMA flow diagram was illustrated in Figure 1.

3.2 Study description and quality assessment

The 13 eligible studies encompassed a total of 1,527 breast cancer patients, with the sample size ranging from 10 to 780 across the studies. Among these, 12 articles adopted a retrospective study design, while 1 article employed a prospective approach. Regarding the analysis methods, 12 studies utilized patient-based analysis, while 1 study employed lesion-based analysis. Detailed characteristics of these studies are summarized in Tables 1, 2, providing an overview of the study and technique specifics related to ^{68}Ga-PSMA-11 PET and mpMRI.

The risk of bias assessment, conducted using the QUADAS-2 tool, is visually represented in Figure 2. Specifically, 5 studies were identified as having a "high risk" in terms of the index test bias due to undetermined cut-off values. Additionally, 3 studies were categorized as "high risk" in terms of the reference standard bias as the final diagnosis lacked independent confirmation by multiple physicians. Moreover, 4 studies were graded as "high risk" in the flow and timing domain due to participant exclusion from data analyses. Overall, despite these specific biases identified, the overall quality assessment did not raise major concerns regarding the quality of the included studies.

3.3 Comparing the sensitivity of ^{68}Ga-PSMA-11 PET and mpMRI for diagnosis of initial lymph node staging of prostate cancer

The analysis included a total of 13 studies. The pooled sensitivity of ^{68}Ga-PSMA-11 PET for diagnosing initial lymph node staging of prostate cancer was 0.73 (95% CI: 0.51–0.91), while mpMRI showed an overall sensitivity of 0.49 (95% CI: 0.30–0.68), as depicted in Figure 3. Interestingly, there was no significant difference in sensitivity between ^{68}Ga-PSMA-11 PET and mpMRI ($p = 0.11$), as indicated by Figure 3.

In terms of heterogeneity, the I^2 values for the pooled overall sensitivity were 84% for ^{68}Ga-PSMA-11 PET and 79% for mpMRI, highlighting substantial heterogeneity (Figure 3). Despite this, meta-regression and sensitivity analysis did not identify any potential sources of heterogeneity, as illustrated in Figures 4, 5 and Table 3. Notably, the results from the sensitivity analysis remained stable, with only minor variations observed (ranging from 0.66 to 0.78 for ^{68}Ga-PSMA-11 PET and from 0.43 to 0.53 for mpMRI), as shown in Figures 4, 5.

3.4 Comparing the specificity of ^{68}Ga-PSMA-11 PET and mpMRI for diagnosis of initial lymph node staging of prostate cancer

The analysis comprised 13 studies. The pooled specificity of ^{68}Ga-PSMA-11 PET for diagnosing initial lymph node staging of prostate cancer was 0.94 (95% CI: 0.88–0.99), while mpMRI demonstrated an overall specificity of 0.90 (95% CI: 0.79–0.98), as illustrated in Figure 6. Notably, there was no significant difference in the overall specificity between ^{68}Ga-PSMA-11 PET and mpMRI ($p = 0.47$), as shown in Figure 6.

In terms of heterogeneity, the pooled overall specificity exhibited I^2 values of 87% for ^{68}Ga-PSMA-11 PET and 91% for mpMRI, indicating substantial heterogeneity (Figures 7, 8). Interestingly, further analysis revealed that the number of patients included in the mpMRI analysis (>50 vs. ≤50, $p = 0.02$) may be the source of this heterogeneity, as detailed in Table 4. However, sensitivity analysis did not identify any potential sources of heterogeneity and the results remained stable, with only minor variations observed (ranging from 0.93 to 0.97 for ^{68}Ga-PSMA-11 PET and from 0.89 to 0.93 for mpMRI), as depicted in Figures 7, 8.

3.5 Publication bias of ^{68}Ga-PSMA-11 PET and mpMRI for diagnosis of initial lymph node staging of prostate cancer

Funnel plot asymmetry test showed that there was a significant publication bias for specificity of ^{68}Ga-PSMA-11 PET and mpMRI (Egger's test: $p = 0.01$ and $p = 0.00$), and no significant publication bias was observed for sensitivity of ^{68}Ga-PSMA-11 PET and mpMRI (Egger's test: $p = 0.89$ and $p = 0.41$) (Supplementary Figures S1–S4).

4 Discussion

In the realm of diagnosing initial lymph node staging in prostate cancer, there exists considerable uncertainty and debate regarding the comparative diagnostic effectiveness of ^{68}Ga-PSMA-11 PET and mpMRI. In 2022, Arslan et al. (20) stated that the sensitivity of both PSMA-PET/CT and mpMRI in the detection of metastatic lymph nodes was low. Berger et al. (19) highlighted the superior lesion detection capabilities of PSMA-PET/CT, particularly in terms of sensitivity, as compared to mpMRI. Conversely, Zhang et al. (8) found no significant difference in the detection of lymph node metastases (LNMs), particularly with respect to the diameter of the LNMs, between these two modalities. This discrepancy in findings

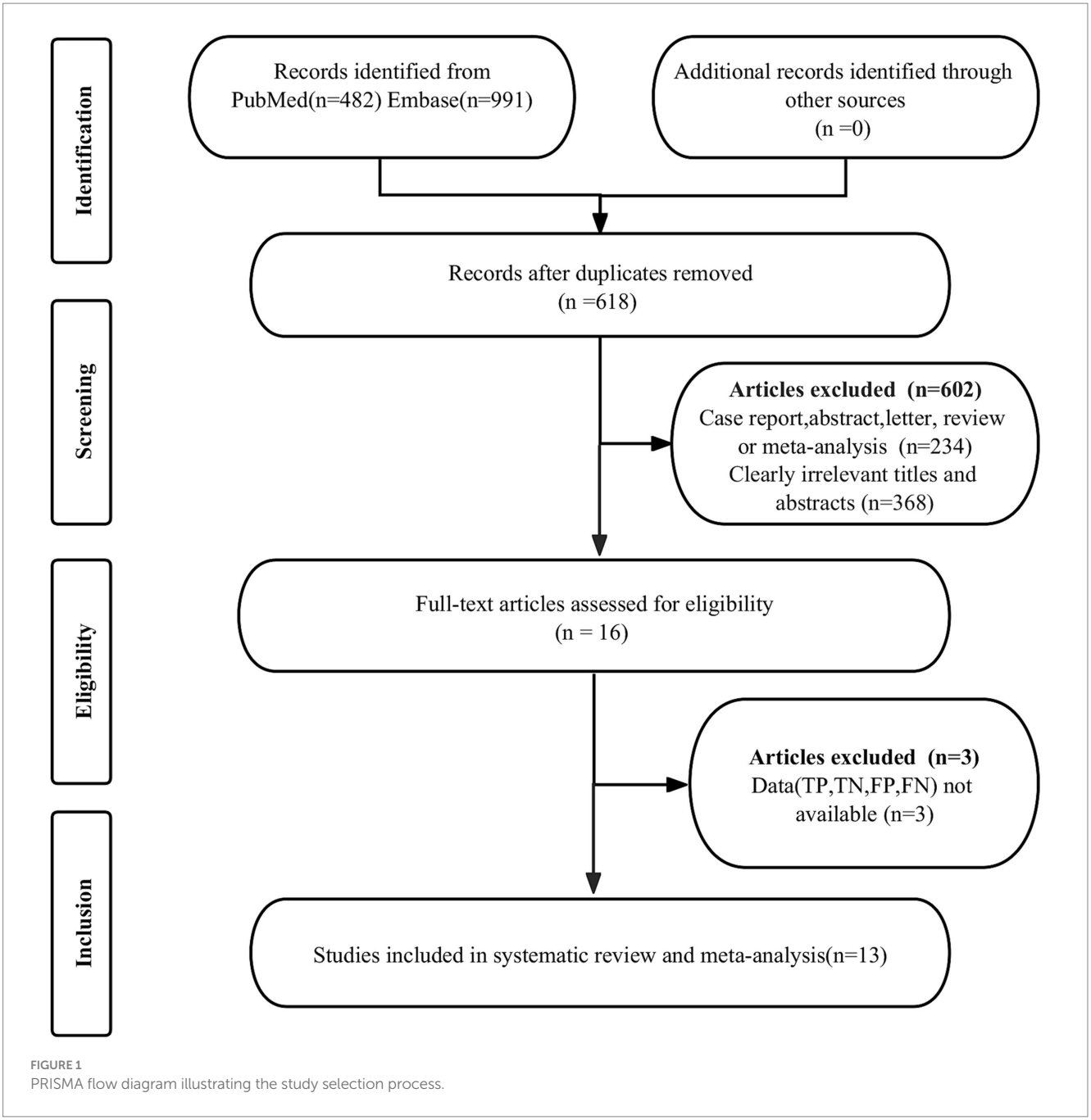

FIGURE 1
PRISMA flow diagram illustrating the study selection process.

underscores the ongoing debate and the need for comprehensive meta-analyses to clarify these differences. To mitigate the impact of bias and enhance the internal validity and reliability, this study using histopathology as the reference, presents a head-to-head comparison of ^{68}Ga-PSMA-11 PET and mpMRI.

In our meta-analysis, the pooled sensitivity of ^{68}Ga-PSMA-11 PET in the initial lymph node staging of prostate cancer was found to be 0.73 (95% CI: 0.51–0.91), while mpMRI demonstrated a sensitivity of 0.49 (95% CI: 0.30–0.68). It can be observed that ^{68}Ga-PSMA-11 PET demonstrates higher sensitivity in detecting early lymph node metastasis in prostate cancer. However, no significant difference was observed. Wang et al. (22) evaluated the diagnostic performance of ^{68}Ga-PSMA-11 PET in comparison to mpMRI for prostate cancer lymph node staging. Their article suggests that ^{68}Ga-PSMA-11 PET/CT exhibits a higher sensitivity (71% vs. 40%). However, statistical tests for differences in sensitivity and specificity between the two diagnostic tools were not performed in their article. Our study conducted statistical tests for differences to determine if there are significant difference in performance between these two methods, rather than merely observing a trend.

Furthermore, the specificity was 0.94 (95% CI: 0.88–0.99) for ^{68}Ga-PSMA-11 PET and 0.90 (95% CI: 0.79–0.98) for mpMRI in our study. Wang's study suggested noting comparable specificity (92% vs. 92%) between the two methods. However, this contrasts with the findings of Chow et al. (23). The direct comparison in the study revealed a significant specificity advantage of 15.0 percentage points for PSMA-PET (95% CI 6.7–23.2; $p < 0.001$). This may be related to this study's use of various tracers in PSMA-PET imaging, such as

TABLE 1 Study and patient characteristics of the included studies.

Author	Year	Study characteristics				Number of patients (lesion)	Patient characteristics			
		Country	Study design	Analysis	Period		PSA level (ng/mL)	Age (year)	Gleason score	Reference standard
Hotker et al.	2023	Switzerland	Retro	PB	2016–2019	41	NA	Median: 65	Gleason = 7 (36.6%) Gleason ≥8 (63.4%)	PLND
Arslan et al.	2022	Turkey	Retro	LB	2015–2020	780	Median: 5.6	Mean: 62.47	Gleason = 7 (84.6%) Gleason ≥8 (15.4%)	ePLND
Skawran et al.	2022	Switzerland	Retro	PB	2016–2019	35	Median: 18.3	Mean: 66	Gleason = 7 (26.5%) Gleason ≥8 (73.5%)	PLND
Szigeti et al.	2022	Austria	Pro	PB	2017–2020	81	Mean: 15.4	Mean: 64.5	Gleason ≤6 (1.9%) Gleason = 7 (59.3%) Gleason ≥8 (38.8%)	ePLND
Damme et al.	2021	Belgium	Retro	PB	2016–2019	81	Median: 12.29	Median: 67	NA	PLND
Celen et al.	2020	Turkey	Retro	PB	NA	22	Mean: 9.49	Mean: 65.07	Gleason ≤6 (23.3%) Gleason = 7 (40.0%) Gleason ≥8 (36.7%)	PLND
Kulkarni et al.	2020	India	Retro	PB	2016–2018	51	Mean: 39.4	Mean: 66	Gleason ≤7 (51.0%) Gleason >7 (49.0%)	PLND
Frumer et al.	2020	Israel	Retro	PB	2016–2019	89	Median: 8.5	Median: 66.9	Gleason ≤7 (79.8%) Gleason >7 (20.2%)	PLND
Franklin et al.	2020	Australia	Retro	PB	2014–2019	233	Mean: 7.4	Mean: 68	NA	PLND
Yilmaz et al.	2019	Turkey	Retro	PB	2016–2018	10	NA	NA	NA	rPLND
Berger et al.	2018	Australia	Retro	PB	2015–2017	50	Mean: 10.6	Mean: 64.9	Gleason ≤6 (2%) Gleason = 7 (66%) Gleason ≥8 (32%)	ePLND
Gupta et al.	2017	India	Retro	PB	2014–2015	12	Median: 24.3	Mean: 61.75	Gleason ≤6 (8.3%) Gleason = 7 (16.7%) Gleason ≥8 (75%)	ePLND
Zhang et al.	2017	China	Retro	PB	2017	42	Mean: 52.31	Mean: 68.86	Gleason = 7 (42.9%) Gleason ≥8 (57.1%)	PLND

Pro, prospective; Retro, retrospective; PB, patient-based; LB, lesion-based; ePLND, extended lymph node dissection; rPLND, retroperitoneal lymph node dissection; PLND, lymph node dissection; NA, not available.

10.3389/fmed.2024.1425134

TABLE 2 Technical aspects of included studies.

Author	Year	Types of imaging tests	Scanner modality for PET	Scanner modality for mpMRI	Ligand dose	Image analysis	TP, FP, FN, TN (PET/CT)	TP, FP, FN, TN (mpMRI)
Hotker et al.	2023	[^{68}Ga]Ga-PSMA PET vs. mpMRI	SIGNA PET/MR, GE Healthcare, Waukesha, United States; or Discovery MI PET/CT, GE Healthcare, Waukesha, WI, United States	MAGNETOM Skyra, Siemens Healthineers, Erlangen, Germany	2 MBq/kg	Visual and semiquantitative	TP: 7, FP: 0, FN: 4, TN: 30	TP: 9, FP: 15, FN: 2, TN: 15
Arslan et al.	2022	[^{68}Ga]Ga-PSMA PET vs. mpMRI	GE Discovery 710 (General Electric, Milwaukee WI), GE Discovery IQ (General Electric, Milwaukee WI), or Siemens (Siemens, Erlangen, Germany) Biograph 20 mCT	3.0 T MR Siemens Healthineers, Magnetom Skyra, Erlangen, Germany	NA	Visual	TP: 2, FP: 4, FN: 9, TN: 765	TP: 4, FP: 3, FN: 7, TN: 766
Skawran et al.	2022	[^{68}Ga]Ga-PSMA PET vs. mpMRI	SIGNA PET/MR; GE Healthcare, Waukesha, USA	MAGNETOM Skyra, Siemens Healthineers, Erlangen, Germany	134 ± 18.8 MBq	Visual and semiquantitative	TP: 5, FP: 0, FN: 4, TN: 26	TP: 9, FP: 3, FN: 5, TN: 6
Szigeti et al.	2022	[^{68}Ga]Ga-PSMA PET vs. mpMRI	Philips Ingenuity TF, Amsterdam/the Netherlands, and Siemens Biograph mCT, Erlangen/Germany	Achieva, Philips Medical Systems, Best/The Netherlands	2.15 MBq/kg	Visual and semiquantitative	TP: 6, FP: 4, FN: 4, TN: 34	TP: 5, FP: 1, FN: 5, TN: 37
Damme et al.	2021	[^{68}Ga]Ga-PSMA PET vs. mpMRI	PSMA-HBED-11 labelling kits provided by ABX, Germany; ^{68}Ge/^{68}Ga Galli Ad generator, IRE Elite, Fleurus, Belgium	Ingenia, Philips Medical Systems, The Netherlands	110 MBq	Visual and semiquantitative	TP: 31, FP: 2, FN: 0, TN: 48	TP: 18, FP: 0, FN: 9, TN: 54
Celen et al.	2020	[^{68}Ga]Ga-PSMA PET vs. mpMRI	Gemini TF TOF PET-CT; Philips, Cleve-land, OH, United States	Ingenia, Philips Medical Systems, The Netherlands	125–317 MBq	Visual and semiquantitative	TP: 1, FP: 11, FN: 0, TN: 10	TP: 1, FP: 0, FN: 9, TN: 12
Kulkarni et al.	2020	[^{68}Ga]Ga-PSMA PET vs. mpMRI	General Electric Medical Systems with eight slice helical CT scanner, Chicago, Illinois, United States	GE Discovery MR 750 W, Illinois, United States	111–166 MBq	Visual and semiquantitative	TP: 13, FP: 3, FN: 3, TN: 16	TP: 7, FP: 9, FN: 4, TN: 15
Frumer et al.	2020	[^{68}Ga]Ga-PSMA PET vs. mpMRI	NA	3.0-T MR scanner or a 1.5-T scanner with a trans-rectal coil	112–187 MBq	Visual and semiquantitative	TP: 3, FP: 4, FN: 9, TN: 73	TP: 1, FP: 2, FN: 8, TN: 71
Franklin et al.	2020	[^{68}Ga]Ga-PSMA PET vs. mpMRI	Philips Healthcare, Best, The Nederlands	Skyra; Siemens healthcare, Erlingen, Germany	200 MBq	Visual and semiquantitative	TP: 28, FP: 14, FN: 30, TN: 161	TP: 13, FP: 9, FN: 45, TN: 166
Yilmaz et al.	2019	[^{68}Ga]Ga-PSMA PET vs. mpMRI	NA	Verio; Siemens Medical Solutions, Erlangen, Germany	175 MBq	Visual and semiquantitative	TP: 2, FP: 0, FN: 0, TN: 8	TP: 2, FP: 5, FN: 0, TN: 3
Berger et al.	2018	[^{68}Ga]Ga-PSMA PET vs. mpMRI	Philips Gemini TF 64 PET/CT	3 Tesla machines	NA	Visual and semiquantitative	TP: 1, FP: 4, FN: 1, TN: 44	TP: 0, FP: 2, FN: 1, TN: 47
Gupta et al.	2017	[^{68}Ga]Ga-PSMA PET vs. mpMRI	Biograph TruePoint40 with LSO crystal from Siemens Healthcare	NA	2 MBq/kg	Visual and semiquantitative	TP: 7, FP: 1, FN: 0, TN: 4	TP: 4, FP: 1, FN: 3, TN: 4
Zhang et al.	2017	[^{68}Ga]Ga-PSMA PET vs. mpMRI	United Imaging Healthcare (UIH), Shanghai, China	Achieva 3.0 T TX, Philips Medical Systems, The Netherlands	130.6–177.6 MBq	Visual and semiquantitative	TP: 14, FP: 1, FN: 1, TN: 26	TP: 14, FP: 2, FN: 1, TN: 25

TP, true positive; TN, true negative; FP, false positive; FN, false positive; NA, not available.

10.3389/fmed.2024.1425134

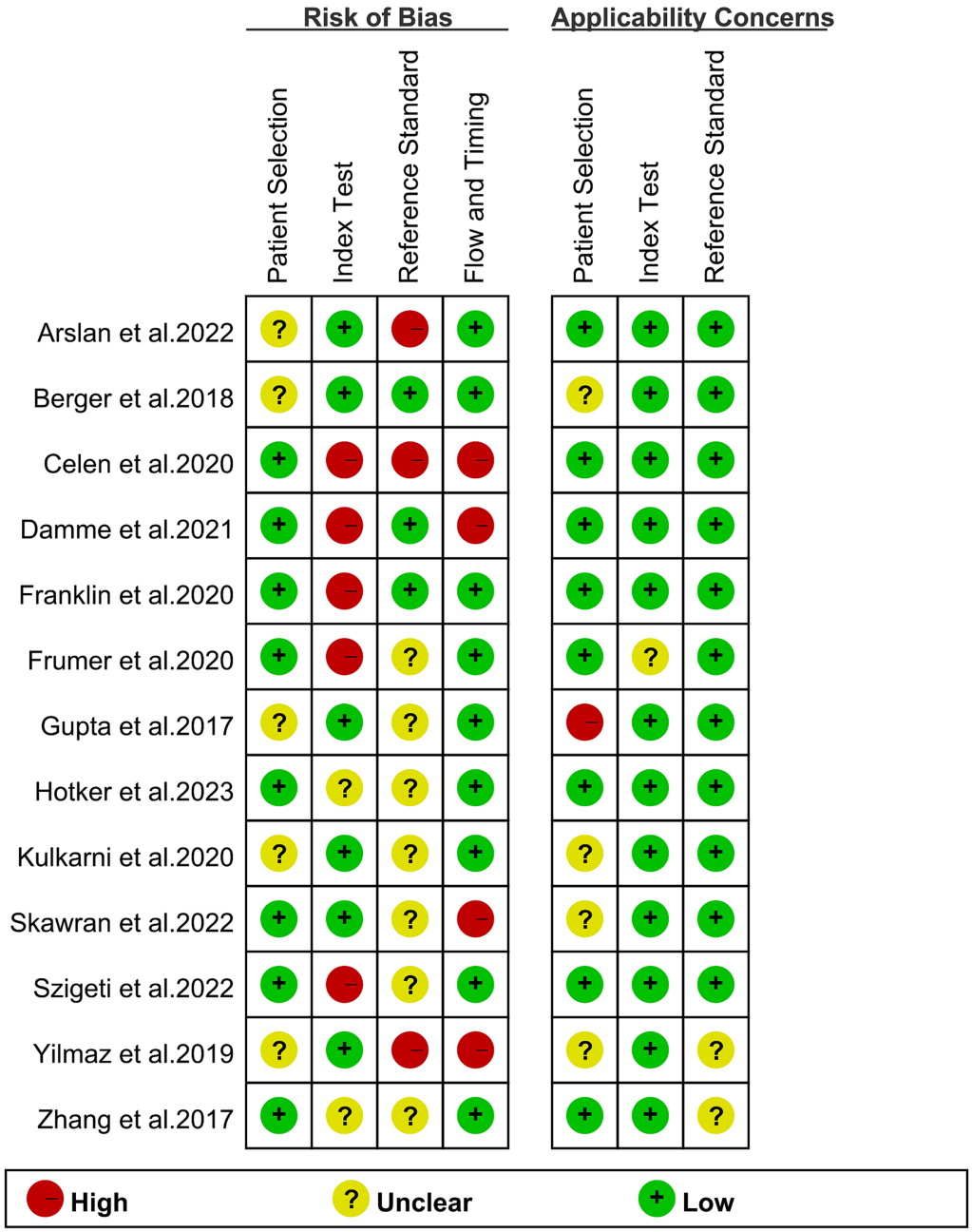

FIGURE 2
Risk of bias and applicability concerns of the included studies using the Quality Assessment of Diagnostic Performance Studies QUADAS-2 tool.

^{68}Ga-PSMA-11, 18F-DCFPyL, 18F-PSMA-1007, leading to higher heterogeneity in the articles. In cases of high heterogeneity, their study did not employ techniques such as meta-regression or sensitivity analysis to explore the source of heterogeneity. Therefore, in our study, we conducted meta-regression and sensitivity analysis specifically for one imaging tracer, ^{68}Ga-PSMA-11, and incorporated the latest studies.

In addition, our study find substantial heterogeneity was identified in the sensitivity and specificity of ^{68}Ga-PSMA-11 PET and mpMRI, as evidenced by high I^2 values (84 and 79% for sensitivity, 87 and 91% for specificity, respectively). Hence, in response to this high level of heterogeneity, we utilized meta-regression and sensitivity analysis to explore potential sources of this heterogeneity. Through meta-regression analysis, only patient numbers emerged as a statistically significant factor for the specificity of mpMRI ($p < 0.05$). This finding suggests the influence of sample size on heterogeneity, yet the limited identification of sources indicates the complexity of factors affecting diagnostic tool performance. The complexity of this outcome may stem from multiple factors. Firstly, the diversity in study samples, encompassing variations in geography, ethnicity, and age among populations, might not have been fully addressed in the analysis. Secondly, the differences in the application of diagnostic tool models and the subjective assessment criteria across various studies may obscure the true sources of heterogeneity. Additionally, although factors such as region, number of patients included, reference standard, image analysis, and study design were incorporated in the meta-analysis, pinpointing specific sources of heterogeneity remains a formidable challenge.

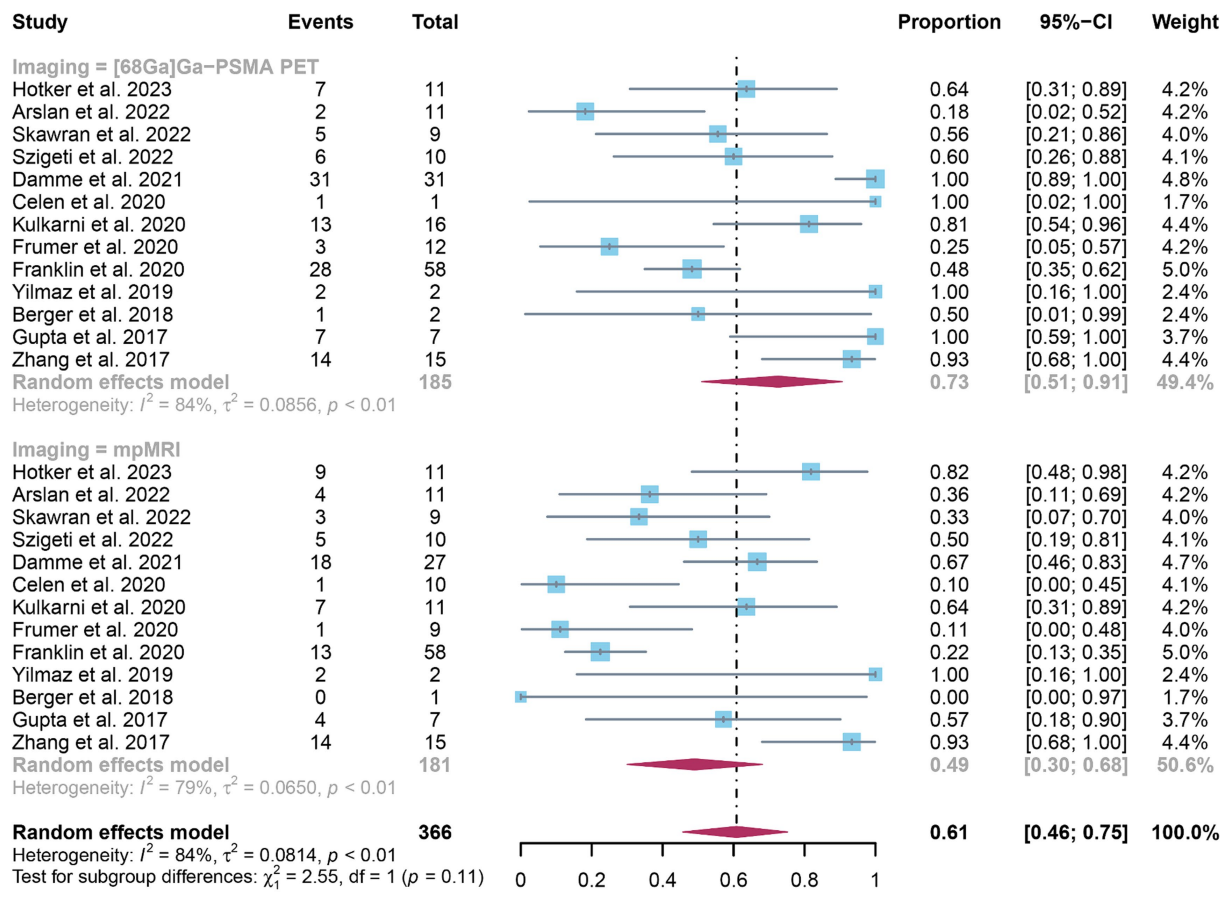

FIGURE 3
Forest plot showing the head-to-head comparison of pooled sensitivities of ^{68}Ga-PSMA-11 PET and mpMRI in pelvic lymph node metastases of prostate cancer patients. The plot displays individual study estimates (squares) with corresponding 95% confidence intervals (horizontal lines) and the pooled sensitivity estimate (diamond) for both modalities. The size of the squares represents the relative weight of each study in the meta-analysis.

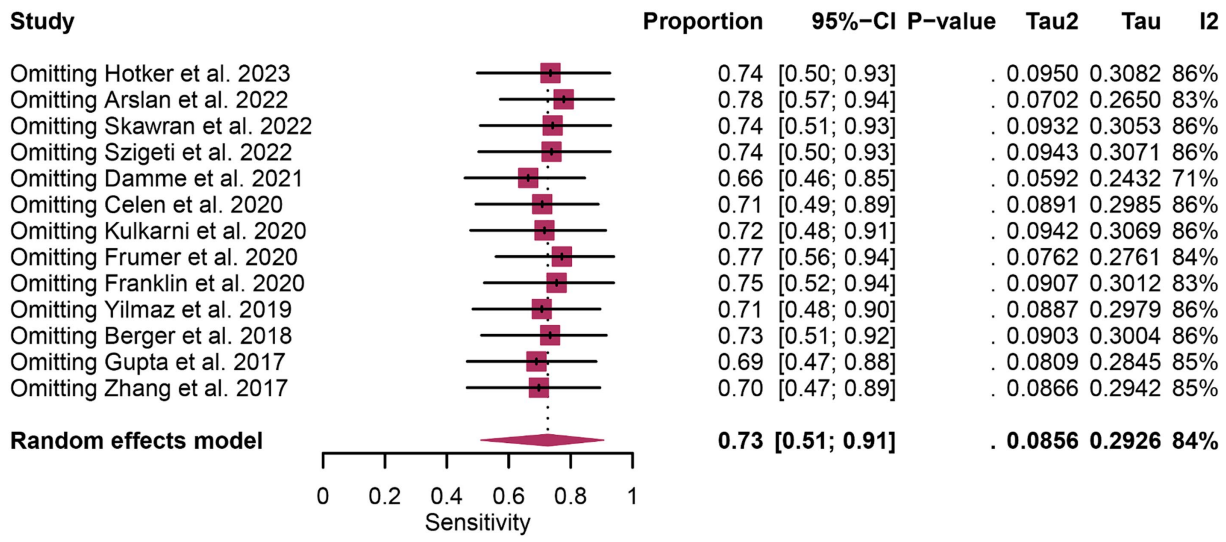

FIGURE 4
Forest plot showing the pooled sensitivity of ^{68}Ga-PSMA-11 PET in pelvic lymph node metastases of prostate cancer patients. The plot displays individual study estimates (squares) with corresponding 95% confidence intervals (horizontal lines) and the pooled sensitivity estimate (diamond). The size of the squares represents the relative weight of each study in the meta-analysis.

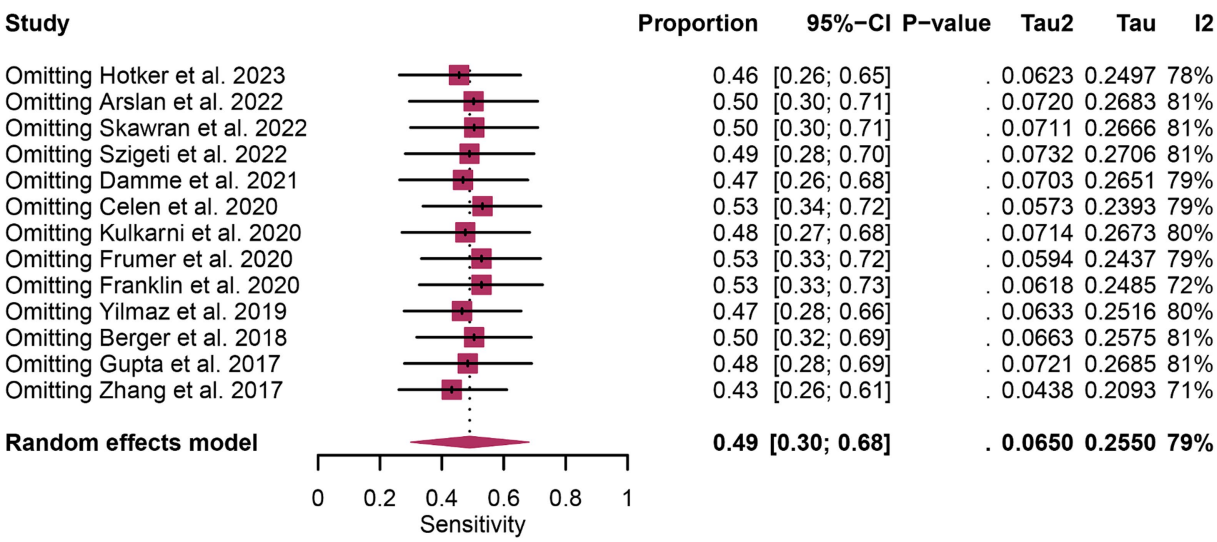

FIGURE 5
Forest plot showing the pooled sensitivity of mpMRI in pelvic lymph node metastases of prostate cancer patients. The plot displays individual study estimates (squares) with corresponding 95% confidence intervals (horizontal lines) and the pooled sensitivity estimate (diamond). The size of the squares represents the relative weight of each study in the meta-analysis.

TABLE 3 Meta-regression analysis for sensitivity of ^{68}Ga-PSMA-11 PET and mpMRI.

Covariate	Studies	Sensitivity for ^{68}Ga-PSMA-11 PET (95% CI)	*p*-value	Sensitivity for mpMRI (95% CI)	*p*-value
Region			0.42		0.16
Oceania	2	0.48 [0.33; 0.63]		0.12 [0.02; 0.27]	
Asia	7	0.76 [0.40; 1.00]		0.51 [0.22; 0.80]	
Europe	4	0.77 [0.43; 0.99]		0.61 [0.42; 0.78]	
Number of patients included			0.33		0.35
>50	6	0.60 [0.29; 0.88]		0.41 [0.22; 0.61]	
≤50	7	0.87 [0.64; 1.00]		0.59 [0.25; 0.90]	
Reference standard			0.99		0.58
PLND	8	0.75 [0.49; 0.95]		0.48 [0.24; 0.72]	
ePLND	4	0.61 [0.16; 0.98]		0.43 [0.22; 0.66]	
rPLND	1	1.00 [0.16; 1.00]		1.00 [0.16; 1.00]	
Image analysis			0.11		0.69
Visual and semiquantitative	12	0.78 [0.57; 0.94]		0.50 [0.30; 0.71]	
Visual	1	0.18 [0.02; 0.52]		0.36 [0.11; 0.69]	
Study design			0.77		0.97
Prospective	1	0.60 [0.26; 0.88]		0.50 [0.19; 0.81]	
Retrospective	12	0.74 [0.50; 0.93]		0.49 [0.28; 0.70]	

The current meta-analysis indicates that ^{68}Ga-PSMA-11 PET exhibits similar sensitivity to mpMRI in detecting initial lymph node staging in prostate cancer patients. However, it's crucial to consider the availability of ^{68}Ga-PSMA-11 PET, which may not be uniformly accessible across medical centers and can be influenced by location and resources. Moreover, one of the main limitations of ^{68}Ga-PSMA-11 PET is the potential exposure to ionizing radiation, particularly concerning for younger patients or those requiring repeated imaging exams. On the other hand, mpMRI combines multiple imaging modalities, providing detailed anatomical and functional information about tumors. Its lower economic cost compared to ^{68}Ga-PSMA-11 PET contributes to its widespread use in clinical practice. The choice between the two modalities will depend on factors such as the clinical scenario, accessibility of the imaging technique, and physician preferences.

Our study has several limitations that need to be acknowledged. Firstly, despite employing rigorous statistical methods, we were unable to identify specific sources of heterogeneity for sensitivity and specificity. This suggests that there may be underlying complexities, highlighting the need for further research to pinpoint these sources of heterogeneity. Secondly, due to the limited number of included

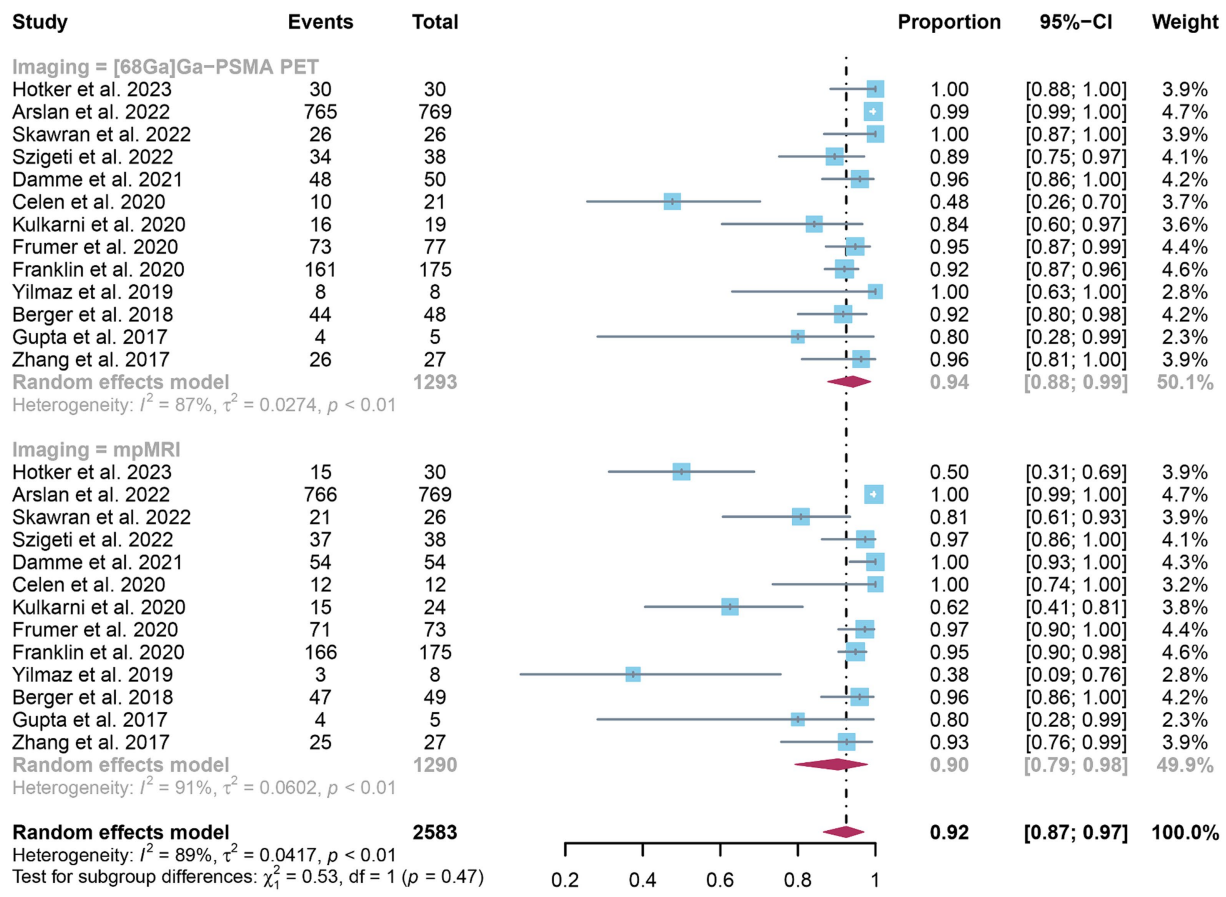

FIGURE 6
Forest plot showing the head-to-head comparison of pooled specificities for ^{68}Ga-PSMA-11 PET and mpMRI in pelvic lymph node metastases of prostate cancer patients. The plot displays individual study estimates (squares) with corresponding 95% confidence intervals (horizontal lines) and the pooled specificity estimate (diamond) for both modalities. The size of the squares represents the relative weight of each study in the meta-analysis.

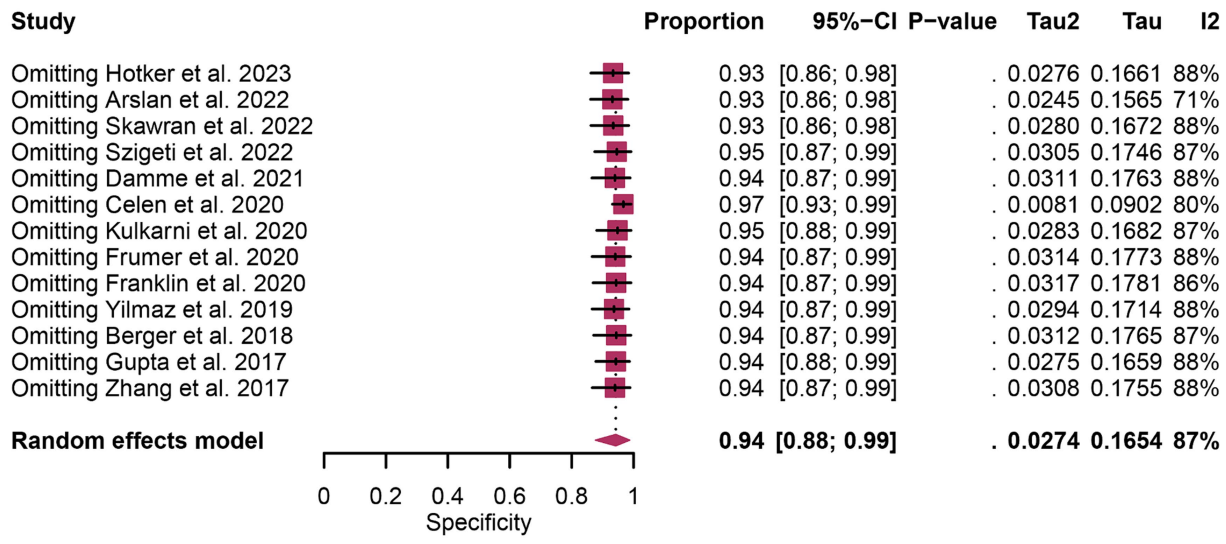

FIGURE 7
Forest plot showing the pooled specificity of ^{68}Ga-PSMA-11 PET in pelvic lymph node metastases of prostate cancer patients. The plot displays individual study estimates (squares) with corresponding 95% confidence intervals (horizontal lines) and the pooled specificity estimate (diamond) for both modalities. The size of the squares represents the relative weight of each study in the meta-analysis.

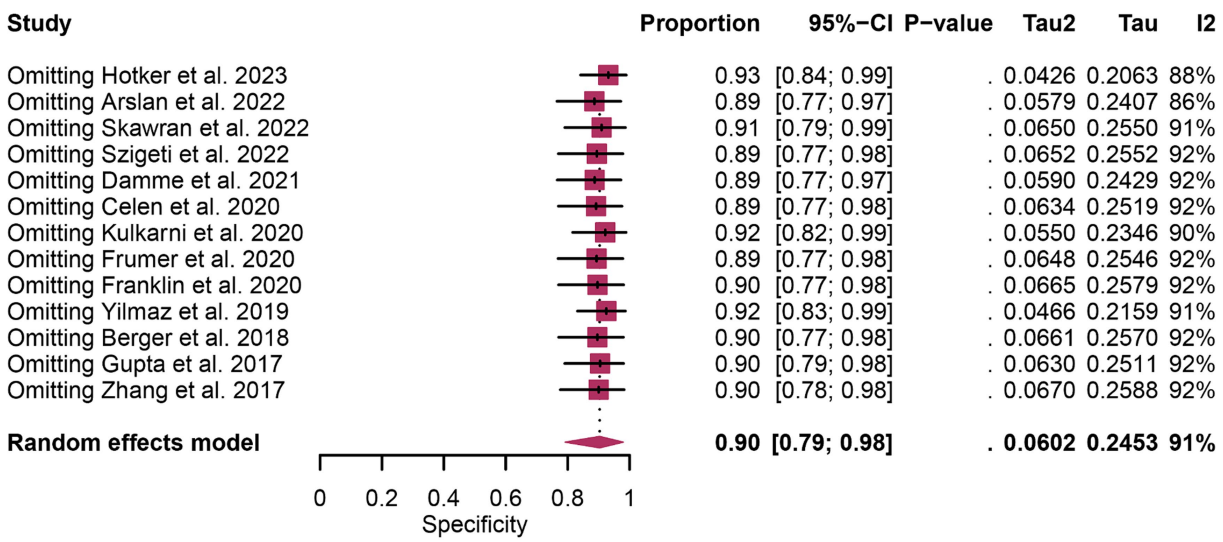

FIGURE 8
Forest plot showing the pooled specificity of mpMRI in pelvic lymph node metastases of prostate cancer patients. The plot displays individual study estimates (squares) with corresponding 95% confidence intervals (horizontal lines) and the pooled specificity estimate (diamond) for both modalities. The size of the squares represents the relative weight of each study in the meta-analysis.

TABLE 4 Meta-regression analysis for specificity of ^{68}Ga-PSMA-11 PET and mpMRI.

Covariate	Studies	Specificity for ^{68}Ga-PSMA-11 PET (95% CI)	*p*-value	Specificity for mpMRI (95%CI)	*p*-value
Region			0.38		0.51
Oceania	2	0.92 [0.88; 0.95]		0.95 [0.92; 0.98]	
Asia	7	0.91 [0.76; 1.00]		0.89 [0.70; 1.00]	
Europe	4	0.97 [0.92; 1.00]		0.88 [0.60; 1.00]	
Number of patients included			0.64		0.02
>50	6	0.95 [0.89; 0.99]		0.96 [0.87; 1.00]	
≤50	7	0.93 [0.78; 1.00]		0.82 [0.62; 0.96]	
Reference standard			0.62		0.53
PLND	8	0.93 [0.82; 0.99]		0.89 [0.75; 0.98]	
ePLND	4	0.96 [0.84; 1.00]		0.99 [0.94; 1.00]	
rPLND	1	1.00 [0.63; 1.00]		0.38 [0.09; 0.76]	
Image analysis			0.09		0.15
Visual and semiquantitative	12	0.93 [0.86; 0.98]		0.89 [0.77; 0.97]	
Visual	1	0.99 [0.99; 1.00]		1.00 [0.99; 1.00]	
Study design			0.69		0.49
Prospective	1	0.89 [0.75; 0.97]		0.97 [0.86; 1.00]	
Retrospective	12	0.95 [0.87; 0.99]		0.89 [0.77; 0.98]	

studies, we were unable to divide our analysis into patient-based and lesion-based analyses. Future head-to-head comparison studies focusing on these distinct analysis methods may provide more precise and accurate conclusions. Thirdly, it's important to note that the majority of studies included in our meta-analysis were retrospective (only one out of 13 was prospective), which could potentially introduce bias into our findings.

5 Conclusion

Our findings indicated that ^{68}Ga-PSMA-11 PET and mpMRI exhibit similar sensitivity and specificity in the diagnosis of initial lymph node staging of prostate cancer. However, given that most included studies were retrospective, further prospective studies with larger sample sizes are essential to validate these results.

Data availability statement

The original contributions presented in the study are included in the article/Supplementary material, further inquiries can be directed to the corresponding author.

Author contributions

YW: Data curation, Formal analysis, Methodology, Software, Writing – original draft. RJ: Data curation, Software, Writing – original draft. HW: Formal analysis, Methodology, Writing – original draft. QZ: Conceptualization, Supervision, Validation, Visualization, Writing – review & editing.

Funding

The author(s) declare that no financial support was received for the research, authorship, and/or publication of this article.

Conflict of interest

The authors declare that the research was conducted in the absence of any commercial or financial relationships that could be construed as a potential conflict of interest.

Publisher's note

Supplementary material

The Supplementary material for this article can be found online at: https://www.frontiersin.org/articles/10.3389/fmed.2024.1425134/full#supplementary-material

References

1. Cancer Research for Cancer Prevention World Health Organization. (Accessed June 20, 2020). Available at: https://publications.iarc.fr/Non-Series-Publications/World-Cancer-Reports/World-Cancer-Report-Cancer-Research-For-Cancer-Prevention-2020

2. Wilczak W, Wittmer C, Clauditz T, Minner S, Steurer S, Büscheck F, et al. Marked prognostic impact of minimal lymphatic tumor spread in prostate cancer. *Eur Urol*. (2018) 74:376–86. doi: 10.1016/j.eururo.2018.05.034

3. Mottet N, van den Bergh RCN, Briers E, Van den Broeck T, Cumberbatch MG, De Santis M, et al. EAU-EANM-ESTRO-ESUR-SIOG guidelines on prostate cancer-2020 update. Part 1: screening, diagnosis, and local treatment with curative intent. *Eur Urol*. (2021) 79:243–62. doi: 10.1016/j.eururo.2020.09.042

4. Briganti A, Chun FK, Salonia A, Suardi N, Gallina A, Da Pozzo LF, et al. Complications and other surgical outcomes associated with extended pelvic lymphadenectomy in men with localized prostate cancer. *Eur Urol*. (2006) 50:1006–13. doi: 10.1016/j.eururo.2006.08.015

5. von Below C, Daouacher G, Wassberg C, Grzegorek R, Gestblom C, Sörensen J, et al. Validation of 3 T MRI including diffusion-weighted imaging for nodal staging of newly diagnosed intermediate- and high-risk prostate cancer. *Clin Radiol*. (2016) 71:328–34. doi: 10.1016/j.crad.2015.12.001

6. Hövels AM, Heesakkers RA, Adang EM, Jager GJ, Strum S, Hoogeveen YL, et al. The diagnostic accuracy of CT and MRI in the staging of pelvic lymph nodes in patients with prostate cancer: a meta-analysis. *Clin Radiol*. (2008) 63:387–95. doi: 10.1016/j.crad.2007.05.022

7. de Kouchkovsky I, Aggarwal R, Hope TA. Prostate-specific membrane antigen (PSMA)-based imaging in localized and advanced prostate cancer: a narrative review. *Transl Androl Urol*. (2021) 10:3130–43. doi: 10.21037/tau-20-1047

8. Zhang Q, Zang S, Zhang C, Fu Y, Lv X, Zhang Q, et al. Comparison of ^{68}Ga-PSMA-11 PET-CT with mpMRI for preoperative lymph node staging in patients with intermediate to high-risk prostate cancer. *J Transl Med*. (2017) 15:230. doi: 10.1186/s12967-017-1333-2

9. Yilmaz B, Turkay R, Colakoglu Y, Baytekin HF, Ergul N, Sahin S, et al. Comparison of preoperative locoregional Ga-68 PSMA-11 PET-CT and mp-MRI results with postoperative histopathology of prostate cancer. *Prostate*. (2019) 79:1007–17. doi: 10.1002/pros.23812

10. Van Damme J, Tombal B, Collette L, Van Nieuwenhove S, Pasoglou V, Gérard T, et al. Comparison of ^{68}Ga-prostate specific membrane antigen (PSMA) positron emission tomography computed tomography (PET-CT) and whole-body magnetic resonance imaging (WB-MRI) with diffusion sequences (DWI) in the staging of advanced prostate cancer. *Cancers*. (2021) 13:5286. doi: 10.3390/cancers13215286

11. Szigeti F, Schweighofer-Zwink G, Meissnitzer M, Hauser-Kronberger C, Hitzl W, Kunit T, et al. Incremental impact of [^{68}Ga]Ga-PSMA-11 PET/CT in primary N and M staging of prostate cancer prior to curative-intent surgery: a prospective clinical trial in comparison with mpMRI. *Mol Imaging Biol*. (2022) 24:50–9. doi: 10.1007/s11307-021-01650-9

12. Skawran SM, Sanchez V, Ghafoor S, Hötker AM, Burger IA, Huellner MW, et al. Primary staging in patients with intermediate- and high-risk prostate cancer: multiparametric MRI and ^{68}Ga-PSMA-PET/MRI—what is the value of quantitative data from multiparametric MRI alone or in conjunction with clinical information? *Eur J Radiol*. (2022) 146:110044. doi: 10.1016/j.ejrad.2021.110044

13. Kulkarni SC, Sundaram PS, Padma S. In primary lymph nodal staging of patients with high-risk and intermediate-risk prostate cancer, how critical is the role of Gallium-68 prostate-specific membrane antigen positron emission tomography-computed tomography? *Nucl Med Commun*. (2020) 41:139–46. doi: 10.1097/mnm.0000000000001110

14. Hötker AM, Mühlematter U, Beintner-Skawran S, Ghafoor S, Burger I, Huellner M, et al. Prediction of pelvic lymph node metastases and PSMA PET positive pelvic lymph nodes with multiparametric MRI and clinical information in primary staging of prostate cancer. *Eur J Radiol Open*. (2023) 10:100487. doi: 10.1016/j.ejro.2023.100487

15. Gupta M, Choudhury PS, Hazarika D, Rawal S. A comparative study of ^{68}Gallium-prostate specific membrane antigen positron emission tomography-computed tomography and magnetic resonance imaging for lymph node staging in high risk prostate cancer patients: an initial experience. *World J Nucl Med*. (2017) 16:186–91. doi: 10.4103/1450-1147.207272

16. Frumer M, Milk N, Rinott Mizrahi G, Bistritzky S, Sternberg I, Leibovitch I, et al. A comparison between ^{68}Ga-labeled prostate-specific membrane antigen-PET/CT and multiparametric MRI for excluding regional metastases prior to radical prostatectomy. *Abdom Radiol*. (2020) 45:4194–201. doi: 10.1007/s00261-020-02640-1

17. Franklin A, Yaxley WJ, Raveenthiran S, Coughlin G, Gianduzzo T, Kua B, et al. Histological comparison between predictive value of preoperative 3-T multiparametric MRI and ^{68}Ga-PSMA PET/CT scan for pathological outcomes at radical prostatectomy and pelvic lymph node dissection for prostate cancer. *BJU Int*. (2021) 127:71–9. doi: 10.1111/bju.15134

18. Çelen S, Gültekin A, Özlülerden Y, Mete A, Sağtaş E, Ufuk F, et al. Comparison of ^{68}Ga-PSMA-I/T PET-CT and multiparametric MRI for Locoregional staging of prostate cancer patients: a pilot study. *Urol Int*. (2020) 104:684–91. doi: 10.1159/000509974

19. Berger I, Annabattula C, Lewis J, Shetty DV, Kam J, Maclean F, et al. ^{68}Ga-PSMA PET/CT vs. mpMRI for locoregional prostate cancer staging: correlation with final histopathology. *Prostate Cancer Prostatic Dis*. (2018) 21:204–11. doi: 10.1038/s41391-018-0048-7

20. Arslan A, Karaarslan E, Güner AL, Sağlıcan Y, Tuna MB, Kural AR. Comparing the diagnostic performance of multiparametric prostate MRI versus ^{68}Ga-PSMA PET-CT in the evaluation lymph node involvement and extraprostatic extension. *Acad Radiol*. (2022) 29:698–704. doi: 10.1016/j.acra.2020.07.011

21. McInnes MDF, Moher D, Thombs BD, McGrath TA, Bossuyt PM, Clifford T, et al. Preferred reporting items for a systematic review and meta-analysis of diagnostic test accuracy studies: the PRISMA-DTA statement. *JAMA*. (2018) 319:388–96. doi: 10.1001/jama.2017.19163

22. Wang X, Wen Q, Zhang H, Ji B. Head-to-head comparison of ^{68}Ga-PSMA-11 PET/CT and multiparametric MRI for pelvic lymph node staging prior to radical prostatectomy in patients with intermediate to high-risk prostate cancer: a meta-analysis. *Front Oncol.* (2021) 11:737989. doi: 10.3389/fonc.2021.737989

23. Chow KM, So WZ, Lee HJ, Lee A, Yap DWT, Takwoingi Y, et al. Head-to-head comparison of the diagnostic accuracy of prostate-specific membrane antigen positron emission tomography and conventional imaging modalities for initial staging of intermediate- to high-risk prostate cancer: a systematic review and meta-analysis. *Eur Urol.* (2023) 84:36–48. doi: 10.1016/j.eururo.2023.03.001

frontiers | Frontiers in Medicine

TYPE Case Report
PUBLISHED 16 July 2024
DOI 10.3389/fmed.2024.1437597

OPEN ACCESS

EDITED BY
Nataliya Lutay,
Skåne University Hospital, Sweden

REVIEWED BY
Yuchun Wei,
Shandong Cancer Hospital, China
Sara Pacella,
IRCCS Ca 'Granda Foundation Maggiore Policlinico Hospital, Italy

*CORRESPONDENCE
Pan Wang
✉ 1298178828@qq.com
Jiong Cai
✉ jiong_cai@163.com

RECEIVED 24 May 2024
ACCEPTED 03 July 2024
PUBLISHED 16 July 2024

CITATION
Hu X, Zhao W, Li F, Wang P and Cai J (2024) Clinical and imaging features of pulmonary mixed squamous cell and glandular papilloma: a case report and literature review. *Front. Med.* 11:1437597. doi: 10.3389/fmed.2024.1437597

Clinical and imaging features of pulmonary mixed squamous cell and glandular papilloma: a case report and literature review

Xianwen Hu[1], Wei Zhao[2], Fangming Li[1], Pan Wang[1]* and Jiong Cai[1]*

[1]Department of Nuclear Medicine, Affiliated Hospital of Zunyi Medical University, Zunyi, China, [2]Department of Pathology, Affiliated Hospital of Zunyi Medical University, Zunyi, China

Pulmonary mixed squamous cell and glandular papilloma (MSGP) is a rare benign lung tumor with both squamous and glandular epithelial components. Reports on primary lung MSGP are few, and the aim of this study is to describe the imaging, including computed tomography (CT) and positron emission tomography (PET) findings, and histopathological characteristics of a case of MSGP in our hospital. A 53-year-old woman with no smoking history who underwent a chest CT scan revealed a nodule in the upper lobe of the left lung. The solid nodule showed no lobulation or spiculation but demonstrated significant enhancement on contrast-enhanced CT and increased fluorine-18 fluorodeoxyglucose (^{18}F-FDG) uptake on PET. Moreover, a literature review identified 19 cases of lung MSGPs involving imaging findings, including CT and/or PET imaging. Except for one patient with a ground glass nodule, the rest were solid and ranged in size from 0.7 to 8.2 cm, which can present as a mildly to significantly increased ^{18}F-FDG uptake on PET. MSGP is a rare benign tumor entity, and understanding its imaging findings and pathological immunohistochemical characteristics will help to improve the accurate diagnosis of MSGP so as to avoid unnecessary lobectomy and mediastinal lymph node dissection.

KEYWORDS

mixed squamous cell and glandular papilloma, lung, lung cancer, PET/CT, CT

Introduction

Solitary papillomas, first reported by Spencer et al. in 1980, are very rare, accounting for less than 0.5% of lung tumors (1). In the fifth edition of the WHO Classification of Thoracic Tumors in 2021, the papillaries of the lungs are divided into three types according to the composition and growth mode of the clad epithelium, namely squamous cell papilloma (including exophytic and varus), glandular papilloma, and mixed squamous cell and glandular papilloma (MSGP) (2). Among them, the MSGP is the rarest, accounting for only 15.7% of solitary papillomas (3). It contains both squamous and glandular epithelial components, each of which accounts for at least one-third of the tumor cells (4). The disease mostly occurs in middle-aged and elderly people with a history of smoking, and the median age of onset is 60 years old, with a male-to-female ratio of 16 to 5 (5). Most tumors occur within the main or lobar bronchi, with only a few occurring within the lumen of the peripheral bronchi. Its clinical manifestations are non-specific and can present as coughing, sputum production, chest pain, and difficulty breathing. Due to the rarity of MSGP and the non-specificity of its clinical

features, it is difficult to obtain a correct diagnosis before surgery. Herein, we present the diagnosis and treatment process of a 53-year-old woman with MSGP and review the relevant literature to systematically summarize its imaging features, aiming to improve understanding of this rare disease.

Case presentation

A 53-year-old woman came to our hospital on 22 September 2023 for medical assistance due to coughing and sputum production for approximately a week. The physical examination did not reveal any positive signs. She had a history of falls a month ago. A chest computed tomography (CT) scan at an external hospital revealed multiple fractures of the right ribs, but there were no obvious signs of dislocation or displacement at the fracture end, so she only received conservative treatment, which improved her condition. Additionally, the CT scan also found a nodule in the upper lobe of her left lung, which she did not notice. She denied that she had a history of chronic diseases such as hypertension, diabetes, coronary heart disease, and infectious diseases such as tuberculosis and hepatitis. Moreover, neither she nor her family had a history of cancer or genetic diseases. On 23 September 2023, the results of the fasting blood routine, tumor markers, and other laboratory tests were negative. On the same day, a chest CT revealed a soft tissue density nodule with a size of approximately 1.1 cm × 1.0 cm in the upper lobe of the left lung, which showed significant enhancement on contrast-enhanced scan (Figure 1), suspected to be lung cancer. To further evaluate the nature of the pulmonary nodule, the patient underwent fluorine-18 fluorodeoxyglucose (^{18}F-FDG) positron emission tomography (PET)/CT examination. The injection dose of ^{18}F-FDG was 8.5 mCi (0.15 mCi/kg), and imaging started 1 h after injection, on 25th September. The results showed significantly increased ^{18}F-FDG uptake of the left upper lobe nodule (Figure 2), and multiple enlarged lymph nodes with increased uptake of ^{18}F-FDG were observed in the mediastinum, suggesting the possibility of left upper lobe lung cancer with mediastinal lymph node metastasis. After completing the relevant preoperative routine examination, the patient underwent surgical resection of the lesion under general anesthesia on 26th September. The results of the intraoperative frozen section indicated lung adenocarcinoma. Consequently, the patient underwent a left superior lobectomy, thoracoscopic mediastinal lymph node dissection, and closed thoracic drainage. Postoperatively, the excised tissue was sent for pathological examination. Hematoxylin–eosin staining showed that the nodule in the left upper lobe of the lung is an epithelial tumor of the lung, with some areas arranged in a papillary pattern and accompanied by mucus secretion. The immunohistochemical results showed that tumor cells expressed cytokeratin (CK), CK5/6, CK7, P63, and thyroid transcription factor 1 (TTF1) positively (Figure 3). However, they did not express CK20 or Napsin-A. Based on these histopathological findings, the final diagnosis of the left upper lobe nodule was an MSGP. Moreover, the pathological results showed that all mediastinal lymph nodes had inflammatory lesions. The patient received anti-infection treatment for 3 days after the operation and was discharged on 29th September. Up to now, the patient has not complained of any discomfort, and no tumor recurrence has been found on the chest CT examination.

Literature review

The PubMed, Embase, and Web of Science databases were searched for English-language case reports and case series of lung MSGPs as of 1 May 2024. The keywords mixed squamous cell, glandular papilloma, or solitary papillomas, and lung or pulmonary were used. For each enrolled case, the first author, publication year, and country, as well as the patient's age, gender, smoking history, clinical symptoms, imaging findings, including CT and PET, and follow-up results, were recorded (Table 1).

Through a systematic search, 19 cases of lung MSGPs involving imaging findings, including CT and/or PET, were identified and published prior to our present case (6–24). In total, there are 20 patients, including our patient, consisting of 9 male (45%) and 11 female (55%) patients, with a median age of 59 years (range, 17–76). All these patients are all from Asia, including Japan, China, and Korea. Among these patients, fewer than half (9 out of 19) had a history of smoking, and there was a lack of characteristic clinical symptoms. The incidence of lesions in the left and right lobes was scattered, and most lesions were in the central region (13 out of 20) of the lung. Except for one case of ground glass nodule, the rest were solid, and two of them were accompanied by cavity formation. The maximum diameter (MD) of the nodule or mass was mostly less than 3.0 cm (14 out of 19), with

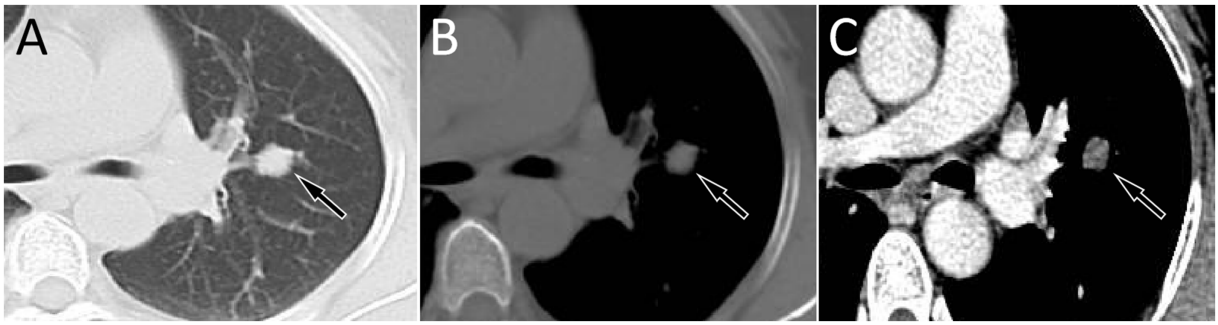

FIGURE 1
Chest computed tomography (CT) pulmonary window (**A**) and mediastinal window (**B**) revealed a soft tissue density nodule with a size of approximately 1.1 cm × 1.0 cm in the upper lobe of the left lung (arrows); no obvious lobulation or spiculation were found, which showed significant enhancement on the contrast-enhanced scan (**C**, arrow).

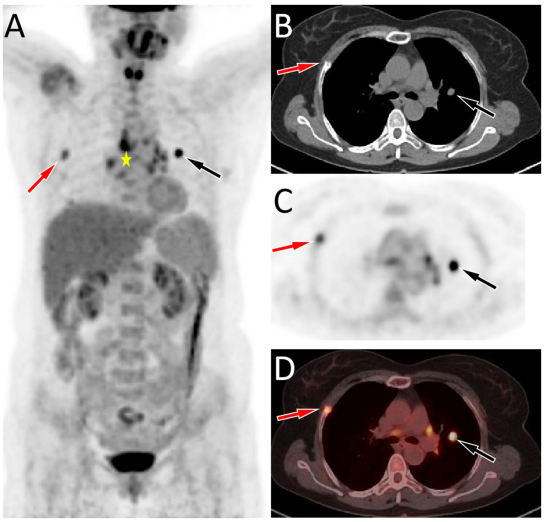

FIGURE 2
(A–D) Fluorine-18 fluorodeoxyglucose (^{18}F-FDG) positron emission tomography (PET)/CT imaging of the patient; The maximum intensity projection (MIP, **A**) showed a significantly increased ^{18}F-FDG uptake in the left lung (black arrow) and a moderately increased ^{18}F-FDG uptake in the right lung (red arrow). Moreover, multiple nodules with increased ^{18}F-FDG uptake were also seen in the mediastinum region (asterisk arrow), which were later pathologically confirmed as inflammatory lymph nodes. Axial CT **(B)**, PET **(C)**, and PET/CT fusion **(D)** show that the nodule with significantly increased ^{18}F-FDG uptake on the left side was located in the upper lobe of the left lung (black arrows), with an SUVmax of 8.8, and the lesion with moderately increased ^{18}F-FDG uptake on the right side was the right rib fracture (red arrows).

a mean MD of 2.4 cm. It can present as a mildly to significantly increased ^{18}F-FDG uptake on PET, with a median maximum standardized uptake value (SUVmax) of 7.8 (range, 1.5–23.8). The detailed imaging features of lung MSGP patients are shown in Figure 4.

Discussion

Pulmonary MSGPs are relatively rare benign tumors, common in middle-aged and elderly patients. They can present with symptoms such as cough, phlegm, chest pain, and other non-specific clinical manifestations (4). Moreover, patients' serum tumor markers are usually negative, and elevation of serum carcinoembryonic antigen is only seen in a small number of patients (6, 16, 19). Our patient is a 53-year-old woman who was found to have pulmonary nodules on imaging examination following trauma, which were subsequently surgically resected and pathologically confirmed as MSGP. To further understand the clinical features of the disease, we conducted a systematic review of the relevant literature. The results showed that the median age of onset of MSGPs is 59 years, and most patients are found by chance during physical examinations, consistent with the characteristics of MSGP reported in the abovementioned literature. However, our results showed no significant difference between men and women in MSGP patients, and most patients had no history of smoking, especially women, which is inconsistent with the literature reporting a preference for men and a history of smoking (3, 4). Thus far, the etiology of MSGP is unclear, and a study suggested that it may be related to human papillomavirus (HPV) infection (25), while the

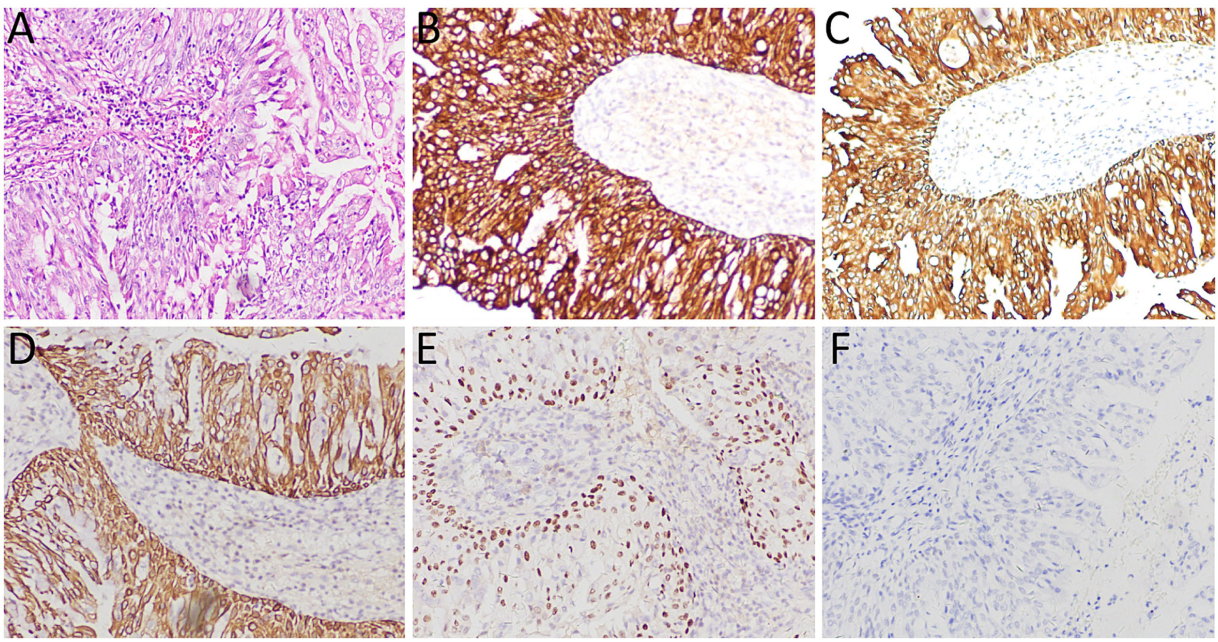

FIGURE 3
(**A**) Hematoxylin–eosin staining showed that the tumor tissue was epithelial, and some areas were arranged in a papillary manner with mucous secretion. Immunohistochemistry showed tumor cells positively expressed CK (**B**), CK5/6 (**C**), CK7 (**D**), P63 (**E**), and TTF1 (**F**). All images are 100 × magnification.

TABLE 1 Clinical and imaging features of the cases of lung MSGP from the literature review and current case.

Case, no.	Author/ year/ country	Gender /age	Smoking	Symptom	CEA (ng/mL; Reference<5.0)	CT imaging						PET (SUVmax)	HPV	Follow-up [month]
						Morphological	MD (cm)	Location	Lobulation	Spiculation	CECT			
1 (6)	Zhang J/ 2024/China	69/F	NA	Chance upon	63.3	Solid	2.6	RLL, central	(−)	(−)	NA	23.8	NA	NA
2 (7)	Abiko T/2010/ Japan	55/F	No	Chance upon	(−)	Solid	2.6	LUL, peripheral	(−)	(+)	NA	9.01	NA	NA
3 (8)	Miyoshi R/ 2017/Japan	72/M	Yes	Chance upon	(−)	Solid	2.3	RML, central	(+)	(+)	NA	2.5	(−)	12/NR
4 (9)	Masunaga A/ 2017/ Japan	56/F	Yes	Chance upon	NA	Solid with voids	1.3	RLL, central	(−)	(+)	NA	4.1	NA	NA
5 (10)	Cao Q/2024/ China	67/M	Yes	Chance upon	NA	Solid	1.5	LUL, central	(−)	(−)	NA	1.5	NA	2/NR
6 (11)	Kozu Y/2014/ Japan	60/M	Yes	Chance upon	NA	Solid	1.8	RML, central	(−)	(−)	NA	3.4	NA	3/NR
7 (12)	An AR/2020/ Korea	76/M	Yes	Cough and sputum	NA,	Solid	4.9	RML, central	(+)	(+)	NA	NA	(−)	NA
8 (13)	Inamura K/ 2011/Japan	49/M	Yes	Hemoptysis	(−)	Solid	3.0	LLL, central	(−)	(−)	OE	NA	(−)	NA
9 (14)	Lin D/2013 /China	64/F	No	Chest pain	NA	Solid	1.3	RLL, peripheral	(−)	(−)	NA	NA	NA	24/NR
10 (15)	Yun JS/2014/ Korea	64/F	No	Chance upon	NA	Solid	4.0	LLL, central	(+)	(−)	NA	6.7	NA	18/NR
11 (16)	Kawamoto N/ 2022/ Japan	59/F	No	Cough	11.0	Solid	8.2	LLL, central	(−)	(−)	OE	20.2	(−)	12/NR
12 (17)	Inamura K/ 2011/Japan	49/M	Yes	Back pain	(−)	Solid	1.1	RLL, peripheral	(−)	(−)	OE	2.29	NA	36/NR

(Continued)

10.3389/fmed.2024.1437597

TABLE 1 (Continued)

Case, no.	Author/ year/ country	Gender /age	Smoking	Symptom	CEA (ng/mL; Reference<5.0)	CT imaging						PET (SUVmax)	HPV	Follow-up [month]
						Morphological	MD (cm)	Location	Lobulation	Spiculation	CECT			
13 (18)	Kawagishi K/ 2023/ Japan	55/M	No	Chance upon	NA	Solid	1.3	RML, peripheral	(−)	(−)	NA	NA	NA	6/NR
14 (19)	Yabuki K/ 2018/Japan	76/M	Yes	Chance upon	7.3	Solid with voids	NA	RLL, central	(−)	(+)	NA	13.3	NA	30/NR
15 (20)	Abe J/2016/ Japan	66/F	Yes	Chance upon	(−)	Solid	1.0	LUL, peripheral	(−)	(−)	NA	NA	(−)	6/NR
16 (21)	Wang X/2022/ China	74/M	Yes	Chance upon	NA	GGO	0.7	RUL, peripheral	(−)	(+)	NA	NA	(−)	16/NR
17 (22)	Saraya T/2019/ Japan	17/F	No	Cough, chest pain	(−)	Solid	3.0	RUL, central	(+)	(+)	OE	11.8	(−)	NA
18 (23)	Yang C/2022/ China	57/F	No	Chance upon	(−)	Solid	2.6	RLL, peripheral	(−)	(−)	NA	NA	NA	6/NR
19 (24)	Zhang Y/2022/ China	52/F	No	Cough	(−)	Solid	1.4	RLL, LUL, central	(−)	(−)	OE	NA	NA	12/NR
20	Our case	53/F	No	Cough and sputum	(−)	Solid	1.1	LUL, central	(−)	(−)	OE	8.8	(−)	7/NR

MSGP, mixed squamous cell and glandular papilloma; MD, maximum diameter; PET, positron emission tomography; SUVmax, maximum standard uptake value; CT, computed tomography; CECT, contrast-enhanced computed tomography; CEA, carcinoembryonic antigen; RLL, right lower lobe; LUL, left upper lobe; RML, right middle lobe; LLL, left lower lobe; OE, obvious enhancement; GGO, ground-glass opacity; RUL, right upper lobe; HPV, human papillomavirus; NR, no recurrence; NA, not applicable; (−), negative; (+) positive.

10.3389/fmed.2024.1437597

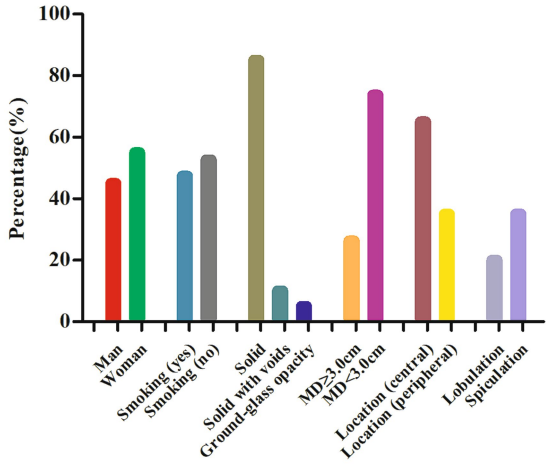

FIGURE 4
Clinical and imaging features of the cases of lung MSGP. MD, maximum diameter.

patient we reported and many studies in the literature have shown negative HPV test results (8, 12, 13, 16, 20–22), so this idea needs to be confirmed in more cases in the future.

The imaging findings of MSGPs are likely to occur at the central or periphery regions of the lungs, where they present as a solid nodule with clear boundaries. Based on the patient we reported and a review of previously published literature, most nodules or masses occurring in the central region of the lungs and almost all occurring in the peripheral region of the lungs were less than 3.0 cm, with few lobulations and spiculations. Only a few tumors occurring in the central region of the lung had an MD greater than or equal to 3.0 cm, which may be accompanied by lobulations and spiculations. On contrast-enhanced CT scans, MGSPs typically showed significant enhancement, with unenhanced low-density necrotic areas visible within larger nodules or masses. These tumors can also present varying degrees of increased uptake of ^{18}F-FDG on PET scans. A previous study (9) suggested that a high SUVmax of MGSPs could predict a potential for malignant transformation, although further confirmation is necessary. In the current case, the SUVmax was 8.8, indicating significantly increased ^{18}F-FDG uptake, making it difficult to differentiate between a benign tumor and lung cancer.

The diagnosis of MSGP mainly depends on histopathological examination, of which classical histological morphology is mainly composed of a mixture of surface-covered glandular epithelial cells and a papilla with a vascular axis consisting of squamous epithelial cells and basal cells below the glandular epithelial cells (13, 15). Due to its complex composition, it is difficult to make an accurate diagnosis in intraoperative frozen sections. A previous study (17) showed that the misdiagnosis rate of MSGP tumor properties based on pathological examination of intraoperative frozen section is 52.6%. This high rate of misdiagnosis can lead to mistaking these benign tumors for various types of lung cancer, resulting in unnecessary overtreatment. The intraoperative frozen section of the patient we reported was also misdiagnosed as adenocarcinoma, resulting in unnecessary mediastinal lymph node dissection. Based on the current cases and misdiagnosed cases in the literature, we analyzed the reasons leading to misdiagnosis. These include: limited sampling of frozen section examination, difficulty in identifying different epithelial components when one component is dominant, and challenges in identifying ciliated columnar epithelium ciliated components in frozen sections (26). Second, the tumor obstructed the bronchial lumen, resulting in mucus extravasation, and the extravasated tumor cells could spread along the alveolar lumen or even float in the mucus lake, which could easily be misdiagnosed as adenocarcinoma or mucinous adenocarcinoma (12, 14). Moreover, MSGPs often contain multiple layers of squamous epithelial cells, which may exhibit atypical features that can be exaggerated in frozen sections, leading to misdiagnosis as squamous cell carcinoma or mucoepidermoid carcinoma (20). When conventional hematoxylin–eosin staining is insufficient for diagnosing MSGP, further immunohistochemical examination is needed. The glandular epithelium of the tumor cells expresses CK7 and TTF1 positively, the mucinous columnar epithelium expresses MUC5AC, and squamous cells express CK5/6, P63, and P40 (1, 26, 27). The tumor tissue of the patient we reported showed characteristic papillary structure and components of papillary epithelium under the microscope, and immunohistochemistry showed that the tumor cells expressed positive CK5/6, CK7, P63, and TTF1, which met the diagnostic criteria of MSGP.

The prognosis of MSGP patients is good, and the purpose of radical treatment can be generally achieved by lung wedge-shaped resection or lesion excision, although postoperative recurrence and malignant transformation are rarely reported (3). In our current case and literature review results, no tumor recurrence or malignant transformation was found during 2–36 months of follow-up.

In conclusion, MSGP is a rare benign tumor entity of the lung. Our current case study reveals that its imaging features and intraoperative frozen section examination should be considered as one of the differential diagnoses of lung cancer. Understanding the imaging and pathological immunohistochemical characteristics of MSGP will help to improve the accurate diagnosis of MSGP so as to avoid unnecessary lobectomy and mediastinal lymph node dissection.

Data availability statement

The original contributions presented in the study are included in the article/supplementary material, further inquiries can be directed to the corresponding authors.

Ethics statement

Written informed consent was obtained from the individual(s) for the publication of any potentially identifiable images or data included in this article.

Author contributions

XH: Conceptualization, Data curation, Formal analysis, Funding acquisition, Writing – original draft. WZ: Data curation, Investigation,

Project administration, Resources, Writing – original draft. FL: Investigation, Methodology, Validation, Writing – original draft. PW: Investigation, Supervision, Visualization, Writing – review & editing. JC: Investigation, Project administration, Supervision, Writing – review & editing.

Funding

The author(s) declare that financial support was received for the research, authorship, and/or publication of this article. This study was funded by the Guizhou Province Science and Technology Plan Project (grant number: Qiankehe-ZK[2024]-329) and Zunyi Science and Technology Joint Fund (grant number: HZ-2023-284).

Conflict of interest

The authors declare that the research was conducted in the absence of any commercial or financial relationships that could be construed as a potential conflict of interest.

Publisher's note

References

1. Spencer H, Dail D, Arneaud J. Non-invasive bronchial epithelial papillary tumors. *Cancer*. (1980) 45:1486–97. doi: 10.1002/1097-0142(19800315)45:6<1486::AID-CNCR2820450632>3.0.CO;2-H

2. Minami Y. The notable topics of the 5th edition of who classification for the thoracic Tumours (2021). *Gan To Kagaku Ryoho*. (2022) 49:847–52.

3. Tryfon S, Dramba V, Zoglopitis F, Iakovidis D, Sakkas L, Kontakiotis T, et al. Solitary Papillomas of the lower airways: epidemiological, clinical, and therapeutic data during a 22-year period and review of the literature. *J Thorac Oncol*. (2012) 7:643–8. doi: 10.1097/Jto.0b013e3182468d06

4. DB F, MN K, Nicholson A, IA S, RE P, WD T. Solitary pulmonary Papillomas in adults: a Clinicopathologic and in situ hybridization study of 14 cases combined with 27 cases in the literature. *Am J Surg Pathol*. (1998) 22:1328–42. doi: 10.1097/00000478-199811000-00003

5. Travis WD, Brambilla E, AG N, Yatabe Y, Austin J, MB B, et al. The 2015 World Health Organization classification of lung tumors: impact of genetic, clinical and radiologic advances since the 2004 classification. *J Thorac Oncol*. (2015) 10:1243–60. doi: 10.1097/Jto.0000000000000630

6. Zhang J, Dong A, Wang Y. Fdg pet/Ct in a case of solitary mixed squamous cell and glandular papilloma of the lung with high Cea level. *Clin Nucl Med*. (2024) 49:e288–9. doi: 10.1097/Rlu.0000000000005025

7. Abiko T, Koizumi S, Takanami I, Tanaka F. 18f-Fdg-pet/Ct findings in primary pulmonary mixed squamous cell and glandular papilloma. *Ann Nucl Med*. (2011) 25:227–9. doi: 10.1007/S12149-010-0454-Y

8. Miyoshi R, Menju T, Yoshizawa A, Date H. Expression of P16(Ink4a) in mixed squamous cell and glandular papilloma of the lung. *Pathol Int*. (2017) 67:306–10. doi: 10.1111/Pin.12531

9. Masunaga A, Oide T, Kamata T, Kou E, Sekine Y, Hiroshima K. Glut-1 expression of pulmonary mixed squamous cell and glandular papilloma may be associated with high Suvmax on Fluorodeoxyglucose-positron emission tomography. *Pathol Int*. (2017) 67:373–4. doi: 10.1111/Pin.12547

10. Cao Q, Li B, Lian H, Li J. Mixed squamous cell and glandular papilloma of the bronchus. *Pulmonology*. (2024) 30:96–7. doi: 10.1016/J.Pulmoe.2023.07.005

11. Kozu Y, Maniwa T, Ohde Y, Nakajima T. A solitary mixed squamous cell and glandular papilloma of the lung. *Ann Thorac Cardiovasc Surg*. (2014) 20:625–8. doi: 10.5761/Atcs.Cr.13-00029

12. AR A, SY P, Kim JH, KJ C, MJ C. Adenocarcinoma-papillary cystic pattern arising in a mixed squamous and glandular papilloma of the lung. *Int J Surg Pathol*. (2020) 28:658–62. doi: 10.1177/1066896920908330

13. Inamura K, Kumasaka T, Furuta R, Shimada K, Hiyama N, Furuhata Y, et al. Mixed squamous cell and glandular papilloma of the lung: a case study and literature review. *Pathol Int*. (2011) 61:252–8. doi: 10.1111/J.1440-1827.2011.02659.X

14. Lin D, Jiang Y, Wang J, Ding L, Xin F, Zhao H, et al. Pulmonary mixed squamous cell and glandular papilloma mimicking adenocarcinoma: a case study and literature review. *J Thorac Dis*. (2013) 5:E129–32. doi: 10.3978/J.Issn.2072-1439.2013.07.38

15. J Y, D K, Choi Y, K N, S S. Mixed squamous cell and glandular papilloma of the lung in a 64-year-old woman. *Korean J Thorac Cardiovasc Surg*. (2014) 47:55–8. doi: 10.5090/Kjtcs.2014.47.1.55

16. Kawamoto N, Okita R, Hayashi M, Osoreda H, Inokawa H, Murakami T. Clinicopathological feature of a resected large mixed squamous cell and glandular papilloma: a case report. *Int J Surg Case Rep*. (2022) 93:106956. doi: 10.1016/J.Ijscr.2022.106956

17. Iijima Y, Nakajima Y, Kinoshita H, Akiyama H, Nishimura Y, Hirata T. Mixed squamous cell and glandular papilloma of the lung-a case report and literature review in Japan. *Int J Surg Case Rep*. (2020) 68:39–42. doi: 10.1016/J.Ijscr.2020.02.021

18. Kawagishi K, Kogita Y, Kagawa Y, Takeuchi Y, Okumura M. Mixed squamous cell and glandular papilloma of the lung increased in twelve years -a case report. *Respir Med Case Rep*. (2023) 46:101949. doi: 10.1016/J.Rmcr.2023.101949

19. Yabuki K, Matsuyama A, Obara K, Takenaka M, Tanaka F, Nakatani Y, et al. A unique case of a huge mixed squamous cell and glandular papilloma of non-Endobronchial origin with a peripheral growth. *Respir Med Case Rep*. (2018) 24:108–12. doi: 10.1016/J.Rmcr.2018.05.001

20. Abe J, Ito S, Takahashi S, Sato I, Tanaka R, Sato T, et al. Mixed squamous cell and glandular papilloma of the lung resembling early adenocarcinoma: a case report. *Ann Med Surg*. (2016) 7:61–4. doi: 10.1016/J.Amsu.2016.03.025

21. Wang X, Liu H, Zhai D, Qin Y, Fan C, Zhang D. Multiple primary lung tumors of different pathological types including squamous cell carcinoma, adenocarcinoma, and mixed squamous cell and glandular papilloma: a case report. *Onco Targets Ther*. (2022) 15:13–9. doi: 10.2147/Ott.S344086

22. Saraya T, Fujiwara M, Kimura H, Takei H, Takizawa H. A 17-year-old woman with a solitary, mixed squamous cell and glandular papilloma of the bronchus. *Respirol Case Rep*. (2019) 7:E00393. doi: 10.1002/Rcr2.393

23. Yang C, Li S, Liang Z, Jiang L. Case report: the first case of primary pulmonary collision tumor comprising mixed squamous cell and glandular papilloma and Glomus tumor. *Front Oncol*. (2022) 12:1050220. doi: 10.3389/Fonc.2022.1050220

24. Zhang Y, Lin J, Zhang J, Zheng J. An adult patient with multiple pulmonary mixed squamous cell and glandular Papillomas. *J Postgrad Med*. (2022) 68:53–4. doi: 10.4103/Jpgm.Jpgm_1079_20

25. Yl H, Yl C, Chen KC, Wu CT. Mixed squamous cell and glandular papilloma of the lung: a case report of a novel mutation in the Braf gene and coexistent Hpv infection, possible relationship to ciliated Muconodular papillary tumor. *Pathol Int*. (2019) 69:104–9. doi: 10.1111/Pin.12747

26. Arora I, Gupta N, Angeles Montero M, Viola P. Pulmonary mixed squamous and glandular papilloma: diagnostic challenges of a rare lesion when the clock is ticking. How to avoid interpretation mistakes. *Pathologica*. (2022) 114:391–4. doi: 10.32074/1591-951x-809

27. Sasaki E, Iwakoshi A, Masago K, Hanai N, Oki M. Sialadenoma Papilliferum of the bronchus: focus on histological and genetic distinction from mixed squamous cell and glandular papilloma. *Pathology*. (2021) 53:788–90. doi: 10.1016/J.Pathol.2020.11.012

frontiers | Frontiers in Medicine

TYPE Case Report
PUBLISHED 13 August 2024
DOI 10.3389/fmed.2024.1461205

OPEN ACCESS

EDITED BY
Nataliya Lutay,
Skåne University Hospital, Sweden

REVIEWED BY
Ding Chong Yang,
Nanjing Medical University, China
Guohua Shen,
Sichuan University, China
Hubing Wu,
Southern Medical University, China

*CORRESPONDENCE
Pan Wang
✉ 1298178828@qq.com

RECEIVED 08 July 2024
ACCEPTED 29 July 2024
PUBLISHED 13 August 2024

CITATION
Hu X, Zhao W, Yu R and Wang P (2024) Imaging findings of inflammatory myofibroblastic tumor of sigmoid colon: literature review and case report.
Front. Med. 11:1461205.
doi: 10.3389/fmed.2024.1461205

Imaging findings of inflammatory myofibroblastic tumor of sigmoid colon: literature review and case report

Xianwen Hu[1], Wei Zhao[2], Ronghua Yu[1] and Pan Wang[1]*

[1]Department of Nuclear Medicine, Affiliated Hospital of Zunyi Medical University, Zunyi, China, [2]Department of Pathology, Affiliated Hospital of Zunyi Medical University, Zunyi, China

Inflammatory myofibroblastic tumor (IMT) is an intermediate tumor composed of differentiated myofibroblastic spindle cells with inflammatory cell infiltration. It can occur in all parts of the body, with the lungs being the most common, while the tissues outside the lungs, including the sigmoid colon, are rare. Herein, we present a case of a 10-year-old girl with sigmoid IMT who presented to our hospital with abdominal pain. An abdominal computed tomography (CT) revealed a well-defined, slightly low-density mass in her lower abdomen that was not clearly demarcated from the sigmoid colon. The mass showed significant uneven enhancement on contrast-enhanced CT and increased fluorine-18 fluorodeoxyglucose (^{18}F-FDG) uptake on positron emission tomography (PET). Moreover, a systematic review of the published literature on sigmoid IMT was conducted and its clinical and radiographic features were summarized to increase the understanding of this rare disease.

KEYWORDS

inflammatory myofibroblastic tumor, sigmoid colon, ^{18}F-FDG, PET/CT, CT

Introduction

Inflammatory myofibroblastic tumor (IMT) is a rare intermediate mesenchymal tumor, which has previously been described as inflammatory pseudotumor, plasma cell granuloma, and inflammatory myofibrous histiocytic proliferation, consisting of differentiated myofibroblastic spindle cells, often accompanied by extensive lymphocyte and/or plasma cell infiltration (1). The etiology of IMTs is unknown and may be related to certain special bacterial or EB virus infections, chromosomal mutations (2). It can be seen at any age, but is mainly found in children and young adults, with females being more common (3). The tumor can occur in various parts of the body, of which the lung is the most common, accounting for 95%, while the organ tissues outside the lung, including mesentery, omentum, liver, retroperitoneum and limbs, are rare (4). The disease symptoms of patients are related to the disease site, including fever, pain, anemia and mass, without specificity (5). It is precisely because of the rarity of IMTs and the non-specificity of clinical manifestations that it is difficult to make a correct diagnosis before surgery. Here, we present the diagnosis and treatment of a rare patient with sigmoid IMT and review the literature with a view to increasing awareness of this rare disease.

Case presentation

A 10-year-old girl with abdominal pain for 3 days underwent an abdominal ultrasound examination in an outside hospital on November 20, 2023 and found a large mass in her pelvic cavity. She was admitted to our hospital on 23 November 2023 for further diagnosis and treatment. She and her family denied any history of tumors or genetic diseases. Physical examination revealed a large, hard, low-motion mass palpable in her pelvic cavity, while no significant positive signs were found in the rest of her body. The laboratory test results, including serum tumor markers, were all negative. On November 24th, the patient underwent an abdominal CT examination (Figure 1) and the results showed a slightly low-density mass with unclear boundary with the sigmoid colon in her pelvic cavity, which presented significant uneven enhancement on contrast-enhanced CT, suggesting a possible malignant tumor. In order to further evaluate the nature of the tumor and determine the treatment plan, she underwent ^{18}F-FDG PET/CT examination the following day. The results showed obviously increased ^{18}F-FDG uptake in this lesion, and no hot spot lesions were observed in the rest of the body (Figure 2). Based on these imaging findings, the patient was initially suspected to have a malignant lesion. After a series of evaluations, the patient underwent an exploratory laparotomy, radical tumor resection and ileostomy on November 29 under anesthesia. Hematoxylin–eosin staining revealed diffuse spindle shaped tumor cells and scattered inflammatory cells in resected tumor tissue (Figure 3). Immunohistochemical results showed that the tumor cells positively expressed smooth muscle actin (SMA), anaplastic lymphoma kinase (ALK), CD117, vimentin, but negatively expressed cytokeratin (CK), Desmin and Dog-1. Based on these histopathological features, the patient was diagnosed with an inflammatory myofibroblastic tumor. The patient improved after receiving 3 days of anti-inflammatory treatment with ceftriaxone after surgery and was discharged on December 1, 2023. On June 2, 2024, she underwent abdominal ultrasound examination and showed no signs of tumor recurrence. The patient has been following up for 6 months now and has not reported any discomfort.

Literature review

The PubMed and Web of Science databases were searched for case reports and series of sigmoid colon IMT as of June 10, 2024, with language limitations in English. The search strategy was as follows: ("inflammatory myofibroblastic tumor" OR "inflammatory pseudotumor" OR "plasma cell granuloma" OR "inflammatory myofibrous histiocytic proliferation") AND "sigmoid colon." For each enrolled case, the first author, publication year, as well as the patient's gender, age, clinical symptoms, imaging findings including CT and PET, and follow-up results were recorded (Table 1).

After a systematic search and careful reading of the full text of the preliminary screening, it was finally determined that there were seven cases of sigmoid IMT published before our case (6–12). Including the current patient that we reported, a total of eight sigmoid IMT cases, consisting of three male (3/8) and five female (5/8) patients, with a median age of 10.5 years (range, 9 months-81 years old), were included in the analysis. Common clinical symptoms include abdominal pain, vomiting, fever, and abdominal discomfort. IMTs are generally large in size, with a mean maximum diameter of 9.1 cm. Most of the patients (7/8) underwent surgery, and only one patient received conservative treatment due to poor lung function. The prognosis of IMT was good, and no significant signs of tumor recurrence were found in all patients who underwent surgical resection of the mass during the follow-up period.

Discussion

IMT in the sigmoid colon is rare. Our current study presents a case of a child diagnosed with sigmoid IMT who complained of abdominal pain. To further understand the characteristics of this disease, we conducted a systematic review of relevant literature, and the results showed that most IMT patients in the sigmoid colon were children and young adults, with more females than males. This is consistent with the epidemiology of IMT patients occurring in other parts of the body (13). Most patients seek medical help due to vomiting, fever, abdominal pain, and abdominal discomfort. The literature reported that the etiology of IMT may be related to chronic infections, autoimmune diseases, and trauma (2). However, our case and previous literature on IMT in the sigmoid colon have not reported any such medical history, so this viewpoint may need to be confirmed in the future.

Imaging examinations play a significant role in the diagnosis of IMT, and the imaging of IMT in the sigmoid colon has certain

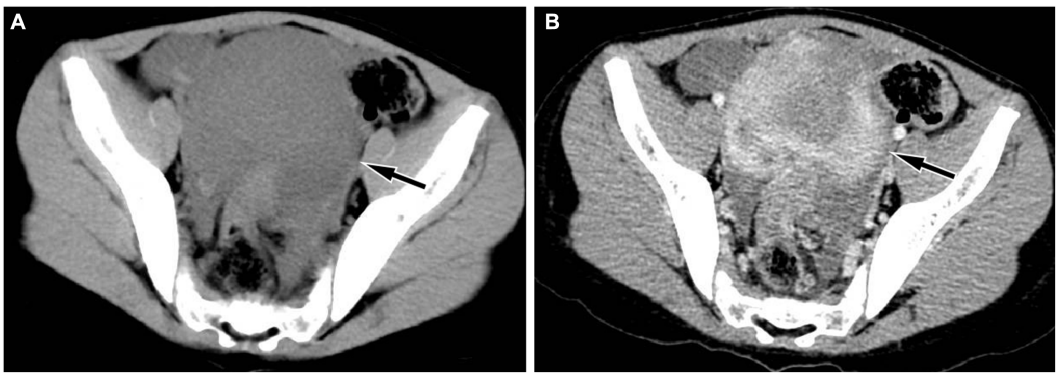

FIGURE 1
Abdominal CT revealed a regular low-density mass (**A**, arrow) in the pelvic cavity, about 9.3 cm × 9.0 cm × 6.7 cm in size; which presented significant uneven enhancement on contrast-enhanced CT (**B**, arrow).

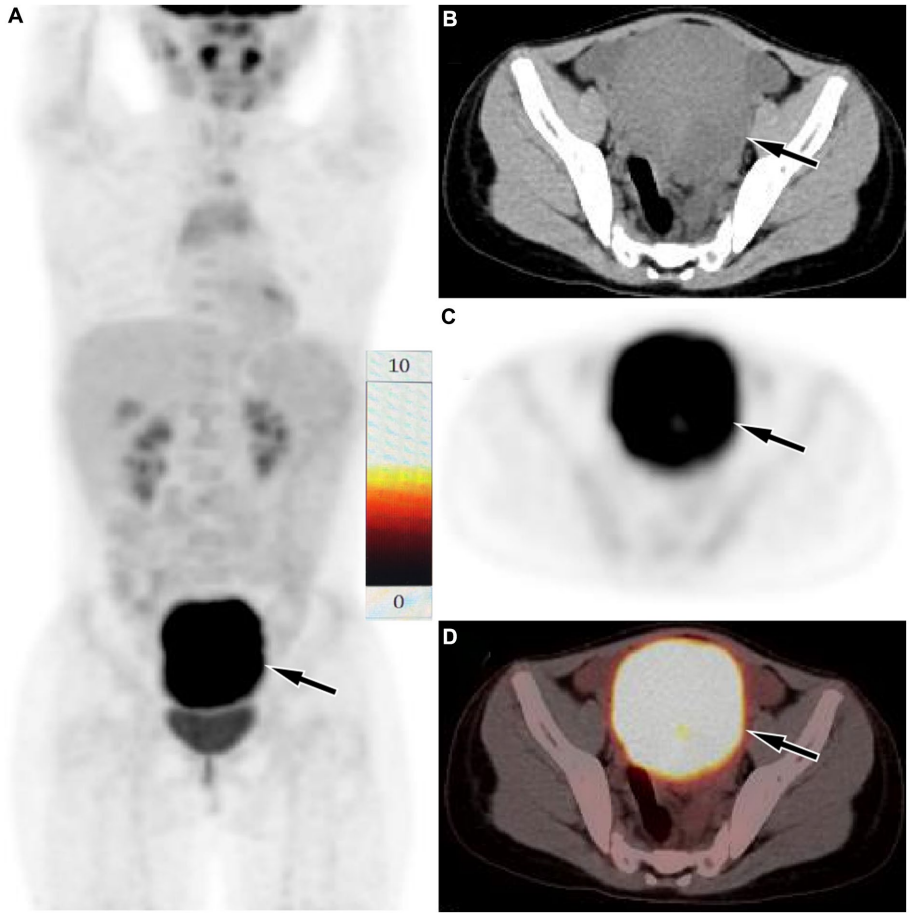

FIGURE 2
Fluorine-18 fluorodeoxyglucose (^{18}F-FDG) positron emission tomography (PET)/CT imaging of the patient. The maximum intensity projection (MIP, **A**) showed a significantly increased ^{18}F-FDG uptake in the lower abdominal area (arrow). Axial CT **(B)**, PET **(C)** and PET/CT fusion **(D)** showed that the lesion with significantly increased ^{18}F-FDG uptake, with a SUVmax of 9.3 (arrows), which was located in the serosal surface of the sigmoid colon, and the adjacent intestinal tube is compressed, the proximal intestinal tube is dilated, and liquid exudation shadow is seen around the mass, and a small amount of fluid is seen in the pelvic cavity.

characteristics. On CT, it usually presents as a large isodense soft tissue mass with smooth edges, and there may be low-density cystic necrosis area within the mass. On contrast-enhanced CT, the mass showed obvious uniform or uneven enhancement (6–10). Unlike previous literature reports, the current case showed a uniform low-density mass on CT, but still showed significant enhancement on contrast-enhanced CT. At present, research on the ^{18}F-FDG/glucose metabolism of IMT is relatively rare and is mostly seen in case reports. Most IMTs present significantly increased ^{18}F-FDG uptake on PET and are often misdiagnosed as malignant tumors in the corresponding area (14–16). The mechanism of ^{18}F-FDG uptake by IMT may be correlated with tumor cellularity, inflammatory cell infiltration and Ki-67 expression. The higher tumor cellularity, more composition of inflammatory cell and higher Ki67 expression, the greater SUVmax (17). The patient we reported presented with low density on CT, with exudative shadows around the mass and obvious uptake of ^{18}F-FDG on PET, which may be related to the strong inflammatory cell infiltration of the mass. To our knowledge, our case study is the first to report PET findings of sigmoid colon IMT, which, like IMT occurring in other organ tissues, also showed significantly increased ^{18}F-FDG uptake.

According to the imaging findings of IMT, IMT originating from the sigmoid colon needs to be differentiated from gastrointestinal stromal tumors (GISTs), lymphoma and sigmoid colon cancer. GISTs also presented as large, circular or lobulated soft tissue masses on CT, with cystic necrosis at the center of the mass and uneven delayed enhancement on contrast-enhanced CT (18). On PET, GISTs with different risk levels show varying levels of increased ^{18}F-FDG uptake, and high-risk GISTs presenting a higher SUVmax than medium-to low-risk GISTs (19). Moreover, due to the fact that GISTs typically grow outside the intestinal lumen, GISTs located in the lower abdomen may exhibit migration of the mass over time on dual-time point PET/CT, which is a relatively specific sign (20). Lymphomas that occur in the intestine are mostly B-cell non-Hodgkin lymphomas. Like IMT, it presents significantly increased ^{18}F-FDG uptake on PET (21). However, intestinal lymphoma usually infiltrates along the intestinal wall, presenting as a circular thickening of the intestinal wall, and rarely causing proximal intestinal duct dilation and obstruction (22). Adenocarcinoma is the most common tumor in the sigmoid colon, and it also shows significantly increased ^{18}FDG uptake on PET. However, sigmoid colon cancer often grows infiltratively along

10.3389/fmed.2024.1461205

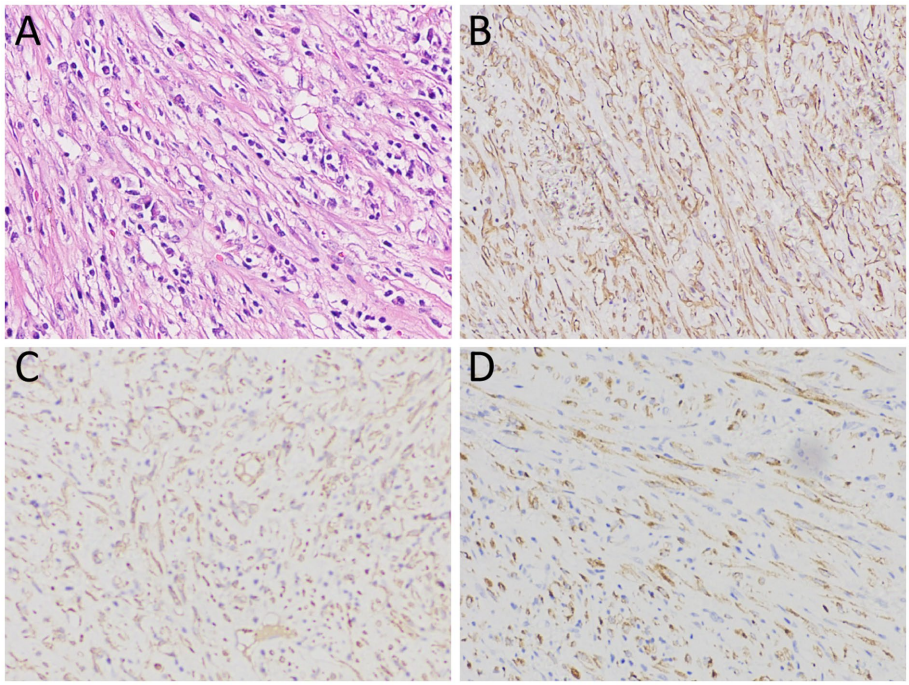

FIGURE 3
(A) Hematoxylin–eosin staining revealed diffuse spindle shaped tumor cells and scattered inflammatory cells within the lesion; Immunohistochemical results showed that the tumor cells positively expressed SMA **(B)**, ALK **(C)** and vimentin **(D)**. Notes: SMA, smooth muscle actin; ALK, anaplastic lymphoma kinase.

TABLE 1 Clinical and imaging features of the cases of sigmoid colon sigmoid colon IMT from the literature review and current case.

Case, no.	Author/ year/ country	Gender / Age (years)	Symptom	CT imaging			PET (SUVmax)	Treatment	Follow-up (month)
				Morphological changes	MD (cm)	CECT			
1(6)	Dhuria S/ 2018/ India	F/2	vomiting, fever,	oval, isodense solid soft tissue mass with low-density necrosis	8.0	OUE	NA	Surgery	36/NR
2 (7)	Pandit N/ 2019/ Nepal	M/35	blood mixed stool, fever, weight loss	lobulated isodense soft tissue mass	8.0	OEE	NA	Surgery	12/NR
3 (8)	Chinnakkulam KS/2020/India	F/40	abdominal pain, vomiting, constipation	suborbicular isodense soft tissue mass	6.0	OEE	NA	Surgery	18/NR
4 (9)	Kavirayani V/ 2023//India	F/9 months	abdominal distension	suborbicular isodense soft tissue mass with low-density necrosis	9.4	OUE	NA	Surgery	6/NR
5 (10)	Wu L/2023 / China	M/11 months	vomiting, fever,	lobulated cystic solid mass	12.0	OUE	NA	Surgery	24/NR
6 (12)	Uysal S/2005 / Turkey	M/11	abdominal pain, difficult defecation	suborbicular isodense soft tissue mass with low-density necrosis	11.0	OUE	NA	Surgery	6/NR
7 (11)	Nakamura Y/ 2010/Japan	F/82	abdominal pain	NA	NA	NA	NA	Conservative treatment	24/NR
8	Present case	F/10	abdominal pain	suborbicular low-density mass	9.3	OUE	15.4	Surgery	6/NR

IMT, inflammatory myofibroblastic tumor; MD, maximum diameter; PET, positron emission tomography; SUVmax, maximum standard uptake value; CT, computed tomography; CECT, contrast-enhanced computed tomography; OUE, obvious uneven enhancement; OEE, obvious even enhancement; NR, no recurrence; NA, not applicable.

the intestinal wall and has an irregular shape on CT (23), which is significantly different from IMT.

Pathological examination is currently the gold standard for diagnosing IMT. Microscopically, the characteristic fusiform myofibroblast proliferation was observed, accompanied by abundant infiltration of chronic inflammatory cells such as plasma cells, T lymphocytes, neutrophils, and eosinophils (24). Immunohistochemistry showed that tumor cells positively expressed vimentin, SMA, and Desmin usually, and CK, CD68, CD30 and ALK were partially expressed positively, while CD117 and CD34 were usually negative expressed (25). In the tumor tissue of the patient we reported, diffuse fusiform tumor cells and scattered inflammatory cells were found in the lesion under microscope. Immunohistochemical results showed that the tumor cells positively expressed vimentin, SMA, and ALK, which was consistent with the pathological diagnosis of IMT.

At present, radical surgical resection of tumor tissue is the preferred treatment for IMT. Only when the tumor cannot be surgically removed, other treatment options including chemotherapy, immunomodulatory therapy, corticosteroids, radiotherapy, nonsteroidal anti-inflammatory drugs and so on should be considered (26, 27). Since IMT is an intermediate tumor with the possibility of recurrence and metastasis, close and careful follow-up after complete surgical resection of the tumor tissue is crucial to improve the prognosis of patients (28). The patient we reported did not show any signs of tumor recurrence or metastasis during follow-up after surgical removal of the tumor.

In conclusion, sigmoid IMT is a relatively rare intermediate tumor and should be considered in the differential diagnosis of other sigmoid malignancies such as GISTs and cancers. It appears as a large, smooth edge, or low-density mass on CT, with obvious uniform or uneven enhancement on contrast-enhanced CT, which showed significantly increased ^{18}F-FDG uptake on PET. These imaging findings contribute to the diagnosis of IMT.

Data availability statement

The original contributions presented in the study are included in the article/supplementary material, further inquiries can be directed to the corresponding author.

Ethics statement

Written informed consent was obtained from the individual(s), and minor(s)' legal guardian/next of kin, for the publication of any potentially identifiable images or data included in this article.

Author contributions

XH: Conceptualization, Data curation, Formal analysis, Funding acquisition, Writing – original draft. WZ: Investigation, Methodology, Project administration, Writing – original draft. RY: Conceptualization, Methodology, Validation, Writing – original draft. PW: Investigation, Project administration, Supervision, Visualization, Writing – review & editing.

Funding

The author(s) declare that financial support was received for the research, authorship, and/or publication of this article. This study was funded by the Guizhou Province Science and Technology Plan Project (grant numbers: Qiankehe-ZK[2024]-329) and Zunyi Science and Technology Joint Fund (grant number: HZ-2023-284).

Conflict of interest

The authors declare that the research was conducted in the absence of any commercial or financial relationships that could be construed as a potential conflict of interest.

Publisher's note

References

1. Pire A, Orbach D, Galmiche L, Berrebi D, Irtan S, Boudjemaa S, et al. Clinical, pathologic, and molecular features of inflammatory myofibroblastic tumors in children and adolescents. *Pediatr Blood Cancer*. (2022) 69:e29460. doi: 10.1002/pbc.29460

2. Lai LM, McCarville MB, Kirby P. Shedding light on inflammatory pseudotumor in children: spotlight on inflammatory myofibroblastic tumor. *Pediatr Radiol*. (2015) 45:1738–52. doi: 10.1007/s00247-015-3360-6

3. Alhumaid H, Bukhari M, Rikabi A, Farahat M, Mesallam TA, Malki KH, et al. Laryngeal myofibroblastic tumor: case series and literature review. *Int J Health Sci (Qassim)*. (2011) 5:187–95.

4. Bennett JA, Nardi V, Rouzbahman M, Morales-Oyarvide V, Nielsen GP, Oliva E. Inflammatory myofibroblastic tumor of the uterus: a clinicopathological, immunohistochemical, and molecular analysis of 13 cases highlighting their broad morphologic spectrum. *Mod Pathol*. (2017) 30:1489–503. doi: 10.1038/modpathol.2017.69

5. Parra-Herran C, Quick CM, Howitt BE, Dal Cin P, Quade BJ, Nucci MR. Inflammatory myofibroblastic tumor of the uterus: clinical and pathologic review of 10 cases including a subset with aggressive clinical course. *Am J Surg Pathol*. (2015) 39:157–68. doi: 10.1097/PAS.0000000000000330

6. Dhuria S, Kwatra KS, Ghosh DN. Inflammatory myofibroblastic tumour of sigmoid mesocolon in a child. *ANZ J Surg*. (2018) 88:E674–6. doi: 10.1111/ans.13625

7. Pandit N, Yadav TN, Shrestha D, Adhikari P, Awale L. IMFT of the sigmoid colon: a case report. *J Surg Case Rep*. (2019) 2019:rjz334. doi: 10.1093/jscr/rjz334

8. Chinnakkulam Kandhasamy S, Sundaramurthi S, Vijayakumar C, Goneppanavar M, Nelamangala Ramakrishnaiah VP. Inflammatory Myofibroblastic tumor of sigmoid Colon: unusual cause of intestinal obstruction. *Cureus*. (2020) 12:e11809. doi: 10.7759/cureus.11809

9. Kavirayani V, Pai NG, Nayal B, Prabhu S. Infantile inflammatory myofibroblastic tumour of the sigmoid colon: a diagnostic dilemma. *BMJ Case Rep*. (2023) 16:e256505. doi: 10.1136/bcr-2023-256505

10. Wu L, Meng X, Wang J, Wang Q, Sun X, Zhu T, et al. Inflammatory Myofibroblastic tumor of the sigmoid Colon in an infant: a case report and literature review. *Fetal Pediatr Pathol*. (2023) 42:123–30. doi: 10.1080/15513815.2022.2062500

11. Nakamura Y, Kayano H, Shimada T, Ito Y, Bessho M. Plasma cell granuloma of the sigmoid colon associated with diverticular disease and accompanying IgM-type

monoclonal gammopathy. *Intern Med*. (2010) 49:227–30. doi: 10.2169/internalmedicine.49.2240

12. Uysal S, Tunçbilek I, Unlübay D, Tiraş U, Bilaloğlu P, Koşar U. Inflammatory pseudotumor of the sigmoid colon mesentery: US and CT findings (2004:12b). *Eur Radiol*. (2005) 15:633–5. doi: 10.1007/s00330-004-2535-6

13. Thompson L. Inflammatory Myofibroblastic tumor. *Ear Nose Throat J*. (2021) 100:520S–1S. doi: 10.1177/0145561319890165

14. Chong A, Ha JM, Hong R, Park SG, Lee HJ. Inflammatory myofibroblastic tumor mimicking gastric gastrointestinal stromal tumor on 18F-FDG PET/CT. *Clin Nucl Med*. (2014) 39:725–7. doi: 10.1097/RLU.0000000000000392

15. Raad RA, Haddad L, Jabbour T, El-Rassi Z. Inflammatory Myofibroblastic tumor of the liver mimicking metastasis on 18F-FDG PET/CT. *Clin Nucl Med*. (2021) 46:47–8. doi: 10.1097/RLU.0000000000003356

16. Tokunaga K, Maeda C, Horikawa S, Nakayama R, Umeoka S. 18F-FDG PET/CT imaging of G-CSF-producing inflammatory Myofibroblastic tumor of the pleura. *Clin Nucl Med*. (2023) 48:e84–6. doi: 10.1097/RLU.0000000000004457

17. Dong A, Wang Y, Dong H, Gong J, Cheng C, Zuo C, et al. Inflammatory myofibroblastic tumor: FDG PET/CT findings with pathologic correlation. *Clin Nucl Med*. (2014) 39:113–21. doi: 10.1097/RLU.0b013e3182952caa

18. Inoue A, Ota S, Yamasaki M, Batsaikhan B, Furukawa A, Watanabe Y. Gastrointestinal stromal tumors: a comprehensive radiological review. *Jpn J Radiol*. (2022) 40:1105–20. doi: 10.1007/s11604-022-01305-x

19. Li S, Lin D, Tang M, Liu D, Lyu Q, Zhang J. Value of (18)F-FDG PET/CT for differentiating diagnosis between malignant and benign primary gastric gastrointestinal mesenchymal tumors: a single-center retrospective study. *J Gastrointest Oncol*. (2022) 13:637–46. doi: 10.21037/jgo-22-287

20. Li C, Li W, Shang M, Wang P, Hu X. Case report: detection of multiple sporadic gastrointestinal stromal tumors by dual-time (18) F-FDG PET/CT. *Front Oncol*. (2024) 14:1321179. doi: 10.3389/fonc.2024.1321179

21. Da B, Zhang J, Zhu F, Wang Z, Diao Y. Extranodal marginal zone lymphoma of mucosa-associated lymphoid tissue of the ileum in an adult presenting with intussusception: a case report and literature review. *Front Oncol*. (2024) 14:1395144. doi: 10.3389/fonc.2024.1395144

22. Liu Y, Peng Y, Li J, Zeng J, Sun G, Gao P. MSCT manifestations with pathologic correlation of abdominal gastrointestinal tract and mesenteric tumor and tumor-like lesions in children: a single center experience. *Eur J Radiol*. (2010) 75:293–300. doi: 10.1016/j.ejrad.2010.05.036

23. Goh V, Glynne-Jones R. Perfusion CT imaging of colorectal cancer. *Br J Radiol*. (2014) 87:20130811. doi: 10.1259/bjr.20130811

24. Surabhi VR, Chua S, Patel RP, Takahashi N, Lalwani N, Prasad SR. Inflammatory Myofibroblastic tumors: current update. *Radiol Clin North Am*. (2016) 54:553–63. doi: 10.1016/j.rcl.2015.12.005

25. Chmiel P, SŁOWIKOWSKA A, Banaszek Ł. Inflammatory myofibroblastic tumor from molecular diagnostics to current treatment. *Oncol Res*. (2024) 32:1141–62. doi: 10.32604/or.2024.050350

26. Liu M, Zhu D. Two cases of inflammatory myofibroblastic tumor treated with targeted drugs: a case report. *Medicine (Baltimore)*. (2024) 103:e38136. doi: 10.1097/MD.0000000000038136

27. Soyer T, Talim B, Karnak İ, Ekinci S, Andiran F, Çiftçi AÖ, et al. Surgical treatment of childhood inflammatory Myofibroblastic tumors. *Eur J Pediatr Surg*. (2017) 27:319–23. doi: 10.1055/s-0036-1593380

28. Nakano K. Inflammatory myofibroblastic tumors: recent progress and future of targeted therapy. *Jpn J Clin Oncol*. (2023) 53:885–92. doi: 10.1093/jjco/hyad074

frontiers | Frontiers in Medicine

TYPE Systematic Review
PUBLISHED 15 October 2024
DOI 10.3389/fmed.2024.1491181

OPEN ACCESS

EDITED BY
Nataliya Lutay,
Skåne University Hospital, Sweden

REVIEWED BY
Francesco Angeli,
University of Bologna, Italy
Francesca Spada,
European Institute of Oncology (IEO), Italy
Kerim Sonmezoglu,
Istanbul University-Cerrahpasa, Türkiye

*CORRESPONDENCE
Giorgio Treglia
✉ giorgiomednuc@libero.it

RECEIVED 04 September 2024
ACCEPTED 03 October 2024
PUBLISHED 15 October 2024

CITATION
Campanale D, Imperiale A, Albano D, Rizzo A, Piccardo A and Treglia G (2024) Detection of cardiac neuroendocrine tumour metastases by somatostatin receptor PET/CT: a systematic review and meta-analysis. *Front. Med.* 11:1491181. doi: 10.3389/fmed.2024.1491181

Detection of cardiac neuroendocrine tumour metastases by somatostatin receptor PET/CT: a systematic review and meta-analysis

Daniela Campanale[1], Alessio Imperiale[2,3], Domenico Albano[4], Alessio Rizzo[5], Arnoldo Piccardo[6] and Giorgio Treglia[7,8,9]*

[1]Division of Cardiology, Istituto Cardiocentro Ticino, Ente Ospedaliero Cantonale, Bellinzona, Switzerland, [2]Division of Nuclear Medicine and Molecular Imaging, Institut de Cancérologie de Strasbourg Europe (ICANS), Strasbourg University Hospitals, Strasbourg, France, [3]Molecular Imaging, DRHIM, Institut Pluridisciplinaire Hubert Curien (IPHC), UMR7178, CNRS, University of Strasbourg, Strasbourg, France, [4]Division of Nuclear Medicine, Università degli Studi di Brescia and ASST Spedali Civili di Brescia, Brescia, Italy, [5]Division of Nuclear Medicine, Candiolo Cancer Institute, FPO-IRCCS, Turin, Italy, [6]Division of Nuclear Medicine, Galliera Hospital, Genoa, Italy, [7]Department of Nuclear Medicine and Molecular Imaging, Lausanne University Hospital and University of Lausanne, Lausanne, Switzerland, [8]Division of Nuclear Medicine, Imaging Institute of Southern Switzerland, Ente Ospedaliero Cantonale, Bellinzona, Switzerland, [9]Faculty of Biomedical Sciences, Università della Svizzera italiana, Lugano, Switzerland

Background: Cardiac neuroendocrine tumour metastases (CNTM) are rare, but advancements in molecular imaging including somatostatin receptor PET/CT (SSTR-PET/CT) could lead to a more frequent identification. The aim of this article is to perform a systematic review and meta-analysis on the detection of CNTM by SSTR-PET/CT.

Methods: A comprehensive literature search of studies on CNTM detected by SSTR-PET/CT was carried out. Three different bibliographic databases were screened (Cochrane library, PubMed/MEDLINE, EMBASE) until 20 August 2024. Two review authors independently selected the eligible original articles and performed the quality assessment and the data extraction. Main findings of eligible studies were summarized and a proportion meta-analysis on the prevalence of patients with CNTM among those with neuroendocrine neoplasm (NEN) performing SSTR-PET/CT was carried out using a random-effects model.

Results: Ten articles reporting data on 163 patients with CNTM were included in the systematic review. SSTR was able to detect CNTM earlier compared to other radiological imaging techniques. Most patients with CNTM had other metastatic sites and CNTM were often asymptomatic. The meta-analysis of seven articles demonstrated a pooled prevalence of 1.5% (95% confidence interval: 1.0–1.9%) of patients with CNTM ($n = 119$) among those performing SSTR-PET/CT for NEN ($n = 9{,}300$). Moderate statistical heterogeneity was found (I^2 test: 62%).

Conclusion: Evidence-based data demonstrate that SSTR-PET/CT enables early and better detection of CNTM compared to other radiological imaging methods. CNTM are encountered with a pooled prevalence of 1.5% of NEN patients performing SSTR-PET/CT. Prospective and multicentric studies are warranted to better clarify the impact of CNTM detection by SSTR-PET/CT on overall survival and clinical decision-making in NEN patients.

KEYWORDS

meta-analysis PET/CT, positron emission tomography, hybrid imaging, cardiac metastases, neuroendocrine tumours, neuroendocrine neoplasm, somatostatin, nuclear medicine

Introduction

Neuroendocrine neoplasms (NEN) include heterogeneous tumours arising from neuroendocrine cells. Most NEN are well-differentiated neuroendocrine tumours with indolent disease biology, whereas poorly differentiated NEN with rapid disease progression are less frequent (1). The incidence and prevalence of NENs continues to rise globally and gastroenteropancreatic NEN represent the most common subtype. Metastatic disease from NEN is frequent and the most frequent metastatic sites are lymph nodes liver, and bone (1).

Cardiac neuroendocrine tumours metastases (CNTM) are rare with an estimated incidence lower than 1% (1, 2). However, the incidence of CNTM is likely underestimated as they often remain undetected until autopsy (1). CTNM are also difficult to diagnose due to their anatomic location and their small size especially in their early stages. Notably, CNTM can lead to a poor clinical outcome and their prompt diagnosis is relevant to start the most effective treatment and for their management (3).

Advancements in molecular imaging including somatostatin receptor PET/CT (SSTR-PET/CT) have led to more frequent identification of NEN lesions compared to conventional imaging including CT and magnetic resonance imaging (MRI). Evidence-based data have demonstrated that SSTR PET/CT (using somatostatin analogues radiolabelled with gallium-68 or copper-64) has high diagnostic performance in detecting NEN lesions due to their usual high SSTR expression (4–6).

After the first case of CNTM detected by SSTR-PET/CT in 2010 (7), several articles and case series were published on this topic (3). Two examples of CNTM detected by SSTR-PET/CT are reported in Figure 1. We hypothesize that SSRT-PET/CT could lead to a more frequent identification of CNTM. Therefore, the aim of this evidence-based article is to perform a systematic review of the literature and a meta-analysis on the detection of CNTM by SSTR-PET/CT.

Methods

Protocol, review authors and review question

This article was written according to a predefined protocol for systematic reviews and meta-analysis of diagnostic tests (8) and following the updated version "Preferred Reporting Items for a Systematic Review and Meta-Analysis of Diagnostic Test Accuracy Studies" statement (9).

The working group was composed of one cardiologist (DC) and five nuclear medicine physicians or radiologists working in different European centers with experience in hybrid imaging in NEN and systematic reviews/meta-analyses (AI, DA, AR, AP, and GT).

The first step of the working group was to formulate a clear review question ("Which is the role of SSTR-PET/CT in detecting CNTM compared to other imaging methods?") created using the following PICO (Patients/Intervention/Comparison/Outcome) framework:

- Patients: individuals with CNTM.
- Intervention: SSTR-PET/CT performed for NEN staging/restaging.
- Comparison: other imaging methods for detecting CNTM.
- Outcomes: in patients with NEN performing SSTR-PET/CT the outcomes evaluated were: prevalence of patients with CNTM, site of CNTM, tracer uptake of CNTM, presence of concurrent metastases, presence of cardiac symptoms, performance of SSTR-PET/CT in detecting CNTM compared to other radiological imaging methods, management of CNTM after SSTR-PET/CT.

Search strategy

To reduce possible biases, two review authors (DC as junior researcher and GT as senior researcher) independently performed a comprehensive literature search using three different bibliographic databases (Cochrane library, PubMed/MEDLINE and EMBASE) to find published original articles on the role of SSTR-PET/CT in detecting CNTM. The following search string combining several free text key words was used: (A) "PET" OR "positron" AND (B) "somatostatin" OR "DOTA*" OR "neuroendocrine" OR "NET" OR "NEN" and (C) "cardiac" OR "myocardial" OR "heart." Last date of the literature search was 20 August 2024. For a more comprehensive literature search no beginning date limit nor language restrictions were used and references of retrieved eligible articles were screened searching for additional studies.

Study selection

Predefined inclusion criteria were: studies or subsets of studies investigating the role of SSTR-PET/CT in detecting CNTM. The predefined exclusion criteria were: (a) articles outside the field of interest of this review (b) review articles, letters, editorials, comments and conference proceedings in the field of interest of this review; (c) case reports (less than 4 patients with CNTM described) in the field of interest of this review.

Three review authors (DC, AR, and GT) applied the inclusion and exclusion criteria mentioned above and independently screened the titles and abstracts of the retrieved records using the predefined search string in the selected bibliographic databases. After the exclusion of non-eligible records, the same three researchers then independently screened the full-texts of the potential eligible articles. Eligible articles were included in the systematic review after a virtual consensus meeting of the whole working group to solve any possible disagreement. Articles included in the systematic review were included in the

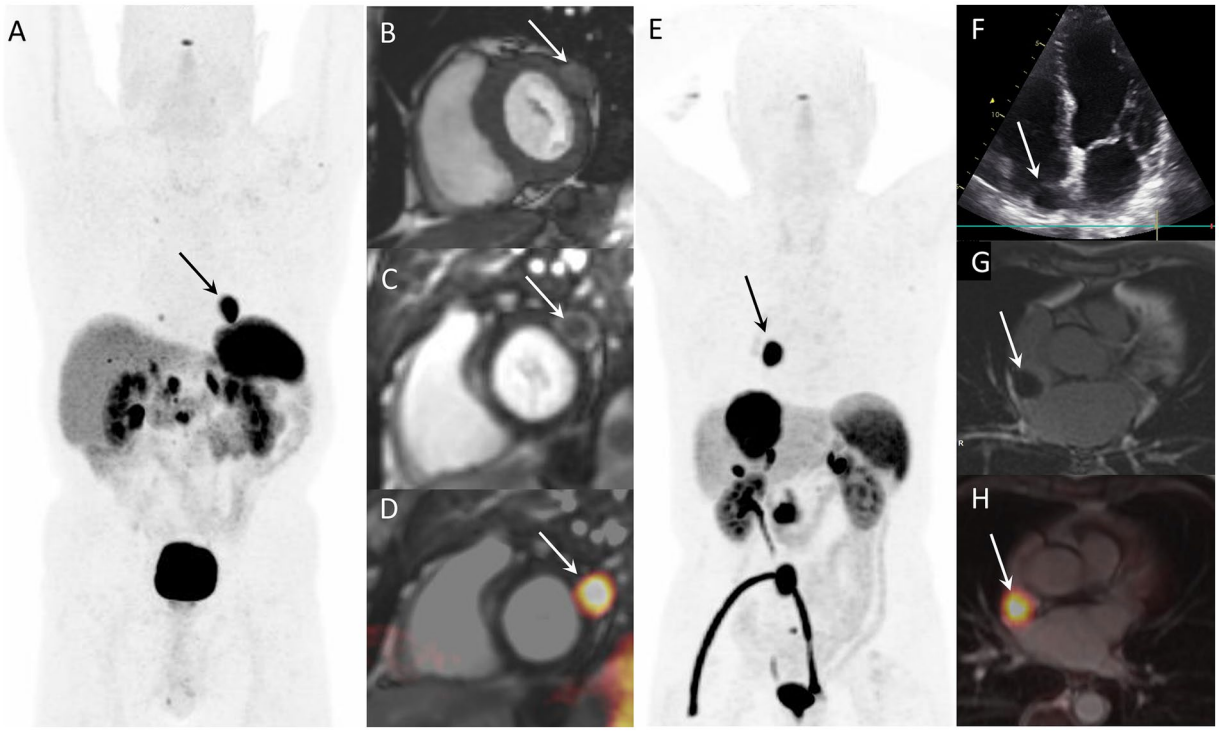

FIGURE 1
Examples of CNTM detected by SSTR-PET/CT in two NEN patients. Case 1: Myocardial metastasis of left ventricular latero-basal wall (arrows) detected by SSTR-PET/CT (A: anterior MIP) in a 74-year-old patient with G2 pancreatic NEN. The CNTM appeared at cardiac magnetic resonance (CMR) as a 22-mm nodule with intermediate intensity on T1-weighted images (B, short axis), with peripheral contrast-enhancement on phase sensitive inversion recovery sequence (C, short axis). Fused SSTR-PET/CMR image is also showed (D, short axis). Case 2: 76-year-old patient with inter-atrial myocardial lesion (arrows) of metastatic G1 small intestinal NEN detected by SSTR-PET/CT (E: anterior MIP). Echocardiography (4-chamber view) showed hypoechoic mass on the right side of interatrial septum (F). The CNTM showed a slight peripheral enhancement on delayed post-contrast inversion recovery CMR sequences (G, short axis). Fused SSTR-PET/CMR image is also showed (H, axial slice).

meta-analysis only when there was absence of patient data overlap and when both overall number of NEN patients performing SSTR-PET/CT and number of CNTM detected by SSTR-PET/CT were specified.

Data extraction

Two review authors (DC and GT) independently extracted the following information from the selected eligible articles using predefined data collection forms: basic study characteristics (authors, year of publication, country of origin, study design and funding), patient characteristics (number and subtype of NEN patients performing SSTR-PET/CT, patients with CNTM detected by SSTR-PET/CT, male percentage and mean age of patients with CNTM, primary NEN site and grading in patients with CNTM), technical aspects (hybrid imaging modality, date of SSTR-PET/CT imaging, PET tracer and injected activity, time interval between tracer injection and image acquisition, image analysis, comparison with other imaging methods), outcome data in patients with NEN performing SSTR-PET/CT (prevalence of patients with CNTM, site of CNTM, tracer uptake of CNTM, presence of concurrent metastases, presence of cardiac symptoms, performance of SSTR-PET/CT in detecting CNTM compared to other radiological imaging methods, therapeutic management of CNTM after SSTR-PET/CT).

Quality assessment

The overall quality of the studies included in this systematic review was performed using the QUADAS-2 tool ("Revised Quality Assessment of Diagnostic Accuracy Studies") (10).

Statistical analysis

We calculated through a meta-analysis the prevalence of patients with CNTM among those with NEN performing SSTR-PET/CT. This proportion meta-analysis was performed using a random-effects model which considers the variability between studies. Pooled data were presented with their respective 95% confidence interval (95%CI) values and displayed using a forest plot. Heterogeneity was estimated through the *I*-square (I^2) or inconsistency index (11). The publication bias was assessed through the Egger's test (12). Subgroup analyses were planned in case of significant statistical heterogeneity. OpenMeta[Analyst] was used as free open-source software for the meta-analyses.[1]

1 http://www.cebm.brown.edu/openmeta/index.html

Results

Literature search

Figure 2 summarizes the results of the systematic literature search. A total of 654 records were identified using the selected databases. Titles and abstracts of 654 records were screened and 619 were excluded because they were outside the field of interest of this review. Then, the full text of 35 remaining records was screened and 25 articles were excluded (22 as case reports and 3 as reviews or editorials). Finally, 10 studies reporting data on 163 patients with CNTM were included in the systematic review (13–22) and no additional studies were found screening the reference list of the retrieved articles. Seven of these 10 studies were also included in the meta-analysis (13, 15, 18–22). Three studies were included in the systematic review but excluded from the meta-analysis because they did not provide sufficient information on the overall number of NEN patients performing SSTR-PET/CT (14, 16, 17).

Qualitative analysis (systematic review)

The characteristics of the included studies are presented in Tables 1–4. The overall quality assessment (including risk of bias and applicability concerns) of the 10 studies included in the systematic review is illustrated in Figure 3.

Basic study characteristics

Ten studies including data on 163 patients with CNTM detected by SSTR-PET/CT were selected (Table 1) (13–22). Publication year of the included studies ranged from 2013 to 2024. The studies were performed mainly in European countries (8 out of 10), one in North America and one in Australia. All the studies were retrospective and most of them were single-centre studies (90%).

Patients' characteristics

Patients' characteristics are summarized in Table 2 (13–22). The number of NEN patients performing SSTR-PET/CT in the included

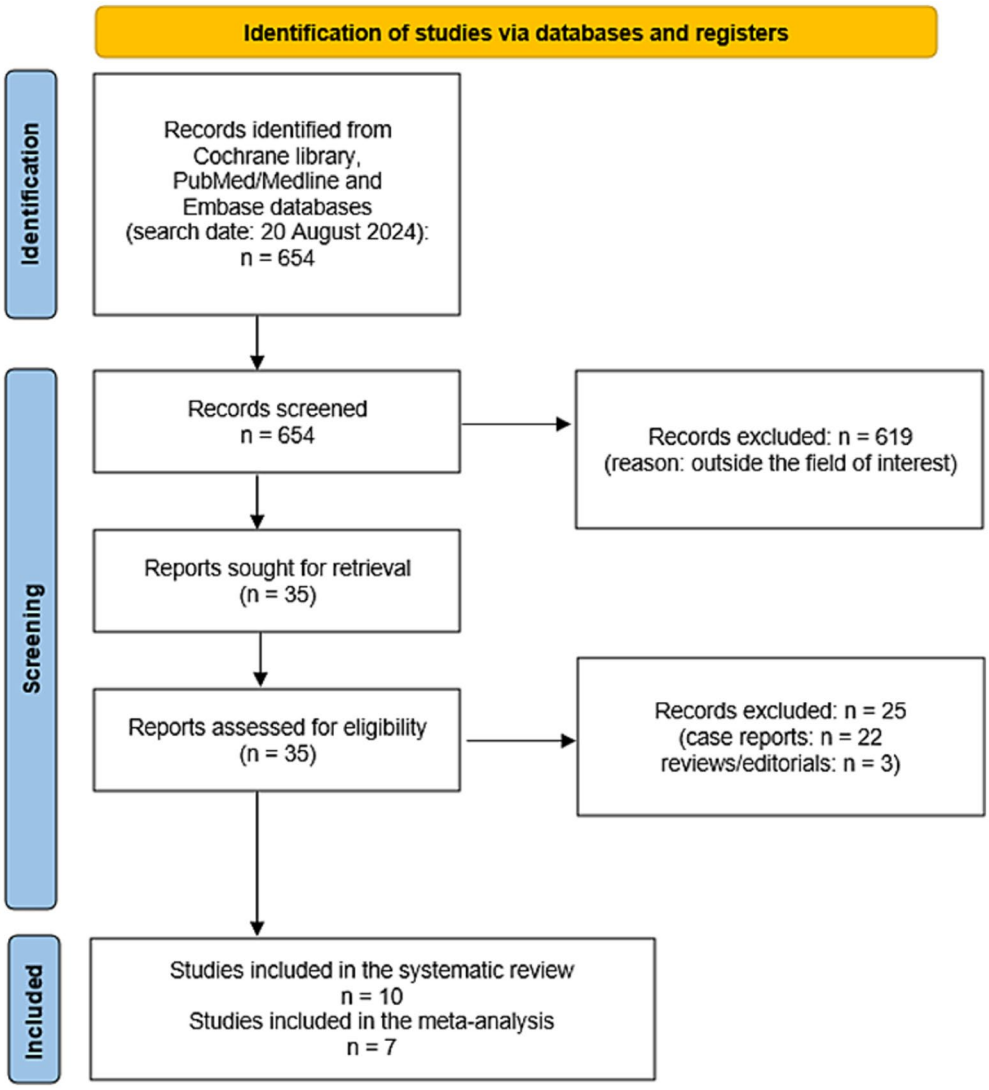

FIGURE 2
Flow chart of the search for eligible studies on the role SSTR-PET/CT for CNTM detection.

TABLE 1 Basic study characteristics of included studies.

Authors	Publication year	Country	Study design	Funding
Wedin et al. (13)	2024	Sweden	Retrospective multicentre	None reported
Arnfield et al. (14)	2023	Australia	Retrospective single centre	None reported
Wang et al. (15)	2023	USA	Retrospective single centre	American Heart Associate Award
El Ghannudi et al. (16)	2022	France	Retrospective single centre	None reported
Liu et al. (17)	2021	United Kingdom	Retrospective single centre	China Postdoctoral Science Foundation
Moyade et al. (18)	2019	United Kingdom	Retrospective single centre	None reported
Kunz et al. (19)	2018	Germany	Retrospective single centre	None reported
Bonsen et al. (20)	2016	Netherlands	Retrospective single centre	None reported
Calissendorff et al. (21)	2014	Sweden	Retrospective single centre	None reported
Carreras et al. (22)	2013	Germany	Retrospective single centre	None reported

studies ranged from 128 to 4,210. The NEN subtypes performing SSTR-PET/CT were not specified in most of the studies. The number of patients with CNTM detected by SSTR-PET/CT in the included studies ranged from 4 to 35 with a prevalence of male patients in most of the studies and a mean age ranging from 54 to 74 years. When reported, the primary NEN site in patients with CNTM was small bowel in most of the cases and the NEN grading was G1 or G2 in the majority of cases thus representing well-differentiated NEN.

Technical aspects

The technical aspects about SSTR-PET/CT are summarized in Table 3 (13–22). The hybrid imaging modality was PET/CT by using low-dose CT or contrast-enhanced CT. When reported the injected PET radiotracer was [^{68}Ga]Ga-DOTATATE or [^{68}Ga]Ga-DOTATOC with heterogeneous injected activity. The time interval between radiotracer injection and image acquisition ranged from 30 to 75 min. Analysis of PET/CT images was performed using visual/qualitative analysis in all studies considering suspicious for CNTM a focal uptake of the tracer higher than the background. In some studies, semi-quantitative image analysis through the calculation of standardized uptake value (SUV_{max}) was carried out. The most frequent radiological imaging methods used for comparison of SSTR-PET/CT findings were CT, cardiac MRI and echocardiography.

Main outcome data

Main outcomes from included studies are showed in Table 4 (13–22). The prevalence of patients with CNTM among NEN patients performing SSTR-PET/CT ranged from 0.8 to 3.1% and the most frequent site of CNTM detected by SSTR-PET/CT was the left ventricle even if other cardiac sites and multifocal CNTM were described. The mean SUV_{max} of CNTM ranged from 7.5 to 25.6 and most of the detected CNTM showed high tracer uptake according to the Krenning score (14, 15). An excellent inter-reader agreement in detecting CNTM by using SSTR-PET/CT was reported (19).

Other NEN metastases were present in most of the patients with CNTM, in particular liver, lymph node and bone metastases. However, no significant difference in median overall survival between metastatic NEN with CNTM and metastatic NEN without CNTM was reported (17).

Most of the patients with CNTM were asymptomatic for cardiac symptoms. The performance of other radiological imaging methods in detecting CNTM was lower compared to SSTR-PET/CT. CT showed a very low sensitivity in detecting CNTM (19) and most CNTM were not visualized by echocardiography (15, 17). Kunz et al. (19) reported that CT showed a sensitivity of 19% and a specificity of 100% for the detection of CNTM. Echocardiography was able to detect CNTM only in 7–18% of patients (15, 17). SSTR-PET/CT identified more CNTM than cardiac MRI. In the study of Arnfield et al. (14) 10 patients with CNTM had performed both cardiac MRI and SSTR-PET/CT. At least one CNTM was identified in 9/10 patients who had cardiac MRI and in 10/10 with SSTR-PET/CT; in these 10 patients, 14 CNTM were identified on cardiac MRI and 25 CNTM were identified on SSTR-PET/CT. Notably, when identified on cardiac MRI, CNTM metastases were more accurately localized (14, 15), thus suggesting a complementary role among SSTR-PET/CT and cardiac MRI for the detection and localization of CNTM (Figure 1).

There were very limited data of SSTR-PET/CT compared to other PET/CT methods in detecting CNTM. However, the diagnostic performance of SSTR-PET/CT in this setting is reported as clearly superior compared to [^{18}F]FDG PET/CT (17) and similar to that of [^{18}F]FDOPA PET/CT (16).

The therapeutic management of CNTM detected by SSTR-PET/CT included therapy with cold somatostatin analogues and/or peptide receptor radionuclide therapy (PRRT) in most of the cases. Few CNTM underwent histological verification of SSTR-PET/CT findings due to the missing necessity for a myocardial biopsy in the overall management of metastatic NEN (13–22). Overall, there were insufficient data about false positive findings for CNTM at SSTR-PET/CT.

Quantitative analysis (meta-analysis)

Seven articles including 9,300 NEN patients performing SSTR-PET/CT for staging/restaging and 119 CNTM detected by SSTR-PET/CT were selected for the meta-analysis. The pooled prevalence of patients of CNTM among those performing SSTR-PET/CT for NEN was 1.5% (95% confidence interval: 1.0–1.9%) as illustrated in Figure 4. A moderate statistical heterogeneity was found (I^2: 62%). A significant publication bias was not demonstrated through the Egger's test ($p = 0.5$).

TABLE 2 Patients' characteristics of included studies.

Authors	Number of NEN patients performing SSTR-PET/CT	Subtype of NEN performing SSTR PET/CT	Patients with CNTM detected by SSTR-PET/CT	Male percentage among patients with CNTM	Mean age of patients with CNTM (years)	Primary NEN site in patients with CNTM	NEN grading in patients with CNTM
Wedin et al. (13)	1,171	Small intestinal and pancreatic NEN	15	NR	NR	Small bowel (93%), pancreas (7%)	NR
Arnfield et al. (14)	NR	Not specified	19	58%	63	Small bowel (79%), lung (21%)	Grade 1: 42% Grade 2: 26% Unknown: 32%
Wang et al. (15)	1,426	Gastroenteropancreatic NEN	25	56%	64	Small bowel (36%), colon (8%), pancreas (16%), mesentery (4%), unknown (36%)	Grade 1: 44% Grade 2: 20% Unknown: 36%
El Ghannudi et al. (16)	NR	Not specified	4	100%	74	Small bowel (100%)	Grade 1: 50% Grade 2: 50%
Liu et al. (17)	NR	Not specified	21	56%	64	Small bowel (84%), pancreas (4%), lung (4%), unknown (8%)	grade 1: 44% Grade 2: 36% Grade 3: 8% Unknown: 12%
Moyade et al. (18)	1,463	Not specified	19	74%	65	Small bowel (32%), colon (16%), pancreas (5%), paraganglia (5%), von Hippel–Lindau syndrome (5%), unknown (37%)	NR
Kunz et al. (19)	629	Not specified	15	60%	65	Small bowel (73%), colon (20%), unknown (7%)	Grade 1: 33% Grade 2: 20% Grade 3: 13% Unknown: 33%
Bonsen et al. (20)	273	Not specified	6	83%	54	Small bowel (50%), rectum (17%), ovary (17%), unknown (17%)	Grade 1: 66% Grade 2: 33%
Calissendorff et al. (21)	128	Ileal NEN	4	25%	62	Small bowel (100%)	Grade 1: 100%
Carreras et al. (22)	4,210	Not specified	35	NR	NR	NR	NR

CNTM, cardiac neuroendocrine tumour metastases; NEN, neuroendocrine neoplasm; NR, not reported; SSTR-PET/CT, somatostatin receptor positron emission tomography/computed tomography.

Performing a subgroup analysis including only the studies published in the last 5 years, a similar pooled prevalence was obtained (1.4%; 95% confidence interval: 1.1–1.8%), respectively, but without statistical heterogeneity (I^2: 0%).

Discussion

To the best of our knowledge, this is the first systematic review and meta-analysis focused on the detection of CNTM by

TABLE 3 Technical aspects of included studies.

Authors	Hybrid imaging modality	Date of SSTR-PET/CT scan	Type of tracer (mean injected activity)	Time interval between tracer injection and image acquisition	Image analysis	Other imaging modalities used for comparison
Wedin et al. (13)	PET/CT (contrast-enhanced CT)	01.2010–06.2022	[^{68}Ga]Ga-DOTATOC (2 MBq/kg)	60 min	Visual	NR
Arnfield et al. (14)	PET/CT	01.2015–05.2020	[^{68}Ga]Ga-DOTATATE (120–200 MBq)	45–75 min	Visual and semiquantitative (SUV_{max})	MRI, echocardiography
Wang et al. (15)	PET/CT	10.2017–03.2020	[^{68}Ga]Ga-DOTATATE (185 MBq)	40 min	Visual and semiquantitative (SUV_{max})	CT, MRI, echocardiography
El Ghannudi et al. (16)	PET/CT	NR	[^{68}Ga]Ga-DOTATOC (NR)	NR	Visual and semiquantitative (SUV_{max})	CT, MRI, echocardiography, [^{18}F] FDOPA PET/CT
Liu et al. (17)	PET/CT	NR	[^{68}Ga]Ga-DOTATATE (NR)	NR	Visual	CT, MRI, echocardiography, [^{111}In] In-pentreotide SPECT/CT, [^{18}F]FDG PET/CT
Moyade et al. (18)	PET/CT	2013–2018	NR (150–250 MBq)	60 min	Visual	NR
Kunz et al. (19)	PET/CT (contrast-enhanced CT)	03.2012–03.2017	[^{68}Ga]Ga-DOTATATE (223 MBq)	60 min	Visual and semiquantitative (SUV_{mean} and SUV_{max})	CT, MRI
Bonsen et al. (20)	PET/CT	08.2011–06.2015	[^{68}Ga]Ga-DOTATATE (NR)	NR	Visual	CT
Calissendorff et al. (21)	PET/CT (contrast-enhanced CT)	01.2010–04.2012	[^{68}Ga]Ga-DOTATOC (135 MBq)	30 min	Visual and semiquantitative (SUV_{mean} and SUV_{max})	CT, echocardiography
Carreras et al. (22)	PET/CT	07.2004–12.2009	NR	NR	Visual	NR

[^{18}F]FDG, fluorine-18 fluorodeoxyglucose; [^{18}F]FDOPA, fluorine-18 dihydroxyphenylalanine; [^{68}Ga]Ga-DOTATOC and [^{68}Ga]Ga-DOTATATE, somatostatina analogues labelled with gallium-68; CT, computed tomography; MBq, megabequerel; min, minutes; MRI, magnetic resonance imaging; NR, not reported; PET, positron emission tomography; SPECT, single photon emission computed tomography; SSTR, somatostatin receptor; SUV_{max}, maximal standardized uptake value; SUV_{mean}, mean standardized uptake value.

SSTR-PET/CT. Compared to a previous evidence-based article on CNTM (23), we have focused our review on SSTR-PET/CT only. The reason of this choice is that we hypothesized a better ability of SSTR-PET/CT in detecting CNTM compared to other radiological imaging methods, including CT, cardiac MRI and echocardiography.

Several studies have used SSTR-PET/CT for detecting CNTM, some of them with few cases of CNTM reported (13–22). We have summarized data from the literature through a systematic review and meta-analysis to provide more robust data on the selected topic compared to the single studies included in our analysis (8).

Our analysis shows that the pooled prevalence of patients with CNTM among those performing SSTR-PET/CT is low as expected, but not negligible (1.5%).

We have also demonstrated that the left ventricle is the most common site of CNTM even if localization to other cardiac sites or multifocal CNTM are described (13–22).

Patients with small bowel NEN have the highest tendency to develop CNTM compared to other NEN subtypes (13–22). This finding is quite expected as well-differentiated small bowel NEN are the most frequent NEN.

Most of the patients with CNTM had concurrent metastatic lesions to other organs and this would suggest that CNTM is correlated with the overall metastatic burden (15).

SSTR-PET/CT allows early detection of CNTM due to their SSTR overexpression and most of the patients with these metastatic lesions did not show any cardiac symptoms (13–22). The clinical manifestations of CNTM are nonspecific and depend on their location; moreover, the clinical pattern correlates with the degree of cardiac infiltration (23). However, as patients with CNTM may develop severe clinical consequences with poor clinical outcome, earlier detection of CNTM is relevant to start the most effective treatment and for their management (23).

Advancements in molecular imaging including SSTR-PET/CT, evaluating the SSTR status of NEN, led to a more frequent identification of CNTM compared to other radiological imaging methods (13–22). This finding is not surprising as hybrid imaging, including SSTR-PET/CT in NEN, may detect early functional abnormalities that usually precede morphological changes detected by conventional radiological imaging (3). On SSTR-PET/CT, CNTM lesions typically demonstrate very high target-to-background radiotracer uptake ratio (due to the absent tracer uptake in the heart

TABLE 4 Outcome data of included studies.

Authors	Prevalence of patients with CNTM among NEN patients performing SSTR-PET/CT	Specific site of CNTM detected by SSTR-PET/CT	Mean SUV_{max} of CNTM (range)	Presence of concurrent metastases in patients with CNTM	Patients with CNTM without cardiac symptoms	Performance of other radiological imaging in detecting CNTM compared to SSTR-PET/CT	Management of CNTM
Wedin et al. (13)	15/1,171 (1.28%)	Left ventricle (60%), pericardium (20%), left atrium (13%), right ventricle (7%)	NR	Most cases	NR	NR	NR
Arnfield et al. (14)	19/NR (NC)	Left ventricle (59%), right ventricle (23%), septum (9%), other sites (9%)	7.5 (2–137.8)	Most cases	Most cases	Lower	PRRT + SSA (58%), SSA (21%), PRRT (5%), other (16%)
Wang et al. (15)	25/1,426 (1.75%)	Left ventricle (50%), septum (21%), right ventricle (19%), pericardium (12%)	9 (NR)	Most cases	Most cases	Lower	NR
El Ghannudi et al. (16)	4/NR (NC)	Left ventricle (75%), septum (25%)	25.6 (5.6–37.1)	Most cases	Most cases	Lower	SSA (75%), SSA + PRRT (25%)
Liu et al. (17)	21/NR (NC)	Left ventricle (52%), right ventricle (44%), pericardium (14%), septum (12%), left atrium (8%), right atrium (4%)	NR	All cases	Most cases	Lower	SSA (88%), PRRT (64%), other (40%)
Moyade et al. (18)	19/1,463 (1.3%)	Left ventricle (42%), pericardium (32%), septum (16%), right ventricle (5%), atrium (5%)	NR	Most cases	Most cases	NR	SSA and/or PRRT
Kunz et al. (19)	15/629 (2.38%)	Left ventricle (43%), septum (43%), right ventricle (14%)	8.6 (5.2–17.4)	Most cases	All cases	Lower	NR
Bonsen et al. (20)	6/273 (2.2%)	Septum (33%), left atrium (17%), right ventricle (17%), pericardium (17%), multiple sites (17%)	NR	Most cases	All cases	Lower	SSA (83%)

(Continued)

TABLE 4 (Continued)

Authors	Prevalence of patients with CNTM among NEN patients performing SSTR-PET/CT	Specific site of CNTM detected by SSTR-PET/CT	Mean SUV_{max} of CNTM (range)	Presence of concurrent metastases in patients with CNTM	Patients with CNTM without cardiac symptoms	Performance of other radiological imaging in detecting CNTM compared to SSTR-PET/CT	Management of CNTM
Calissendorff et al. (21)	4/128 (3.12%)	Left ventricle (25%), right ventricle (25%), multiple sites (50%)	14.2 (7.7–29.8)	All cases	All cases	Lower	SSA (100%)
Carreras et al. (22)	35/4,210 (0.83%)	NR	NR	NR	NR	NR	NR

CNTM, cardiac neuroendocrine tumour metastases; NEN, neuroendocrine neoplasm; NR, not reported; PRRT, peptide receptor radionuclide therapy; SSTR-PET/CT, somatostatin receptor positron emission tomography/computed tomography; SSA, somatostatin analogues; SUV_{max}, maximal standardized uptake value.

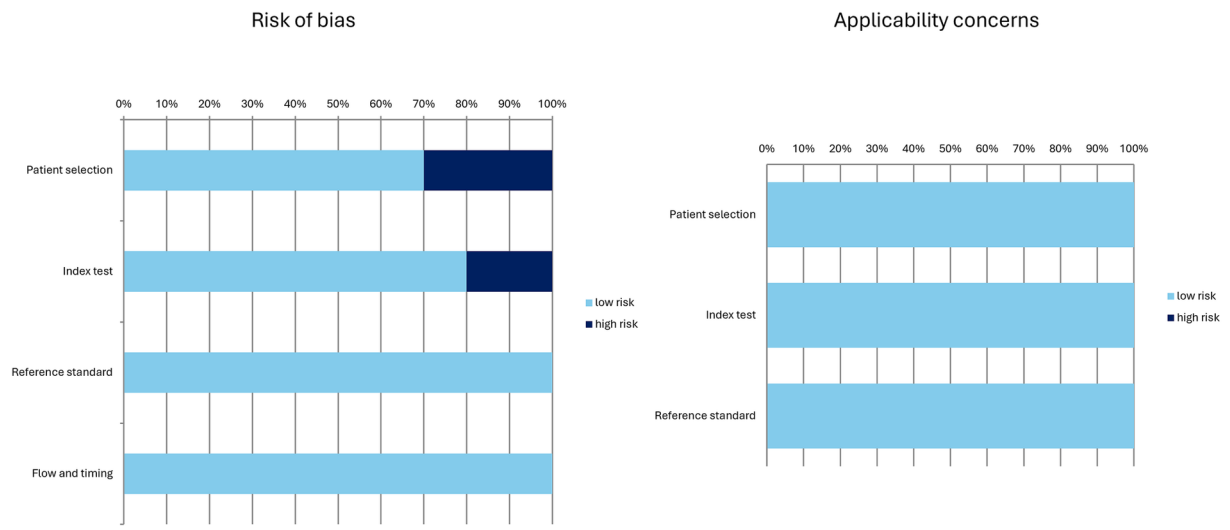

FIGURE 3
Overall quality assessment of the studies included in the systematic review according to the QUADAS-2 tool.

and the usually high tracer uptake in CNTM), thus facilitating the excellent lesion detection.

Available literature data clearly demonstrate that echocardiography and CT miss most of the CNTM detected by SSTR-PET/CT (15, 17, 19). The main limitations of echocardiography are the operator dependence, the poor tissue contrast and the low performance in detecting small lesions (14). Echocardiography remains the imaging modality of choice to identify and characterize carcinoid heart disease which is a separate clinical manifestation of NEN involving the cardiac valves (15).

About cardiac MRI, this imaging method evaluating mass morphology and tissue characterization, showed excellent accuracy, superior to echocardiography and CT, representing the gold standard imaging method for detection and characterization of cardiac masses (24). Even if cardiac MRI may detect a lower number of CNTM compared to SSTR-PET/CT, it may have a complementary role in this setting providing a more accurate localization and lesion characterization of CNTM compared to SSTR-PET/CT due to its high contrast resolution and tissue characterization; anatomical information is crucial for surgical planning optimization (14). The limitation of SSTR-PET/CT in determining the exact location, size and functional significance of CNTM may be explained by several factors including the relatively limited spatial resolution of PET, the possible misregistration among PET and CT data due to cardiac or respiratory motion and the relatively lower anatomical details provided by low-dose CT compared to MRI (14). Overall, the clinical role of cardiac MRI could be limited to a further delineation of CNTM identified by SSTR-PET/CT rather than its use as frontline screening of CNTM (14, 15).

Even if cardiac MRI remains the preferred radiological imaging method for CNTM characterization, cardiac CT offers a valuable diagnostic alternative, superior to echocardiography, in further evaluation of CNTM detected by SSTR-PET/CT in particular in patients with contraindications to cardiac MRI (16).

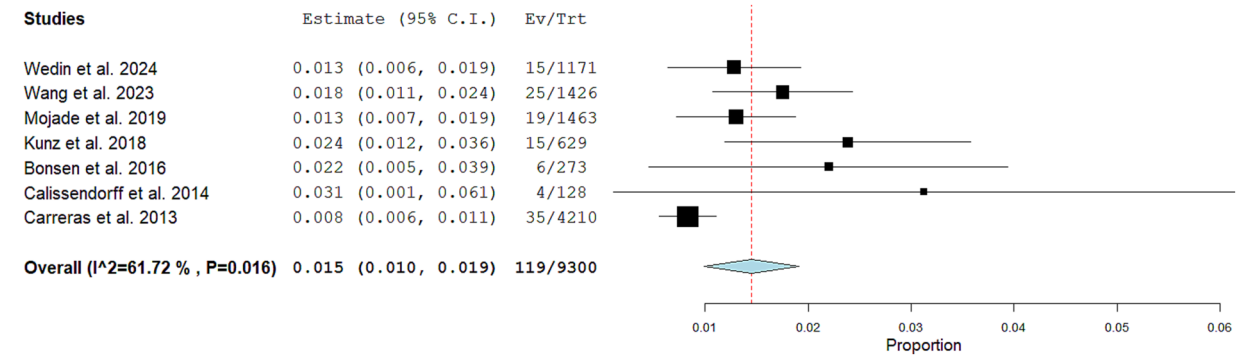

FIGURE 4
Plots of individual studies and pooled prevalence of patients with CNTM among those with NEN performing SSTR-PET/CT, including 95% confidence intervals (95% CI). The size of the squares indicates the weight of each study. A random-effect model was used for the statistical analysis.

Notably, there are no published studies performing SSTR-PET/MRI instead of SSTR-PET/CT in CNTM. Hybrid PET/MRI combining the advantages of PET and MRI could be particularly useful and effective in this setting (3, 25), but its availability in clinical routine is still relatively limited compared to PET/CT (26).

About other PET tracers, compared to [^{18}F]FDG PET/CT, SSTR-PET/CT has a higher performance in detecting CNTM (17). This is not surprising as most NEN usually have slow growth and low glucose consumption compared to more aggressive tumours, explaining their usually low [^{18}F]FDG uptake (5). Furthermore, unlike SSTR tracers, the heart could be a site of physiological [^{18}F]FDG uptake and this is another factor explaining the low sensitivity of [^{18}F]FDG PET/CT in detecting CNTM (17).

[^{18}F]FDOPA is another PET tracer used NEN imaging, because these tumours can accumulate decarboxylate biogenic amines such as L-DOPA (27). In patients with serotonin-secreting small bowel NEN the ability of [^{18}F]FDOPA PET/CT to detect CNTM is expected to be similar compared to SSTR-PET/CT (16, 28, 29).

Clinical management of CNTM includes different therapeutic options. To date, no standard treatment has been defined for CNTM. Specific treatment is often not needed due to the lack of functional cardiac involvement. As most patients with CNTM present concurrent metastatic sites in other organs, a systemic treatment is usually performed. The most frequent therapeutic options used in patients with CNTM in the included studies were cold somatostatin analogues or PRRT, which are safe and justified by the usually high expression of SSTR by neuroendocrine tumours metastases. More invasive treatments were performed only in few cases, mainly due to the functional consequences of CNTM (13–22).

The prognostic implication of CNTM detection by SSTR-PET/CT is still unknown. The clinical significance of CNTM detection could be not high, due to the relatively slow evolution of well-differentiated NEN, leading to a comparable survival in NEN patients without CNTM (17). However, the early CNTM detection would allow the introduction of different treatments in the earliest stages of the disease reducing the functional impact of CNTM with potential better outcome (16).

Some limitations of our analysis should be underlined. The first limitation is the relative low number of included studies, but this number is in line with the infrequent finding of CNTM. The second limitation is the retrospective nature of all the included studies resulting in possible selection bias. Third, we have found a moderate degree of heterogeneity among the included studies, in particular related to patients' characteristics and technical aspects. Lastly, histopathological verification of SSTR-PET/CT findings in CNTM as gold-standard is reported only in few cases, but invasive diagnosis was not justified in most of the patients included in the selected studies considering their characteristics (most of them were metastatic patients with a known primary NEN and without cardiac symptoms) and the high diagnostic accuracy of SSTR-PET/CT. However, as only few CNTM detected by SSTR-PET/CT were confirmed through histology, false positive cases cannot be excluded.

Based on the data reported in our systematic review and meta-analysis, we would like to suggest the design of a large multicentric and prospective study on the detection of CNTM by SSTR-PET/CT. In particular, further studies are needed to analyze the clinical impact of CNTM detection by SSTR-PET/CT on the outcome of patients with metastatic NEN.

Conclusion

Evidence-based data demonstrate that SSTR-PET/CT enables early detection of CNTM which are encountered with a pooled prevalence of 1.5% of NEN patients performing SSTR-PET/CT. The ability of SSTR-PET/CT in detecting CNTM is better compared to other radiological imaging methods. Prospective and multicentric studies are warranted to better clarify the impact of CNTM detection by SSTR-PET/CT on overall survival and clinical decision-making in NEN patients.

Data availability statement

The original contributions presented in the study are included in the article/supplementary material, further inquiries can be directed to the corresponding author.

Author contributions

DC: Data curation, Conceptualization, Writing – review & editing, Writing – original draft. AI: Writing – review & editing, Writing – original draft, Data curation. DA: Writing – review & editing, Writing – original draft. AR: Writing – review & editing, Writing – original draft. AP:

Writing – review & editing, Writing – original draft. GT: Writing – review & editing, Writing – original draft, Methodology, Conceptualization.

Funding

The author(s) declare that no financial support was received for the research, authorship, and/or publication of this article.

Conflict of interest

The authors declare that the research was conducted in the absence of any commercial or financial relationships that could be construed as a potential conflict of interest.

The author(s) declared that they were an editorial board member of Frontiers, at the time of submission. This had no impact on the peer review process and the final decision.

Publisher's note

References

1. Lacalle-González C, Estrella Santos A, Landaeta Kancev LC, Castellano VM, Macia Palafox E, Paniagua Ruíz A, et al. Management of non-hepatic distant metastases in neuroendocrine neoplasms. *Best Pract Res Clin Endocrinol Metab*. (2023) 37:101784. doi: 10.1016/j.beem.2023.101784

2. Pavel M, Grossman A, Arnold R, Perren A, Kaltsas G, Steinmüller T, et al. ENETS consensus guidelines for the management of brain, cardiac and ovarian metastases from neuroendocrine tumors. *Neuroendocrinology*. (2010) 91:326–32. doi: 10.1159/000287277

3. Marketou ME, Kapsoritakis N, Bourogianni O, Patrianakos A, Kochiadakis G, Plevritaki A, et al. Hybrid imaging of neuroendocrine tumors in the heart: union is strength. *J Nucl Cardiol*. (2023) 30:298–312. doi: 10.1007/s12350-021-02804-6

4. Treglia G, Sadeghi R, Giovinazzo F, Galiandro F, Annunziata S, Muoio B, et al. PET with different radiopharmaceuticals in neuroendocrine neoplasms: an umbrella review of published meta-analyses. *Cancers*. (2021) 13:5172. doi: 10.3390/cancers13205172

5. Treglia G, Kroiss AS, Piccardo A, Lococo F, Santhanam P, Imperiale A. Role of positron emission tomography in thyroid and neuroendocrine tumors. *Minerva Endocrinol*. (2018) 43:341–55. doi: 10.23736/S0391-1977.17.02742-0

6. De Dosso S, Treglia G, Pascale M, Tamburello A, Santhanam P, Kroiss AS, et al. Detection rate of unknown primary tumour by using somatostatin receptor PET/CT in patients with metastatic neuroendocrine tumours: a meta-analysis. *Endocrine*. (2019) 64:456–68. doi: 10.1007/s12020-019-01934-9

7. Jann H, Wertenbruch T, Pape U, Ozcelik C, Denecke T, Mehl S, et al. A matter of the heart: myocardial metastases in neuroendocrine tumors. *Horm Metab Res*. (2010) 42:967–76. doi: 10.1055/s-0030-1267204

8. Sadeghi R, Treglia G. Systematic reviews and meta-analyses of diagnostic studies: a practical guideline. *Clin Transl Imaging*. (2017) 5:83–7. doi: 10.1007/s40336-016-0219-2

9. Page MJ, McKenzie JE, Bossuyt PM, Boutron I, Hoffmann TC, Mulrow CD, et al. The PRISMA 2020 statement: an updated guideline for reporting systematic reviews. *J Clin Epidemiol*. (2021) 134:178–89. doi: 10.1016/j.jclinepi.2021.03.001

10. Whiting PF, Rutjes AW, Westwood ME, Mallett S, Deeks JJ, Reitsma JB, et al. QUADAS-2: a revised tool for the quality assessment of diagnostic accuracy studies. *Ann Intern Med*. (2011) 155:529–36. doi: 10.7326/0003-4819-155-8-201110180-00009

11. Higgins JP, Thompson SG. Quantifying heterogeneity in a meta-analysis. *Stat Med*. (2002) 21:1539–58. doi: 10.1002/sim.1186

12. Harbord RM, Egger M, Sterne JA. A modified test for small-study effects in meta-analyses of controlled trials with binary endpoints. *Stat Med*. (2006) 25:3443–57. doi: 10.1002/sim.2380

13. Wedin M, Janson ET, Wallin G, Sundin A, Daskalakis K. Prevalence of metastases outside the liver and abdominal lymph nodes on ^{68}Ga-DOTATOC-PET/CT in patients with small intestinal and pancreatic neuroendocrine tumours. *J Neuroendocrinol*. (2024) 36:e13391. doi: 10.1111/jne.13391

14. Arnfield EG, Tam L, Pattison DA, Younger J, Chikatamarla VA, Wyld D, et al. Cardiac metastases from neuroendocrine neoplasms: complementary role of SSTR PET/CT and cardiac MRI. *J Nucl Cardiol*. (2023) 30:2676–91. doi: 10.1007/s12350-023-03345-w

15. Wang Y, Ayoub C, Yang AF, Sonbol MB, Butterfield R, Halfdanarson TR, et al. Gastroenteropancreatic neuroendocrine tumor metastasis to the heart: evaluation of imaging manifestations. *Curr Probl Diagn Radiol*. (2023) 52:340–5. doi: 10.1067/j.cpradiol.2022.11.011

16. El Ghannudi S, Ouvrard E, Mikail N, Leroy Freschini B, Schindler TH, Imperiale A. Cutting-edge imaging of cardiac metastases from neuroendocrine tumors: lesson from a case series. *Diagnostics*. (2022) 12:1182. doi: 10.3390/diagnostics12051182

17. Liu M, Armeni E, Navalkissoor S, Davar J, Sullivan L, Leigh C, et al. Cardiac metastases in patients with neuroendocrine tumours: clinical features, therapy outcomes, and prognostic implications. *Neuroendocrinology*. (2021) 111:907–24. doi: 10.1159/000510444

18. Moyade P, Vinjamuri S. The heart matters: a review of incidental cardiac uptake on Ga-68 DOTA peptide PET-CT scans. *Nucl Med Commun*. (2019) 40:1081–5. doi: 10.1097/MNM.0000000000001064

19. Kunz WG, Eschbach RS, Stahl R, Kazmierczak PM, Bartenstein P, Rominger A, et al. Identification and characterization of myocardial metastases in neuroendocrine tumor patients using ^{68}Ga-DOTATATE PET-CT. *Cancer Imaging*. (2018) 18:34. doi: 10.1186/s40644-018-0168-2

20. Bonsen LR, Aalbersberg EA, Tesselaar M, Stokkel MP. Cardiac neuroendocrine tumour metastases: case reports and review of the literature. *Nucl Med Commun*. (2016) 37:461–5. doi: 10.1097/MNM.0000000000000464

21. Calissendorff J, Sundin A, Falhammar H. ^{68}Ga-DOTA-TOC-PET/CT detects heart metastases from ileal neuroendocrine tumors. *Endocrine*. (2014) 47:169–76. doi: 10.1007/s12020-013-0108-7

22. Carreras C, Kulkarni HR, Baum RP. Rare metastases detected by ^{68}Ga-somatostatin receptor PET/CT in patients with neuroendocrine tumors. *Recent Results Cancer Res*. (2013) 194:379–84. doi: 10.1007/978-3-642-27994-2_20

23. Hamza M, Manasrah N, Patel NN, Sattar Y, Patel B. A systematic review and meta-analysis of prevalence and outcomes of cardiac metastasis of neuroendocrine malignancies. *Am J Cardiol*. (2023) 194:86–92. doi: 10.1016/j.amjcard.2023.02.011

24. Paolisso P, Bergamaschi L, Angeli F, Belmonte M, Foà A, Canton L, et al. Cardiac magnetic resonance to predict cardiac mass malignancy: the CMR mass score. *Circ Cardiovasc Imaging*. (2024) 17:e016115. doi: 10.1161/CIRCIMAGING.123.016115

25. Jain S, Dhingra V, Girdhani B. Scope of PET imaging in the evaluation of cardiac tumors. *Cancer Treat Res Commun*. (2023) 37:100754. doi: 10.1016/j.ctarc.2023.100754

26. Hope TA, Fayad ZA, Fowler KJ, Holley D, Iagaru A, McMillan AB, et al. Summary of the first ISMRM-SNMMI workshop on PET/MRI: applications and limitations. *J Nucl Med*. (2019) 60:1340–6. doi: 10.2967/jnumed.119.227231

27. Rufini V, Treglia G, Montravers F, Giordano A. Diagnostic accuracy of [^{18}F]DOPA PET and PET/CT in patients with neuroendocrine tumors: a meta-analysis. *Clin Translat Imaging*. (2013) 1:111–22. doi: 10.1007/s40336-013-0005-3

28. Noordzij W, van Beek AP, Tio RA, van der Horst-Schrivers AN, de Vries EG, van Ginkel B, et al. Myocardial metastases on 6-[^{18}F] fluoro-L-DOPA PET/CT: a retrospective analysis of 116 serotonin producing neuroendocrine tumour patients. *PLoS One*. (2014) 9:e112278. doi: 10.1371/journal.pone.0112278

29. El Ghannudi S, Ben Abdelghani M, Germain P, Blondet C, Romain B, Imperiale A. Cardiac metastases of small-bowel. Added value of ^{18}F-fluorodihydroxyphenylalanine positron emission tomography combined to magnetic resonance imaging. *Circ Cardiovasc Imaging*. (2019) 12:e008405. doi: 10.1161/CIRCIMAGING.118.008405

frontiers | Frontiers in Medicine

TYPE Original Research
PUBLISHED 07 November 2024
DOI 10.3389/fmed.2024.1464779

OPEN ACCESS

EDITED BY
Francesco Dondi,
Università degli Studi di Brescia, Italy

REVIEWED BY
Shun Huang,
Southern Medical University, China
Cyrus Ayubcha,
Harvard Medical School, United States

*CORRESPONDENCE
Hui Ye
✉ yuxin75831@163.com

†These authors have contributed equally to this work and share first authorship

RECEIVED 15 July 2024
ACCEPTED 28 October 2024
PUBLISHED 07 November 2024

CITATION
Dai J, Zhou W, Liu H, Jiang C and Ye H (2024) Impact of fat intake on [18F]AlF-NOTA-FAPI-04 uptake in normal abdominal organs. *Front. Med.* 11:1464779. doi: 10.3389/fmed.2024.1464779

Impact of fat intake on [^{18}F] AlF-NOTA-FAPI-04 uptake in normal abdominal organs

Jiashun Dai[1†], Wanjing Zhou[1†], Huaping Liu[2†], Chengzhi Jiang[1] and Hui Ye[1*]

[1]Department of PET-CT Center, The Affiliated Cancer Hospital of Xiangya School of Medicine, Central South University/Hunan Cancer Hospital, Changsha, China, [2]Department of Radiology, The Affiliated Cancer Hospital of Xiangya School of Medicine, Central South University/Hunan Cancer Hospital, Changsha, China

Purpose: [^{18}F]AlF-NOTA-FAPI-04 demonstrates significant physiological uptake in the gallbladder and biliary tract system, representing a limitation of this positron emission tomography (PET) tracer. The aim of this study was to evaluate the impact of milk consumed prior to a PET/CT scan on [^{18}F]AlF-NOTA-FAPI-04 uptake in normal abdominal organs.

Materials and methods: A total of 86 patients who underwent [^{18}F]AlF-NOTA-FAPI-04 PET/CT imaging took part in this single-center retrospective clinical study at the Hunan Cancer Hospital between December 2020 and August 2021. Patients were divided into two groups according to their pre-PET scan diet: treated group, who consumed 250 mL of milk 10 ± 5 min after the tracer injection, while the control group was permitted no food intake subsequent to the radiotracer administration. The mean standardized uptake value (SUV_{mean}) of gallbladder, liver, small intestine and pancreas were measured in ^{18}F-FAPI and ^{18}F-FDG PET/CT.

Results: There was a statistically significant difference in the ^{18}F-FAPI uptake in the gallbladder between the treated group and the control group ($p < 0.001$). The average SUV_{mean} in the treated group was 2.19 ± 2.01, which was significantly lower than the average SUV_{mean} of 10.04 ± 9.66 in the control group. In the subgroup analysis of patients who underwent paired [^{18}F]FDG and [^{18}F]FAPI PET/CT scans, the ^{18}F-FAPI uptake of liver and small intestine was significantly lower than the ^{18}F-FDG uptake in both the treated group and the control group ($p < 0.001$).

Conclusion: This study suggests that milk consumption decreases physiological ^{18}F-FAPI uptake in the gallbladder, potentially enhancing the diagnostic accuracy for gallbladder cancer.

KEYWORDS

milk, [^{18}F]AlF-NOTA-FAPI-04, positron emission tomography, gallbladder, SUV_{mean}

Introduction

Fibroblast activation protein (FAP), highly expressed in cancer-associated fibroblasts, is a type II transmembrane glycoprotein enzyme with peptidase activity (1–4). FAP inhibitors (FAPIs) labeled with radioactive tracers (^{68}Ga, ^{18}F, or ^{177}Lu) are currently utilized in clinical practice for diagnosis and treatment in a wide range of malignant tumors and their associated metastases, demonstrating significant superiority over

^{18}F-fluoro-2-deoxy-D-glucose (^{18}F-FDG) in certain contexts. FAPI PET/CT has considerable promise for precise cancer assessment (5–9).

Among the extensively studied and reported PET molecular imaging probes, ^{68}Ga-FAPI-04 demonstrates a remarkably high tumor-to-background ratio across more than 30 different types of cancer (10–13). However, the application of ^{68}Ga-FAPI-04 is limited due to its relatively short half-life (68 min), low overall activity production (only sufficient for 2–3 patients in one batch), and sub-optimal spatial resolution. Due to its longer half-life of 110 min compared to [^{68}Ga], [^{18}F] facilitates large-scale production and long-distance transportation, making it the most commonly used radioisotope in clinical practice (14, 15). Several ^{18}F-labeled FAPIs have been developed for either preclinical or clinical evaluation (16–21). [^{18}F]AlF-NOTA-FAPI-04 is one of the ^{18}F-labeled FAPIs that has demonstrated superior tumor imaging capabilities in several clinical evaluations, exhibiting improved physical properties, high yields, and favorable imaging characteristics. [^{18}F]AIF-NOTA-FAPI-04 has the potential to serve as an ideal radiopharmaceutical for PET imaging (18, 22, 23). However, there are abundant differences in biodistribution between ^{18}F-FAPI and ^{18}F-FDG. Although ^{18}F-FAPI uptake was lower than ^{18}F-FDG in most normal tissues, the SUV_{mean} of the gallbladder and pancreas was notably higher in ^{18}F-FAPI compared to ^{18}F-FDG (24). Previous studies have reported that ^{18}F-FAPI demonstrates significant physiological uptake in the gallbladder and biliary tract system, which hampers the detection of their associated malignancies (20, 24). Oral intake of milk after ^{18}F-FAPI administration may increase the hepatobiliary clearance rate of ^{18}F-FAPI. Full-fat milk can induce the secretion of cholecystokinin(CCK) from the cells of the small intestine mucosa, with effects similar to those observed after direct administration of cholecystokinin, potentially stimulating gallbladder contraction and accelerating the transit of the tracer from the liver to the gastrointestinal tract (25). This approach, which involves the consumption of items such as full-fat milk or milkshakes, is commonly employed in nuclear medicine for myocardial perfusion imaging (26, 27).

The aim of this study was to assess the impact of fat intake on normal abdominal organs uptake of [^{18}F] AlF-NOTA-FAPI-04 and to conduct a comparison on the physiological abdominal organ uptake of [^{18}F] AlF-NOTA-FAPI-04 and ^{18}F-FDG.

Materials and methods

Patients

A total of 86 patients who underwent whole-body/abdominal [^{18}F]AlF-NOTA-FAPI-04 PET/CT imaging at the Hunan Cancer Hospital between December 2020 and August 2021 were included in our study. Informed consent was obtained from each participant prior to ^{18}F-FAPI PET/CT imaging. Patients were divided into two groups according to their diet before the PET scan: treated group, comprised of patients who consumed 250 mL milk 10 ± 5 min after the tracer injection. The volume of the milk was 250 mL, and contained 284 kJ/100 mL, fat content per 100 milliliters was 4.0 g. Control group, permitted no food intake subsequent to the radiotracer administration, which was the standard patient preparation. 64 patients underwent paired ^{18}F-FDG and [^{18}F]AlF-NOTA-FAPI-04 PET/CT scans.

Study design

This was a single-center retrospective study conducted at Hunan Cancer Hospital. This research complied with the Declaration of Helsinki's recommendations for biomedical research involving human subjects and received approval from the Medical Ethics Committee of Hunan Cancer Hospital. Prior to the scan, patients in the treated group did give verbal informed consent to consume milk. The primary endpoint of this study was the physiological ^{18}F-FAPI and ^{18}F-FDG uptake in the gallbladder, liver, small intestine and pancreas, measured as mean standardized uptake value (SUV_{mean}).

Radiosynthesis and quality control

The F-18 radionuclide was synthesized *in situ* by subjecting O-18-H2O to a 9.8 MeV proton bombardment using a GE MINItrace cyclotron (GE HealthCare, Milwaukee, WI, USA). The FAPI-04 precursor was procured from PET Science and Technology CO., LTD (Beijing, China). [^{18}F]AlF-NOTA-FAPI-04 was labeled using the procedure detailed by Jiang et al. (18). The manufacturing of ^{18}F-FDG followed the standard procedure, utilizing the coincidence ^{18}F-FDG synthesis module (AIO; TRSIS, China). Both [^{18}F] AlF-NOTA-FAPI-04 and ^{18}F-FDG exhibited a radiochemical purity exceeding 95%. The final product was sterile and met all the requirements stipulated by our institution before to use.

PET/CT scanning

Patients must strictly fast for 4 h before imaging. The administered intravenous dose of both ^{18}F-FAPI and ^{18}F-FDG was 3.7 MBq (0.1 mCi)/kg. Fifteen minutes before the ^{18}F-FDG injection, height, weight, and fasting blood glucose levels should be measured, with the blood glucose level required to be below 7.0 mmol/L; otherwise, an appropriate amount of insulin should be administered subcutaneously to ensure compliance with the standard. An hour following intravenous delivery, all patients underwent a PET/CT scan on a digital detector scanner (Discovery MI, GE, Healthcare, Milwaukee, WI, USA). The computed tomography (CT) scan covered the area from the whole skull to the upper thighs, using a tube voltage of 110 kV, a tube current of 120 mA, and a slice thickness of 3.75 mm. After the CT scan, a PET scan was done right away in 3D acquisition mode, taking 2 min for each position and 5 to 6-bed positions. Ordered subset expectation maximization (OSEM) was used to construct ^{18}F-FDG and ^{18}F-FAPI PET/CT images on an Advantage Workstation (AW 4.7, GE HealthCare, Milwaukee, WI, USA). After attenuation correction using the CT data, the reconstructed images were co-registered for analysis. The paired ^{18}F-FDG and [^{18}F]AlF-NOTA-FAPI-04 PET/CT scans were performed within 14 days.

^{18}F-FAPI and ^{18}F-FDG PET data analysis

All images were independently reviewed by two board-certified nuclear medicine physicians with expertise in interpreting PET/CT examinations. Any discrepancies in the image interpretations were

resolved through consensus discussion. The intensity of physiological ^{18}F-FAPI and ^{18}F-FDG uptake in organs was quantified as the mean standardized uptake value (SUV_{mean}). Areas of interest were drawn from tissues on the gallbladder, liver (right lobe), proximal jejunum and pancreas (tail/corpus). The volumes of interest (VOIs) were drawn in three consecutive slices on the PET images focused on the maximum voxel value for the mentioned organs, and the mean values of the SUV in the VOIs were recorded. To minimize a partial volume effect, VOIs were always positioned inside the bounds of the activity distribution. VOIs were delineated at 1 cm for minor tissues and at 2 cm for major organs such as the liver. Additionally, VOIs included intestinal walls and possible luminal content but not extraintestinal content. SUV_{mean} were automatically extracted from the defined VOIs using the AW Workstation.

Statistical analysis

SPSS (version 25.0; SPSS Inc., Chicago, IL, USA) was employed for the analysis. Continuous variables were expressed as mean ± standard deviation (SD) when the data were normally distributed, otherwise, the median and interquartile range were reported. Categorical variables were represented as percentages (%). Fisher's exact test or chi-square test was used to compare unordered categorical variables represented as numbers and percentages. Semiquantitative parameters measured using the ^{18}F-FAPI and ^{18}F-FDG were analyzed using the Mann–Whitney U test, with statistical significance defined by a probability (p) value ≤0.05.

Results

Participant characteristics

Our cohort initially enrolled 105 consecutive patients, however, after excluding 15 patients with cholecystectomy and 4 patients with poor image quality, a total of 86 patients were ultimately included for the evaluation of the effect of pre-scan dietary preparations on the physiologic ^{18}F-FAPI and ^{18}F-FDG uptake of the gallbladder. The characteristics of the patients are summarized in Table 1. The treated group comprised 67 patients who drank milk subsequent to the radiotracer administration, while the Control group included 19 patients who underwent no food intake after the tracer injection. No statistically significant differences were observed between the two groups of patients in terms of age, gender, weight, body mass index, injection dose, and history of gastrectomy. All patients tolerated this test well, with no drug-related pharmacologic effects or physiologic reactions. No patient noticed any symptoms or experienced any adverse reactions during the injection process until the end of the examination.

Comparison of physiological ^{18}F-FAPI uptake in treated group versus control group

The physiological ^{18}F-FAPI uptake in various organs for the two groups are presented in Table 2. Quantitative analysis revealed

TABLE 1 Patients' characteristics of the treated group and control group (n = 86).

Characteristics	Treated (n = 67)	Control (n = 19)	p-value
Age, years	54.34 ± 11.63	49.0 ± 10.82	0.076
Gender			
Male	36	9	0.624
Female	31	10	
Weight, kg	56.0 ± 11.62	57.42 ± 9.59	0.627
Height, cm	160.57 ± 7.56	160.05 ± 7.91	0.796
BMI, kg/m2	21.61 ± 3.59	22.47 ± 3.71	0.361
Injected dose, MBq	236.3 ± 34.45	242.3 ± 24.85	0.477
Resection			
Gastric resection	18	5	0.962
Non-gastric resection	49	14	

TABLE 2 Physiological ^{18}F-FAPI uptake (SUV_{mean}) per food intake protocol and per organ.

Organ	Treated (n = 67)	Control (n = 19)	p-value
Gallbladder	2.19 ± 2.01	10.04 ± 9.66	<0.001
Liver	0.80 ± 1.08	0.62 ± 0.12	0.216
Small intestine	0.65 ± 0.19	0.64 ± 0.14	0.923
Pancreas	1.78 ± 1.02	2.92 ± 3.60	0.545

Values are presented as average and standard deviation.

moderate-to-low uptake in the average SUV_{mean} in the liver, small intestine and pancreas. No significant differences were observed in the physiologic ^{18}F-FAPI uptake in these organs between treated group and control group. There was a statistically significant difference in the ^{18}F-FAPI uptake in the gallbladder between the treated group and the control group ($p < 0.001$). The average SUV_{mean} in the treated group was 2.19 ± 2.01, which was significantly lower than the average SUV_{mean} of 10.04 ± 9.66 in the control group. Figure 1 illustrates the distribution of physiological tracer uptake in the gallbladder, liver, small intestine and pancreas between the treated group and control group.

Comparison of physiological ^{18}F-FAPI uptake and physiological ^{18}F-FDG uptake in treated group/control group

Subgroup analysis was performed on patients ($n = 64$) who underwent both ^{18}F-FAPI and ^{18}F-FDG PET/CT scan, In the treated group and control group, the ^{18}F-FAPI uptake of the liver ($p \leq 0.001$) and small intestine ($p \leq 0.001$) were significantly lower compared to ^{18}F-FDG uptake. However, in the treated group and control group, the ^{18}F-FAPI uptake of the gallbladder ($p \leq 0.002$) and pancreas ($p \leq 0.005$) were significantly higher compared to ^{18}F-FDG uptake (Table 3).

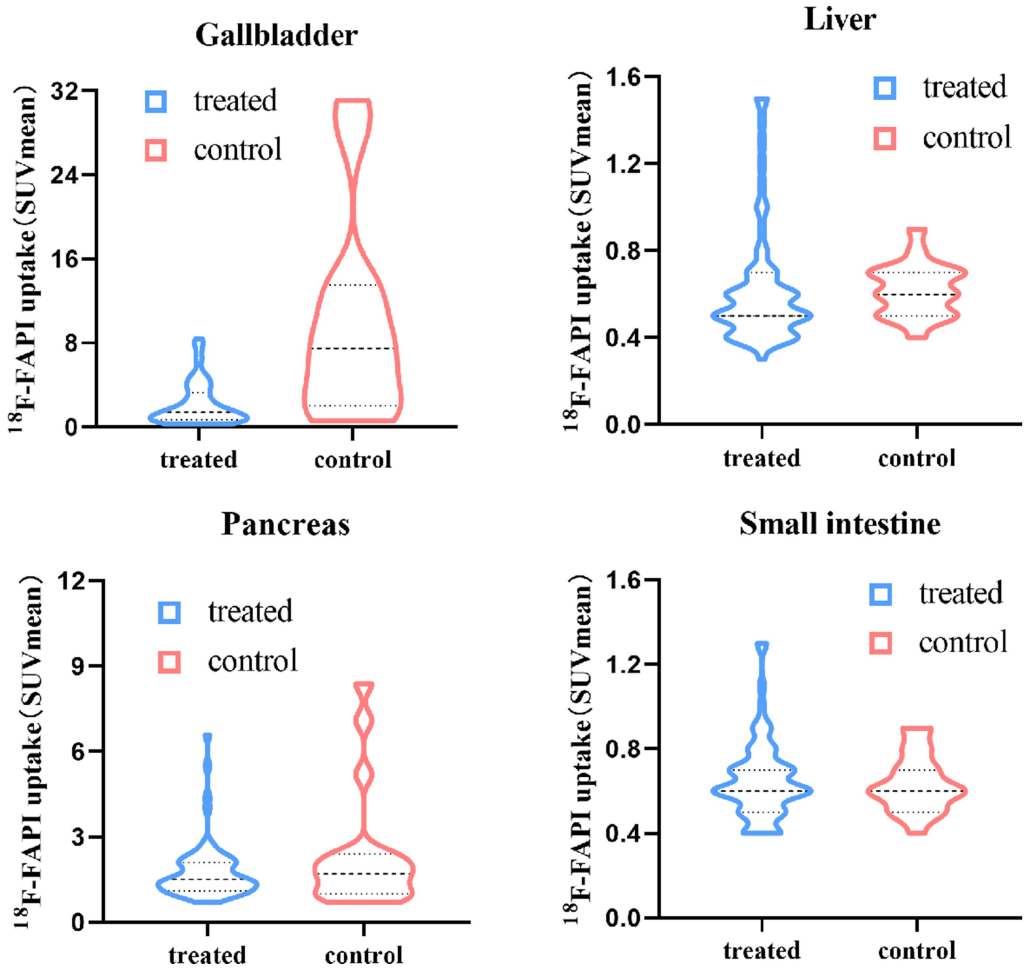

FIGURE 1
Physiological ^{18}F-FAPI uptake in gallbladder, liver, small intestine and pancreas for different food intake protocols.

TABLE 3 Physiological ^{18}F-FAPI and ^{18}F-FDG uptake (SUV_{mean}) in treated group and control group.

Organ	Treated ($n = 51$)			Control ($n = 13$)		
	^{18}F-FAPI	^{18}F-FDG	p-value	^{18}F-FAPI	^{18}F-FDG	p-value
Gallbladder	2.41 ± 2.18	0.76 ± 0.39	<0.001	9.30 ± 9.63	0.83 ± 0.35	0.002
Liver	0.87 ± 1.23	2.10 ± 0.68	<0.001	0.62 ± 0.14	1.85 ± 0.30	0.001
Small intestine	0.68 ± 0.20	1.45 ± 0.47	<0.001	0.68 ± 0.13	1.18 ± 0.27	0.001
Pancreas	1.90 ± 1.12	1.37 ± 0.47	0.002	3.33 ± 3.09	1.26 ± 0.17	0.005

Comparison of physiological ^{18}F-FAPI uptake (SUV_{mean}) in treated group/control group after gastric resection

In a subgroup analysis of gastrectomy patients, there was significant difference in physiologic gallbladder uptake between two groups($p = 0.04$), the average SUV_{mean} in the treated group was 2.56 ± 2.12, which was significantly lower than the average SUV_{mean} of 14.62 ± 14.71 in the control group. Apart from this, there were no difference in the physiologic ^{18}F-FAPI uptake of liver, small intestine and pancreas between treated and control group after gastric resection (Table 4). Figure 2 illustrates the clear visual difference in the physiological ^{18}F-FAPI uptake of gallbladder between the treated group and control group after gastric resection or without gastric resection.

Discussion

Radiolabelled FAPI has been reported to achieve better results in a variety of tumor imaging and is considered a suitable

TABLE 4 Physiological ^{18}F-FAPI uptake (SUV_{mean}) in treated group and control group after gastric resection.

Organs	Treated ($n = 18$)	Control ($n = 5$)	p-value
Gallbladder	2.56 ± 2.12	14.62 ± 14.71	0.04
Liver	0.64 ± 0.29	0.64 ± 0.05	0.234
Small intestine	0.81 ± 0.23	0.74 ± 0.13	0.596
Pancreas	2.37 ± 1.39	4.30 ± 3.20	0.191

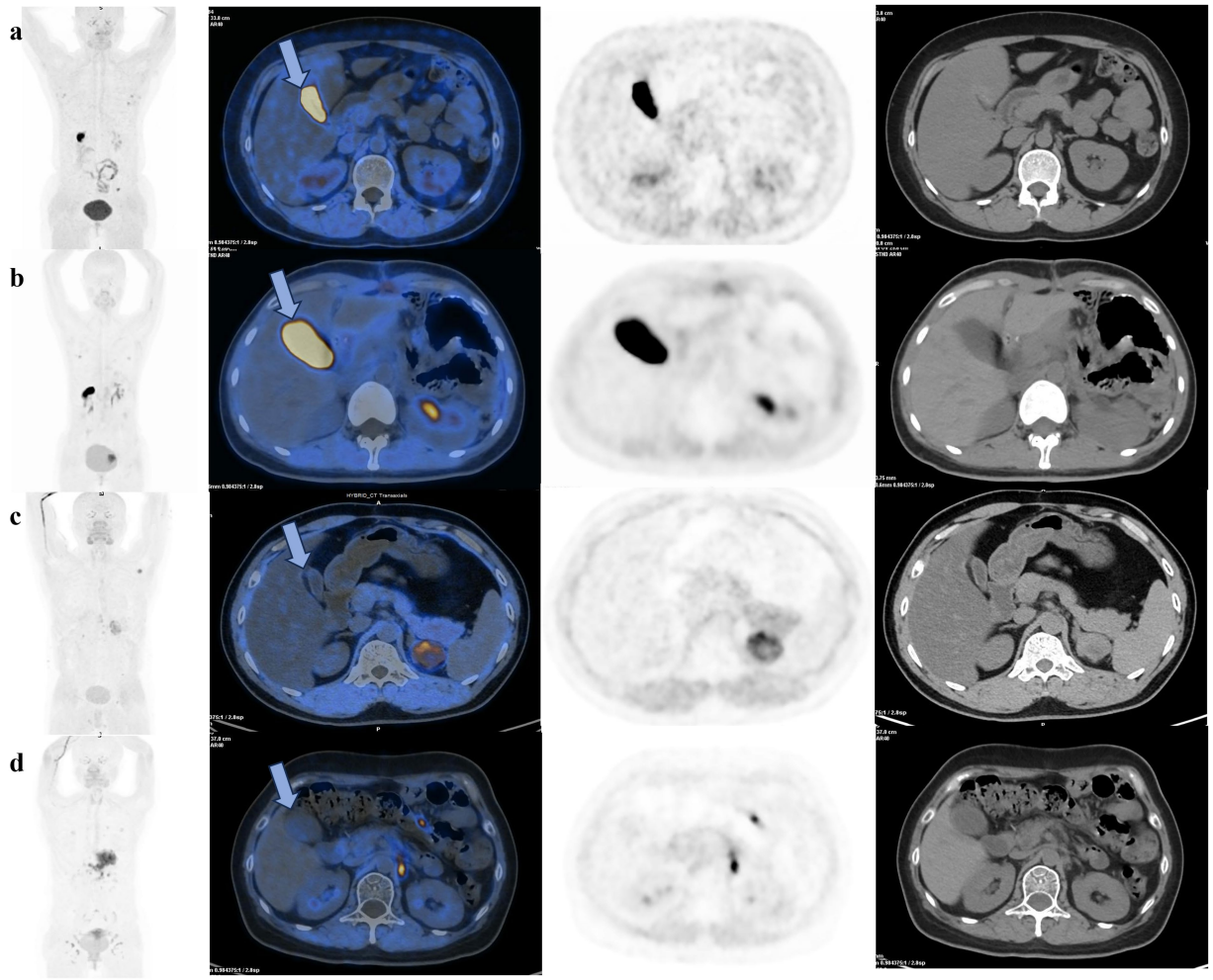

FIGURE 2
^{18}F-FAPI PET/CT scans of cancer patients demonstrate that pre-scan milk has a significant effect on reducing physiological uptake in the gallbladder after gastric resection or without gastric resection. (a) A patient without gastric resection in the control group showed significantly ^{18}F-FAPI uptake in the gallbladder (blue arrow). (b) A patient after gastric resection in control group, with increased physiological uptake in the gallbladder (blue arrow). (c) A patient without gastric resection in the treated group, without visible gallbladder uptake (blue arrow). (d) A patient after gastric resection in the treated group, without visible gallbladder uptake (blue arrow) due to gallbladder emptying.

alternative to ^{18}F-FDG (28, 29). The application of ^{68}Ga-FAPI-04 is restricted due to its relatively short half-life, low overall activity production, and sub-optimal spatial resolution. On the other hand, ^{18}F-labeled FAPIs have shown to possess superior tumor imaging abilities in various clinical evaluations, which exhibit improved physical properties, high yields, and favorable imaging characteristics (14, 15). Nevertheless, previous research demonstrated that ^{18}F-FAPI has a generally high physiologic uptake in the normal gallbladder, reducing the diagnostic accuracy of primary and metastatic gallbladder lesions (20, 22, 24). We assessed the impact of pre-PET/CT ingestion of milk on the biodistribution of ^{18}F-FAPI within normal abdominal organs in a tumor patient cohort.

In this study, physiological uptake of ^{18}F-FAPI in the gallbladder was significantly lower in the treated group patients compared to the control group, which facilitates the visualization of gallbladder tumors. The principle of decreased gallbladder uptake of ^{18}F-FAPI is based on the physiological metabolic characteristics of ^{18}F-FAPI. Previous experiments on animals have indicated that ^{18}F-FAPI is mainly excreted through the urinary and biliary systems (16). FAPI is a lipophilic tracer that can be excreted into the intestine by binding to bile acids in the biliary system (16, 18, 30). According to Heraghty's study (31), a fatty meal can increase the hepatobiliary clearance of contrast agent, which is consistent with our findings. It is noteworthy that among the control group, two patients with the highest gallbladder uptake had undergone gastric cancer surgery years ago. Postoperative metabolic changes may alter bile acid production and lead to the formation of biliary sludge, increasing the incidence of gallbladder pathology and thus affecting gallbladder uptake (32).

Furthermore, we compared the results of 64 patients who underwent both ^{18}F-FDG and ^{18}F-FAPI PET/CT scans. We observed the physiologic ^{18}F-FAPI uptake by the liver and small intestine in the treated group and control group was lower than ^{18}F-FDG, and the ^{18}F-FDG uptake of gallbladder and pancreas was significantly lower than the ^{18}F-FAPI uptake in the treated group and control group, which is aligned with the previous studies (20, 22, 24, 33). Our study demonstrated that ^{18}F-FAPI PET/CT can effectively reduce the physiological uptake of liver and small intestine, improving the ^{18}F-FAPI visualization, thereby improving the lesion detection rate. A higher background ^{18}F-FAPI uptake in gallbladder and pancreas might unbeneficial in detecting tumors and metastatic lesions in the abdominal cavity. However, one study has indicated that FAPI-PET is a reliable diagnostic method for pancreatic cancers (34), which suggests that a minor difference of SUV_{mean} between ^{18}F-FAPI and ^{18}F-FDG cannot affect the accuracy of diagnosis in this type of cancer. We hypothesized that the slight increase in gallbladder uptake of treated group on ^{18}F-FAPI PET/CT did not affect the detection of gallbladder lesions.

In the subgroup analysis of gastrectomy patient, the treated group and control groups did not exhibit substantial changes in liver, small intestines and pancreas uptake. However, the physiologic ^{18}F-FAPI uptake of gallbladder in the treated group was significantly lower than the control group. There is a lack of definitive studies on physiologic ^{18}F-FAPI uptake in gastrectomy patient. The physiological mechanisms related to the effect of fat intake on gallbladder contraction after gastrectomy remain unclear. Inoue. K highlighted that the release of CCK serves as the chief mechanism through which the ingestion of a fatty meal causes contraction of the gallbladder even after gastrectomy as well as before gastrectomy (35). Watanapa. P suggested that hypercholecystokininaemia persists for up to 15 months and may even increase with time after gastrectomy (36). However, some studies showed delayed emptying of the gallbladder after a gastric resection or vagotomy. The contraction of the gallbladder is caused by the stimulation of the vagal nerve and impaired gallbladder motor function could result from vagal denervation (37). Our study shows that milk consumption similarly promotes gallbladder emptying and decreases physiological gallbladder ^{18}F-FAPI uptake in gastrectomy patients, which supports a major role for CCK in gallbladder contraction after gastrectomy.

Our study has several limitations: firstly, the sample size was small and the number of patients in the two groups were unbalanced. Statistical analysis may lack generalizability, and the conclusion need to be verified in larger studies. Secondly, SUV_{bw} (normalized by Body Weight) is occasionally overestimated, particularly in obese individuals, which can lead to systematic bias for serial scans of patients with multiple follow-ups throughout the course of treatment. Our study would benefit from SUV measures normalized by lean body mass (38). Thirdly, the ^{18}F-FAPI uptake of gallbladder was higher than the ^{18}F-FDG uptake in the treated group. Consideration of ^{18}F-FAPI or ^{18}F-FDG for visualization is crucial in the comprehensive assessment of gallbladder cancer patients. Despites these limitations, it is believed that this study has undoubtedly enhanced our understanding of the influence of fat intake on [^{18}F] AlF-NOTAFAPI-04 uptake in the normal abdominal organs.

Conclusion

In this retrospective study, we showed that the ^{18}F-FAPI uptake of gallbladder in treated group was significantly lower than control group, which suggested that consumption of 250 mL of milk after the tracer injection potentially stimulate gallbladder contraction. Integration of pre-scan milk into routine ^{18}F-FAPI PET/CT may enhance identification of gallbladder lesions, and may improve the diagnosis of gallbladder cancer in the future. On the other hand, the ^{18}F-FAPI uptake of liver and small intestine was significantly lower than the ^{18}F-FDG uptake, and the ^{18}F-FDG uptake of gallbladder and pancreas was significantly lower than the ^{18}F-FAPI uptake in both the treated group and the control group. ^{18}F-FDG and ^{18}F-FAPI serve as complementary tracers, thus dual tracer imaging holds significant clinical value.

Data availability statement

The raw data supporting the conclusions of this article will be made available by the authors, without undue reservation.

Ethics statement

The studies involving humans were approved by Medical Ethics Committee of Hunan Cancer Hospital. The studies were conducted in accordance with the local legislation and institutional requirements. Written informed consent for participation was not required from the participants or the participants' legal guardians/

next of kin in accordance with the national legislation and institutional requirements. Written informed consent was obtained from the individual(s) for the publication of any potentially identifiable images or data included in this article.

Author contributions

JD: Conceptualization, Data curation, Formal analysis, Investigation, Methodology, Project administration, Resources, Supervision, Validation, Visualization, Writing – original draft, Writing – review & editing. WZ: Conceptualization, Data curation, Formal analysis, Investigation, Methodology, Project administration, Resources, Supervision, Validation, Visualization, Writing – original draft, Writing – review & editing. HL: Conceptualization, Data curation, Formal analysis, Investigation, Methodology, Project administration, Resources, Supervision, Validation, Visualization, Writing – original draft, Writing – review & editing. CJ: Supervision, Validation, Visualization, Writing – review & editing. HY: Funding acquisition, Supervision, Validation, Visualization, Writing – review & editing.

Funding

The author(s) declare that financial support was received for the research, authorship, and/or publication of this article. This work was supported by Health Research Project of Hunan Provincial Health Commission (grant number W20243245), and Hunan Provincial Natural Science Foundation of China (grant number 2024JJ9250).

Conflict of interest

The authors declare that the research was conducted in the absence of any commercial or financial relationships that could be construed as a potential conflict of interest.

Publisher's note

Supplementary material

The Supplementary material for this article can be found online at: https://www.frontiersin.org/articles/10.3389/fmed.2024.1464779/full#supplementary-material

SUPPLEMENTARY FIGURE S1
Schematic diagram of the volume of interest (VOI) delineation. The volumes of interest (VOIs) were drawn in three consecutive slices on the PET images focused on the maximum voxel value for the mentioned organs, and the mean values of the SUV in the VOIs were recorded. VOIs were delineated at 1 cm for minor tissues and at 2 cm for major organs such as the liver. The VOI of gallbladder and small intestine are located within the lumen, excluding the wall.

References

1. Brennen WN, Isaacs JT, Denmeade SR. Rationale behind targeting fibroblast activation protein-expressing carcinoma-associated fibroblasts as a novel chemotherapeutic strategy. *Mol Cancer Ther*. (2012) 11:257–66. doi: 10.1158/1535-7163.Mct-11-0340

2. Liu R, Li H, Liu L, Yu J, Ren X. Fibroblast activation protein: a potential therapeutic target in cancer. *Cancer Biol Ther*. (2012) 13:123–9. doi: 10.4161/cbt.13.3.18696

3. Christiansen VJ, Jackson KW, Lee KN, Downs TD, McKee PA. Targeting inhibition of fibroblast activation protein-α and prolyl oligopeptidase activities on cells common to metastatic tumor microenvironments. *Neoplasia*. (2013) 15:348–58. doi: 10.1593/neo.121850

4. Hamson EJ, Keane FM, Tholen S, Schilling O, Gorrell MD. Understanding fibroblast activation protein (FAP): substrates, activities, expression and targeting for cancer therapy. *Proteomics Clin Appl*. (2014) 8:454–63. doi: 10.1002/prca.201300095

5. Lindner T, Loktev A, Altmann A, Giesel F, Kratochwil C, Debus J, et al. Development of Quinoline-based Theranostic ligands for the targeting of fibroblast activation protein. *J Nucl Med*. (2018) 59:1415–22. doi: 10.2967/jnumed.118.210443

6. Giesel FL, Kratochwil C, Lindner T, Marschalek MM, Loktev A, Lehnert W, et al. (68)Ga-FAPI PET/CT: biodistribution and preliminary dosimetry estimate of 2 DOTA-containing FAP-targeting agents in patients with various cancers. *J Nucl Med*. (2019) 60:386–92. doi: 10.2967/jnumed.118.215913

7. Kratochwil C, Flechsig P, Lindner T, Abderrahim L, Altmann A, Mier W, et al. (68) Ga-FAPI PET/CT: tracer uptake in 28 different kinds of Cancer. *J Nucl Med*. (2019) 60:801–5. doi: 10.2967/jnumed.119.227967

8. Lindner T, Altmann A, Krämer S, Kleist C, Loktev A, Kratochwil C, et al. Design and development of (99m)Tc-labeled FAPI tracers for SPECT imaging and (188)re therapy. *J Nucl Med*. (2020) 61:1507–13. doi: 10.2967/jnumed.119.239731

9. Watabe T, Liu Y, Kaneda-Nakashima K, Shirakami Y, Lindner T, Ooe K, et al. Theranostics targeting fibroblast activation protein in the tumor stroma: (64)cu- and (225)ac-labeled FAPI-04 in pancreatic Cancer xenograft mouse models. *J Nucl Med*. (2020) 61:563–9. doi: 10.2967/jnumed.119.233122

10. Guo W, Pang Y, Yao L, Zhao L, Fan C, Ke J, et al. Imaging fibroblast activation protein in liver cancer: a single-center post hoc retrospective analysis to compare [(68)Ga]Ga-FAPI-04 PET/CT versus MRI and [(18)F]-FDG PET/CT. *Eur J Nucl Med Mol Imaging*. (2021) 48:1604–17. doi: 10.1007/s00259-020-05095-0

11. Pang Y, Zhao L, Luo Z, Hao B, Wu H, Lin Q, et al. Comparison of (68)Ga-FAPI and (18)F-FDG uptake in gastric, duodenal, and colorectal cancers. *Radiology*. (2021) 298:393–402. doi: 10.1148/radiol.2020203275

12. Qin C, Liu F, Huang J, Ruan W, Liu Q, Gai Y, et al. A head-to-head comparison of (68)Ga-DOTA-FAPI-04 and (18)F-FDG PET/MR in patients with nasopharyngeal carcinoma: a prospective study. *Eur J Nucl Med Mol Imaging*. (2021) 48:3228–37. doi: 10.1007/s00259-021-05255-w

13. Zhang Z, Jia G, Pan G, Cao K, Yang Q, Meng H, et al. Comparison of the diagnostic efficacy of (68) Ga-FAPI-04 PET/MR and (18)F-FDG PET/CT in patients with pancreatic cancer. *Eur J Nucl Med Mol Imaging*. (2022) 49:2877–88. doi: 10.1007/s00259-022-05729-5

14. Fowler JS, Ido T. Initial and subsequent approach for the synthesis of 18FDG. *Semin Nucl Med*. (2002) 32:6–12. doi: 10.1053/snuc.2002.29270

15. Sahnoun S, Conen P, Mottaghy FM. The battle on time, money and precision: Da[(18)F] id vs. [(68)Ga]liath. *Eur J Nucl Med Mol Imaging*. (2020) 47:2944–6. doi: 10.1007/s00259-020-04961-1

16. Toms J, Kogler J, Maschauer S, Daniel C, Schmidkonz C, Kuwert T, et al. Targeting fibroblast activation protein: Radiosynthesis and preclinical evaluation of an (18)F-labeled FAP inhibitor. *J Nucl Med*. (2020) 61:1806–13. doi: 10.2967/jnumed.120.242958

17. Giesel FL, Adeberg S, Syed M, Lindner T, Jiménez-Franco LD, Mavriopoulou E, et al. FAPI-74 PET/CT using either (18)F-AlF or cold-kit (68)Ga labeling: biodistribution, radiation dosimetry, and tumor delineation in lung Cancer patients. *J Nucl Med*. (2021) 62:201–7. doi: 10.2967/jnumed.120.245084

18. Jiang X, Wang X, Shen T, Yao Y, Chen M, Li Z, et al. FAPI-04 PET/CT using [(18)F]AlF labeling strategy: automatic synthesis, quality control, and in vivo assessment in patient. *Front Oncol*. (2021) 11:649148. doi: 10.3389/fonc.2021.649148

19. Lindner T, Altmann A, Giesel F, Kratochwil C, Kleist C, Krämer S, et al. (18) F-labeled tracers targeting fibroblast activation protein. *EJNMMI Radiopharm Chem*. (2021) 6:26. doi: 10.1186/s41181-021-00144-x

20. Wang S, Zhou X, Xu X, Ding J, Liu S, Hou X, et al. Clinical translational evaluation of Al(18)F-NOTA-FAPI for fibroblast activation protein-targeted tumour imaging. *Eur J Nucl Med Mol Imaging*. (2021) 48:4259–71. doi: 10.1007/s00259-021-05470-5

21. Hu K, Li J, Wang L, Huang Y, Li L, Ye S, et al. Preclinical evaluation and pilot clinical study of [(18)F]AlF-labeled FAPI-tracer for PET imaging of cancer associated fibroblasts. *Acta Pharm Sin B*. (2022) 12:867–75. doi: 10.1016/j.apsb.2021.09.032

22. Wei Y, Zheng J, Ma L, Liu X, Xu S, Wang S, et al. [(18)F]AlF-NOTA-FAPI-04: FAP-targeting specificity, biodistribution, and PET/CT imaging of various cancers. *Eur J Nucl Med Mol Imaging*. (2022) 49:2761–73. doi: 10.1007/s00259-022-05758-0

23. Li X, Lu N, Lin L, Chen Y, Yang S, Wang H, et al. (18)F-FAPI-04 outperforms (18) F-FDG PET/CT in clinical assessments of patients with pancreatic adenocarcinoma. *J Nucl Med*. (2024) 65:206–12. doi: 10.2967/jnumed.123.266283

24. Mu X, Huang X, Li M, Sun W, Fu W. Comparison of physiological uptake of normal tissues in patients with cancer using 18F-FAPI-04 and 18F-FAPI-42 PET/CT. *Front Nucl Med*. (2022) 2:2. doi: 10.3389/fnume.2022.927843

25. Inoue Y, Komatsu Y, Yoshikawa K, Akahane M, Isayama H, Ohtomo K, et al. Biliary motor function in gallstone patients evaluated by fatty-meal MR cholangiography. *J Magn Reson Imaging*. (2003) 18:196–203. doi: 10.1002/jmri.10340

26. Purbhoo K, Vangu MD. Efficacy of full-fat milk and diluted lemon juice in reducing infra-cardiac activity of (99m)Tc sestamibi during myocardial perfusion imaging. *Cardiovasc J Afr*. (2015) 26:171–6. doi: 10.5830/cvja-2015-033

27. Hofman M, McKay J, Nandurkar D. Efficacy of milk versus water to reduce interfering infra-cardiac activity in 99mTc-sestamibi myocardial perfusion scintigraphy. *Nucl Med Commun*. (2006) 27:837–42. doi: 10.1097/01.mnm.0000237989.60196.71

28. Dong Y, Zhou H, Alhaskawi A, Wang Z, Lai J, Yao C, et al. The superiority of fibroblast activation protein inhibitor (FAPI) PET/CT versus FDG PET/CT in the diagnosis of various malignancies. *Cancers (Basel)*.. (2023) 15:1193. doi: 10.3390/cancers15041193

29. Li C, Tian Y, Chen J, Jiang Y, Xue Z, Xing D, et al. Usefulness of [(68)Ga]FAPI-04 and [(18)F]FDG PET/CT for the detection of primary tumour and metastatic lesions in gastrointestinal carcinoma: a comparative study. *Eur Radiol*. (2023) 33:2779–91. doi: 10.1007/s00330-022-09251-y

30. Kou Y, Jiang X, Yao Y, Shen J, Jiang X, Chen S, et al. Physiological tracer distribution and benign lesion incidental uptake of Al18F-NOTA-FAPI-04 on PET/CT imaging. *Nucl Med Commun*. (2022) 43:847–54. doi: 10.1097/mnm.0000000000001563

31. Heraghty N, Peters AM. Hepatic bile acid transport increases in the postprandial state: a functional (11)C-CSar PET/CT study in healthy humans. *JHEP Rep*. (2021) 3:100357. doi: 10.1016/j.jhepr.2021.100357

32. Alsallamin I, Chakhachiro D, Bawwab A, Nassar M, Alsallamin A. Prevalence of symptomatic gallbladder disease after bariatric surgery: a literature review. *Cureus*. (2023) 15:e37777. doi: 10.7759/cureus.37777

33. Giesel FL, Kratochwil C, Schlittenhardt J, Dendl K, Eiber M, Staudinger F, et al. Head-to-head intra-individual comparison of biodistribution and tumor uptake of (68) Ga-FAPI and (18)F-FDG PET/CT in cancer patients. *Eur J Nucl Med Mol Imaging*. (2021) 48:4377–85. doi: 10.1007/s00259-021-05307-1

34. Chen H, Pang Y, Wu J, Zhao L, Hao B, Wu J, et al. Comparison of [(68)Ga]Ga-DOTA-FAPI-04 and [(18)F] FDG PET/CT for the diagnosis of primary and metastatic lesions in patients with various types of cancer. *Eur J Nucl Med Mol Imaging*. (2020) 47:1820–32. doi: 10.1007/s00259-020-04769-z

35. Inoue K, Fuchigami A, Hosotani R, Kogire M, Huang YS, Miyashita T, et al. Release of cholecystokinin and gallbladder contraction before and after gastrectomy. *Ann Surg*. (1987) 205:27–32.

36. Watanapa P, Flaks B, Oztas H, Deprez PH, Calam J, Williamson RC. Enhancing effect of partial gastrectomy on pancreatic carcinogenesis. *Br J Cancer*. (1992) 65:383–7. doi: 10.1038/bjc.1992.77

37. Hahm J, Park J, Cho Y, Eun C, Lee Y, Choi H, et al. Changes in gallbladder motility in gastrectomized patients. *Korean J Intern Med*. (2000) 15:19–24. doi: 10.3904/kjim.2000.15.1.19

38. Hume R. Prediction of lean body mass from height and weight. *J Clin Pathol*. (1966) 19:389–91. doi: 10.1136/jcp.19.4.389

frontiers | Frontiers in Medicine

TYPE Systematic Review
PUBLISHED 13 January 2025
DOI 10.3389/fmed.2024.1517805

OPEN ACCESS

EDITED BY
Nataliya Lutay,
Skåne University Hospital, Sweden

REVIEWED BY
Salvatore Annunziata,
Fondazione Policlinico Universitario A. Gemelli IRCCS, Italy
Silvia Taralli,
Fondazione Policlinico Universitario A. Gemelli IRCCS, Italy
Quaovi Sodji,
University of Wisconsin-Madison, United States

*CORRESPONDENCE
Chaolin Chen
✉ lucky01042023@163.com

RECEIVED 27 October 2024
ACCEPTED 30 December 2024
PUBLISHED 13 January 2025

CITATION
Yu D and Chen C (2025) [18F]FDG PET/CT versus [18F]FDG PET/MRI in staging of non-small cell lung cancer: a head-to-head comparative meta-analysis.
Front. Med. 11:1517805.
doi: 10.3389/fmed.2024.1517805

[18F]FDG PET/CT versus [18F]FDG PET/MRI in staging of non-small cell lung cancer: a head-to-head comparative meta-analysis

Dandan Yu and Chaolin Chen*

Department of Clinical Pharmacy, Traditional Chinese Medical Hospital of Zhuji, Shaoxing, China

Purpose: This meta-analysis aims to compare the diagnostic efficacy of [18F]FDG PET/CT and [18F]FDG PET/MRI in patients with non-small cell lung cancer (NSCLC).

Methods: An extensive literature search was conducted throughout the PubMed, Embase, and Web of Science databases for works accessible through September 2024. We included studies assessed the diagnostic efficacy of [18F]FDG PET/CT and [18F]FDG PET/MRI in NSCLC.

Results: The meta-analysis includes six studies with a total of 437 patients. The sensitivity and specificity of [18F]FDG PET/CT and [18F]FDG PET/MRI for detecting lymph node metastasis were similar, at 0.82 (0.68–0.94) vs. 0.86 (0.70–0.97) and 0.88 (0.76–0.96) vs. 0.90 (0.85–0.94), respectively, with no significant differences (p = 0.70 for sensitivity, p = 0.75 for specificity). For distant metastasis, the sensitivity of [18F]FDG PET/CT and [18F]FDG PET/MRI was 0.86 (0.60–1.00) and 0.93 (0.63–1.00), and specificity was 0.89 (0.65–1.00) vs. 0.90 (0.64–1.00), respectively, also showing no significant differences (p = 0.66 for sensitivity, p = 0.97 for specificity).

Conclusion: Our meta-analysis shows that [18F]FDG PET/MRI has similar sensitivity and specificity to [18F]FDG PET/CT in identifying lymph node and distant metastases in patients with NSCLC. Additional larger sample prospective studies are needed to confirm these findings.

Systematic review registration: https://www.crd.york.ac.uk/prospero/display_record.php?ID=CRD42023479817, CRD42023479817.

KEYWORDS

[18F]FDG PET/CT, [18F]FDG PET/MRI, non-small cell lung cancer, meta-analysis, staging

1 Introduction

Lung cancer is recognized as the most typical diagnosis malignancy globally, also notable for its high mortality rates (1). Lung cancer remains the most prevalent cancer globally in 2022, accounting for approximately 2.5 million new cases, which represents one in eight cancer diagnoses worldwide (12.4% of all global cancer incidences) (2). In this setting, roughly 80% of lung malignancies are categorized as non-small cell lung cancer (NSCLC), which is the main cancer diagnosis worldwide (3, 4). Surgery, radiation, chemotherapy, immunotherapy, and targeted therapy can all be used to treat

NSCLC, depending on the stage of the tumor (5). The effectiveness of these treatments and the overall prognosis of the patient are profoundly impacted by the initial stage of the cancer (6). As a result, thorough and precise imaging-based staging is important for optimal care of NSCLC patients.

Currently, clinical methods used for NSCLC staging include computed tomography (CT), magnetic resonance imaging (MRI), and biopsy (7, 8). However, each of these modalities has its inherent limitations. While CT scanning excels in identifying the tumor's location and determining lymph node enlargement, its limited ability to determine or exclude mediastinal metastasis imposes certain constraints on the accurate staging of lung cancer (9). MRI is often considered less effective than CT for detecting small cancer lesions, due to its sensitivity to cardiac and respiratory motion artifacts, extremely low T2 values, lung magnetic field heterogeneity, and the low proton density of lung parenchyma (10). Biopsies, although crucial for delivering definitive results, are associated with inherent risks and may not always be feasible. The most common complication encountered is pneumothorax, which occurs in 20–64% of all CT-guided biopsies (11, 12). Additionally, hemorrhage from the lung parenchyma stands as another notable complication, frequently resulting from the needle track crossing a pulmonary vessel (13).

Positron emission tomography (PET) plays a crucial role in diagnosing NSCLC, from initial detection to staging and monitoring tumor metastasis (14). Integrating PET with 18F-fluorodeoxyglucose ([^{18}F]FDG) into PET/CT and PET/MRI systems has considerably revolutionized cancer imaging by integrating metabolic and anatomical information (15). [^{18}F]FDG PET/CT plays an important role in managing NSCLC, notably in evaluating the nodal status and finding occult metastatic disease, where it outperforms the capabilities of CT scanning alone (16). The NCCN guidelines emphasize the importance of rapid access to PET/CT for accurate staging in NSCLC, highlighting its role in guiding management decisions and predicting prognosis across all stages of the disease, particularly in detecting metastases (17). One of its main benefits over traditional imaging approaches is its increased sensitivity for detecting extra-thoracic metastases (18, 19). Dahlsgaard-Wallenius et al. found that PET/MRI and PET/CT had comparable diagnostic capacities for N-staging in NSCLC (20). Combining the metabolic data from PET with the special characteristics of MRI—such as low radiation exposure and excellent soft tissue contrast—makes PET/MRI an advantageous test (21). In several studies, evidence suggested that PET/MRI may outperform PET/CT in detecting metastases within the pleura, brain, liver, and bone (22, 23). This is also in accordance with the results of a prospective single-center research of 330 exams, where PET/MRI found brain and liver metastases that were undetectable by PET/CT (24). Thus, the use of a hybrid PET/MRI in lung cancer patients may sometimes assist the detection of distant metastases, because NSCLC metastases are primarily situated in the brain, liver, and bone (25, 26). However, the included trials gave minimal data on extra-thoracic metastatic illness, making it unable to draw conclusions about the potential advantage of PET/MRI. Due to the relative novelty of PET/MRI and the limited availability of direct comparison studies, inconsistencies in the literature regarding their comparative efficacy warrant careful examination.

The goal of this meta-analysis is to comprehensively evaluate the diagnostic performance of [^{18}F]FDG PET/MRI to [^{18}F]FDG PET/CT in NSCLC through head-to-head comparison.

2 Methods

The meta-analysis followed the Preferred Reporting Items for Systematic Reviews and Meta-Analyses of Diagnostic Test Accuracy (PRISMA-DTA) standards (27). The protocol for this meta-analysis is registered with PROSPERO (CRD42023479817).

2.1 Search strategy

An extensive literature search was conducted in PubMed, Embase, and Web of Science to identify pertinent publications available up to September 2024. The search utilized the following keywords: ("PET/MRI" or "PET/CT") AND ("lymph node metastasis") AND ("distant metastasis") AND ("non-small cell lung cancer"). Further details are available in Supplementary Table S1. The reference lists of the listed studies were meticulously manually examined to identify additional relevant literature.

2.2 Inclusion and exclusion criteria

This meta-analysis included studies that satisfied the PICOS framework: Population (P): patients diagnosed with NSCLC; Intervention (I): diagnostic imaging using [^{18}F]FDG PET/CT and/or [^{18}F]FDG PET/MRI; Comparison (C): studies comparing PET/CT and PET/MRI; Outcomes (O): studies that report diagnostic performance in assessing lymph node involvement and/or distant metastases; Study design (S): studies with a sample size greater than ten.

Studies were excluded if they were (1) animal studies, (2) non-research articles such as reviews, case reports, conference abstracts, meta-analyses, letters to the editor, or (3) non-randomized designs including case–control, cohort, and cross-sectional studies. Additionally, studies employing other radiotracers were also omitted. For studies utilizing the same data sets, only the most recent were considered.

2.3 Quality assessment

Two researchers independently evaluated the quality of the included studies using the Quality Assessment of Diagnostic Accuracy Studies-2 (QUADAS-2) tool (28). This tool addresses four key domains: patient selection, index test, reference standard, and flow and timing. Each study was independently rated, and any disagreements were resolved through discussion to reach consensus. The QUADAS-2 tool allowed for a structured and transparent appraisal of study quality, highlighting areas with potential risk of bias or applicability concerns.

2.4 Data extraction

Two researchers extracted data separately from the selected papers. This data encompassed details as author, year of publication,

imaging test type, study characteristics (country, study design, study duration, analysis, and reference standard), patient characteristics (number of patients, radiologists involved, and mean/median age), and technical specifics [scanner modality, ligand dose, image analysis, and true positives (TP), false positives (FP), false negatives (FN), true negatives (TN)].

2.5 Outcome measures

The primary endpoints were the sensitivity and specificity of [^{18}F]FDG PET/CT and [^{18}F]FDG PET/MRI in detecting lymph node metastasis and distant metastasis. Sensitivity was defined as the proportion of TP scans relative to the sum of TP and FN scans, reported at either the patient or lesion level. Specificity was defined as the proportion of TN scans relative to the total of TN and FP scans, as documented.

2.6 Statistical analysis

The DerSimonian and Laird methods were used to assess sensitivity and specificity, which were then combined with the Freeman-Tukey double inverse sine transformation. Confidence intervals were calculated employing the Jackson method. Heterogeneity both within and across groups was evaluated using the Cochrane Q and I^2 statistics (29). Significant heterogeneity ($p < 0.10$ or $I^2 > 50\%$) warranted sensitivity analysis and meta-regression to identify individual studies contributing to heterogeneity.

Both funnel plots and Egger's test were used to investigate publication bias. For all statistical analyses, a significance level of $p < 0.05$ was set. R software version 4.1.2 was used for computation and graphical display of statistical analyses.

3 Results

3.1 Study selection

A total of 1,515 publications were found in the first search. Nevertheless, 323 studies were found to be duplicates and were not eligible for this study, leaving 1,192 studies for further analysis. After a thorough review of the remaining 13 articles, 7 more were deemed ineligible due to unavailable data (TP, FP, FN, and TN) ($n = 1$) or different radiotracers ($n = 4$). Additionally, non-English articles ($n = 2$) were excluded. Ultimately, the meta-analysis included 6 articles (23, 30–34) evaluating the diagnostic efficacy of [^{18}F]FDG PET/CT and [^{18}F]FDG PET/MRI. The article PRISMA selection process is illustrated in Figure 1.

3.2 Study description and quality assessment

The six qualifying trials included a total of 437 NSCLC patients aged 35 to 89. All included articles were prospective design. All studies included N-stage evaluations, and three studies provided data regarding distant metastasis (23, 31, 32). Concerning analysis methods, each of the six articles employed patient-level analysis. Two articles adopted pathology as the reference standard, whereas four utilized either pathology or follow-up imaging for this purpose. Table 1 shows the study and patient characteristics for [^{18}F]FDG PET/CT and [^{18}F]FDG PET/MRI, whereas Tables 2, 3 describes the technical parameters.

Figure 2 depicts the risk of bias in each study, as assessed using the QUADAS-2 technique. When examining the risk of bias for patient selection, we discovered that one research was classified as "high risk" due to the absence of consecutive patients. One research classified the flow and timing criteria as "high risk" because certain subjects were excluded from the data analysis. The overall quality evaluation found that the included studies were good in quality.

3.3 Comparing the sensitivity of [^{18}F]FDG PET/CT and [^{18}F]FDG PET/MRI for detecting lymph node metastasis in NSCLC

The analysis incorporated six studies, revealing a pooled sensitivity of 0.82 (95% CI: 0.68–0.94) for [^{18}F]FDG PET/CT in detecting lymph node metastases in NSCLC. On the other hand, [^{18}F]FDG PET/MRI showed an overall sensitivity of 0.86 (95% CI: 0.70–0.97). As shown in Figure 3, there was no discernible change in sensitivity between [^{18}F]FDG PET/CT and [^{18}F]FDG PET/MRI ($p = 0.70$).

I^2 values for [^{18}F]FDG PET/CT and [^{18}F]FDG PET/MRI were 84 and 90%, respectively. No discernible sources of heterogeneity were found using leave-one-out sensitivity analysis (Supplementary Figures S1, S2). The meta-regression analysis for [^{18}F]FDG PET/CT also failed to find the origin of heterogeneity (Table 4). According to the meta-regression analysis for [^{18}F]FDG PET/MRI, the difference in reference standard ($p = 0.01$) might be the source of heterogeneity (Table 5).

3.4 Comparing the specificity of [^{18}F]FDG PET/CT and [^{18}F]FDG PET/MRI for detecting lymph node metastases in NSCLC

Six studies were included, and a pooled specificity of 0.88 (95% CI: 0.76–0.96) for [^{18}F]FDG PET/CT in identifying lymph node metastases in NSCLC. In contrast, [^{18}F]FDG PET/MRI had a pooled specificity of 0.90 (95% CI: 0.85–0.94) (Figure 4). There was no significant difference in specificity between [^{18}F]FDG PET/CT and [^{18}F]FDG PET/MRI ($p = 0.75$).

The I^2 for sensitivity of [^{18}F]FDG PET/CT was 74%. After omitting Lee et al.'s study, the I^2 value reduced to 21%, indicating that this study might be a source of heterogeneity. Nonetheless, the findings of the specificity study were similar, with only modest differences between 0.85 and 0.93, as shown in Supplementary Figure S3.

3.5 Comparing the sensitivity of [^{18}F]FDG PET/CT and [^{18}F]FDG PET/MRI for detecting distant metastases in NSCLC

The analysis incorporated three studies, revealing a pooled sensitivity of 0.86 (95% CI: 0.60–1.00) for [^{18}F]FDG PET/CT in detecting distant metastases in NSCLC. In contrast, [^{18}F]FDG PET/

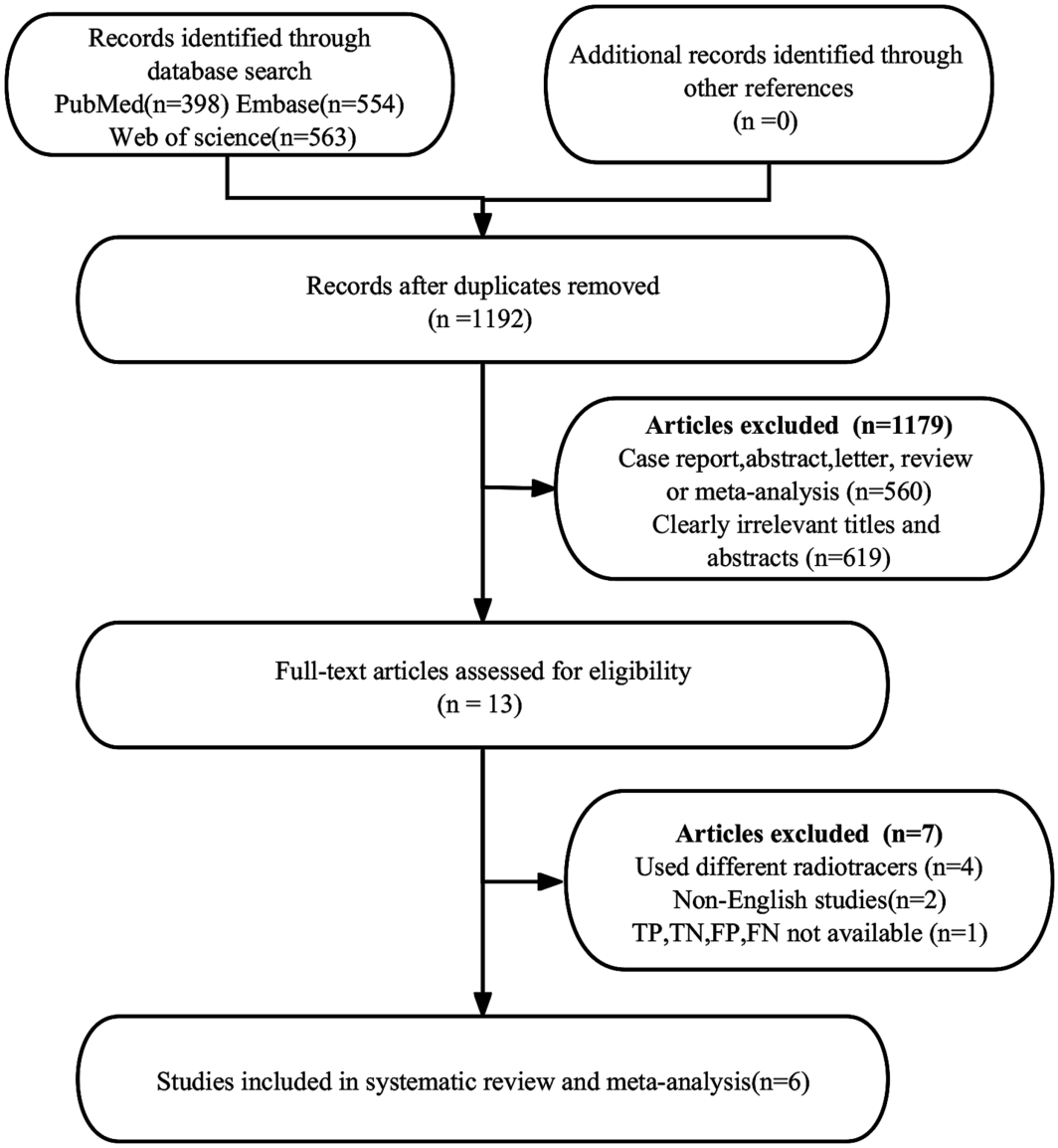

FIGURE 1
PRISMA flow diagram illustrating the study selection process.

MRI had an overall sensitivity of 0.93 (95% CI: 0.63–1.00) (Figure 5). There was no significant difference in sensitivity between [^{18}F]FDG PET/CT and [^{18}F]FDG PET/MRI (p = 0.66).

3.6 Comparing the specificity of [^{18}F]FDG PET/CT and [^{18}F]FDG PET/MRI for detecting distant metastases in NSCLC

The analysis incorporated three studies, revealing a pooled specificity of 0.89 (95% CI: 0.65–1.00) for [^{18}F]FDG PET/CT in detecting distant metastases in NSCLC. In contrast, [^{18}F]FDG PET/MRI had an overall specificity of 0.90 (95% CI: 0.64–1.00) (Figure 6). There was no significant difference in specificity between [^{18}F]FDG PET/CT and [^{18}F]FDG PET/MRI (p = 0.97).

3.7 Publication bias

Funnel plot asymmetry tests were conducted to assess publication bias in [^{18}F]FDG PET/CT and PET/MRI. For PET/CT, results indicated no significant bias for sensitivity (Egger's p = 0.33, Supplementary Figure S4) or specificity (Egger's p = 0.13, Supplementary Figure S5). For PET/MRI, significant bias was found in sensitivity (Egge's p = 0.04, Supplementary Figure S6), while specificity showed no substantial bias (Egger's p = 0.84, Supplementary Figure S7).

4 Discussion

The continuing controversy in the field of nuclear medicine regarding the comparative usefulness of [^{18}F]FDG PET/CT and [^{18}F]

TABLE 1 Study and patient characteristics of the included studies.

Author	Year	Country	Study duration	Study design	Analysis	Reference standard	No. of expert readers	No. of patients	Mean/median age
Heusch et al.	2014	Germany	NA	Pro	PB	Pathology	2	22	Mean ± SD:65.1 ± 9.1
Ohno et al.	2015	Japan	2012–2013	Pro	PB	Pathology	2	140	Mean ± SD:72.0 ± 7.4
Huellner et al.	2016	Switzerland	2012–2014	Pro	PB	Pathology and/or follow-up imaging	2	42	Median(range):65(35–89)
Lee et al.	2016	Korea	2013–2014	Pro	PB	Pathology and/or follow-up imaging	3	45	Mean ± SD:62.9 ± 9.9
Kirchner et al.	2018	Germany	NA	Pro	PB	Pathology and/or follow-up imaging	2	84	Mean ± SD:62.5 ± 9.1
Ohno et al.	2020	Japan	2014–2015	Pro	PB	Pathology and/or follow-up imaging	2	104	Mean ± SD:71.1 ± 6.3

PB patient-based; LB lesion-based; pro prospective; retro retrospective; NA not available.

TABLE 2 Technical aspects of included studies.

Author	Year, journal	Histological subtypes (percentage)	Distribution of TNM stages (percentage)	Manufacturer for PET/CT	Manufacturer and magnet strength for PET/MRI	Ligand dose	Image analysis
Heusch et al.	2014, Journal of Nuclear Medicine	Adenocarcinoma: 63.6%, Squamous cell carcinoma: 22.7%, Large cell carcinoma: 13.6%	NA	Siemens Molecular Imaging	Siemens Healthcare, Biograph mMR, 1.5 T	300 ± 45 MBq	Visual and semiquantitative
Ohno et al.	2015, Radiology	Adenocarcinoma:87.9%, Squamous cell carcinoma:9.3%, Adenosquamous cell carcinoma:2.1%, Large cell carcinoma: 0.7%	T stages: T1a 14.3%, T1b 37.1%, T2a 21.4%, T2b 14.3%, T3 7.1%, T4 5.7%; N stages: N0 55.7%, N1 24.3%, N2 11.4%, N3 8.6%; M stages: M0 88.6%, M1a 4.3%, M1b 7.1%	Aquilion 64 and One, Toshiba Medical Systems	GE Healthcare, Signa Excite XL Echospeed, 1.5 T; Philips Healthcare, Achieva 1.5 T	3.3 MBq/kg	Visual
Huellner et al.	2016, Journal of Nuclear Medicine	NA	NA	Discovery PET/CT 690 VCT; GE Healthcare	GE Healthcare, Discovery MR 750w, 1.5 T	350 MBq	Visual and semiquantitative
Lee et al.	2016, European Radiology	Adenocarcinoma: 71.1%, Squamous cell carcinoma: 17.8%, Other subtypes: 11.1%	T stages: T1 32.5%, T2 52.5%, T3 15.0%; N stages: N0 50.0%, N1 16.7%, N2 28.6%, N3 4.8%; M stages: M0 86.7%, M1 13.3%	Siemens Medical Solutions, Knoxville, TN	Siemens Healthcare, Biograph mMR, 1.5 T	5.2 MBq/kg	Visual and semiquantitative
Kirchner et al.	2018, European Journal of Nuclear Medicine and Molecular Imaging	Adenocarcinoma: 70.2%, Squamous cell carcinoma: 25.0%, Large cell carcinoma: 2.4%, Others: 2.4%	NA	Siemens Healthcare GmbH, Erlangen, Germany	Siemens Healthcare GmbH, Biograph mMR, 1.5 T	275.7 ± 47.4 MBq	Visual and semiquantitative
Ohno et al.	2020, American Journal of Roentgenology	Adenocarcinoma: 74%; Squamous cell carcinoma: 20.2%, Large cell carcinoma: 5.8%	T stages: T1 35.6%, T2 36.5%, T3 6.7%, T4 6.7%; N stages: N0 60.6%, N1 15.4%, N2 13.5%, N3 10.6%; M stages: M0 87.5%, M1 12.5%	Discovery ST Elite Performance, GE Healthcare	Canon Medical Systems, Vantage Titan 3 T	3.3 MBq/kg	Visual

NA not available; T primary tumor; N lymph node metastasis; M distant metastasis.

FDG PET/MRI in the assessment of lymph node and distant metastases in NSCLC requires a comprehensive meta-analysis (20, 22, 23). This analysis is critical for elucidating the diagnostic accuracy of these modalities, thereby informing clinical decision-making.

Our meta-analysis incorporated six studies to compare these imaging techniques. We discovered that [^{18}F]FDG PET/CT had a pooled sensitivity of 0.82 and specificity of 0.88 in identifying lymph node metastases, whereas [^{18}F]FDG PET/MRI had a

TABLE 3 Summary of 2×2 contingency table for diagnostic performance for N and M staging using [^{18}F]FDG PET/CT and [^{18}F]FDG PET/MRI.

Author	Modality	N staging				M staging				Total patients
		TP (No. patients)	FP (no. patients)	FN (no. patients)	TN (no. patients)	TP (no. patients)	FP (no. patients)	FN (no. patients)	TN (no. patients)	
Heusch et al. (30)	[^{18}F]FDG PET/CT	6	2	2	12	NA	NA	NA	NA	22
	[^{18}F]FDG PET/MRI	7	1	1	13	NA	NA	NA	NA	22
Ohno et al. (31)	[^{18}F]FDG PET/CT	105	4	7	24	115	4	9	12	140
	[^{18}F]FDG PET/MRI	112	2	0	36	124	2	0	14	140
Huellner et al. (32)	[^{18}F]FDG PET/CT	14	3	1	24	10	3	5	24	42
	[^{18}F]FDG PET/MRI	11	6	1	24	9	9	3	21	42
Lee et al. (23)	[^{18}F]FDG PET/CT	10	14	6	12	8	11	7	16	42
	[^{18}F]FDG PET/MRI	3	0	3	39	5	0	1	39	45
Kirchner et al. (33)	[^{18}F]FDG PET/CT	42	1	5	36	NA	NA	NA	NA	84
	[^{18}F]FDG PET/MRI	42	2	5	35	NA	NA	NA	NA	84
Ohno et al. (34)	[^{18}F]FDG PET/CT	23	3	18	60	NA	NA	NA	NA	104
	[^{18}F]FDG PET/MRI	33	8	8	55	NA	NA	NA	NA	104

TP true positive; TN true negative; FP false positive; FN false positive; N lymph node metastasis; M distant metastasis; NA not available.

sensitivity of 0.86 and specificity of 0.90, with no significant differences identified. Similarly, in identifying distant metastases, [^{18}F]FDG PET/CT had a sensitivity of 0.86 and specificity of 0.89, whereas [^{18}F]FDG PET/MRI had a sensitivity of 0.93 and specificity of 0.90, with no significant differences found. The slightly higher sensitivity of PET/MRI may be attributed to its superior soft tissue contrast provided by MRI, which enables better differentiation between tissues, especially in complex anatomical areas such as the lungs and lymph nodes (35). Unlike PET/CT, which uses X-ray imaging, MRI offers much higher resolution for soft tissue, allowing for more accurate detection of small or ambiguous lesions (36). However, the overlapping confidence intervals suggest that these differences might not be clinically significant.

Compared to the previous studies by Mojahed et al. (37) and Zhang et al. (35), which evaluated the diagnostic accuracy of [^{18}F]FDG PET/CT versus [^{18}F]FDG PET/MRI in T and N staging, our analysis reveals equivalent effectiveness of these modalities in detecting N and M stages in NSCLC patients. However, unlike Mojahed et al. and Zhang et al., we included evaluations of distant metastases, a crucial aspect of NSCLC staging. In addition to building on the previous analyses, our meta-analysis incorporates four new studies (23, 31, 32, 34), particularly those focusing on M stage (distant metastasis) assessment (23, 31, 32). This addition provides a more comprehensive understanding of [18F]FDG PET/MRI's capabilities, addressing both nodal and metastatic assessments in NSCLC staging.

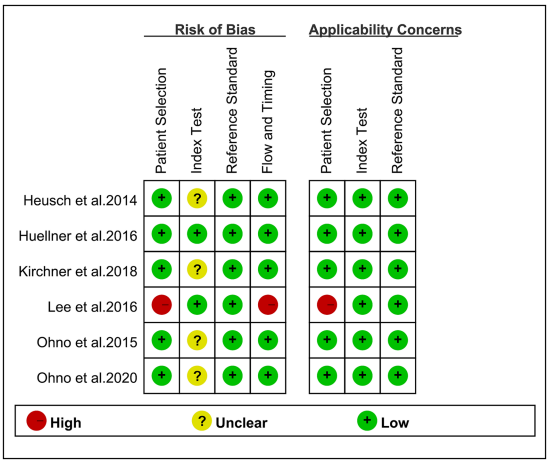

FIGURE 2
Risk of bias and applicability concerns of the included studies using the quality assessment of diagnostic performance studies QUADAS-2 tool.

Zhang et al.'s (21) meta-analysis included 14 papers, five of which focused on lung cancer. In an analysis of five lung cancer trials including 429 patients, [^{18}F]FDG PET/CT exhibited better sensitivity

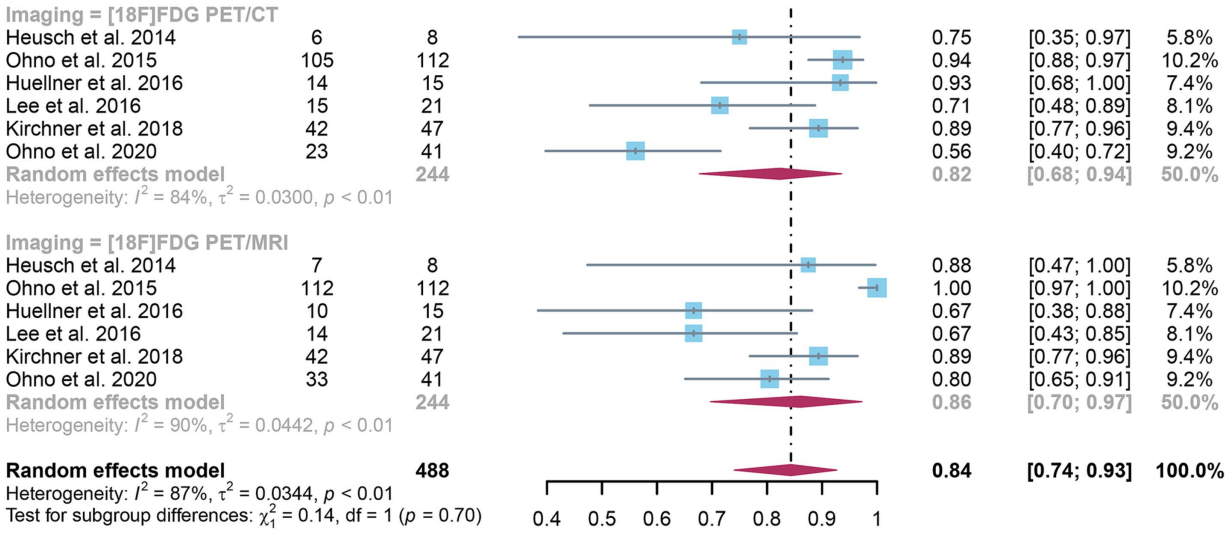

FIGURE 3
Forest plot of sensitivity comparison between [18F]FDG PET/CT and [18F]FDG PET/MRI in detecting lymph node metastasis in non-small cell lung cancer.

TABLE 4 Subgroup and meta-regression analysis of lymph node metastasis detection for [18F]FDG PET/CT.

Covariate	Studies, *n*	Sensitivity (95%CI)	*p*-value	Specificity (95%CI)	*P*-value
Reference standard			0.49		0.78
Pathology	2	0.90[0.66–1.00]		0.86[0.73–0.95]	
Pathology and/or follow-up imaging	4	0.79[0.60–0.93]		0.88[0.69–0.99]	
Race			0.55		0.46
White	3	0.90(0.81–0.97)		0.93[0.83–0.99]	
Yellow	3	0.77(0.49–0.96)		0.83[0.57–0.99]	
Image analysis			0.83		0.55
Visual and semiquantitative	4	0.86(0.78–0.93)		0.88(0.80–0.94)	
Visual	2	0.86(0.80–0.92)		0.93(0.86–0.98)	

TABLE 5 Subgroup and meta-regression analysis of lymph node metastasis detection for [18F]FDG PET/MRI.

Covariate	Studies, *n*	Sensitivity (95%CI)	*P*-value
Reference standard			0.01
Pathology	2	0.99[0.74–1.00]	
Pathology and/or follow-up imaging	4	0.79[0.66–0.89]	
Race			0.70
White	3	0.84[0.67–0.96]	
Yellow	3	0.88[0.58–1.00]	
Image analysis			0.22
Visual and semiquantitative	4	0.82[0.73–0.90]	
Visual	2	0.98[0.95–1.00]	

(0.87 vs. 0.84) and slightly worse specificity (0.95 vs. 0.96) than PET/MRI. In contrast, our meta-analysis found that [18F]FDG PET/MRI had similar sensitivity and specificity to [18F]FDG PET/CT in detecting lymph nodes and distant metastases in NSCLC patients. The discrepancy may stem from several factors. One key reason could be that Zhang et al.'s meta-analysis included patients with small cell lung cancer in addition to those with NSCLC. Small cell lung cancer generally presents with different patterns of lymph node and metastatic involvement compared to NSCLC, which may affect the diagnostic performance of [18F]FDG PET/CT and PET/MRI.

While PET/CT and PET/MRI modalities offer similar diagnostic efficacy, their cost and accessibility differ markedly, influencing their clinical integration. PET/CT, significantly more affordable, emerges as a cost-effective solution for healthcare providers (38). Its broader availability enhances its utility across diverse medical environments, proving especially advantageous in areas lacking advanced medical infrastructure. In instances where both techniques yield comparable sensitivity and

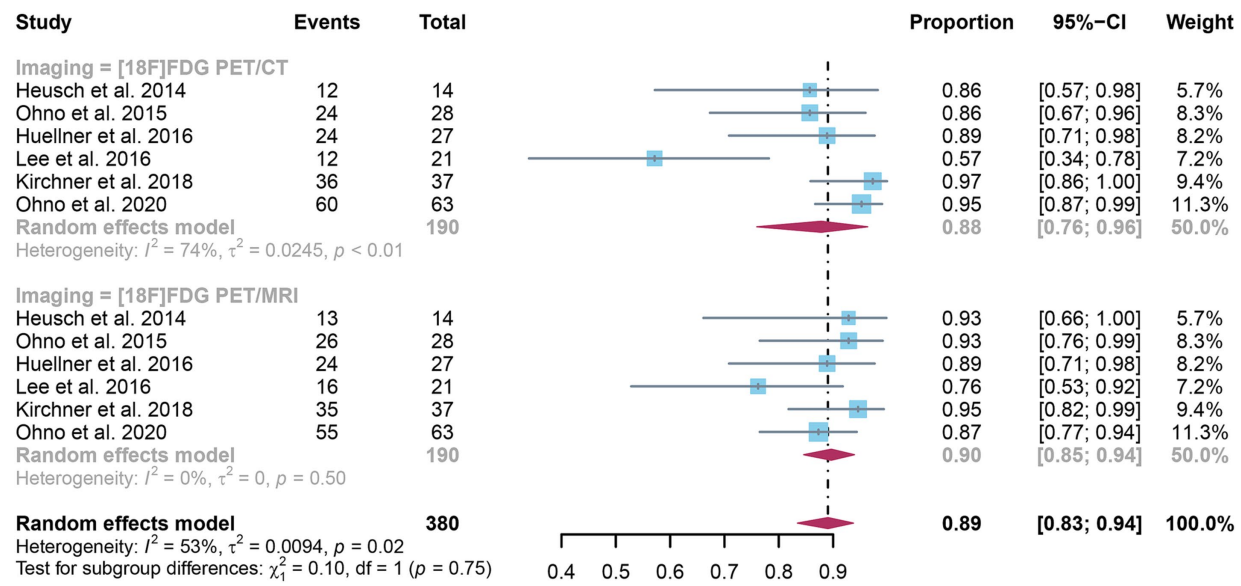

FIGURE 4
Forest plot of specificity comparison between [18F]FDG PET/CT and [18F]FDG PET/MRI in detecting lymph node metastasis in non-small cell lung cancer.

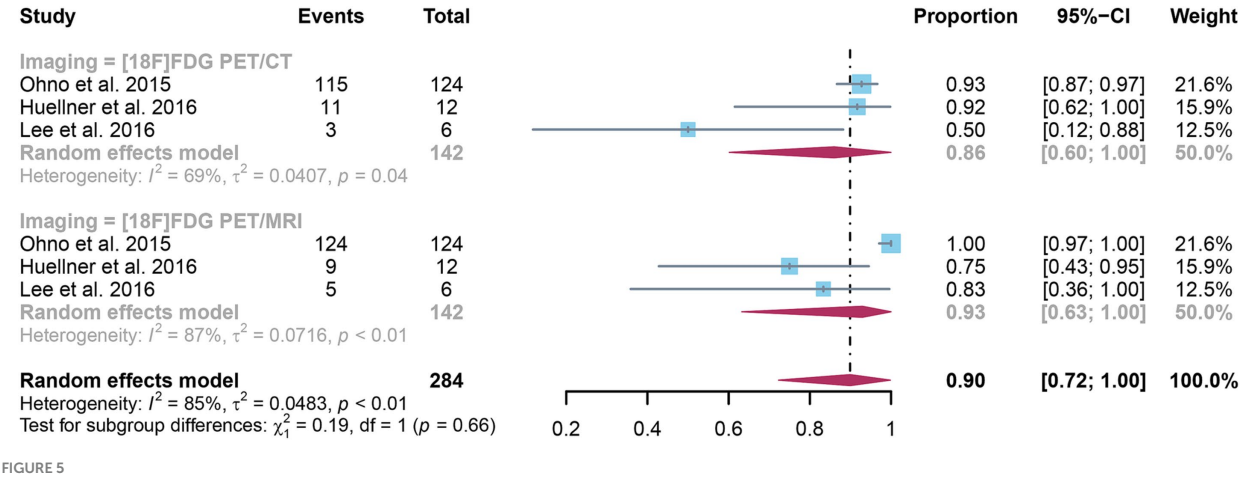

FIGURE 5
Forest plot of sensitivity comparison between [18F]FDG PET/CT and [18F]FDG PET/MRI in detecting distant metastasis in non-small cell lung cancer.

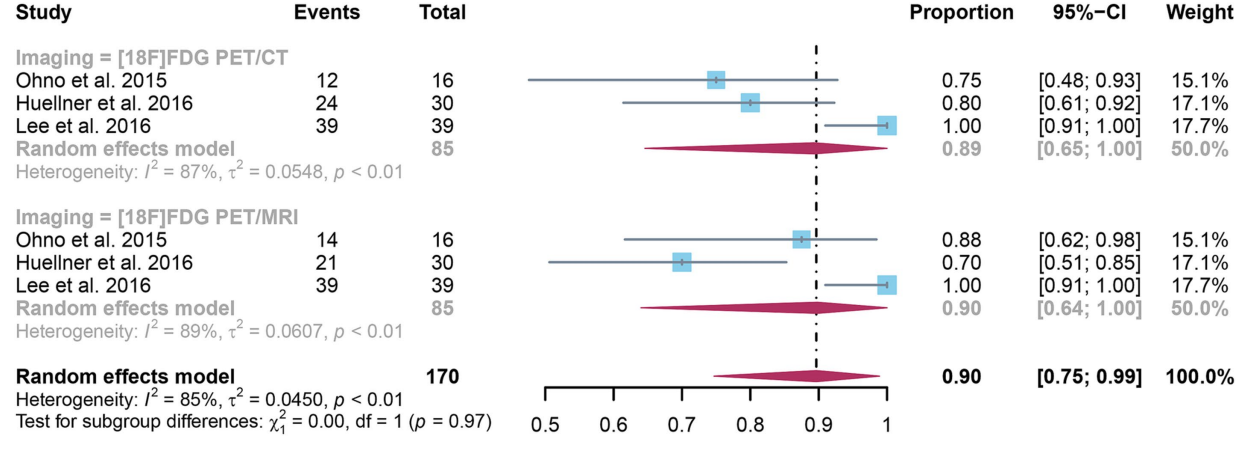

FIGURE 6
Forest plot of specificity comparison between [18F]FDG PET/CT and [18F]FDG PET/MRI in detecting distant metastasis in non-small cell lung cancer.

specificity, PET/CT is frequently the preferred option. This preference stems not only from its cost-efficiency and wider accessibility, which promote extensive use, but also from its role in fostering more equitable healthcare access, particularly in under-resourced regions. Thus, balancing sophisticated diagnostic capabilities for practicalities such as affordability and accessibility, PET/CT distinctly outperforms when both modalities present equivalent diagnostic outcomes (36). A comprehensive comparison of the pros and cons of both imaging modalities is detailed in Supplementary Table S2.

Our study has some limitations. The inclusion of only six studies, and our analysis limited by the lack of detailed diagnostic performance data for different organ sites of metastasis, suggests a need for more extensive research in this area. Additionally, not all patients underwent pathological biopsy, some diagnoses were based on a combination of biopsy and clinical imaging follow-up. Future research should focus on studies using pathology as the sole gold standard to further validate these findings.

5 Conclusion

Our meta-analysis shows that [^{18}F]FDG PET/MRI has similar sensitivity and specificity to [^{18}F]FDG PET/CT in identifying lymph node and distant metastases in patients with NSCLC. Additional larger sample prospective studies are needed to confirm these findings.

Data availability statement

The original contributions presented in the study are included in the article/Supplementary material, further inquiries can be directed to the corresponding author.

Author contributions

DY: Conceptualization, Data curation, Formal analysis, Methodology, Software, Writing – original draft, Writing – review & editing. CC: Conceptualization, Methodology, Project administration, Software, Writing – original draft, Writing – review & editing.

Funding

The author(s) declare that no financial support was received for the research, authorship, and/or publication of this article.

Conflict of interest

The authors declare that the research was conducted in the absence of any commercial or financial relationships that could be construed as a potential conflict of interest.

Generative AI statement

The author(s) declare that no Gen AI was used in the creation of this manuscript.

Publisher's note

Supplementary material

The Supplementary material for this article can be found online at: https://www.frontiersin.org/articles/10.3389/fmed.2024.1517805/full#supplementary-material

References

1. Li C, Lei S, Ding L, Xu Y, Wu X, Wang H, et al. Global burden and trends of lung cancer incidence and mortality. *Chin Med J*. (2023) 136:1583–90. doi: 10.1097/cm9.0000000000002529

2. Bray F, Laversanne M, Sung H, Ferlay J, Siegel RL, Soerjomataram I, et al. Global cancer statistics 2022: GLOBOCAN estimates of incidence and mortality worldwide for 36 cancers in 185 countries. *CA Cancer J Clin*. (2024) 74:229–63. doi: 10.3322/caac.21834

3. Barta JA, Powell CA, Wisnivesky JP. Global epidemiology of lung Cancer. *Ann glob. Health*. (2019) 85, 1–16. doi: 10.5334/aogh.2419

4. Abdo M, Belloum Y, Heigener D, Welker L, von Weihe S, Schmidt M, et al. Comparative evaluation of PD-L1 expression in cytology imprints, circulating tumour cells and tumour tissue in non-small cell lung cancer patients. *Mol Oncol*. (2023) 17:737–46. doi: 10.1002/1878-0261.13415

5. Hendriks LE, Remon J, Faivre-Finn C, Garassino MC, Heymach JV, Kerr KM, et al. Non-small-cell lung cancer. *Nat Rev Dis Prim*. (2024) 10:71. doi: 10.1038/s41572-024-00551-9

6. Bi JH, Tuo JY, Xiao YX, Tang DD, Zhou XH, Jiang YF, et al. Observed and relative survival trends of lung cancer: a systematic review of population-based cancer registration data. *Thoracic Cancer*. (2024) 15:142–51. doi: 10.1111/1759-7714.15170

7. Owens C, Hindocha S, Lee R, Millard T, Sharma B. The lung cancers: staging and response, CT, (18)F-FDG PET/CT, MRI, DWI: review and new perspectives. *Br J Radiol*. (2023) 96:20220339. doi: 10.1259/bjr.20220339

8. Amicizia D, Piazza MF, Marchini F, Astengo M, Grammatico F, Battaglini A, et al. Systematic review of lung cancer screening: advancements and strategies for implementation. *Healthcare*. (2023), 11. doi: 10.3390/healthcare11142085

9. Silvestri GA, Gonzalez AV, Jantz MA, Margolis ML, Gould MK, Tanoue LT, et al. Methods for staging non-small cell lung cancer: diagnosis and management of lung cancer, 3rd ed: American College of Chest Physicians evidence-based clinical practice guidelines. *Chest*. (2013) 143:e211S–50S. doi: 10.1378/chest.12-2355

10. Kim TJ, Kim CH, Lee HY, Chung MJ, Shin SH, Lee KJ, et al. Management of incidental pulmonary nodules: current strategies and future perspectives. *Expert Rev Respir Med*. (2020) 14:173–94. doi: 10.1080/17476348.2020.1697853

11. Sabatino V, Russo U, D'Amuri F, Bevilacqua A, Pagnini F, Milanese G, et al. Pneumothorax and pulmonary hemorrhage after CT-guided lung biopsy: incidence, clinical significance and correlation. *Radiol Med*. (2021) 126:170–7. doi: 10.1007/s11547-020-01211-0

12. Nour-Eldin NE, Alsubhi M, Naguib NN, Lehnert T, Emam A, Beeres M, et al. Risk factor analysis of pulmonary hemorrhage complicating CT-guided lung biopsy in coaxial and non-coaxial core biopsy techniques in 650 patients. *Eur J Radiol*. (2014) 83:1945–52. Epub 2014/07/27. doi: 10.1016/j.ejrad.2014.06.023

13. Philip B, Jain A, Wojtowicz M, Khan I, Voller C, Patel RSK, et al. Current investigative modalities for detecting and staging lung cancers: a comprehensive summary. *Indian J Thorac Cardiovasc Surg*. (2023) 39:42–52. doi: 10.1007/s12055-022-01430-2

14. Zhu J, Pan F, Cai H, Pan L, Li Y, Li L, et al. Positron emission tomography imaging of lung cancer: an overview of alternative positron emission tomography tracers beyond F18 fluorodeoxyglucose. *Front Med (Lausanne)*. (2022) 9:945602. doi: 10.3389/fmed.2022.945602

15. Yap JT, Carney JP, Hall NC, Townsend DW. Image-guided cancer therapy using PET/CT. *Cancer J*. (2004) 10:221–33. doi: 10.1097/00130404-200407000-00003

16. Gao SJ, Kim AW, Puchalski JT, Bramley K, Detterbeck FC, Boffa DJ, et al. Indications for invasive mediastinal staging in patients with early non-small cell lung cancer staged with PET-CT. *Lung Cancer*. (2017) 109:36–41. doi: 10.1016/j.lungcan.2017.04.018

17. Riely GJ, Wood DE, Ettinger DS, Aisner DL, Akerley W, Bauman JR, et al. Non–small cell lung Cancer, version 4.2024, NCCN clinical practice guidelines in oncology. *J Natl Compr Cancer Netw*. (2024) 22:249–74. doi: 10.6004/jnccn.2204.0023

18. Farsad M. FDG PET/CT in the staging of lung Cancer. *Curr Radiopharm*. (2020) 13:195–203. doi: 10.2174/1874471013666191223153755

19. Schaarschmidt BM, Grueneisen J, Metzenmacher M, Gomez B, Gauler T, Roesel C, et al. Thoracic staging with (18)F-FDG PET/MR in non-small cell lung cancer—does it change therapeutic decisions in comparison to (18)F-FDG PET/CT? *Eur Radiol*. (2017) 27:681–8. doi: 10.1007/s00330-016-4397-0

20. Dahlsgaard-Wallenius SE, Hildebrandt MG, Johansen A, Vilstrup MH, Petersen H, Gerke O, et al. Hybrid PET/MRI in non-small cell lung cancer (NSCLC) and lung nodules-a literature review. *Eur J Nucl Med Mol Imaging*. (2021) 48:584–91. doi: 10.1007/s00259-020-04955-z

21. Zhang C, Liang Z, Liu W, Zeng X, Mo Y. Comparison of whole-body 18F-FDG PET/CT and PET/MRI for distant metastases in patients with malignant tumors: a meta-analysis. *BMC Cancer*. (2023) 23:37. doi: 10.1186/s12885-022-10493-8

22. Fraioli F, Screaton NJ, Janes SM, Win T, Menezes L, Kayani I, et al. Non-small-cell lung cancer resectability: diagnostic value of PET/MR. *Eur J Nucl Med Mol Imaging*. (2015) 42:49–55. doi: 10.1007/s00259-014-2873-9

23. Lee SM, Goo JM, Park CM, Yoon SH, Paeng JC, Cheon GJ, et al. Preoperative staging of non-small cell lung cancer: prospective comparison of PET/MR and PET/CT. *Eur Radiol*. (2016) 26:3850–7. doi: 10.1007/s00330-016-4255-0

24. Mayerhoefer ME, Prosch H, Beer L, Tamandl D, Beyer T, Hoeller C, et al. PET/MRI versus PET/CT in oncology: a prospective single-center study of 330 examinations focusing on implications for patient management and cost considerations. *Eur J Nucl Med Mol Imaging*. (2020) 47:51–60. doi: 10.1007/s00259-019-04452-y

25. Popper HH. Progression and metastasis of lung cancer. *Cancer Metastasis Rev*. (2016) 35:75–91. doi: 10.1007/s10555-016-9618-0

26. Milovanovic IS, Stjepanovic M, Mitrovic D. Distribution patterns of the metastases of the lung carcinoma in relation to histological type of the primary tumor: an autopsy study. *Ann Thorac Med*. (2017) 12:191–8. doi: 10.4103/atm.ATM_276_16

27. McInnes MDF, Moher D, Thombs BD, McGrath TA, Bossuyt PM, Clifford T, et al. Preferred reporting items for a systematic review and Meta-analysis of diagnostic test accuracy studies: the PRISMA-DTA statement. *JAMA*. (2018) 319:388–96. doi: 10.1001/jama.2017.19163

28. Whiting PF, Rutjes AW, Westwood ME, Mallett S, Deeks JJ, Reitsma JB, et al. QUADAS-2: a revised tool for the quality assessment of diagnostic accuracy studies. *Ann Intern Med*. (2011) 155:529–36. doi: 10.7326/0003-4819-155-8-201110180-00009

29. Higgins JP, Thompson SG. Quantifying heterogeneity in a meta-analysis. *Stat Med*. (2002) 21:1539–58. doi: 10.1002/sim.1186

30. Heusch P, Buchbender C, Köhler J, Nensa F, Gauler T, Gomez B, et al. Thoracic staging in lung cancer: prospective comparison of 18F-FDG PET/MR imaging and 18F-FDG PET/CT. *J Nucl Med*. (2014) 55:373–8. doi: 10.2967/jnumed.113.129825

31. Ohno Y, Koyama H, Yoshikawa T, Takenaka D, Seki S, Yui M, et al. Three-way comparison of whole-body MR, Coregistered whole-body FDG PET/MR, and integrated whole-body FDG PET/CT imaging: TNM and stage assessment capability for non-small cell lung Cancer patients. *Radiology*. (2015) 275:849–61. doi: 10.1148/radiol.14140936

32. Huellner MW, de Galiza BF, Husmann L, Pietsch CM, Mader CE, Burger IA, et al. TNM staging of non-small cell lung Cancer: comparison of PET/MR and PET/CT. *J Nucl Med*. (2016) 57:21–6. doi: 10.2967/jnumed.115.162040

33. Kirchner J, Sawicki LM, Nensa F, Schaarschmidt BM, Reis H, Ingenwerth M, et al. Prospective comparison of (18)F-FDG PET/MRI and (18)F-FDG PET/CT for thoracic staging of non-small cell lung cancer. *Eur J Nucl Med Mol Imaging*. (2019) 46:437–45. doi: 10.1007/s00259-018-4109-x

34. Ohno Y, Takeshi Y, Takenaka D, Koyama H, Aoyagi K, Yui M. Comparison of diagnostic accuracy for TNM stage among whole-body MRI and Coregistered PET/MRI using 1.5-T and 3-T MRI systems and integrated PET/CT for non-small cell lung Cancer. *AJR Am J Roentgenol*. (2020) 215:1191–8. doi: 10.2214/ajr.19.22565

35. Zhang M, Liu Z, Yuan Y, Yang W, Cao X, Ma M, et al. Head-to-head comparison of 18F-FDG PET/CT and 18F-FDG PET/MRI for lymph node metastasis staging in non-small cell lung cancer: a meta-analysis. *Diagn Interv Radiol*. (2024) 30:99–106. doi: 10.4274/dir.2023.232280

36. Weber W. Clinical PET/MR. *Recent Results Cancer Res*. (2020) 216:747–64. doi: 10.1007/978-3-030-42618-7_22

37. Shahraki Mojahed B, Saravani K, Parooie F. Thoracic staging in patients with non-small cell lung cancer: a systematic review and meta-analysis on diagnostic accuracy of [^{18}F]FDG PET/MRI and [^{18}F]FDG PET/CT. *Nucl Med Rev Cent East Eur*. (2022) 26:11–9. doi: 10.5603/NMR.a2022.0037

38. Evangelista L, Cuocolo A, Pace L, Mansi L, Del Vecchio S, Miletto P, et al. Performance of FDG-PET/CT in solitary pulmonary nodule based on pre-test likelihood of malignancy: results from the ITALIAN retrospective multicenter trial. *Eur J Nucl Med Mol Imaging*. (2018) 45:1898–907. doi: 10.1007/s00259-018-4016-1

frontiers | Frontiers in Medicine

TYPE Original Research
PUBLISHED 10 February 2025
DOI 10.3389/fmed.2024.1511710

OPEN ACCESS

EDITED BY
Nataliya Lutay,
Skåne University Hospital, Sweden

REVIEWED BY
Emmanouil Magiorkinis,
Athens Chest Hospital Sotiria, Greece
Franca Chierichetti,
Azienda Provinciale per i Servizi Sanitari (APSS), Italy

*CORRESPONDENCE
Na Du
✉ du_na@jlu.edu.cn
Hongguang Zhao
✉ zhaohg@jlu.edu.cn

RECEIVED 15 October 2024
ACCEPTED 16 December 2024
PUBLISHED 10 February 2025

CITATION
Yu X, Wang S, Du N, Zhao H and Chen H (2025) Diagnostic efficacy and necessity of 18F-FDG PET/CT in fever of unknown origin: insights from a retrospective cohort study.
Front. Med. 11:1511710.
doi: 10.3389/fmed.2024.1511710

Diagnostic efficacy and necessity of 18F-FDG PET/CT in fever of unknown origin: insights from a retrospective cohort study

Xiaoman Yu[1], Shuang Wang[1], Na Du[1]*, Hongguang Zhao[2]* and Haiying Chen[1]

[1]Department of Infectious Diseases, The First Affiliated Hospital of Jilin University, Changchun, China, [2]Department of Nuclear Medicine, The First Hospital of Jilin University, Changchun, China

Background: Despite advancements in medical examination equipment and techniques, fever of unknown origin (FUO) remains challenging in internal medicine.

Purpose: This study evaluates the diagnostic efficacy and necessity of 18F-fluorodeoxyglucose positron emission tomography/computed tomography (18F-FDG PET/CT) in patients with FUO.

Methods: We retrospectively analyzed the results of 18F-FDG PET/CT in a cohort of 284 patients with FUO admitted to the Department of Infection at the First Hospital of Jilin University between January 2018 and March 2024. All patients received a final clinical diagnosis after various treatments, which helped determine the diagnostic relevance of identified lesions using 18F-FDG PET/CT. Additionally, univariate and multivariate logistic regression analyses were performed to evaluate the predictive value of relevant laboratory indices on the true-positive results of 18F-FDG PET/CT. The diagnostic performance for different etiologies of FUO was assessed by calculating the area under the receiver operating characteristic curve.

Results: Of the 284 enrolled patients, infectious diseases were diagnosed in 53 (18.7%), non-infectious inflammatory diseases in 76 (26.8%), malignant tumors in 66 (23.2%), and 89 (31.3%) remained undiagnosed. The final diagnoses of 136 patients (47.9%) correlated with their 18F-FDG PET/CT results, yielding a sensitivity of 79.5%, specificity of 61.1%, positive predictive value of 75.6%, and negative predictive value of 66.3%. Furthermore, a correlation was found between localized pain, prolonged activated partial thromboplastin time, and true-positive 18F-FDG PET/CT results.

Conclusion: The high diagnostic efficacy of 18F-FDG PET/CT in FUO suggests its potential as a routine imaging modality, which could enhance patient management and reduce the need for costly and unnecessary invasive procedures. The identification of clinical factors that are predictive of true-positive diagnosis could facilitate more effective allocation of PET/CT imaging.

KEYWORDS

fever of unknown origin (FUO), 18F-FDG PET/CT, diagnostic value, image analysis, final diagnosis

1 Introduction

Fever of unknown origin (FUO) was first defined in 1961 by Petersdorf and Beeson as a recurrent fever exceeding 38.3°C, persisting for more than 3 weeks, and remaining undiagnosed after at least 1 week of hospitalization" (1). In 1991, Durack and Street revised these criteria to "include recurrent fevers above 38.3°C lasting over 3 weeks, which remain undiagnosed following either a three-day inpatient stay or 3 outpatient visits" (2). Currently, FUO is defined by (1) at least two episodes of fever ≥38.3°C (≥ 101°F), (2) an illness duration of ≥ 3 weeks, or multiple fever episodes within this timeframe; and (3) the absence of any known immunocompromised state (excluding patients with nosocomial infections, known HIV infections, or other immune-compromised conditions); (4) despite comprehensive history taking, physical examinations, and relevant testing, the diagnosis remains elusive (3).

Currently, more than 200 causes of FUO (50) are identified. Differential diagnosis traditionally categorizes these into four types: infectious diseases, non-infectious inflammatory diseases (NIID), malignant tumors, and miscellaneous causes. With advances in examination techniques, the precision of instruments, and broader scientific knowledge, the proportion of FUO cases attributed to infections and malignant tumors has decreased. Nonetheless, the rate of undiagnosed FUO cases in various studies still ranges from 7 to 53% (4).

FUO continues to pose significant challenges in internal medicine, often due to undetectable molecular, cellular, or microbial abnormalities in a patient's blood or body fluids. While traditional non-invasive imaging tests such as X-rays, ultrasound, computed tomography (CT), and magnetic resonance imaging (MRI) can identify localized lesions, they may fall short in detecting early-stage diseases that exhibit primarily metabolic rather than anatomical changes. Therefore, these conventional imaging methods frequently lack accuracy in early-stage infections, inflammatory conditions, or patients with unaltered anatomy due to the disease process (5). Contrarily, 18F-FDG, a glucose analog, behaves similarly to glucose in the bloodstream and tissues, entering cells via GLU-1 to GLU-5 transporter proteins on the cell membrane. Once inside the cell, phosphorylated 18F-FDG cannot be further metabolized and thus remains trapped. Crucially, 18F-FDG uptake is not exclusive to tumor cells; it also occurs in all activated leukocytes (granulocytes, lymphocytes, and monocytes), which enables the imaging of both acute and chronic inflammatory processes (6). 18F-FDG PET can detect disease activity at the cellular and even molecular levels before morphological changes occur, and it can differentiate between active and inactive disease states, as well as distinguish between infections and sterile inflammatory or malignant tumors (7).

Following the introduction of PET/CT, integrating metabolic pathophysiological data with anatomical-pathological information from CT has significantly enhanced clinical disease diagnosis, improved anatomical resolution, and increased the accuracy of 18F-FDG PET (8). In clinical practice, 18F-FDG PET/CT is instrumental in diagnosing patients with FUO, offering high accuracy, sensitivity, resolution, and a brief interval between injection and imaging time (3, 9, 10).

For patients with FUO, enduring fever without identifying a specific cause imposes a significant economic burden and psychological strain. Therefore, timely diagnosis and appropriate treatment are crucial for improving the prognosis of patients with FUO.

2 Materials and methods

2.1 Patient population

In this study, we conducted a comprehensive search of the clinical database at the First Affiliated Hospital of Jilin University for patients with FUO who were admitted to the Department of Infectious Diseases and underwent 18F-FDG PET/CT scans between January 2018 and March 2024. All included patients met the current criteria for FUO, and despite exhaustive investigations—including detailed history taking, physical examination, and relevant laboratory testing—the cause of the fever remained undetermined. The laboratory tests conducted included routine blood and urine analysis, culture of various body fluids, measurement of ultrasensitive C-reactive protein and calcitoninogen levels, erythrocyte count determination, testing for EBV and cytomegalovirus antibodies or nucleic acids, rubella virus antibody and toxoplasmosis antibody testing, brucella agglutination tests, HIV tests, testing for *Mycobacterium tuberculosis* and non-tuberculosis mycobacteria, tuberculosis T-spot testing, and parasitic worm antibody and egg testing. Additional diagnostics included anti-nuclear and anti-neutrophil antibody screening, cyclic citrullinated peptide antibody testing, anti-cardiac phospholipid antibody screening, bone marrow smears, immunohistochemical examination, and imaging tests such as X-ray, ultrasound, CT, and MRI.

Ultimately, 284 patients were enrolled. We retrospectively analyzed the 18F-FDG PET/CT findings and clinicopathological data of these patients. All patients were followed for at least 3 months to establish a definitive diagnosis. Consistent with prior studies and consensus, symptoms of the disease typically manifest within this timeframe; hence, only diagnoses made within 3 months (11) post-18F-FDG PET/CT were deemed pertinent to the findings. The Regional Ethics Committee of the First Hospital of Jilin University approved this study (2024-1133). Given its retrospective nature, informed consent from the patients was deemed unnecessary.

2.2 18F-FDG PET/CT imaging

Patients were instructed to adhere to a high-fat, low-carbohydrate diet and fast for a minimum of 6 h before undergoing 18F-FDG PET/CT, ensuring glucose levels were below 11.1 mmol/L before administering the radiotracer. For those with cardiovascular implantable electronic devices or prosthetic heart valves, where cardiac infection is suspected to cause FUO, a specific preparatory regimen was initiated to inhibit glucose metabolism in cardiomyocytes. This involved starting a high-fat, low-carbohydrate diet 3 days before imaging (4).

An intravenous injection of 3.7 MBq/KG of 18F-FDG was administered 60 min before scanning, using an integrated PET/CT scanner (Siemens Biograph 16 HR, 2 min/bed). The scanning protocol covered from head to mid-thigh, with additional lower extremity scans performed as clinically necessary.

2.3 18F-FDG PET/CT image analysis

All 18F-FDG PET/CT images were reviewed by at least one experienced nuclear medicine physician and one radiologist, both familiar with the clinical data. A positive result was defined as 18F-FDG uptake intensity exceeding the physiologic biodistribution of the radiopharmaceutical in any anatomical structure not attributable to physiologic processes. Negative results indicated 18F-FDG uptake of only physiologic significance, with no pathological findings on CT images. Scans deemed inconclusive were reassessed by another nuclear medicine physician blind to the original image interpretation, the patient's clinical history, and all associated laboratory and microbiological data.

2.4 Diagnostic reference criteria

The final diagnosis of a patient with fever of FUO relies not solely on the results of 18F-FDG PET/CT but on an integrative analysis encompassing various laboratory tests conducted during hospitalization, microbiological cultures, other imaging modalities, biopsies of pathological tissues, the empirical judgment of the clinician, and at least 3 months of clinical follow-up. The diagnostic efficacy of 18F-FDG PET/CT is assessed according to these multifaceted criteria.

When abnormal 18F-FDG uptake in organs or tissues correlates with clinical, imaging, and histopathological findings confirming it as the cause of the fever, it is classified as a "True Positive" (TP). Conversely, if the uptake is deemed unrelated to the fever's cause or if the cause remains unidentified during follow-up, it is categorized as a "False Positive" (FP).

A "True Negative" (TN) classification is assigned when there is no abnormal 18F-FDG uptake, and one of the following conditions is met: the cause of the fever remains undetected after at least 3 months of clinical follow-up, the fever resolves spontaneously without specific treatment, or the patient succumbs to another illness unrelated to the fever.

Conversely, a "False Negative" (FN) is recorded when an infection, malignancy, or other disease is identified as the fever's cause within the three-month follow-up, the fever persists beyond the follow-up period, or if the patient dies from FUO without a definitive diagnosis.

2.5 Data analysis

The data collected for this study were organized, tabulated, and analyzed using SPSS 27.0 (Statistical Product and Service Solutions) software. The diagnostic performance of 18F-FDG PET/CT for identifying active disease—including sensitivity, specificity, accuracy, positive predictive value (PPV), and negative predictive value (NPV)—was calculated based on standard definitions. Count data were represented as [*n* (%)]; Receiver operating characteristic (ROC) curve analysis was conducted using Medcalc software, with subsequent plotting of ROC curves. The DeLong test evaluated differences in the AUC between the new and existing models.

Additionally, factors such as age, gender, medical history, duration of fever, and various laboratory test results were analyzed as independent variables, with 18F-FDG PET/CT outcomes as the dependent variables. These outcomes were classified into two categories: true positive and non-true positive (encompassing false positive, false negative, or true negative). Odds ratios (OR) and 95% CI were computed for these classifications. A *p*-value of less than 0.05 was considered to indicate statistical significance.

Variables exhibiting a *p*-value of 0.10 or less in univariate analysis were further included in stepwise multivariate logistic regression models to refine the predictive accuracy. The significance level for tests was set at $\alpha = 0.05$, where $p < 0.05$ indicated a statistically significant difference.

3 Results

3.1 Patient characteristics and final diagnosis

This study included 284 subjects, comprising 149 males (52.5%) and 135 females (47.5%). Fifteen patients (5.3%) had positive blood cultures, and four patients (1.4%) succumbed to their conditions. Most of 208 out of 284 patients (73.2%) received empirical antibiotic treatment, while 34 patients (12.0%) were treated with glucocorticoids before undergoing 18F-FDG PET/CT. Subsequent adjustments to the treatment regimen were made for 125 patients (44.0%) based on the PET/CT results. Age distribution was represented by a quartile range of 63 years (interquartile range: 47.25 to 69 years), hospitalization duration was 12 days (interquartile range: 8 to 16), duration of intermittent fever prior to admission was 25 days (interquartile range: 18.25, 40), and the peak temperature during fever episodes was 39°C (interquartile range: 38.7 to 39.5°C). The main demographic and clinical characteristics of the patients included in this study are summarized in Table 1.

TABLE 1 Basic information about the research subjects.

Characteristic	Categorization	[*n* (%), *M* (P_{25}, P_{75})]
Genders	Male	149 (52.5)
	Female	135 (47.5)
Final diagnosis	Infectious diseases	53 (18.7)
	Malignant tumors	66 (23.2)
	Non-infectious inflammatory diseases	76 (26.8)
	FUO	89 (31.3)
Blood culture	Negative	269 (94.7)
	Positive	15 (5.3)
Vest	Existence	280 (98.6)
	Dead	4 (1.4)
Treatment change	No	159 (56.0)
	Yes	125 (44.0)
Age		63 (47.25, 69)
Days of hospitalization		12 (8, 16)
Number of days of intermittent fever before hospitalization		25 (18.25, 40)
High temperature at the time of fever		39 (38.7, 39.5)

Among the 284 cases enrolled, 53 patients (18.7%) were diagnosed with infectious diseases, including tuberculosis (TB, $n = 3$), Epstein–Barr virus and cytomegalovirus infection ($n = 7$), other viral infections ($n = 4$), brucellosis ($n = 3$), liver abscess ($n = 5$), abdominal infections ($n = 1$), pelvic infections ($n = 1$), parasitic infections ($n = 2$), infective pericarditis ($n = 1$), infective endocarditis ($n = 1$), sepsis ($n = 10$), pulmonary invasive aspergillosis ($n = 1$), co-infection with pseudoaneurysm of the head and arm trunks ($n = 1$), bronchiectasis with pneumonia ($n = 11$), and other unspecified infections ($n = 2$). Additionally, 76 patients (26.8%) were diagnosed with non-infectious inflammatory diseases, including vasculitis ($n = 18$), adult-onset Still's disease (AOSD, $n = 19$), hemophagocytic syndrome ($n = 7$), necrotizing lymphadenitis ($n = 14$), IgG4-related disease ($n = 2$), eosinophilic dermatitis ($n = 1$), recurrent polychondritis ($n = 2$), arthritis ($n = 5$), interstitial pneumonia ($n = 1$), cutaneous lymphadenitis ($n = 1$), reactive lymphadenitis ($n = 1$), and undifferentiated connective tissue disease (UCTD) ($n = 5$). Furthermore, 66 patients (23.2%) were diagnosed with malignant tumors, including bladder cancer ($n = 4$), nasopharyngeal carcinoma ($n = 1$), lymphoma ($n = 28$), other hematologic malignancies ($n = 1$), lung cancer ($n = 17$), hepatocellular carcinoma ($n = 3$), renal cancer ($n = 2$), prostate cancer ($n = 2$), colorectal cancer ($n = 3$), duodenal adenocarcinoma ($n = 1$), adrenal carcinoma ($n = 1$), endometrial carcinoma ($n = 1$), squamous carcinoma of the groin ($n = 1$), and invasive squamous cell carcinoma of the skin ($n = 1$).

Ultimately, the cause of fever remained unknown in 89 patients (89/284, 31.3%), as detailed in Table 2.

TABLE 2 Disease spectrum profile of the study population.

Final diagnosis	Total cases	Number of true-positive PET/CT results
Infectious diseases	53	29
Virus infection	11	5
Bacterial infection	36	19
Mycobacterium tuberculosis infection	3	2
Parasitic and fungal infections	3	3
Malignant tumors	66	61
Solid tumor	37	34
Lymphomas	28	26
Other hematologic tumors	1	1
Non-infectious inflammatory diseases	76	46
Adult-onset Still's disease	19	9
Vasculitis	18	17
Osteoarthritis	5	5
Necrotizing lymphadenitis	14	9
Other types of connective tissue diseases	20	6
Fever of unknown origin	89	0

3.2 Diagnostic performance of 18F-FDG PET/CT imaging

There is a debate regarding the diagnostic utility of 18F-FDG PET/CT for patients with FUO. Some scholars, such as Jaruskova and Belohlavek (12), assert that negative 18F-FDG PET/CT scans do not aid in diagnosing FUO, similar to the findings of Georgia et al. (13), who noted that scans other than true positives do not contribute to the diagnosis (4). Conversely, Keidar et al. (13) argue that true negatives can be crucial by essentially excluding focal infections, malignant tumors, arthritis, vasculitis, and other immune system disorders, which are vital for shaping the patient's future treatment plan and improving prognosis.

In our study, only true-positive scans were considered beneficial for clinical diagnosis, as negative 18F-FDG PET/CT scans failed to elucidate the cause of the fever until the patient's symptoms resolved spontaneously. A retrospective evaluation of the diagnostic performance of 18F-FDG PET/CT, based on the final clinical diagnosis of enrolled patients18F-FDG PET/CT imaging, identified characteristic changes corresponding to a confirmed diagnosis in 136 of the 284 patients with FUO (47.9%). 18F-FDG PET/CT may have contributed to the final clinical diagnosis in 47.9% of FUO cases. The sensitivity of 18F-FDG PET/CT in diagnosing FUO was 79.5% (136/171), the specificity was 61.1% (69/113), the positive predictive value was 75.6% (136/180), and the negative predictive value was 66.3% (69/104). Detailed sensitivity, specificity, and accuracy for each disease category are provided in Table 3.

3.3 Clinicopathologic features and 18F-FDG PET/CT findings

18F-FDG PET/CT is not recommended for general screening in the early stages of clinical assessment due to its high cost compared to other diagnostic tests. Therefore, timing the use of 18F-FDG PET/CT is crucial to maximize its diagnostic value for fever of FUO. This study collected clinicopathologic data including gender, age, medical history, white cell count, neutrophil percentage, lymphocyte percentage, C-reactive protein (CRP) levels, procalcitonin (PCT) levels, erythrocyte sedimentation rate (ESR), and ferritin levels as independent variables,18F-FDG PET/CT outcomes were analyzed as dependent variables through both univariate and multivariate logistic regression to determine the association of these risk factors with true-positive 18F-FDG PET/CT results. Only the most recent data preceding the 18F-FDG PET/CT exam were considered for statistical analysis. Our findings indicate that a clinical presentation of fever with localized pain and prolonged activated partial thromboplastin time (APTT) is associated with true-positive 18F-FDG PET/CT results, as detailed in Table 4 (14).

3.4 Cost-effectiveness of 18F-FDG PET/CT in diagnosing FUO

For patients with FUO 18F-FDG PET/CT, this imaging technique shows potential as a routine, cost-effective option. It can avoid unnecessary, invasive, and costly investigations while providing timely diagnostic clues that expedite the diagnostic process and reduce

TABLE 3 Diagnostic performance of 18F-FDG PET/CT in various disease categories.

Final diagnosis	Sensitivity	Specificity	Accuracy
Infectious diseases	54.7%	89.6%	83.1%
Malignant tumors	92.4%	91.3%	91.5%
Non-infectious inflammatory diseases	60.5%	96.2%	86.6%

hospitalization duration. Although our study lacks a control group—since all participants underwent 18F-FDG PET/CT post-admission—previous research reveals its cost-effectiveness when performed early during hospitalization. A 2020 retrospective study revealed that patients undergoing 18F -FDG PET/CT within the first 7 days of admission experienced significantly fewer mean hospitalization days and lower healthcare costs before diagnosis than those scanned after 7 days (15). Another study compared 46 FUO patients who underwent 18F-FDG PET/CT upon admission against 46 who did not, finding that the latter group had more extended hospital stays (21 days vs. 6.9 days) and higher costs (€5,298 vs. €12,614) (16).

The early use of 18F -FDG PET/CT in the diagnostic workflow can facilitate prompt diagnosis, streamline decision-making, shorten hospital stays, and reduce costs by avoiding redundant tests. Additionally, some researchers highlight that early 18F-FDG PET/CT applications can allow for timely adjustments in treatment regimens, enhancing therapeutic outcomes. For instance, a retrospective study (17) observed that 53% of FUO patients had their treatment regimens adjusted 18F-FDG PET/CT. In our study, 44% (125/284) of patients had adjustments made to their treatment 18F-FDG PET/CT. However, due to the retrospective nature of these studies, it is sometimes challenging to directly attribute clinical treatment adjustments to 18F-FDG PET/CT results, particularly when changes involve the same class of drugs. For example, most patients suspected of having connective tissue disease in our study were already receiving empirical treatment with glucocorticoids, immunosuppressants, or nonsteroidal anti-inflammatory drugs before undergoing 18F-FDG PET/CT, and some reported symptomatic relief, leading to minimal changes in their treatment approach post-imaging.

4 Discussion

In their seminal study defining FUO, Petersdorf and Beeson identified the etiologies as infectious diseases (36%), tumors (19%), and miscellaneous or unknown causes (26%) (1). Since that time, the disease characteristics of FUO have evolved significantly due to advancements in diagnostic technologies. A recent cohort study by Yong et al. (18). analyzed retrospective data from 2002 to 2012, revealing that in northern China, the prevalence of infectious diseases, NIID, malignant tumors, and other undiagnosed cases was 51.5, 18.4, 11.9, and 7.1%, respectively. Their analysis of six studies from Western countries between 2003 and 2016 showed frequencies of 29.1% for infectious diseases, 25.8% for NIID, 11.6% for malignant tumors, and 26.1% for other undiagnosed cases.

Currently, infectious diseases are the predominant cause of FUO. Another study retrospectively analyzed data from 2005 to 2015, encompassing 18 studies and 3,164 patients, and identified infectious diseases as the primary cause (19). Most participants in this study were from Jilin Province in northern China, which features a subtropical, inland, and dry climate. The incidence of infectious diseases in this study (18.7%, 53/284) was lower compared to the broader region of northern China. However, the incidences of NIID (26.8%, 76/284) and malignant tumors (23.2%, 66/284) were higher. These discrepancies likely stem from regional environmental, geographic, and economic differences. For instance, healthcare teams in infectious disease departments may conduct pathogen identification tests more rapidly, leading to earlier detection of infectious diseases before cases are classified as FUO. Furthermore, the preliminary use of antibiotic therapy prior to examinations with ^18F-FDG PET/CT might influence the diagnosis of infectious diseases.

These variations are also attributable to advanced diagnostic techniques and the continuous refinement of diagnostic approaches. For example, the rising frequency of diagnosed malignant tumors may relate to enhanced cancer detection methods in hospitals. Fusco et al. (19) observed a significant increase in confirmed NIID diagnoses over time, which they attributed not only to advances in medical knowledge and greater awareness among clinicians but also to the integration of basic immunologic tests into the FUO diagnostic process, thereby aiding in the identification of NIID clues in patients. Therefore, optimizing FUO diagnostic strategies should consider the prevalent causes of fever in different regions, local epidemiology, and available resources.

Minamimoto et al. (20) synthesized findings from previous meta-analyses on the diagnostic role of 18F-FDG PET/CT in managing FUO, demonstrating that this imaging technique offers high sensitivity (79.5%, 136/171) and moderate specificity (61.1%, 69/113) for FUO diagnosis. These figures align with the results from two recent meta-analyses that also support the utility of 18F-FDG PET/CT in this context (21–23).

However, the absence of a universally accepted gold standard for FUO complicates comparisons of sensitivity and specificity across different studies due to variations in patient characteristics and diagnostic test sequencing. Therefore, assessing the clinical usefulness of 18F-FDG PET/CT, rather than its sensitivity and specificity alone, becomes more relevant (7). Kouijzer et al. (3) concluded that 18F-FDG PET/CT is particularly valuable when it leads to a definitive etiological diagnosis of FUO, contributing to the final diagnosis in 38 to 75% of cases. In this specific study, 18F-FDG PET/CT proved helpful in 47.9% (136/284) of cases and contributed to the final diagnosis in 69.7% (136/195) of the 195 patients who received a definitive diagnosis, consistent with earlier research (7, 24, 25).

The timing of 18F-FDG PET/CT in the diagnostic process is critical; earlier use can potentially alter the course of the investigation, as preliminary blood results and other imaging studies might already provide diagnostic clues, discouraging further testing and reserving ^18F-FDG PET/CT for more challenging cases.

Moreover, the pre-examination use of empirical treatments, such as glucocorticoids or antibiotics, remains contentious. In this cohort, 73.2% (208/284) of patients were given antibiotics, and 12.0% (34/284) received glucocorticoids before undergoing 18F-FDG PET/CT. While some studies suggest that antibiotics might reduce the detection of infected lesions in 18F-FDG PET/CT

10.3389/fmed.2024.1511710

TABLE 4 Regression analysis of clinical history data and true-positive 18F-FDG PET/CT.

	Single factor regression analysis		Multifactor regression analysis	
Indicators	OR(95%)	*p*	OR(95%)	*p*
Chills	1.335 (0.83, 2.147)	0.233		
Muscle pain	0.62 (0.362, 1.064)	0.083		
Joint pain	0.909 (0.518, 1.593)	0.738		
Localized pain	2.108 (1.248, 3.559)	0.005	2.491 (1.398, 4.436)	0.002
Diabetes	1.529 (0.8, 2.924)	0.199		
High blood pressure	1.167 (0.702, 1.94)	0.552		
Chronic kidney disease	2.25 (0.662, 7.649)	0.194		
Chronic lung disease	0.589 (0.193, 1.805)	0.355		
Heart attack	0.872 (0.403, 1.887)	0.728		
Gout	1.647 (0.271, 10.007)	0.588		
Connective tissue disease	0.212 (0.024, 1.837)	0.159		
Disease of the blood	1.465 (0.322, 6.666)	0.622		
Surgical history	1.097 (0.666, 1.806)	0.717		
Allergy history	1.231 (0.647, 2.343)	0.527		
Previous antibiotic use	0.891 (0.527, 1.507)	0.667		
Prior glucocorticoid use	0.639 (0.307, 1.333)	0.233		
Hepatosplenomegaly	0.673 (0.37, 1.223)	0.194		
Lymph node Enlargement	1.168 (0.705, 1.935)	0.547		
Skin rash	0.831 (0.485, 1.422)	0.499		
Days of hospitalization	1.011 (0.983, 1.04)	0.429		
Age	1.003 (0.99, 1.017)	0.642		
Number of days of intermittent fever before hospitalization	1.002 (0.999, 1.005)	0.126		
High temperature at the time of fever	0.997 (0.692, 1.436)	0.986		
WBC	0.993 (0.957, 1.031)	0.729		
N%	1.252 (0.261, 6.004)	0.779		
L%	0.451 (0.086, 2.362)	0.346		
Creatinine	1.008 (1, 1.016)	0.053		
ALT	1.001 (0.999, 1.003)	0.442		
AST	0.999 (0.997, 1.002)	0.59		
Ferrous protein	1 (1, 1)	0.113		
Lactate dehydrogenase	1 (0.999, 1)	0.414		
Cholesterol	1.275 (0.983, 1.652)	0.067		
Triglyceride	0.876 (0.647, 1.188)	0.395		
PCT	1.005 (0.968, 1.044)	0.782		
CRP	1 (0.997, 1.003)	0.913		
ESR	1.004 (0.997, 1.011)	0.315		
APTT	0.939 (0.886, 0.996)	0.035	0.933 (0.876, 0.994)	0.031
PT	0.997 (0.88, 1.13)	0.964		
PTA	1.006 (0.991, 1.021)	0.443		
FBG	0.957 (0.851, 1.075)	0.455		
HB	1.003 (0.992, 1.013)	0.607		

(Continued)

TABLE 4 (Continued)

	Single factor regression analysis		Multifactor regression analysis	
Indicators	OR(95%)	*p*	OR(95%)	*p*
PLT	0.999 (0.998, 1.001)	0.499		
Albumin	1.003 (0.962, 1.046)	0.889		

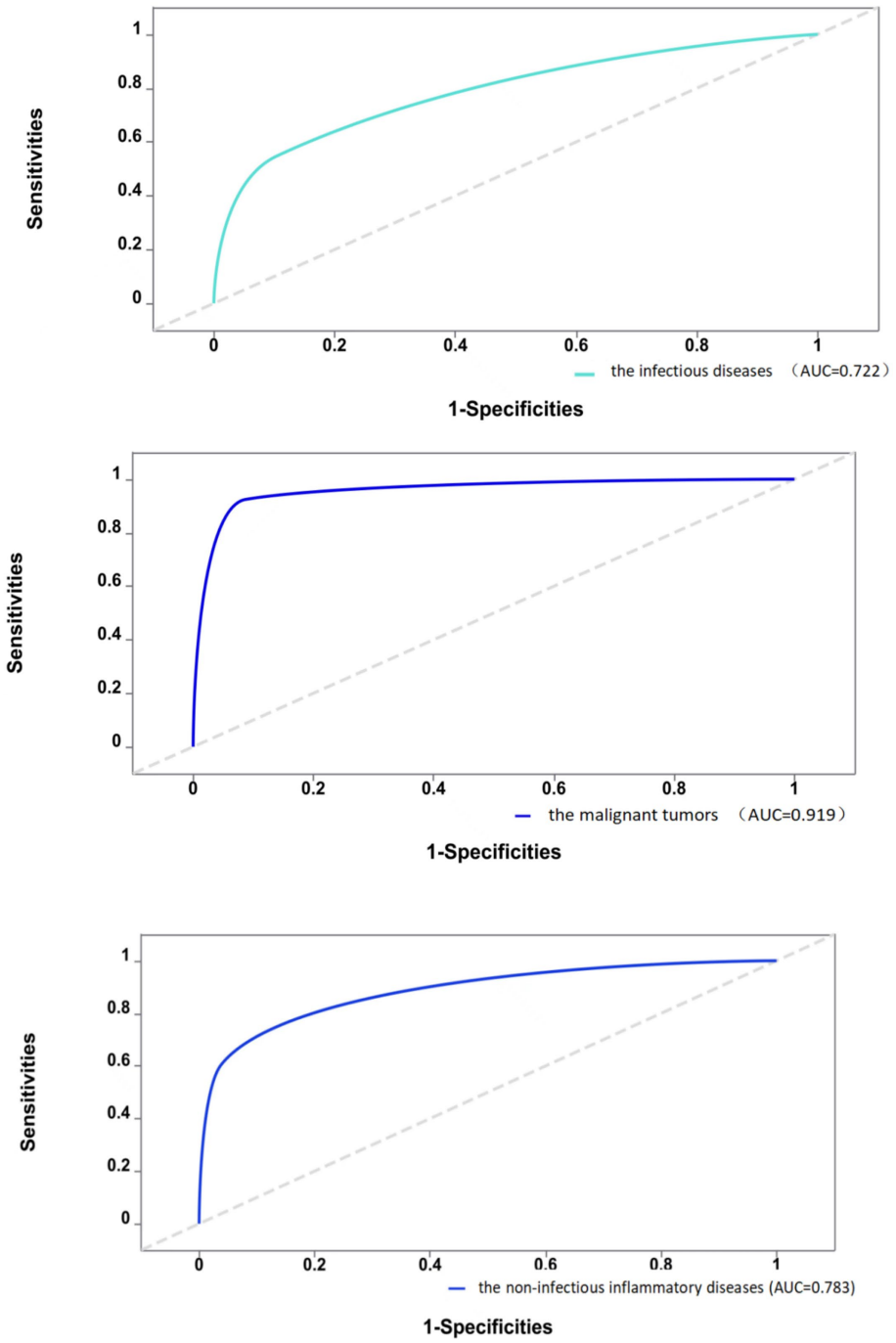

FIGURE 1
Diagnostic efficacy of 18F-FDG PET/CT in different types of diseases.

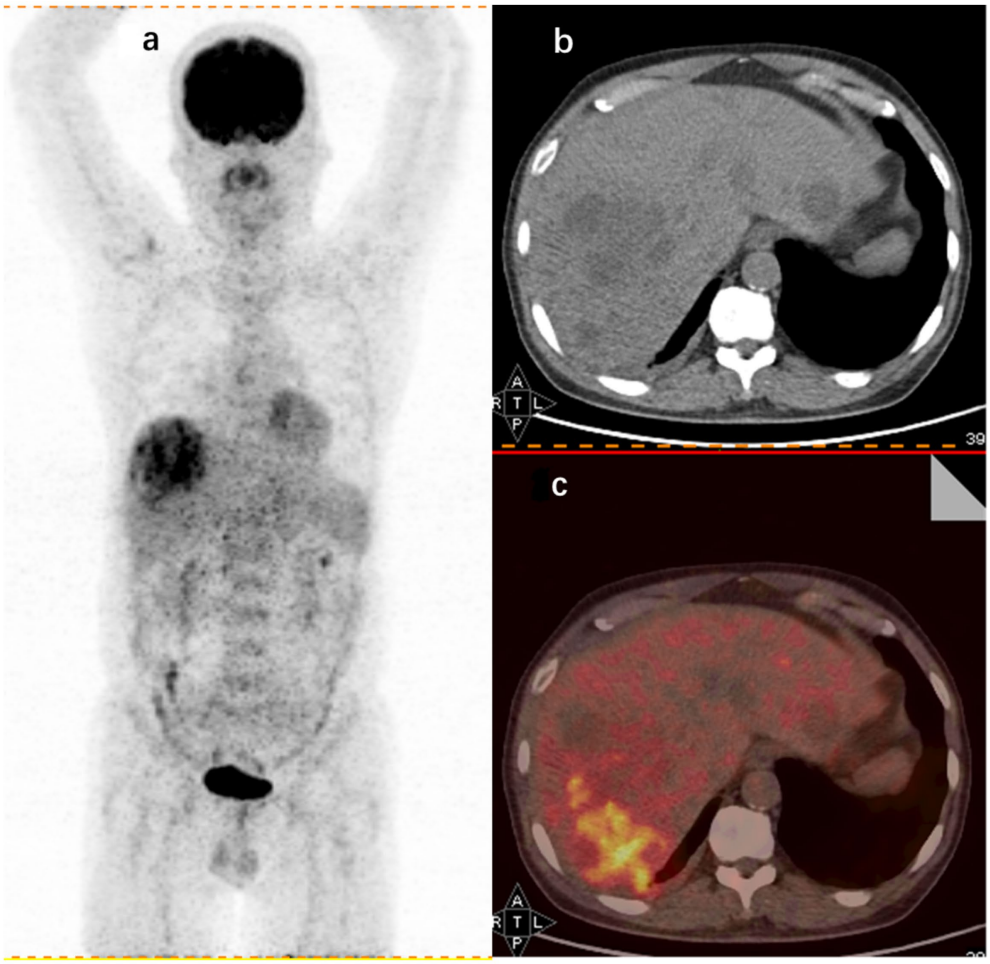

FIGURE 2
18F-FDG PET/CT findings in a 60-year-old male FUO patient with a final diagnosis of liver abscess. **(A)** Whole-body 18F-FDG PET coronal section showing an aggregated foci of metabolic activity in the right hepatic lobe. CT axial section **(B)** and imaging fusion **(C)** showing foci of increased uptake in the right hepatic lobe (SUVmax 8.1).

TABLE 5 **Delong test results between the new and the old models.**

Type of disease	Old model		New model		Statistic	*p*	NRI
	AUC	95%CI	AUC	95%CI			
Infectious diseases	0.634	0.556–0.712	0.774	0.696–0.852	−3.751	0.0002	0.858
Malignant tumors	0.664	0.591–0.738	0.931	0.889–0.973	−7.3795	<0.001	1.647
Non-infectious inflammatory diseases	0.708	0.641–0.775	0.857	0.805–0.910	−4.993	<0.001	1.122

(26), others argue that antibiotics do not significantly impact diagnostic accuracy. Conversely, corticosteroid use is associated with false-negative results (27), particularly affecting the detection of inflammatory diseases such as vasculitis and polymyalgia rheumatica. The prolonged use of corticosteroids before 18F-FDG PET/CT examinations tends to have a more significant negative impact, thus halting their use prior to imaging is recommended to enhance diagnostic accuracy (28, 29).

In this study, 89 patients remained with an unresolved cause of fever; 69 of these individuals exhibited no positive results from 18F-FDG PET/CT scans. Among these, one patient died due to diabetic complications, one from a cerebral infarction, and two from cardiac infarctions. The remaining 65 patients saw their fever symptoms resolve post-discharge, as confirmed through subsequent follow-up. Retrospective analysis suggests a high likelihood of spontaneous fever resolution in patients without anemia or

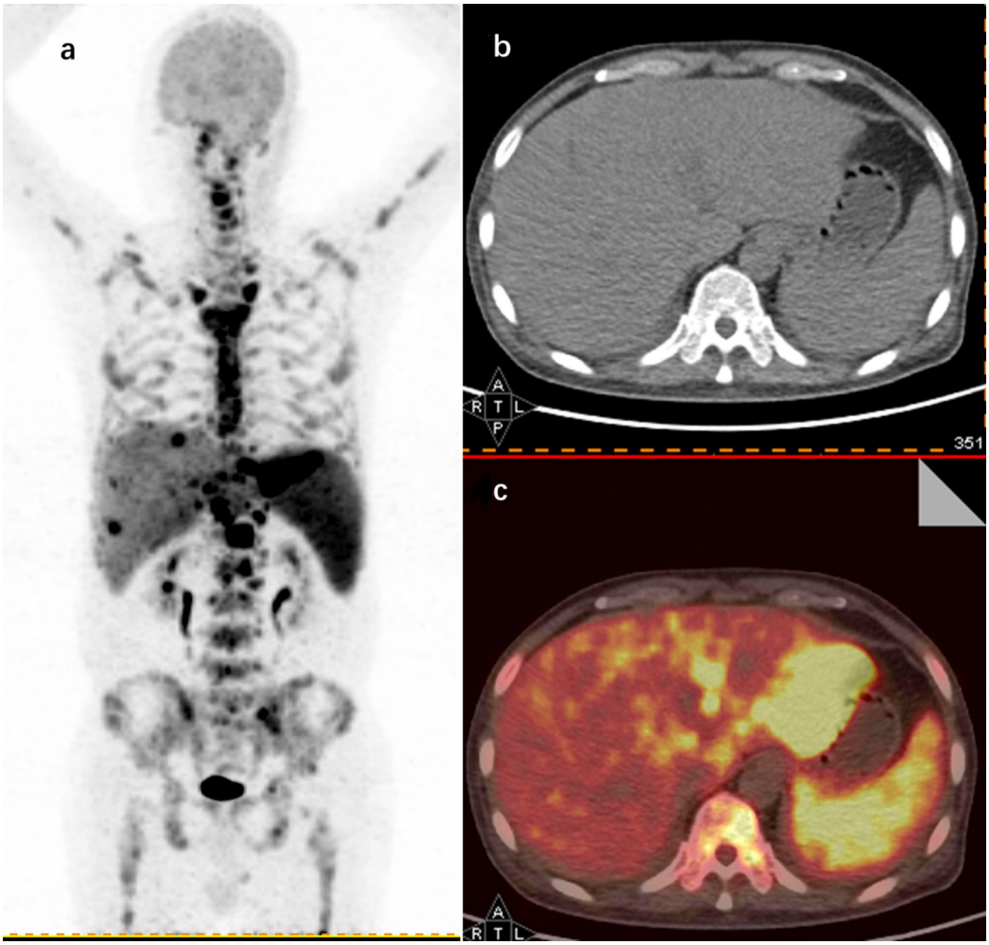

FIGURE 3
18F-FDG PET/CT findings in a 62-year-old male FUO patient with a final diagnosis of lymphoma. **(A)** Maximum intensity projection (MIP) images of whole-body 18F-FDG PET coronal sections show hypermetabolic sites in the left hepatic lobe (SUVmax 23.1), spleen (SUVmax 8.5), and throughout the skeleton (SUVmax 16.8). Representative axial sections of CT **(B)** and image fusion **(C)** show increased uptake in the left hepatic lobe and spleen.

hypoalbuminemia (30). Takeuchi et al. (31) similarly noted that patients with FUO, who lacked a definitive diagnosis after extensive diagnostic evaluations and had negative 18F-FDG PET/CT results, were likely to experience spontaneous symptom remission.

Kouijzer et al. (3) observed that in cases of persistent FUO with negative 18F-FDG PET/CT results, it may be more prudent to await the emergence of new diagnostic clues rather than to proceed immediately with further testing. Therefore, if 18F-FDG PET/CT does not yield significant positive findings, additional testing might not be recommended; instead, a wait-and-see approach or the empirical application of NSAIDs and corticosteroid therapy could be considered in the clinical management of patients with undiagnosed FUO (3, 32–34).

Furthermore, this study assessed the diagnostic efficacy of 18F-FDG PET/CT in identifying different types of diseases causing FUO through ROC analysis, as detailed in Figure 1. The ROC analysis showed an AUC of 0.722 for infectious diseases, with a sensitivity of 54.7% and a specificity of 89.6%. The analysis for non-infectious inflammatory diseases showed an AUC of 0.783, sensitivity of 60.5%, and specificity of 96.2%. The AUC was notably higher for malignant tumors at 0.919, with a sensitivity of 92.4% and a specificity of 91.3%. Thus, compared to infectious and non-infectious inflammatory diseases,18F-FDG PET/CT demonstrates greater sensitivity and specificity in diagnosing malignant diseases.

The final diagnosis of a disease relies on a multifactorial analysis rather than the outcome of a single diagnostic test. This study evaluated whether the diagnostic efficacy improved when 18F-FDG PET/CT results were integrated into the existing diagnostic model. The original model included five independent variables: CRP, ESR, PCT, leukocytes, and ferritin. The new model incorporated the results of 18F-FDG PET/CT alongside these existing variables.

To assess the effectiveness of the updated model, we employed the Delong test to analyze the difference in the AUC between the old and new models. A positive NRI indicates that the revised model offers superior diagnostic capabilities compared to its predecessor. The findings revealed that the AUC for the new model was superior in diagnosing infectious diseases, malignant neoplastic diseases, and non-infectious inflammatory diseases. This enhancement suggests that including 18F-FDG PET/CT results significantly improves predictive efficacy. As detailed in Table 5, integrating 18F-FDG PET/CT findings into the diagnostic process mainly benefits the management of suspected malignancies causing FUO, showing the

FIGURE 4
18F-FDG PET/CT findings in a 72-year-old patient with a final diagnosis of large vessel vasculitis. **(A)** Coronal section of whole-body 18F-FDG PET showing cumulative FDG uptake in the aorta, subclavian artery, and carotid artery (SUVmax 5.2).

heightened diagnostic performance of 18F-FDG PET/CT in these scenarios. This refined approach allows for more accurate and timely identification of the underlying causes of FUO, facilitating more targeted and effective clinical interventions (35).

This study also explored the specific diagnostic capabilities of 18F-FDG PET/CT for different causes of FUO. Over the past decade, 18F-FDG PET/CT has become a staple in tumor imaging due to its ability to detect cells with high glycolytic activity. However, 18F-FDG is not specific to tumor cells; it also accumulates in activated leukocytes (36), which is pivotal in its application beyond oncology. Since the initial observation of high FDG uptake in abdominal abscesses (37), 18F-FDG PET/CT has been extensively utilized in diagnosing and managing infectious diseases. In the context of this study, abnormal 18F-FDG PET/CT findings were present in all patients diagnosed with liver abscesses. This is consistent with early findings that FDG is taken up by large numbers of neutrophils and lymphocytes at infection sites, which supports the idea (38) that 18F-FDG PET/CT is particularly effective in identifying abscessed lesions due to their significant leukocyte infiltration compared to other infections. For illustration, Figure 2 in this study depicts a hypermetabolic lesion in the right hepatic lobe of a 60-year-old patient with an FUO-related liver abscess.

18F-FDG PET/CT also demonstrates considerable diagnostic value for identifying lymphoma as a cause of fever of FUO. This study identified 28 of the 66 patients diagnosed with malignant tumors with lymphoma. Among these, 18F-FDG PET/CT imaging strongly suggested lymphoma in 26 patients, aligning with their final diagnoses. However, two patients presented with 18F-FDG PET/CT findings indicative of inflammatory lesions but were later diagnosed with lymphoma, highlighting some challenges in differential diagnosis.

Conversely, there were 17 cases where 18F-FDG PET/CT was highly suggestive of lymphoma, yet subsequent pathologic evaluation of lymph node biopsies ruled out lymphoma. These patients were diagnosed with other conditions: three with necrotizing lymphadenitis, 2 with Adult Still's disease, 2 with mixed hepatocellular carcinoma-cholangiocarcinoma, 2 with hemophagocytic syndrome, and 1 with an infectious disease. The remaining seven cases remained undiagnosed, although their conditions improved following relevant treatments.

The sensitivity of 18F-FDG PET/CT in diagnosing lymphoma in patients with FUO was notably high at 92.9% (26/28) with a PPV of 60.5% (26/43). Another study supports these findings and emphasizes the importance of 18F-FDG PET/CT in the diagnostic workflow for suspected lymphoma in FUO cases. Additionally, the study developed a lymphoma prediction model based on 18F-FDG PET/CT characteristics, further enhancing the diagnostic efficiency for FUO (39).

Retrospective analyses have explored the prognostic capabilities of 18F-FDG PET/CT parameters such as maximum standardized uptake value (SUVmax), whole-body metabolic tumor volume, and whole-body total lesion glycolysis (40, 41). These metrics are instrumental in not only diagnosing but also predicting the prognosis of lymphoma in FUO patients.

Illustratively, Figure 3 in this study shows 18F-FDG PET/CT detecting hypermetabolic activity in the left liver lobe, spleen, and bones of a 62-year-old patient with FUO, who was later diagnosed with lymphoma.

In this study, NIID emerged as the second most frequent cause of FUO (accounting for 26.8%, 76/284) cases, with vasculitis being particularly prevalent within this group, representing 23.7% (18/76) of the NIID cases. 18F-FDG PET/CT played a pivotal role in diagnosing these conditions, aligning with the final diagnosis of vasculitis in 17 of the 18 patients diagnosed with this condition. The high diagnostic yield of 18F-FDG PET/CT for detecting active large vessel vasculitis is well-documented (42–44). The utility of 18F-FDG PET/CT in this context is indicated by its favorable diagnostic performance, making it a valuable tool in the clinical evaluation of patients with suspected active large vessel vasculitis.

Illustratively, Figure 4 highlights the capabilities of 18F-FDG PET/CT in this regard. The imaging detected a significant accumulation of FDG, with a maximum SUV of 5.2, in the aorta, subclavian arteries, and carotid arteries of a 72-year-old patient diagnosed with large vessel vasculitis.

In recent years, researchers have started leveraging traditional risk factors to enhance the diagnostic performance of 18F-FDG PET/CT for FUO by identifying characteristics of patients who are most likely to benefit from this imaging modality. Our study observed a notable correlation between localized pain, prolonged APTT, and true-positive 18F-FDG PET/CT results.

Prolonged APTT can occur in various febrile conditions, though the mechanisms behind this are not fully understood. For instance, one study linked prolonged APTT in severe fever with thrombocytopenia syndrome (SFTS) to a deficiency in coagulation

TABLE 6 Infectious diseases.

Indicators	Single-factor regression analysis		Multifactor regression analysis	
	OR (95%)	*p*	OR (95%)	*p*
Chills	1.31 (0.44–3.89)	0.631		
Muscle pain	0.16 (0.04–0.68)	0.013	0.24 (0.03–2.30)	0.218
Joint pain	0.80 (0.18–3.61)	0.771		
Localized pain	0.45 (0.14–1.44)	0.178		
Chronic kidney disease	0.18 (0.02–1.72)	0.136		
Chronic lung disease	0.11 (0.01–0.97)	0.046	2.78 (0.08–97.44)	0.573
Heart attack	0.25 (0.07–0.86)	0.029	0.21 (0.02–2.17)	0.191
Gout	0.25 (0.02–2.58)	0.244		
Connective tissue disease	0.10 (0.00–3.38)	0.199		
Disease of the blood	0.09 (0.00–2.03)	0.132		
Hepatosplenomegaly	1.04 (0.25–4.41)	0.956		
Lymph node Enlargement	0.03 (0.01–1.14)	<0.001	0.16 (0.02–1.16)	0.070
Skin rash	0.81 (0.15–4.42)	0.806		
WBC	0.83 (0.72–0.96)	0.013	1.06 (0.83–1.37)	0.626
N%	2.62 (0.06–116.72)	0.619		
L%	0.11 (0.00–8.65)	0.319		
HB	1.01 (0.98–1.04)	0.409		
PLT	1.00 (0.99–1.00)	0.100		
Creatinine	0.98 (0.97–1.00)	0.087		
ALT	1.00 (1.00–1.00)	0.639		
AST	1.00 (0.99–1.00)	0.618		
Albumin	0.97 (0.88–1.08)	0.585		
Ferrous protein	1.00 (1.00–1.00)	0.452		
Lactate dehydrogenase	1.00 (1.00–1.00)	0.356		
Cholesterol	0.88 (0.50–1.55)	0.662		
Triglyceride	0.52 (0.23–1.13)	0.098		
PCT	1.08 (0.89–1.30)	0.454		
CRP	1.00 (0.99–1.00)	0.400		
ESR	0.99 (0.98–1.01)	0.402		
APTT	0.99 (0.88–1.12)	0.908		
PT	1.11 (0.85–1.44)	0.448		
PTA	0.99 (0.96–1.03)	0.642		
FBG	0.80 (0.59–1.08)	0.143		

factor XI caused by SFTS virus infection (45). Similarly, another study indicated that in dengue hemorrhagic fever, prolonged APTT may result from the secretion of dengue virus nonstructural protein 1 (NS 1), which inhibits plasminogen activation (46). These complex underlying mechanisms warrant further investigation.

Moreover, other variables have been identified as relevant in previous studies. Mahajna et al. (11) found associations between weight loss, low hemoglobin levels, and diagnostic outcomes via 18F-FDG PET/CT. Another retrospective study suggested that combining 18F-FDG PET/CT findings with CRP levels could improve the accuracy of FUO diagnoses (47). A comprehensive retrospective analysis involving 498 patients established the predictive value of CRP and ESR in producing positive 18F-FDG PET/CT results. Notably, elevated CRP levels more accurately reflected the presence and extent of inflammation compared to ESR, with the study reporting a 100% true negative rate for 18F-FDG PET/CT in patients with CRP levels below 5 mg/L. However, while diagnosis rates increased with rising CRP levels, no optimal CRP threshold was determined (14).

Crouzet et al. (48) found significant correlations between high CRP levels (>30 mg/L), anemia, and beneficial 18F-FDG PET/CT results. Contrarily, Bleeker-Rovers et al. (49) noted that 18F-FDG PET/CT may not be indicated for FUO patients with normal CRP and

10.3389/fmed.2024.1511710

TABLE 7 Non-infectious inflammatory diseases.

Indicators	Single-factor regression analysis		Multifactor regression analysis	
	OR (95%)	*p*	OR (95%)	*p*
Chills	0.42 (0.16–1.09)	0.075		
Muscle pain	2.34 (0.80–6.88)	0.121		
Joint pain	0.67 (0.26–1.71)	0.401		
Localized pain	0.31 (0.12–0.82)	0.018	0.23 (0.02–2.84)	0.251
Chronic kidney disease	0.04 (0.00–0.32)	0.003	0.03 (0.00–0.92)	0.044
Chronic lung disease	2.44 (0.03–212.56)	0.696		
Heart attack	0.35 (0.08–1.59)	0.173		
Gout	1.36 (0.00–597.98)	0.921		
Connective tissue disease	1.37 (0.02–103.81)	0.888		
Disease of the blood	1.38 (0.06–30.67)	0.838		
Hepatosplenomegaly	0.62 (0.14–2.69)	0.522		
Lymph node Enlargement	0.26 (0.09–0.70)	0.008	0.10 (0.01–1.19)	0.069
Skin rash	2.13 (0.72–6.29)	0.169		
WBC	0.98 (0.91–1.06)	0.567		
N%	0.09 (0.00–3.16)	0.186		
L%	10.79 (0.24–494.01)	0.223		
HB	1.01 (0.98–1.03)	0.583		
PLT	1.01 (1.00–1.01)	0.006	1.00 (0.99–1.01)	0.453
Creatinine	1.00 (0.98–1.03)	0.690		
ALT	1.00 (0.99–1.01)	0.917		
AST	1.00 (0.99–1.00)	0.504		
Albumin	1.01 (0.92–1.10)	0.896		
Ferrous protein	1.00 (1.00–1.00)	0.777		
Lactate dehydrogenase	1.00 (1.00–1.00)	0.440		
Cholesterol	1.31 (0.75–2.31)	0.346		
Triglyceride	0.82 (0.42–1.60)	0.569		
PCT	1.25 (0.76–2.05)	0.382		
CRP	1.00 (1.00–1.01)	0.549		
ESR	1.02 (1.00–1.03)	0.066		
APTT	0.97 (0.87–1.07)	0.519		
PT	1.22 (0.86–1.74)	0.264		
PTA	0.98 (0.94–1.01)	0.158		
FBG	1.59 (1.20–2.10)	0.001	0.79 (0.36–1.72)	0.548

ESR levels. These differences among studies can be attributed to variations in research methodology, including how true positives are defined (i.e., whether they are useful solely for diagnosis or include both true positives and true negatives).

Additionally, while CRP and white blood cell counts generally indicate infection and inflammation, their patterns may not uniformly align across different diseases. For example, high CRP levels are common in autoinflammatory diseases, such as vasculitis and arthritis, even when white blood cell counts remain normal or only moderately elevated (17).

To address this, our study also examined the predictive value of the same laboratory indicators for true-positive 18F-FDGPET/CT results across different disease types. Surprisingly, only patients with a history of chronic kidney disease who were diagnosed with non-infectious inflammatory diseases demonstrated a higher likelihood of a true-positive 18F-FDG PET/CT result, a finding not previously reported. This novel insight is detailed in Tables 6–8.

There are several limitations in our study. Firstly, the definition of FUO in some current studies is not uniform and lacks a diagnostic gold standard, which may introduce some errors in comparison. Secondly, due to the retrospective design of this study, the diagnostic workup of patients prior to 18F-FDG PET/CT was

TABLE 8 Malignant tumors.

Indicators	Single factor regression analysis		Multifactor regression analysis	
	OR (95%)	*p*	OR (95%)	*p*
Chills	0.60 (0.09–3.87)	0.595		
Muscle pain	0.29 (0.04–1.99)	0.210		
Joint pain	0.67 (0.26, 1.70)	0.401		
Localized pain	0.32 (0.05–2.10)	0.238		
Chronic kidney disease	0.08 (0.01–0.65)	0.019	0.14 (0.01–1.44)	0.099
Chronic lung disease	4.95 (0.01–2135.30)	0.605		
Heart attack	0.35 (0.08–1.58)	0.173		
Gout	0.09 (0.00–37.08)	0.428		
Connective tissue disease	0.09 (0.00–37.08)	0.428		
Disease of the blood	0.03 (0.00–7.49)	0.206		
Hepatosplenomegaly	1.81 (0.19–17.29)	0.607		
Lymph node Enlargement	0.35 (0.05–2.26)	0.270		
Skin rash	2.13 (0.72–6.28)	0.170		
WBC	0.99 (0.86–1.14)	0.867		
N%	0.09 (0.00–3.19)	0.189		
L%	0.07 (0.00–26.49)	0.382		
HB	1.01 (0.97–1.05)	0.772		
PLT	1.00 (0.99–1.01)	0.822		
Creatinine	1.00 (0.97–1.03)	0.830		
ALT	0.99 (0.98–1.00)	0.039	1.00 (0.99–1.01)	0.949
AST	0.99 (0.99–1.00)	0.103		
Albumin	1.14 (0.92–1.41)	0.228		
Ferrous protein	1.00 (1.00–1.00)	0.552		
Lactate dehydrogenase	1.00 (1.00–1.00)	0.093		
Cholesterol	1.76 (0.52–5.92)	0.361		
Triglyceride	13.03 (0.36–476.74)	0.162		
PCT	0.99 (0.91–1.08)	0.793		
CRP	1.00 (0.98–1.01)	0.618		
ESR	0.99 (0.97–1.02)	0.544		
APTT	1.00 (0.82–1.23)	0.977		
PT	1.00 (0.59–1.70)	0.999		
PTA	1.00 (0.95–1.06)	0.982		
FBG	0.87 (0.53–1.42)	0.571		

not fully standardized. Clinicians determined the patient's overall course of treatment at their discretion, including adjusting treatment regimens and selecting examination sequences. Therefore, we could not ascertain whether comprehensive preliminary evaluations were conducted on every FUO patient before performing 18F-FDG PET/CT. Thirdly, there is controversy among various studies regarding whether true-negative 18F-FDG PET/CT results have diagnostic value, introducing some bias when comparing the diagnostic utility of 18F-FDG PET/CT across different studies. Fourthly, because this was a retrospective study, all patients enrolled underwent 18F-FDG PET/CT; thus, a control group was lacking.

5 Conclusion

The use of 18F-FDG PET/CT in our department has aided in the diagnosis of tuberculosis, abscesses, solid tumors, lymphomas, and vasculitis in patients with FUO and achieved high diagnostic accuracies in those diseases. Since early potential diagnostic clues can be obtained from 18F-FDG PET/CT, unnecessary further testing can be avoided, thus facilitating the initiation of the most effective treatments more rapidly and improving the overall prognosis of patients. The identifications of clinical factors that related to true-positive PET/CT diagnosis could further improve the diagnostic accuracy and facilitate more effective imaging allocation.

Data availability statement

The raw data supporting the conclusions of this article will be made available by the authors, without undue reservation.

Ethics statement

The studies involving humans were approved by the Ethics Committee of Changchun Infectious Disease Hospital and the Ethics Committee of the 1st Hospital of Jilin University, China. The studies were conducted in accordance with the local legislation and institutional requirements. The participants provided their written informed consent to participate in this study. Written informed consent was obtained from the individual(s) for the publication of any potentially identifiable images or data included in this article.

Author contributions

XY: Validation, Writing – original draft. SW: Validation, Writing – review & editing. ND: Conceptualization, Writing – review & editing. HZ: Conceptualization, Writing – review & editing. HC: Visualization, Writing – review & editing.

Funding

The author(s) declare that no financial support was received for the research, authorship, and/or publication of this article.

Conflict of interest

The authors declare that the research was conducted in the absence of any commercial or financial relationships that could be construed as a potential conflict of interest.

Generative AI statement

The authors declare that no Gen AI was used in the creation of this manuscript.

Publisher's note

All claims expressed in this article are solely those of the authors and do not necessarily represent those of their affiliated organizations, or those of the publisher, the editors and the reviewers. Any product that may be evaluated in this article, or claim that may be made by its manufacturer, is not guaranteed or endorsed by the publisher.

References

1. Petersdorf RG, Beeson PB. Fever of unexplained origin: report on 100 cases. *Medicine (Baltimore)*. (1961) 40:1–30. doi: 10.1097/00005792-196102000-00001

2. Durack DT, Street AC. Fever of unknown origin--reexamined and redefined. *Curr Clin Top Infect Dis*. (1991) 11:35–51.

3. Kouijzer IJE, Mulders-Manders CM, Bleeker-Rovers CP, Oyen WJG. Fever of unknown origin: the value of FDG-PET/CT. *Semin Nucl Med*. (2018) 48:100–7. doi: 10.1053/j.semnuclmed.2017.11.004

4. Letertre S, Fesler P, Zerkowski L, Picot MC, Ribstein J, Guilpain P, et al. Place of the 18F-FDG-PET/CT in the diagnostic workup in patients with classical fever of unknown origin (FUO). *J Clin Med*. (2021) 10:3831. doi: 10.3390/jcm10173831

5. Corstens FH, van der Meer JW. Nuclear medicine's role in infection and inflammation. *Lancet*. (1999) 354:765–70. doi: 10.1016/S0140-6736(99)06070-5

6. Bleeker-Rovers CP, Boerman OC, Rennen HJJM, Corstens FHM, Oyen WJG. Radiolabeled compounds in diagnosis of infectious and inflammatory disease. *Curr Pharm Des*. (2004) 10:2935–50. doi: 10.2174/1381612043383539

7. Meller J, Sahlmann C-O, Scheel AK. 18F-FDG PET and PET/CT in fever of unknown origin. *J Nucl Med*. (2007) 48:35–45.

8. Hadad ZSH, Afzelius P, Sørensen SM, Jurik AG. Clinical relevance of 18F-FDG-PET/CT incidental findings. *Dan Med J*. (2020) 67:A10190553.

9. Hess S, Noriega-Álvarez E, Leccisotti L, Treglia G, Albano D, Roivainen A, et al. EANM consensus document on the use of [18F]FDG PET/CT in fever and inflammation of unknown origin. *Eur J Nucl Med Mol Imaging*. (2024) 51:2597–613. doi: 10.1007/s00259-024-06732-8

10. Ly K-H, Costedoat-Chalumeau N, Liozon E, Dumonteil S, Ducroix JP, Sailler L, et al. Diagnostic value of 18F-FDG PET/CT vs. chest-abdomen-pelvis CT scan in Management of Patients with fever of unknown origin, inflammation of unknown origin or episodic fever of unknown origin: a comparative multicentre prospective study. *J Clin Med*. (2022) 11:386. doi: 10.3390/jcm11020386

11. Mahajna H, Vaknin K, Ben Shimol J, Watad A, Abu-Much A, Mahroum N, et al. The utility of 18FDG-PET/CT in diagnosing fever of unknown origin: the experience of a large tertiary medical center. *Int J Environ Res Public Health*. (2021) 18:5360. doi: 10.3390/ijerph18105360

12. Jaruskova M, Belohlavek O. Role of FDG-PET and PET/CT in the diagnosis of prolonged febrile states. *Eur J Nucl Med Mol Imaging*. (2006) 33:913–8. doi: 10.1007/s00259-006-0064-z

13. Keidar Z, Gurman-Balbir A, Gaitini D, Israel O. Fever of unknown origin: the role of 18 F-FDG PET/CT. *J Nucl Med*. (2008) 49:1980–5. doi: 10.2967/jnumed.108.054692

14. Balink H, Veeger NJGM, Bennink RJ, Slart RHJA, Holleman F, van Eck-Smit BLF, et al. The predictive value of C-reactive protein and erythrocyte sedimentation rate for 18F-FDG PET/CT outcome in patients with fever and inflammation of unknown origin. *Nucl Med Commun*. (2015) 36:604–9. doi: 10.1097/MNM.0000000000000300

15. Chen J-C, Wang Q, Li Y, Zhao YY, Gao P, Qiu LH, et al. Current situation and cost-effectiveness of 18F-FDG PET/CT for the diagnosis of fever of unknown origin and inflammation of unknown origin: a single-center, large-sample study from China. *Eur J Radiol*. (2022) 148:110184. doi: 10.1016/j.ejrad.2022.110184

16. Balink H, Tan SS, Veeger NJGM, Holleman F, van Eck-Smit BLF, Bennink RJ, et al. 18F-FDG PET/CT in inflammation of unknown origin: a cost-effectiveness pilot-study. *Eur J Nucl Med Mol Imaging*. (2015) 42:1408–13. doi: 10.1007/s00259-015-3010-0

17. Pijl JP, Kwee TC, Legger GE, Peters HJH, Armbrust W, Schölvinck EH, et al. Role of FDG-PET/CT in children with fever of unknown origin. *Eur J Nucl Med Mol Imaging*. (2020) 47:1596–604. doi: 10.1007/s00259-020-04707-z

18. Zhai Y-Z, Chen X, Liu X, Zhang ZQ, Xiao HJ, Liu G. Clinical analysis of 215 consecutive cases with fever of unknown origin: a cohort study. *Medicine (Baltimore)*. (2018) 97:e10986. doi: 10.1097/MD.0000000000010986

19. Fusco FM, Pisapia R, Nardiello S, Cicala SD, Gaeta GB, Brancaccio G. Fever of unknown origin (FUO): which are the factors influencing the final diagnosis? A 2005-2015 systematic review. *BMC Infect Dis*. (2019) 19:653. doi: 10.1186/s12879-019-4285-8

20. Minamimoto R. Optimal use of the FDG-PET/CT in the diagnostic process of fever of unknown origin (FUO): a comprehensive review. *Jpn J Radiol*. (2022) 40:1121–37. doi: 10.1007/s11604-022-01306-w

21. Kan Y, Wang W, Liu J, Yang J, Wang Z. Contribution of 18F-FDG PET/CT in a case-mix of fever of unknown origin and inflammation of unknown origin: a meta-analysis. *Acta Radiol*. (2019) 60:716–25. doi: 10.1177/0284185118799512

22. Takeuchi M, Dahabreh IJ, Nihashi T, Iwata M, Varghese GM, Terasawa T. Nuclear imaging for classic fever of unknown origin: Meta-analysis. *J Nucl Med*. (2016) 57:1913–9. doi: 10.2967/jnumed.116.174391

23. Update A. van Rijsewijk, N. D., IJpma, F. F. A., Wouthuyzen-Bakker, M. & Glaudemans, A. W. J. M. Molecular imaging of fever of unknown origin. *Semin Nucl Med*. (2023) 53:4–17. doi: 10.1053/j.semnuclmed.2022.07.002

24. Federici L, Blondet C, Imperiale A, Sibilia J, Pasquali JL, Pflumio F, et al. Value of (18)F-FDG-PET/CT in patients with fever of unknown origin and unexplained prolonged inflammatory syndrome: a single Centre analysis experience. *Int J Clin Pract*. (2010) 64:55–60. doi: 10.1111/j.1742-1241.2008.01774.x

25. Kei PL, Kok TY, Padhy AK, Ng DC, Goh AS. [18F] FDG PET/CT in patients with fever of unknown origin: a local experience. *Nucl Med Commun*. (2010) 31:788–92. doi: 10.1097/MNM.0b013e32833d0281

26. Pijl JP, Glaudemans AWJM, Slart RHJA, Yakar D, Wouthuyzen-Bakker M, Kwee TC. FDG-PET/CT for detecting an infection focus in patients with bloodstream infection: factors affecting diagnostic yield. *Clin Nucl Med*. (2019) 44:99–106. doi: 10.1097/RLU.0000000000002381

27. Kagna O, Kurash M, Ghanem-Zoubi N, Keidar Z, Israel O. Does antibiotic treatment affect the diagnostic accuracy of 18F-FDG PET/CT studies in patients with suspected infectious processes? *J Nucl Med*. (2017) 58:1827–30. doi: 10.2967/jnumed.117.192062

28. Nielsen BD, Gormsen LC, Hansen IT, Keller KK, Therkildsen P, Hauge EM. Three days of high-dose glucocorticoid treatment attenuates large-vessel 18F-FDG uptake in large-vessel giant cell arteritis but with a limited impact on diagnostic accuracy. *Eur J Nucl Med Mol Imaging*. (2018) 45:1119–28. doi: 10.1007/s00259-018-4021-4

29. Nielsen AW, Hansen IT, Nielsen BD, Kjær SG, Blegvad-Nissen J, Rewers K, et al. The effect of prednisolone and a short-term prednisolone discontinuation for the diagnostic accuracy of FDG-PET/CT in polymyalgia rheumatica-a prospective study of 101 patients. *Eur J Nucl Med Mol Imaging*. (2024) 51:2614–24. doi: 10.1007/s00259-024-06697-8

30. Eynath Y, Halperin E, Buchrits S, Gafter-Gvili A, Bernstine H, Catalano O, et al. Predictors for spontaneous resolution of classical FUO in patients undergoing PET-CT. *Intern Emerg Med*. (2023) 18:367–74. doi: 10.1007/s11739-022-03171-x

31. Takeuchi M, Nihashi T, Gafter-Gvili A, García-Gómez FJ, Andres E, Blockmans D, et al. Association of 18F-FDG PET or PET/CT results with spontaneous remission in classic fever of unknown origin: a systematic review and meta-analysis. *Medicine (Baltimore)*. (2018) 97:e12909. doi: 10.1097/MD.0000000000012909

32. Knockaert DC, Vanderschueren S, Blockmans D. Fever of unknown origin in adults: 40 years on. *J Intern Med*. (2003) 253:263–75. doi: 10.1046/j.1365-2796.2003.01120.x

33. García-Vicente AM, Tello-Galán MJ, Amo-Salas M, Ros-Izquierdo J, Jiménez-Londoño GA, la Rosa Salas B, et al. Do clinical and laboratory variables have any impact on the diagnostic performance of 18F-FDG PET/CT in patients with fever of unknown origin? *Ann Nucl Med*. (2018) 32:123–31. doi: 10.1007/s12149-017-1226-8

34. Singh SB, Shrestha N, Bhandari S, Shrestha S, Shrestha B, Shrestha N, et al. [18F] FDG PET/CT for identifying the causes of fever of unknown origin (FUO). *Am J Nucl Med Mol Imaging*. (2024) 14:87–96. doi: 10.62347/OQQC6007

35. Pereira AMV, Husmann L, Sah B-R, Battegay E, Franzen D. Determinants of diagnostic performance of 18F-FDG PET/CT in patients with fever of unknown origin. *Nucl Med Commun*. (2016) 37:57–65. doi: 10.1097/MNM.0000000000000395

36. Kubota R, Yamada S, Kubota K, Ishiwata K, Tamahashi N, Ido T. Intratumoral distribution of fluorine-18-fluorodeoxyglucose in vivo: high accumulation in macrophages and granulation tissues studied by microautoradiography. *J Nucl Med*. (1992) 33:1972–80.

37. Tahara T, Ichiya Y, Kuwabara Y, Otsuka M, Miyake Y, Gunasekera R, et al. High [18F]-fluorodeoxyglucose uptake in abdominal abscesses: a PET study. *J Comput Assist Tomogr*. (1989) 13:829–31. doi: 10.1097/00004728-198909000-00014

38. FORSTROM L, DUNN W, MULLAN B, HUNG J, LOWE V, THORSON L. Biodistribution and dosimetry of [(18)F]fluorodeoxyglucose labelled leukocytes in normal human subjects. *Nucl Med Commun*. (2002) 23:721–5. doi: 10.1097/00006231-200208000-00004

39. Chen J, Xu D, Sun WJ, Wang WX, Xie NN, Ruan QR, et al. Differential diagnosis of lymphoma with 18F-FDG PET/CT in patients with fever of unknown origin accompanied by lymphadenopathy. *J Cancer Res Clin Oncol*. (2023) 149:7187–96. doi: 10.1007/s00432-023-04665-7

40. Liang J-H, Ding CY, Gale RP, Wang L, Xu J, Qu XY, et al. Prognostic value of whole-body SUVmax of nodal and extra-nodal lesions detected by 18F-FDG PET/CT in extra-nodal NK/T-cell lymphoma. *Oncotarget*. (2017) 8:1737–43. doi: 10.18632/oncotarget.13873

41. Xia J, Zhu HY, Liang JH, Ding CY, Wang L, Wu W, et al. The prognostic role of 18F-FDG PET/CT baseline quantitative metabolic parameters in peripheral T-cell lymphoma. *J Cancer*. (2019) 10:5805–11. doi: 10.7150/jca.30415

42. Singh N, Kumar R, Malhotra A, Bhalla AS, Kumar U, Sood R. Diagnostic utility of fluorodeoxyglucose positron emission tomography/computed tomography in pyrexia of unknown origin. *Indian J Nucl Med*. (2015) 30:204–12. doi: 10.4103/0972-3919.158528

43. Slart RHJA, Writing groupReviewer groupMembers of EANM CardiovascularMembers of EANM Infection & InflammationMembers of Committeeset al. FDG-PET/CT(a) imaging in large vessel vasculitis and polymyalgia rheumatica: joint procedural recommendation of the EANM, SNMMI, and the PET interest group (PIG), and endorsed by the ASNC. *Eur J Nucl Med Mol Imaging*. (2018) 45:1250–69. doi: 10.1007/s00259-018-3973-8

44. Lee S-W, Kim SJ, Seo Y, Jeong SY, Ahn BC, Lee J. F-18 FDG PET for assessment of disease activity of large vessel vasculitis: a systematic review and meta-analysis. *J Nucl Cardiol*. (2019) 26:59–67. doi: 10.1007/s12350-018-1406-5

45. Mizoe A, Sakaue J, Takahara N. Why does activated partial thromboplastin time prolongation occur in severe fever with thrombocytopenia syndrome? *BMJ Case Rep*. (2020) 13:e235447. doi: 10.1136/bcr-2020-235447

46. Lin S-W, Chuang YC, Lin YS, Lei HY, Liu HS, Yeh TM. Dengue virus nonstructural protein NS1 binds to prothrombin/thrombin and inhibits prothrombin activation. *J Infect*. (2012) 64:325–34. doi: 10.1016/j.jinf.2011.11.023

47. Zhu W, Cao W, Zheng X, Li X, Li Y, Chen B, et al. The diagnostic value of 18 F-FDG PET/CT in identifying the causes of fever of unknown origin. *Clin Med*. (2020) 20:449–53. doi: 10.7861/clinmed.2020-0268

48. Crouzet J, Boudousq V, Lechiche C, Pouget JP, Kotzki PO, Collombier L, et al. Place of 18F-FDG-PET with computed tomography in the diagnostic algorithm of patients with fever of unknown origin. *Eur J Clin Microbiol Infect Dis*. (2012) 31:1727–33. doi: 10.1007/s10096-011-1440-6

49. Bleeker-Rovers CP, Oyen WJG. Clinical value of FDG PET in patients with fever of unknown origin and patients suspected of focal infection or inflammation. *Eur J Nucl Med Mol Imaging*. (2004) 31:29–37. doi: 10.1007/s00259-003-1338-3

50. Mourad O, Palda V, Detsky AS. A comprehensive evidence-based approach to fever of unknown origin. *Arch Intern Med*. (2003) 163:545–51. doi: 10.1001/archinte.163.5.545

frontiers | Frontiers in Medicine

TYPE Original Research
PUBLISHED 07 April 2025
DOI 10.3389/fmed.2025.1548132

OPEN ACCESS

EDITED BY
Nataliya Lutay,
Skåne University Hospital, Sweden

REVIEWED BY
Gayane Aghakhanyan,
University of Pisa, Italy
Mahboubeh Nabavinia,
The Research Institute at Nationwide Children's Hospital, United States
Aditi Mulgaonkar,
University of Texas Southwestern Medical Center, United States
Pengpeng Zhang,
Nanjing Medical University, China

*CORRESPONDENCE
Frezghi Habte
✉ fhabte@stanford.edu
Arutselvan Natarajan
✉ anatarajan@stanford.edu

RECEIVED 19 December 2024
ACCEPTED 20 March 2025
PUBLISHED 07 April 2025

CITATION
Habte F and Natarajan A (2025) Ultra-low dose immunoPET using ^{64}Cu-rituximab tracer for a human CD20 mouse model.
Front. Med. 12:1548132.
doi: 10.3389/fmed.2025.1548132

Ultra-low dose immunoPET using ^{64}Cu-rituximab tracer for a human CD20 mouse model

Frezghi Habte* and Arutselvan Natarajan*

Department of Radiology, Stanford School of Medicine, Stanford University, Stanford, CA, United States

Antibodies (Abs) and their fragments can be labeled with PET radioisotope (immunoPET) for *in vivo* diagnostic imaging. Compared to the conventional FDG-PET, immunoPET can be designed to target *in vivo* cancer-specific antigen expression levels for various tumors and metastasis, which makes immunoPET (iPET) a powerful technique for molecular imaging and therapy monitoring. However, achieving the optimal dose to minimize radioisotope toxicity without compromising the visualization of the smallest tumor is challenging. To find an ultra-minimal tracer dose, we have developed a novel iPET with an intact rituximab Ab labeled with ^{64}Cu to image human CD20 (hCD20) in a transgenic mouse model for non-Hodgkin's lymphoma (NHL) imaging. Using phantom and *in vivo* mouse models, we optimized the minimal dose that can be administered in a mouse using a high-specific iPET tracer prepared from ^{64}Cu-rituximab. A phantom study was used to characterize the scanner capability and limit for imaging using low doses. An ultra-minimal dose administered in a mouse model showed good image quality with high signal-to-noise ratio without compromising quantitative accuracy. The phantom study with below 50 μCi dose level indicated a slight increase in variability due to reduced dose specifically for target regions with lower uptakes (<3:1 ratio) relative to the background. *In vivo* study performed with four groups of mice (n = 3), each group injected with ~90, ~50, ~25, and ~10 μCi showed a linear increase of tracer uptake measured as percentage injected dose per gram (%ID/g). This tracer has shown high specific uptake in the spleen, where most B-cells are engineered to express hCD20. The study demonstrated that the lowest dose threshold limit for ^{64}Cu-antibody-based iPET was about 25 μCi while achieving a high-quality image and quantitative accuracy.

KEYWORDS

immunoPET, ultra low dose, PET/CT imaging, human CD20, dosimetry

1 Introduction

Immuno-positron emission tomography (immunoPET) a.k.a. antibody-based PET molecular imaging strategy is performed taking advantage of the high specificity of monoclonal antibody (mAb) and the inherent high sensitivity of PET (1–10). Several radionuclides and mAbs have been exploited to develop immunoPET (iPET) probes, some of which have already been successfully translated for clinical use (4, 7, 8, 11–13). iPET is becoming the method of choice for imaging specific tumor markers, immune cells, immune checkpoints, inflammatory processes, and guide mAb-based therapy (12, 14–18). Superior to conventional FDG-PET, immunoPET can characterize and quantify antigen expression specific to a tumor type, making iPET a powerful molecular strategy for tracking, visualizing, and measuring the tumor gene expression (18–24). FDG-PET, taken up into the body through glucose transporters, has very poor specificity and can be seen in areas with high levels of metabolism and glycolysis,

such as sites with inflammation or tissue repair (23–28). iPET has the potential to image specific diseases and quantify them for clinical diagnostic applications. Several iPETs are already in clinical investigations for cancer staging and therapy monitoring using FDA-approved mAbs (4, 29). We have recently developed a novel iPET tracer using mAb (rituximab) labeled with ^{64}Cu and ^{89}Zr to image human CD20 as a marker for NHL. Evaluation of these new tracers in a transgenic mouse model and humans showed specific imaging of hCD20-expressing B-cells (30–33). Such new iPET tracers in development have immense potential in the clinical setting as the antibody can bring radiation directly to the lymphoma cells (34–38).

When compared to FDG-PET, the iPET is linked with long-half-life radioisotopes to match the slow uptake and clearance of antibodies selected for iPET imaging. As a result, the radiation burden on the patient when using antibody-based tracers is relatively high compared to conventional rapidly clearing PET tracers such as [^{18}F]FDG (35, 36). This limitation could hinder the development and practical application of antibody-based tracers, and therefore, it is paramount to reduce the radiation exposure whenever feasible. Advances in iPET imaging uses modified antibody fragments with small size and shorter elimination half-life allowing the use of short half-life radioligands to perform iPET imaging on the same day while reducing radiation exposure (38–43).

Engineered smaller size affibody proteins and antibody fragments retaining the essential specificities and affinities of a full antibodies, have become desirable pharmacokinetics for PET imaging using various options of PET isotopes (3, 38, 40). While these new iPET imaging strategies will play a big role in reducing radiation exposure, we also believe that administration of an optimized minimum dose could also substantially decrease the overall radiation burden on the patient (43–45). However, since PET inherently produces noisy images, it is challenging to optimize the minimum dose (46–49). Reducing the injected dose amount may further compromise the image quality (44, 45). Since PET measures the biodistribution of a particular tracer administrated to the body, the number of detected tracers counts on a selected region of interest defines the image quality and quantitative accuracy. Hence, dose administration could be specific to each tracer behavior or condition of the study. This means, there is a limit and variation to the minimum dose required that provides adequate counts for obtaining a non-biased signal-to-noise ratio and quantitative diagnostic value specific to each study (45). To evaluate this more quantitatively, in this study we evaluated the ultra-low injected dosage capability of iPET using phantom and live animal models. The combined effect of the high sensitivity of PET/CT and the high specificity of iPET tracers (32, 43) may allow the administration of ultra-low doses without compromising the image quality and quantitative accuracy.

2 Materials and methods

2.1 iPET tracer and animal model

GMP grade ^{64}Cu labeled iPET tracer preparation was already reported (33, 50). To test the tracer capability for low-dose diagnostic imaging, we have used a transgenic mouse model that expresses hCD20. In this mouse model, hCD20 is expressed in B cells homing in the spleen, providing the highest tracer uptake. For this tracer development, the anti-hCD20 antibody (IgG; rituximab) was conjugated to DOTA for radiolabeling of ^{64}Cu. In another study, we have reported the evaluation of the dosimetry of ^{64}Cu-mAb tracer in the hNSG mouse model using the standard average injected dose of 100 μCi (32).

2.2 Phantom study

To evaluate the ultra-low dose counting accuracy of the scanner, we used a cylindrical phantom (Data Spectrum Corp) with a 40 mm inner diameter, 82 mm height, and four micro-hollow fillable spheres (Figure 1). The cylindrical phantom was filled with water and ~95 μCi of ^{64}Cu to provide ~1 μCi/cc radiotracer concentration as a background signal for the phantom study. To represent the foreground signal and emulate high tracer uptake in an animal model, we prepared a 20 ml methanol and ~150 μCi of ^{64}Cu solution. Due to its lower density relative to water, methanol was used as a contrast agent to provide slight CT image contrast in the PET/CT imaging. The mix provided ~7.5 μCi/cc ^{64}Cu tracer concentration to fill each hollow four spheres (~1, 0.5, 0.25, and 0.031 ml). For the first scan, the total initial activity of the background and foreground was ~92 μCi. The Phantom was scanned using Inveon MicroPET/CT (Preclinical Solutions; Siemens Healthcare Molecular Imaging, Knoxville, TN) for 30 min at different time points while decaying over 48 h. Three image frames of 5, 10, and 20 min from the acquired images were reconstructed using the Ordered-subset expectation maximization (OSEM 2D) algorithm (51). Inveon Research Workspace (IRW) analysis software (Siemens Healthcare) was used for analysis and quantitation. Regions of Interest (ROI) were drawn over the four spheres and the background to obtain

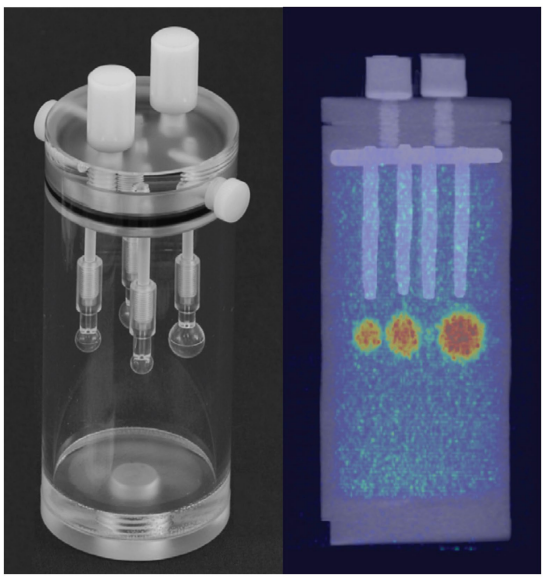

FIGURE 1
Left, Cylindrical tube with four insertable fillable hollow spheres of different sizes (~1, 0.5, 0.25, and 0.031 ml) used as a phantom. Right, PET/CT image of phantom after filling the cylinder tube with low radiotracer concentration (~1 μCi/cc) as background and hollow spheres with ~7.5 μCi/cc as foreground uptake.

the mean radiotracer distribution (μCi/cc). Doses at each scan time were calculated from the decayed ^{64}Cu tracer.

2.3 Animal study

Animal studies were performed in compliance with approval from the Administrative Panel on Laboratory Animal Care (APLAC) at Stanford University. The hCD20 transgenic mice models (Genentech, South San Francisco, CA) were used for the experiment. Prior to the animal study, transgenic mice were screened by RT-PCR to confirm the expression of hCD20 positivity. We injected 8–10, 20–25, 45–55, and 75–80 μCi via the tail vein in a group of four mice for each dose. After radiotracer administration, the animals were imaged at ~1–5, 15, and 24 h using Inveon MicroPET/CT within 20–30 min intervals.

2.4 PET imaging and analysis

PET imaging was performed on the Inveon MicroPET/CT system following standard routine acquisition protocol in our facility. The CT scan was acquired using an 80 kVp and 500 μA, two-bed position, half scan 220° of rotation, and 120 projections per bed position for both anatomic reference and PET attenuation correction. PET scans were performed using the default settings of a coincidence timing window of 3.4 ns and an energy window of 350 to 650 keV. Static 5 min was used to acquire first-time point acquisitions (1–5 h post-injection), followed by static 10 min acquisition for later time points (15 and 24 h). The images were reconstructed using the OSEM 2D algorithm. Using IRW, manual three-dimensional regions of interest (ROIs) were drawn over the heart, liver, and leg muscles. A semi-automatic ROI histogram-based segmentation technique was used to segment the spleen to reduce reader variability. The average radioactivity concentration in the ROI was obtained from the mean pixel values within the ROI volume, which is converted to a percentage injected dose per gram of tissue (%ID/g).

2.5 Statistical analysis

The quantitative data were expressed as mean ± SD. Means were compared using the student *t* test. A 95% confidence level was chosen to determine the significance between groups, with *p* values of less than 0.05 indicating significant differences.

3 Results

3.1 Phantom study

Figure 2 shows a qualitative comparison of phantom images between conventional and ultra-low doses at scan time. After a suitable image intensity adjustment, the effect of low ultra-low dose <10 μCi shows nonhomogeneous uptake in all spheres. However, all hollow spheres, including the smallest (0.031 ml, S4), which shows the lowest uptake due to the partial volume effect, showed higher uptake than the background. Figure 3 quantitatively assesses the mean values extracted from ROIs drawn over each hollow sphere based on the CT images. The computed mean ROI vs. dose at scan time showed comparable linearity with the expected partial volume effect (Figure 3A). For comparison, we also computed the coefficient of variance of images reconstructed at different times of acquisition (5, 10, and 20 min) for each dose (Figure 3B, showing only the S2 (second largest) and S4 (smallest) sphere sizes). The result indicates that the computed variability increases slightly for doses less than 40 μCi for larger spheres independent of scan duration with expected improvement for images acquired with longer acquisition time (10 and 20 min).

3.2 Animal study

In vivo, animal imaging using the target-specific ^{64}Cu iPET radiotracer, as expected, showed high uptake in the spleen for all dose amounts (Figure 4A). Relatively low uptake was also seen in the heart and liver. The spleen consistently showed increased uptake in %ID/g of 3 to 10 folds relative to the liver with a decreased injected dose (Figure 4D), showing improved tracer specificity and image contrast. In contrast, the spleen-to-liver uptake ratio steadily increased (3–5 folds) with a decrease of dose up to 20 μCi. The spleen-to-liver uptake increased non-linearly over nine-fold for ultra-low injected dose <10 μCi ($p < 0.03$). At 15 h post-injection (p.i.), high tracer uptake in the spleen was obtained (Figure 4D).

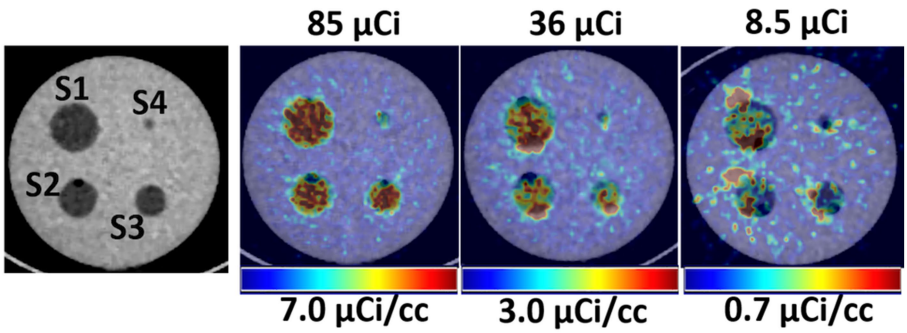

FIGURE 2
Left, CT images showing the hollow fillable spheres of the phantom. Right, Qualitative comparison of PET/CT images of the phantom for selected three low doses.

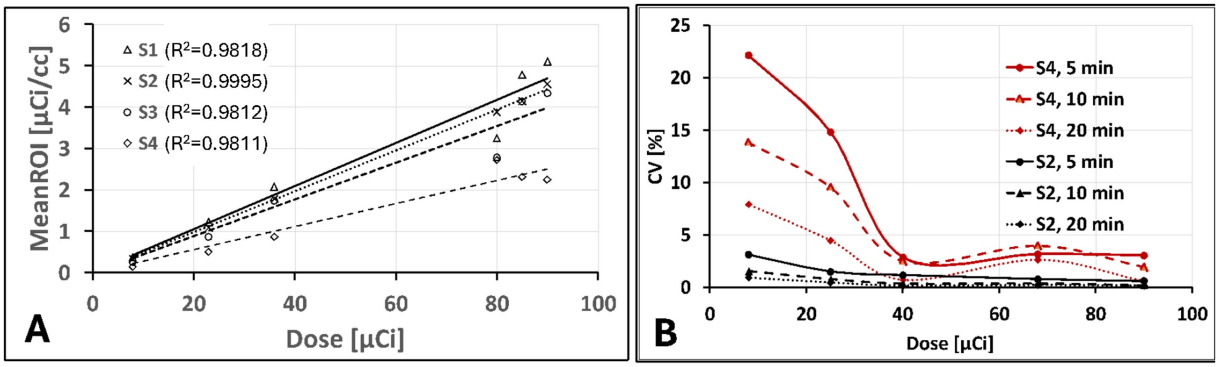

FIGURE 3
Phantom images quantitative assessments: **(A)** extracted mean ROI value vs. administered dose showing an expected linear increase with lower slop for smaller size spheres due to partial volume effect and **(B)** Computed percentage coefficient of variation showing only for S2 (second to largest) and S4 (smallest) sphere sizes for 5, 10, 20 min acquisition time as function of administrated dose.

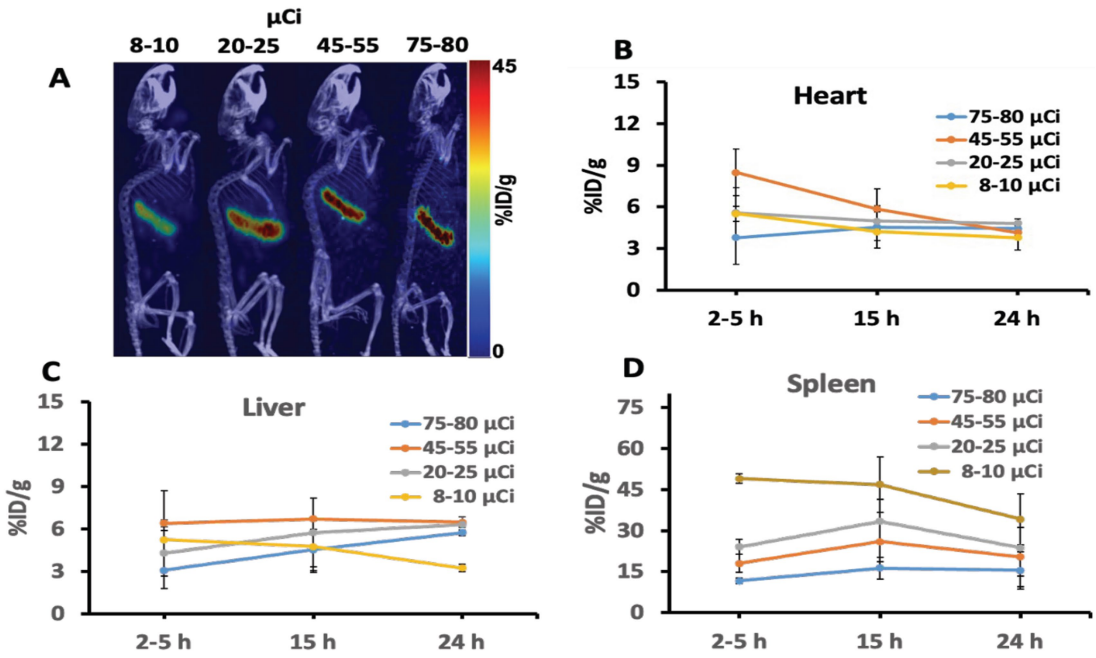

FIGURE 4
(A) Representative iPET/CT images showing tracer uptake 24 hr post injection in the spleen of the humanized transgenic mice. Each mice group received doses (ranging from 8 to 80 µCi). **(B–D)** Depicted the iPET signal corresponding to the tracer uptake from the heart, liver, and spleen of the mouse at different time points.

Figure 5 shows a quantitative assessment of inter-subject variability. For the spleen, we observed similar inter-subject variability with slight variation between doses (Figure 5A) and slightly higher variability (CV = ~30%) at the early time points (1 to 5 h). At the later time point (24 h.), the variability drops on average to one-third (CV = ~10%) due to tracer clearance (Figure 5B).

4 Discussion

As the most popular molecular imaging tool, PET/CT imaging has always been attractive for both preclinical and clinical applications due to its superior sensitivity. However, the inability to accurately determine the optimum dose that may be administrated to the subject may make to operate non optimally especially regarding minimization of radiation exposure to the subject and associated cost of the target tracer (43, 45). Specifically, the challenge is to find a standard minimum dosage (SMD) that is sufficient to acquire clinically relevant diagnostic information, which inherently involves multiple factors. Assuming a fixed scanner sensitivity limited by its specific geometric configuration and detector characteristics, the optimum minimum dosage may vary on several image acquisition parameters such as reconstruction type, subject size and positioning, and scanner acquisition protocols (43). Within the selected optimum acquisition

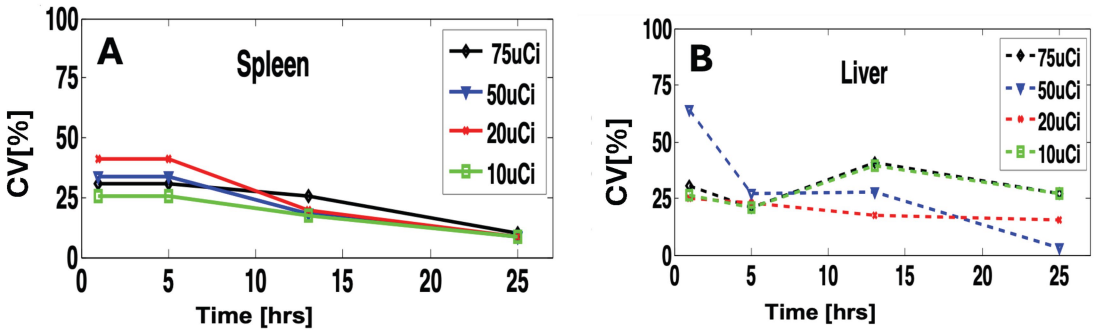

FIGURE 5
Quantitative comparison of variability within different doses and scan time. **(A)** for the spleen and **(B)** for the liver.

and reconstruction parameters, dosage may also vary with the specific choice of radiopharmaceutical and its associated factors, including the tracer uptake specificity, clearance pattern, molecular size of the tracer, tracer half-life, and others.

Imaging of iPET using mAb labeled with Cu-64 or Zr-89 isotope provides relatively high specificity compared to the non-specific tracer such as FDG. This is because mAbs are specifically designed to bind to targeted organs or tumors selectively. Hence, a small tracer dose (26, 32) could specifically bind to the intended *in vivo* target organ or receptors. Using phantom and animal studies, our results indicated that as low as 20 μCi of tracer dose can be sufficient to image using the most commonly available MicroPET/CT scanners without significantly affecting or compromising image quality and quantitative value. Furthermore, iPET animal imaging has shown better image contrast with reduced background noise at lower doses compared to conventionally administered doses (~100 μCi per mouse). The overall results (Figure 4) indicate that an optimal suitable lower dose may improve image quality and quantitative accuracy while reducing radiation exposure. It is also expected to improve the image quality at lower doses by extending the scanning time (Figure 3B).

In the animal study, the spleen express hCD20 marker for NHL, showing the highest uptake of iPET tracer which is consistent as reported elsewhere (33, 50). This gives a promising application for tracing and tracking the metabolic activity in tumors expressing antigen CD20. This tracer has been specifically developed to target B-lymphocytes expressing hCD20 seen in the spleen with increased numbers in non-Hodgkin's Lymphoma (32). It was anticipated to accumulate in the spleen with some lower uptakes in the heart and liver due to their roles in removing toxins from the body. If the tracer uptake in the spleen saturates, the extra tracer clears through the liver. Hence, the increased amount of tracer doses tends to bind on other organs non-specifically, such as the uptake seen in the liver (Figure 4C). On the other hand, lower administrated doses show to decrease non-specific organs uptake while increasing target-specificity. Spleen-to-liver ratios demonstrated distinctively that even at the lowest doses (<8 μCi) and after 24 h of decay, the spleen shows strong uptake with relatively good image quality. An estimated dose of 20 to 25 μCi, as reported in this study, could be assumed as the lower dose limit that may provide comparable image quality and accuracy relative to the commonly used higher doses for *in vivo* mouse iPET imaging. This study provides initial validation for the important and challenging tradeoffs in PET imaging between image quality and radiation exposure. The study demonstrates that with increased specificity of specific tracer a significantly lower dose up to one fourth as estimated in Figure 4 relative to conventional dose (~100 μCi) may be used without changes of the imaging protocols and compromising the image quality. Minimizing radiation exposure reduces the risks associated with ionizing radiation and the overall imaging costs, but it is also very important to have good image quality practically for all clinical and research applications (47, 48). We also expect this study to provide a bases for further validation of the optimum minimum dose for clinical practice, which is relatively more important due to the ever-increasing concerns related to radiation exposure in patients requiring multiple examinations or those at a higher lifetime risk for developing cancer (e.g., pediatric patients) (49).

5 Conclusion

Our study provides the basis for the initial validation of the potential usage of ultra-low-dose clinical practices using target-specific iPET imaging studies without impacting the overall image quality and quantitative accuracy. Low doses may also improve specificity and reduce radiation in non-targeted areas and non-specific uptake by other clearing organs such as the liver and kidney. With the evolving research on early cancer detection and immunotherapies, imaging with more targeted tracers will help reduce misdiagnoses and unnecessary radiation exposure. This study reveals that optimal low-dose estimation is vital to all diagnostic imaging tracers prior to clinical translation studies, saving tracer costs and reducing systemic radiation exposure.

Data availability statement

The raw data supporting the conclusions of this article will be made available by the authors, without undue reservation.

Ethics statement

The animal study was approved by Administrative Panel on Laboratory Animal Care (APLAC) at Stanford University. The study

was conducted in accordance with the local legislation and institutional requirements.

Author contributions

FH: Conceptualization, Data curation, Formal analysis, Funding acquisition, Methodology, Project administration, Software, Validation, Visualization, Writing – original draft, Writing – review & editing. AN: Conceptualization, Data curation, Funding acquisition, Methodology, Software, Validation, Writing – review & editing.

Funding

The author(s) declare that financial support was received for the research and/or publication of this article. We thank the Canary Center for Early Cancer Detection, the National Cancer Institute (P50CA114747) and the Stanford Cancer Institute Support Grant (5P30CA124435-10) for supporting and funding this research.

Acknowledgments

We acknowledge the support of Stephani Stepane, a research intern, for performing image analysis. MicroPET/CT imaging was performed in the Stanford Center for Innovation in *In-Vivo* Imaging.

Conflict of interest

The authors declare that the research was conducted in the absence of any commercial or financial relationships that could be construed as a potential conflict of interest.

Generative AI statement

The author(s) declare that no Gen AI was used in the creation of this manuscript.

Publisher's note

Supplementary material

The Supplementary material for this article can be found online at: https://www.frontiersin.org/articles/10.3389/fmed.2025.1548132/full#supplementary-material

References

1. Wei W, Rosenkrans ZT, Liu J, Huang G, Luo QY, Cai W. ImmunoPET: concept, design, and applications. *Chem Rev*. (2020) 120:3787–851. doi: 10.1021/acs.chemrev.9b00738

2. Rolle AM, Hasenberg M, Thornton CR, Solouk-Saran D, Männ L, Weski J, et al. ImmunoPET/MR imaging allows specific detection of *Aspergillus fumigatus* lung infection *in vivo*. *Proc Natl Acad Sci*. (2016) 113:E1026–33. doi: 10.1073/pnas.1518836113

3. Manafi-Farid R, Ataeinia B, Ranjbar S, Jamshidi Araghi Z, Moradi MM, Pirich C, et al. ImmunoPET: antibody-based PET imaging in solid tumors. *Front Med*. (2022) 9:916693. doi: 10.3389/fmed.2022.916693

4. Mohr P, van Sluis J, Lub-de Hooge MN, Lammertsma AA, Brouwers AH, Tsoumpas C. Advances and challenges in immunoPET methodology. *Front Nucl Med*. (2024) 4:1360710. doi: 10.3389/fnume.2024.1360710

5. Beckford-Vera DR, Flavell RR, Seo Y, Martinez-Ortiz E, Aslam M, Thanh C, et al. First-in-human immunoPET imaging of HIV-1 infection using 89Zr-labeled VRC01 broadly neutralizing antibody. *Nat Commun*. (2022) 13:1219. doi: 10.1038/s41467-022-28727-5

6. Wu AM, Pandit-Taskar N. ImmunoPET: harnessing antibodies for imaging immune cells. *Mol Imaging Biol*. (2022) 24:181–97. doi: 10.1007/s11307-021-01652-7

7. Bhargava KK, Acharya SA. Labeling of monoclonal antibodies with radionuclides. *Semin Nucl Med*. (1989) 19:187–201. doi: 10.1016/S0001-2998(89)80013-3

8. Chomet M, van Dongen GAMS, Vugts DJ. State of the art in radiolabeling of antibodies with common and uncommon Radiometals for preclinical and clinical Immuno-PET. *Bioconjug Chem*. (2021) 32:1315–30. doi: 10.1021/acs.bioconjchem.1c00136

9. Giammarile F, Delgado Bolton RC, Novruzov F, Paez D. ImmunoPET in high-grade neuroendocrine tumours. *Lancet Oncol*. (2024) 25:949–50. doi: 10.1016/S1470-2045(24)00314-0

10. Fan X, Nijman HW, de Bruyn M, Elsinga PH. ImmunoPET provides a novel way to visualize the CD103(+) tissue-resident memory T cell to predict the response of immune checkpoint inhibitors. *EJNMMI Res*. (2024) 14:5. doi: 10.1186/s13550-023-01062-6

11. Wei W, Huang W. ImmunoPET imaging of Trop2 in solid tumors: a translational study. *J Nucl Med*. (2024) 65:242012. doi: 10.1007/s00259-023-06454-3

12. Abenavoli EM, Linguanti F, Calabretta R, Delgado Bolton RC, Berti V, Lopci E. Clinical application of ImmunoPET targeting checkpoint inhibitors. *Cancer*. (2023) 15:5675. doi: 10.3390/cancers15235675

13. Parakh S, Lee ST, Gan HK, Scott AM. Radiolabeled antibodies for Cancer imaging and therapy. *Cancers*. (2022) 14:1454. doi: 10.3390/cancers14061454

14. Yang K, Lu R, Mei J, Cao K, Zeng T, Hua Y, et al. The war between the immune system and the tumor - using immune biomarkers as tracers. *Biomark Res*. (2024) 12:51. doi: 10.1186/s40364-024-00599-5

15. Ephraim R, Fraser S, Nurgali K, Apostolopoulos V. Checkpoint markers and tumor microenvironment: what do we know? *Cancer*. (2022) 14:3788. doi: 10.3390/cancers14153788

16. Topalian SL, Taube JM, Anders RA, Pardoll DM. Mechanism-driven biomarkers to guide immune checkpoint blockade in cancer therapy. *Nat Rev Cancer*. (2016) 16:275–87. doi: 10.1038/nrc.2016.36

17. Wang Y, Zhang H, Liu C, Wang Z, Wu W, Zhang N, et al. Immune checkpoint modulators in cancer immunotherapy: recent advances and emerging concepts. *J Hematol OncolJ Hematol Oncol*. (2022) 15:111. doi: 10.1186/s13045-022-01325-0

18. Rakhshandehroo T, Smith BR, Glockner HJ, Rashidian M, Pandit-Taskar N. Molecular immune targeted imaging of tumor microenvironment. *Nano*. (2022) 6:286–305. doi: 10.7150/ntno.66556

19. Alam IS, Simonetta F, Scheller L, Mayer AT, Murty S, Vermesh O, et al. Visualization of activated T cells by OX40-ImmunoPET as a strategy for diagnosis of acute graft-versus-host disease. *Cancer Res*. (2020) 80:4780–90. doi: 10.1158/0008-5472.CAN-20-1149

20. Keinänen O, Sarrett SM, Delaney S, Rodriguez C, Dayts EJ, Capone E, et al. Visualizing Galectin-3 binding protein expression with ImmunoPET. *Mol Pharm*. (2023) 20:3241–8. doi: 10.1021/acs.molpharmaceut.3c00241

21. Kist de Ruijter L, van de Donk PP, Hooiveld-Noeken JS, Giesen D, Elias SG, Lub-de Hooge MN, et al. Whole-body CD8+ T cell visualization before and during cancer immunotherapy: a phase 1/2 trial. *Nat Med*. (2022) 28:2601–10. doi: 10.1038/s41591-022-02084-8

22. Zhou M, Chen B, Lu C, Yang J, Liu P, Wang X, et al. ImmunoPET imaging of LAG-3 expression in tumor microenvironment with 68Ga-labelled cyclic peptides tracers: from bench to bedside. *J Immunother Cancer*. (2024) 12:9153. doi: 10.1136/jitc-2024-009153

23. Ye B, Fan J, Xue L, Zhuang Y, Luo P, Jiang A, et al. iMLGAM: integrated machine learning and genetic algorithm-driven multiomics analysis for pan-cancer immunotherapy response prediction. *iMeta*. (2025) 4:e70011. doi: 10.1002/imt2.70011

24. Sonanini D, Schwenck J, Blaess S, Schmitt J, Maurer A, Ehrlichmann W, et al. CD19-immunoPET for noninvasive visualization of CD19 expression in B-cell lymphoma patients. *Biomark Res*. (2024) 12:50. doi: 10.1186/s40364-024-00595-9

25. Ancey PB, Contat C, Meylan E. Glucose transporters in cancer – from tumor cells to the tumor microenvironment. *FEBS J*. (2018) 285:2926–43. doi: 10.1111/febs.14577

26. Bailly C, Gouard S, Lacombe M, Remaud-Le Saëc P, Chalopin B, Bourgeois M, et al. Comparison of Immuno-PET of CD138 and PET imaging with (64) CuCl(2) and (18) F-FDG in a preclinical syngeneic model of multiple myeloma. *Oncotarget*. (2018) 9:9061–72. doi: 10.18632/oncotarget.23886

27. Evangelista L, Bianchi A, Annovazzi A, Sciuto R, Di Traglia S, Bauckneht M, et al. ITA-IMMUNO-PET: the role of [18F]FDG PET/CT for assessing response to immunotherapy in patients with some solid tumors. *Cancer*. (2023) 15:878. doi: 10.3390/cancers15030878

28. Rousseau C, Goldenberg DM, Colombié M, Sébille JC, Meingan P, Ferrer L, et al. Initial clinical results of a novel Immuno-PET Theranostic probe in human epidermal growth factor receptor 2-negative breast Cancer. *J Nucl Med Off Publ Soc Nucl Med*. (2020) 61:1205–11. doi: 10.2967/jnumed.119.236000

29. Slebe M, Pouw JEE, Hashemi SMS, der Houven M-v, van Oordt CW, Yaqub MM, et al. Current state and upcoming opportunities for immunoPET biomarkers in lung cancer. *Lung Cancer*. (2022) 169:84–93. doi: 10.1016/j.lungcan.2022.05.017

30. Mayer AT, Natarajan A, Gordon SR, Maute RL, McCracken MN, Ring AM, et al. Practical Immuno-PET radiotracer design considerations for human immune checkpoint imaging. *J Nucl Med*. (2017) 58:538–46. doi: 10.2967/jnumed.116.177659

31. Ilovich O, Natarajan A, Sathirachinda A, Kimura R, Srinivasan A, Gebauer M, et al. Development and validation of an immuno-PET tracer for patient stratification and therapy monitoring of antibody-drug conjugate therapy. *J Clin Oncol*. (2013) 31:11006. doi: 10.1200/jco.2013.31.15_suppl.11006

32. Natarajan A, Patel CB, Habte F, Gambhir SS. Dosimetry prediction for clinical translation of 64Cu-Pembrolizumab ImmunoPET targeting human PD-1 expression. *Sci Rep*. (2018) 8:633. doi: 10.1038/s41598-017-19123-x

33. Natarajan A, Mayer AT, Reeves RE, Nagamine CM, Gambhir SS. Development of novel ImmunoPET tracers to image human PD-1 checkpoint expression on tumor-infiltrating lymphocytes in a humanized mouse model. *Mol Imaging Biol*. (2017) 19:903–14. doi: 10.1007/s11307-017-1060-3

34. Gosmann D, Russelli L, Weber WA, Schwaiger M, Krackhardt AM, D'Alessandria C. Promise and challenges of clinical non-invasive T-cell tracking in the era of cancer immunotherapy. *EJNMMI Res*. (2022) 12:5. doi: 10.1186/s13550-022-00877-z

35. Quinn B, Dauer Z, Pandit-Taskar N, Schoder H, Dauer LT. Radiation dosimetry of 18F-FDG PET/CT: incorporating exam-specific parameters in dose estimates. *BMC Med Imaging*. (2016) 16:41. doi: 10.1186/s12880-016-0143-y

36. Knowles SM, Wu AM. Advances in immuno-positron emission tomography: antibodies for molecular imaging in oncology. *J Clin Oncol*. (2012) 30:3884–92. doi: 10.1200/JCO.2012.42.4887

37. van Rij CM, Frielink C, Goldenberg DM, Sharkey RM, Franssen GM, Lütje S, et al. Pretargeted ImmunoPET of prostate Cancer with an anti-TROP-2 x anti-HSG bispecific antibody in mice with PC3 xenografts. *Mol Imaging Biol*. (2015) 17:94–101. doi: 10.1007/s11307-014-0772-x

38. Fu R, Carroll L, Yahioglu G, Aboagye EO, Miller PW. Antibody fragment and Affibody ImmunoPET imaging agents: Radiolabelling strategies and applications. *ChemMedChem*. (2018) 13:2466–78. doi: 10.1002/cmdc.201800624

39. Touchefeu Y, Bailly C, Frampas E, Eugène T, Rousseau C, Bourgeois M, et al. Promising clinical performance of pretargeted immuno-PET with anti-CEA bispecific antibody and gallium-68-labelled IMP-288 peptide for imaging colorectal cancer metastases: a pilot study. *Eur J Nucl Med Mol Imaging*. (2021) 48:874–82. doi: 10.1007/s00259-020-04989-3

40. Bansal A, Lavoie RR, Lucien F, Kethamreddy M, Wootla B, Dong H, et al. Synthesis and evaluation of anti-PD-L1-B11 antibody fragments for PET imaging of PD-L1 in breast cancer and melanoma tumor models. *Sci Rep*. (2024) 14:19561. doi: 10.1038/s41598-024-70385-8

41. Zettlitz KA, Salazar FB, Yamada RE, Trinh KR, Vasuthasawat A, Timmerman JM, et al. 89Zr-ImmunoPET shows therapeutic efficacy of anti-CD20-IFNα fusion protein in a murine B-cell lymphoma model. *Mol Cancer Ther*. (2022) 21:607–15. doi: 10.1158/1535-7163.MCT-21-0732

42. Triumbari EKA, Morland D, Laudicella R, Baucknehtt M, Albano D, Annunziata S. Clinical applications of Immuno-PET in lymphoma: a systematic review. *Cancers*. (2022) 14:3488. doi: 10.3390/cancers14143488

43. Karakatsanis NA, Fokou E, Tsoumpas C. Dosage optimization in positron emission tomography: state-of-the-art methods and future prospects. *Am J Nucl Med Mol Imaging*. (2015) 5:527–47.

44. Nguyen NC, Vercher-Conejero JL, Sattar A, Miller MA, Maniawski PJ, Jordan DW, et al. Image quality and diagnostic performance of a digital PET prototype in patients with oncologic diseases: initial experience and comparison with analog PET. *J Nucl Med Off Publ Soc Nucl Med*. (2015) 56:1378–85. doi: 10.2967/jnumed.114.148338

45. Yan J, Schaefferkoetter J, Conti M, Townsend D. A method to assess image quality for low-dose PET: analysis of SNR, CNR, bias and image noise. *Cancer Imaging*. (2016) 16:26. doi: 10.1186/s40644-016-0086-0

46. Zaman MU, Fatima N, Zaman A, Zaman U, Tahseen R. Significantly low effective dose from 18FDG PET/CT scans using dose reducing strategies: "lesser is better". *Asian Pac J Cancer Prev*. (2016) 17:3465–8. doi: 10.3390/cancers15215173

47. Molinos C, Sasser T, Salmon P, Gsell W, Viertl D, Massey JC, et al. Low-dose imaging in a new preclinical Total-body PET/CT scanner. *Front Med*. (2019) 6:88. doi: 10.3389/fmed.2019.00088

48. Chaudhari AS, Mittra E, Davidzon GA, Gulaka P, Gandhi H, Brown A, et al. Low-count whole-body PET with deep learning in a multicenter and externally validated study. *Npj Digit Med*. (2021) 4:127. doi: 10.1038/s41746-021-00497-2

49. Catana C. The dawn of a new era in low-dose PET imaging. *Radiology*. (2019) 290:657–8. doi: 10.1148/radiol.2018182573

50. Natarajan A, Mayer AT, Xu L, Reeves RE, Gano J, Gambhir SS. Novel radiotracer for ImmunoPET imaging of PD-1 checkpoint expression on tumor infiltrating lymphocytes. *Bioconjug Chem*. (2015) 26:2062–9. doi: 10.1021/acs.bioconjchem.5b00318

51. Zhu YM. Ordered subset expectation maximization algorithm for positron emission tomographic image reconstruction using belief kernels. *J Med Imaging Bellingham Wash*. (2018) 5:044005. doi: 10.1117/1.JMI.5.4.044005

frontiers | Frontiers in Neuroimaging

TYPE Original Research
PUBLISHED 31 October 2025
DOI 10.3389/fnimg.2025.1613078

OPEN ACCESS

EDITED BY
Nataliya Lutay,
Skåne University Hospital, Sweden

REVIEWED BY
Yaode He,
Zhejiang University, China
Chen Ping,
Yan'an University, China

*CORRESPONDENCE
Maximilian Thormann
✉ maximilian.thormann@charite.de

†These authors have contributed equally to this work

RECEIVED 16 April 2025
ACCEPTED 15 September 2025
PUBLISHED 31 October 2025

CITATION
Thormann M, Faltass M, Schwab R, Klebingat S and Behme D (2025) Assessing the accuracy of automated CT perfusion software in excluding acute stroke: a comparative study of two software packages. *Front. Neuroimaging* 4:1613078. doi: 10.3389/fnimg.2025.1613078

Assessing the accuracy of automated CT perfusion software in excluding acute stroke: a comparative study of two software packages

Maximilian Thormann[1,2]*, Maria Faltass[1], Roland Schwab[1], Stefan Klebingat[1†] and Daniel Behme[1,3†]

[1]Department of Neuroradiology, University Hospital Magdeburg, Magdeburg, Germany, [2]Department of Nuclear Medicine, Charité Berlin, Berlin, Germany, [3]Stimulate Research Campus Magdeburg, Magdeburg, Germany

Background: Computed tomography perfusion (CTP) is frequently used for the rapid assessment of suspected acute ischemic stroke (AIS). However, small lacunar infarcts often remain undetected by automated software, leading to false negatives and additional imaging. We compared the specificity of two commonly used CTP software packages in patients without evidence of stroke on follow-up diffusion-weighted imaging (DWI).
Methods: In this single-center retrospective study, 58 consecutive patients with suspected AIS but negative follow-up DWI–MRI were included. All patients underwent CTP on the same scanner. Perfusion data were processed using (1) syngo.via (Siemens Healthcare) with three parameter settings—A: CBV < 1.2 mL/100 mL, B: additional smoothing filter, and C: rCBF <30%—and (2) Cercare Medical Neurosuite (CMN). Software-reported ischemic core volumes were compared with the MRI findings.
Results: CMN showed the highest specificity, indicating zero infarct volume in 57/58 patients (98.3%). Conversely, all three syngo.via settings produced false-positive ischemic cores, with median volumes ranging from 21.3 mL (setting C) to 92.1 mL (setting A). Only syngo.via setting C reported zero infarct volume in some patients, yet still showed substantial overestimation (maximum 207.9 mL).
Conclusion: Our findings underscore the significant variability in the ability of different CTP software packages to reliably rule out small (lacunar) infarcts. CMN demonstrated good specificity, suggesting that dependable CTP-based stroke exclusion is achievable with advanced post-processing. High specificity could reduce reliance on follow-up MRI in acute stroke pathways if validated, thereby improving resource allocation and patient throughput.

KEYWORDS

computed tomography perfusion, acute ischemic stroke, diagnostic accuracy, lacunar infarct, neuroimaging

Introduction

Computed tomography perfusion (CTP) is frequently utilized to assess patients with clinical suspicion of acute ischemic stroke (AIS), as it offers rapid assessment of cerebral perfusion deficits and core size (Koopman et al., 2019; Kim et al., 2024; Hoving et al., 2022; Abdalkader et al., 2023). The two main aims of CTP are to identify patients with large vessel occlusions (LVOs) or distal vessel occlusions (DVOs) suitable for endovascular treatment and to assess tissue viability (Zedde et al., 2023). Perfusion parameters can influence clinical decision-making and shape prognosis. For example, Mei et al. (2025) showed that CTP results and applied thresholds influence triage decisions. Lakhani et al. (2024) demonstrated that CTP parameters predicted poor functional outcomes in AIS.

Lacunar strokes, primarily resulting from small vessel disease or atherothrombotic involvement of the parent artery that occludes a perforating branch, are not commonly addressed in this context. Perfusion changes corresponding to lacunar infarcts are often not detectable on post-processed core-penumbra maps due to smoothing by automated software, which only includes relatively large clusters of hypoperfused pixels in the map (Zedde et al., 2023). The reliability of perfusion maps is therefore low. In current practices, patients with suspected stroke but inconclusive CTP findings often undergo an additional MRI to confirm or exclude ischemia, since diffusion-weighted imaging (DWI) has excellent sensitivity for acute infarction.

However, MRI is costly and often not promptly accessible in hyperacute and acute stroke management. As a more widely available alternative, CTP performance varies significantly due to differences in patient characteristics, spatial/temporal resolution, and post-processing methods (Biesbroek et al., 2013). Notably, CTP maps have lower sensitivity for small lacunar infarcts, which can lead to false-negative results (Biesbroek et al., 2013). For better patient triage and the efficient use of healthcare resources, high specificity of CTP in detecting lacunar infarcts is warranted. Ideally, this would eliminate the need for MRI resources for patients without a detected stroke.

The purpose of this study was to compare the specificity of CTP for ischemic stroke using two commonly used perfusion software packages: syngo.via (Siemens Healthcare, Erlangen, Germany) and Cercare Medical Neurosuite (CMN, Cercare Medical, Aarhus, Denmark), a newly developed automated CTP analysis package.

Materials and methods

Study population

In this single-center retrospective analysis, we included all consecutive patients with no detectable stroke on DWI–MRI between January 2021 and November 2022. The sample size reflects all eligible patients during the study period.

The inclusion criteria were as follows:

- Clinical suspicion of acute ischemic stroke.
- Availability of a CTP dataset prior to treatment.
- Follow-up MRI with DWI sequence performed, confirming no infarct.

The exclusion criteria were as follows:

- Patients who received intravenous (IV) thrombolysis between CTP and MRI.
- Severe motion artifacts or poor scan quality on CTP or MRI.
- Failed automated perfusion post-processing.
- Evidence of chronic infarct on FLAIR/DWI in the region of perfusion abnormality.
- Vessel occlusion or stenosis on CT angiography.

The patient selection process is detailed in Figure 1.
The study was approved by the local ethics committee.

Imaging acquisition and post-processing

All CTP scans were performed on the same scanner model (Somatom Definition AS)+ (Siemens Healthcare, Germany). Imaging parameters were as follows: Kernel: T20F, contrast agent: Imeron 300 (Bracco Imaging, Germany), injection rate: 5 mL/s, and start of acquisition: 3 s after injection.

MRI examinations were performed using three scanner models with different field strengths (1.5 T systems Intera, Philips Healthcare, Best, The Netherlands or Magnetom Sola, Siemens Healthcare, Erlangen, Germany; 3.0 T system Achieva, Philips Healthcare, Best, The Netherlands). B-values were 0 and 1,000 s/mm^2 on all scanners to minimize potential scanner-related variability. The reference standard was no acute infarct on follow-up MRI (DWI ± FLAIR), with a mean delay of 68.1 ± 38.5 h, to minimize DWI-negative early scans. The risk of interval infarction or lesion evolution was minimized by the study design. A false-positive CTP core was defined on a per-patient basis as an automated CTP-identified ischemic core volume >0 with no corresponding acute infarct on follow-up DWI and FLAIR imaging. Conversely, true negatives were defined as patients with no core on CTP and no lesion on DWI.

All perfusion data were post-processed using two fully automated software packages: syngo.via CT Neuro Perfusion (version VB60A) and CMN (version CMN 15.0). All software packages apply automated registration, segmentation, and motion correction. Outputs were recorded as calculated by the software. We focused on infarction core calculations only.

syngo.via CT Neuro Perfusion employs a delay-insensitive deconvolution model and interhemispheric comparison. It determines the lesion side by identifying the highest time-to-drain, using the contralateral side as a reference for relative values. Summary maps emphasize the ischemic core and its volumes.

Adopting the approach by Koopman et al. (2019), analysis with syngo.via was performed using three different settings. In method A, maps were generated based on the software's default settings. Ischemic core volume was defined as a CBV of <1.2 mL/100 mL. In method B, an additional smoothing filter was added to the same threshold. In method C, the ischemic core was defined as a reduction in cerebral blood flow (CBF) to < 30% compared to healthy brain tissue. The standard software setting for syngo.via corresponded to setting B.

Cercare Medical Neurosuite (CMN) is a recent addition to the market. The software uses a model-based approach to quantify

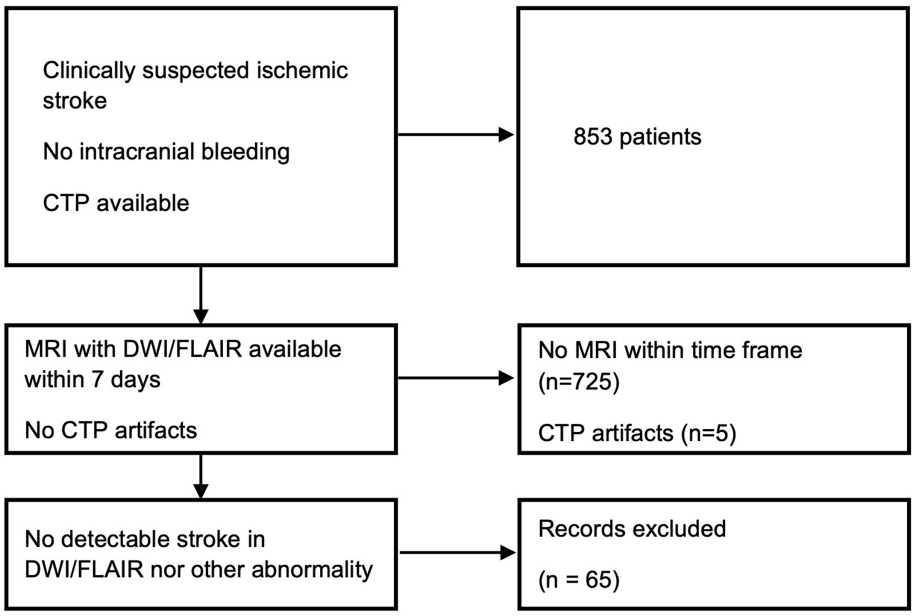

FIGURE 1
Screening and inclusion flowchart. The final dataset comprised 58 patients.

cerebral blood flow (CBF). Instead of relying solely on standard mathematical deconvolution via singular value decomposition (SVD), CMN uses a gamma distribution-based model of the tissue residue function. By capturing the natural variability in transit times through the microvasculature, CMN claims its method provides accurate measurements in low-flow regions, ensuring that ischemic tissue is properly identified and leading to a more precise depiction of the affected area.

A total of two neuroradiologists independently reviewed each software's perfusion maps to verify the presence or absence of a core lesion as defined by the software and rule out potential matches with older tissue defects. There were no disagreements.

Clinical data collection

All case-specific and demographic data were obtained from the hospital information system.

Statistical analysis

Data were presented as mean +/− standard deviation (SD), median (interquartile range (IQR)), and number (percentage), as appropriate. The Wilcoxon test for paired differences was used as a non-parametric test. The root mean square error (RMSE) and mean absolute error (MAE) were calculated to quantify the errors. Furthermore, 95% confidence intervals were estimated using bootstrap resampling (1,000 iterations) of the residuals, without assuming normality. A p-value of <0.05 was considered statistically significant.

Results

A total of 58 patients met the inclusion criteria for analysis. The average age was 69.6 years (SD 15.7 years). A total of 29 patients were male, and 29 patients were female. In addition, six patients received intravenous thrombolysis. The patients' baseline characteristics are summarized in Table 1. Extended patient details are given in Supplementary Table 1. The average time from CTP to MRI was 68.12 h (SD 38.53 h). One CTP scan could not be processed by syngo.via B and C due to unknown errors. Exemplary outputs are illustrated in Figure 2.

CMN yielded a median ischemic core volume of 0.0 mL (IQR 0.0–0.0 mL, range 0.0–4.7 mL) and a mean of 0.1 mL (SD 0.5 mL) on CTP, matching the 0 mL infarct confirmed on DWI in 57 out of the 58 cases.

By contrast, perfusion analysis with syngo.via indicated substantially higher core volumes in the patients with no infarct:

- Setting A: median 92.1 mL (IQR 66.2–117.8 mL), minimum 29.6 mL, maximum 203.1 mL; mean 94.7 ± 41.4 mL.
- Setting B: median 37.8 mL (IQR 24.6–51.5 mL), minimum 9.5 mL, maximum 93.9 mL; mean 40.8 ± 22.6 mL.
- Setting C: median 21.3 mL (IQR 6.7–40.3 mL), minimum 0.0 mL, maximum 207.9 mL; mean 39.0 ± 31.1 mL.

The results are summarized in Table 2.

Figure 3 illustrates the infarct volumes calculated by each software for all 58 patients (true infarct volume by DWI = 0 for all). Notably, syngo.via *setting C* was the only setting to report a 0 mL core volume in one patient, but it still calculated false-positive infarction volumes in most cases. Settings A and B falsely identified a non-zero infarct core in every patient within this no-stroke cohort.

Figure 4 illustrates the cumulative distribution of the ischemic core volumes calculated by each software across all included patients. CMN reported negligible infarct volumes, closely matching the DWI findings. Syngo.via overestimated infarct volumes for almost all patients. Figure 5 shows the corresponding histogram analysis comparing the calculated infarct volume distributions.

Discussion

Our study aimed to determine the specificity of two CT perfusion software packages in acute ischemic stroke. Overall, CMN demonstrated higher accuracy than syngo.via settings in correctly ruling out infarction. Our results indicate that CMN shows high specificity in excluding infarction in a DWI-negative cohort suspected of AIS, while syngo.via calculations are prone to false-positive results across all three settings, as illustrated in Figure 5. As previously shown, applying an additional smoothing filter to syngo.via improved agreement, albeit with reduced accuracy compared to CMN (Koopman et al., 2019).

DWI, while highly sensitive for infarction, can miss a small subset of strokes— reported to be up to 6.8% in the literature—particularly minor strokes and those in the posterior circulation (Edlow et al., 2017; Alkhiri et al., 2024). However, Chalela et al. found that DWI negativity was strongly associated with MRI acquisition within less than 3 h. Similarly, Simonsen et al. (2015) found that patients with DWI-negative stroke underwent MRI scanning sooner after symptom onset compared to patients with DWI-positive infarction (Chalela et al., 2007). Generally, the specificity of DWI is reported to

TABLE 1 Patients' baseline characteristics.

Characteristic	Value
Total patients	58
Male — *n* (%)	29 (50.0%)
Female — *n* (%)	29 (50.0%)
Intravenous thrombolysis	6 (10.3%)
Age, mean (SD)	69.6 (15.7)
NIHSS, median (min–max)	1 (0–10)
mRS (pre-admission), median (min–max)	0 (0–4)
mRS (at admission), median (min–max)	2 (0–5)
mRS (at discharge), median (min–max)	1 (0–4)

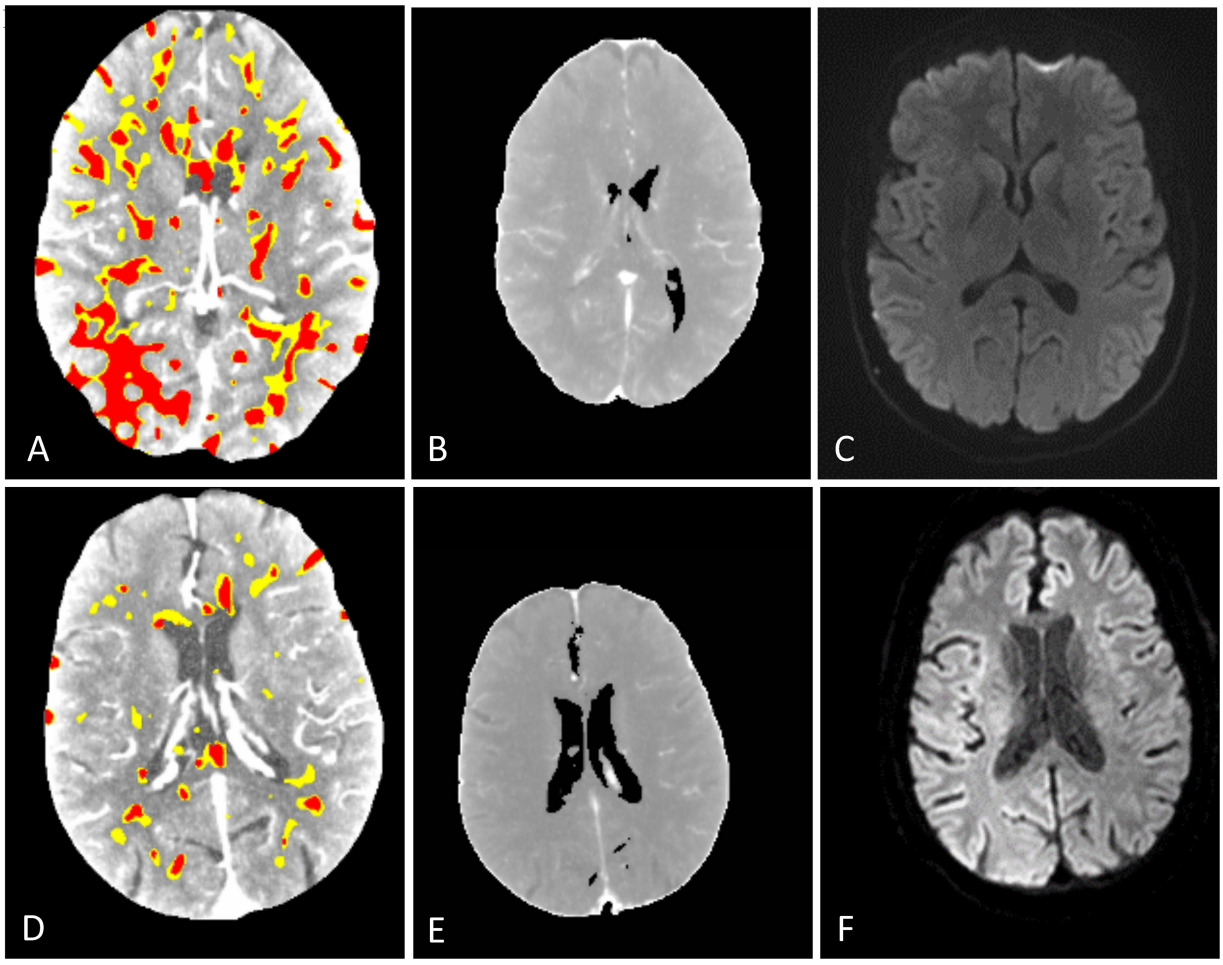

FIGURE 2
Representative CTP output maps of syngo.via **(A,D)** showing diffuse hypoperfused (yellow) and infarct core (red) areas. CMN hyperperfusion/core maps **(B,E)** show no infarct core. Corresponding MRI DWI **(C,F)** images show no signs of acute infarction

TABLE 2 Summary of ischemic core volume measurements by Cercare Medical Neurosuite (CMN) and syngo.via software settings (A, B, C) in the patients without detectable infarcts on follow-up diffusion-weighted imaging (DWI).

Parameter	Vol	CMN	syngo.via A	syngo.via B	syngo.via C
Median (IQR) infarct volume, ml	0.0 (0.0 to 0.0)	0.0 (0.0 to 0.2)	92.1 (66.2 to 117.8)	37.4 (24.6 to 51.5)	21.6 (6.7 to 40.3)
Min/Max infarct volume, ml	0.0/0.0	0.0/4.7	29.6/203.2	9.5/93.9	0.0/207.9
Mean (STD) infarct volume, ml	0.0 (0.0)	0.2 (0.7)	94.7 (41.4)	40.8 (22.6)	29.0 (32.1)
Infarct volume normal distribution (Shapiro–Wilk) (*p*-value)	1.000	0.000	0.088	0.001	0.000
Mean (SD) error, ml		0.2 (0.7)	94.7 (41.4)	40.8 (22.6)	29.0 (32.1)
Mean Absolute Error (CI 95%), ml		0.2 (0.1 to 0.4)	94.7 (84.5 to 105.7)	40.8 (35.0 to 47.1)	29.0 (22.0 to 38.3)
Root Mean Square Error (CI 95%), ml		0.7 (0.2 to 1.1)	103.3 (92.0 to 114.2)	46.5 (40.1 to 52.4)	43.1 (29.1 to 59.8)
Median (IQR) error, ml		0.0 (0.0 to 0.2)	92.1 (66.2 to 117.8)	37.4 (24.6 to 51.5)	21.6 (6.7 to 40.3)
Limits of agreement, ml		−1.1, 1.6	13.5, 176.0	−3.5, 85.1	−34.0, 92.0
Wilcoxon-Signed-Rank		715.500 (*p*-val: 0.230)	0.000 (*p*-val: 0.000)	0.000 (*p*-val: 0.000)	0.500 (*p*-val: 0.000)

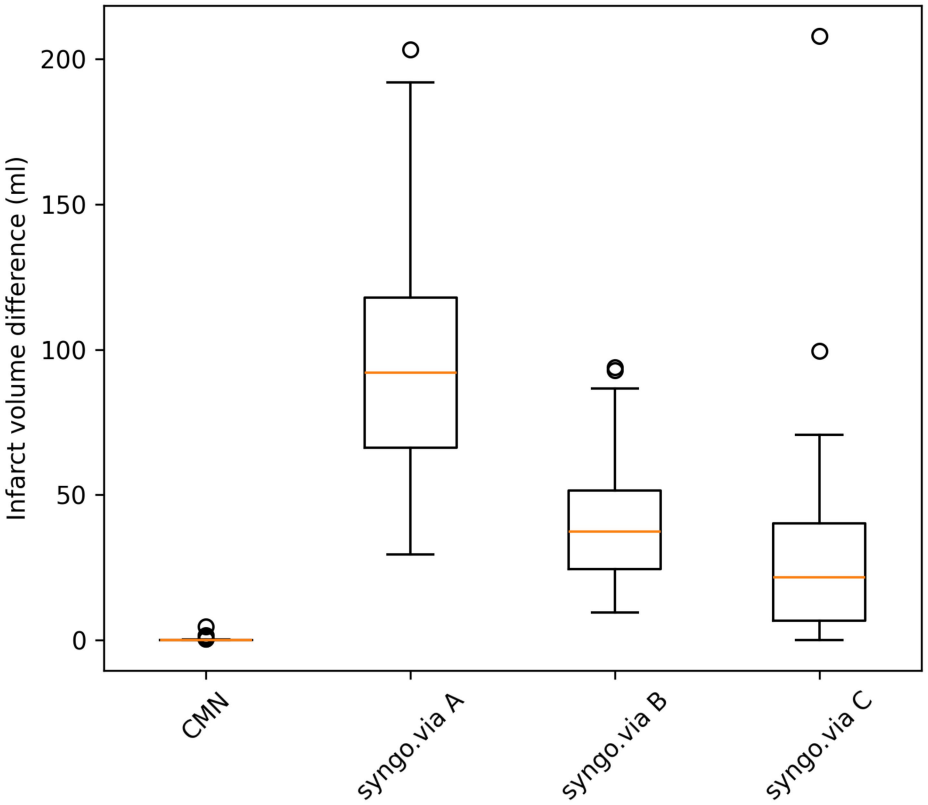

FIGURE 3
Scatter plot displaying ischemic core volumes calculated by CMN and syngo.via (settings A, B, and C) in a DWI-negative cohort (reference infarct volume = 0 mL). Note the consistent overestimation by syngo.via, potentially risking patient mis-triage. CMN estimates were zero for 57/58 patients.

be 95–100% (Abdalkader et al., 2023). We attempted to mitigate the DWI-negativity effect by performing delayed MRI (mean: 68 h after CTP). By this time, even small infarcts are typically detectable on DWI/FLAIR. However, we acknowledge that MRI is not infallible and very small or rapidly resolved infarcts (e.g., in a TIA) could have escaped our detection.

Differences in perfusion processing techniques and threshold definitions across software platforms lead to substantial variability in calculated core volumes (Katyal and Bhaskar, 2021). The specificity of various CTP software packages has been assessed in prior studies. For example, Straka et al. (2010) reported approximately 91% specificity for perfusion-diffusion mismatch detection using RAPID software. Similarly, Benson et al. (2016) found specificity up to 98.7% for lacunar infarct detection with Vitrea.

Despite these generally high specificity values, most automated solutions still struggle to *rule out* small infarcts. In one study by Lin et al. (2009) 13 of 23 infarcts missed on initial CTP were small cortical or lacunar infarcts. Consistently, Biesbroek et al. (2013) found an

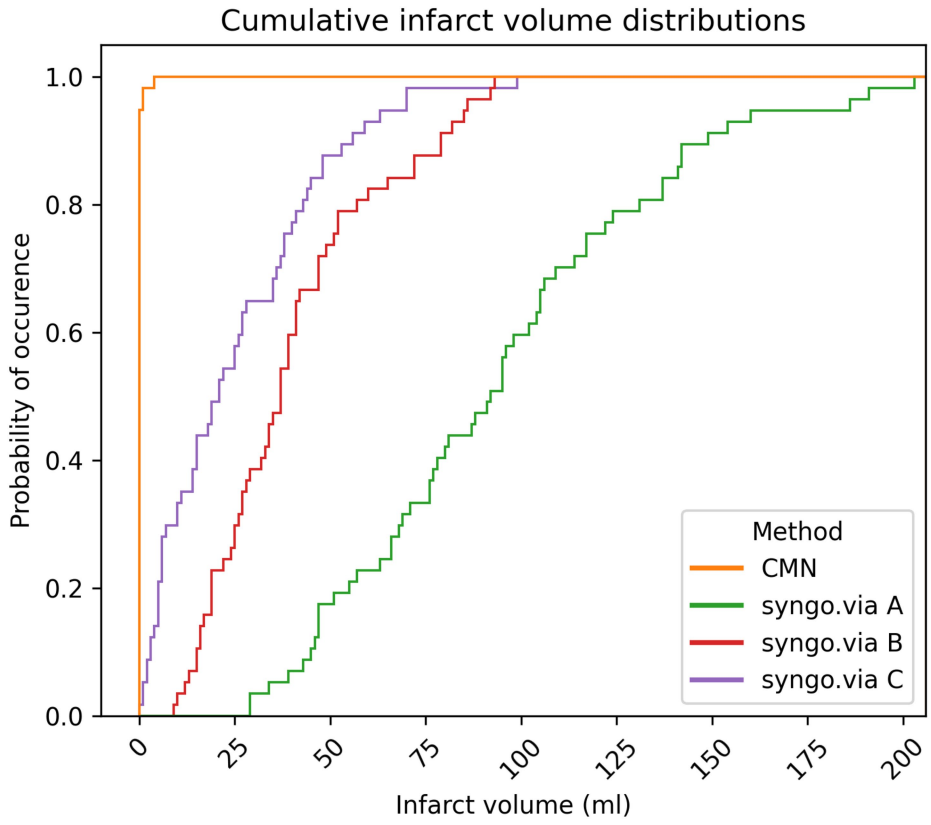

FIGURE 4
Cumulative distribution of calculated ischemic core volumes by the software packages (CMN and syngo.via settings A, B, C, n = 58), illustrating the disparity between the true negative results from CMN and the false-positive core volumes reported by syngo.via.

overall CTP specificity of ~95% for acute ischemic stroke, with nearly two-thirds of false negatives attributable to lacunar infarcts. Similarly, Eckert et al. (2011) noted that lacunar infarcts were the most frequent cause of false-negative findings on multimodal CT imaging. A 2017 meta-analysis by Shen et al. (2017) also confirmed that most stroke cases missed by CTP were of the lacunar subtype.

Lacunar strokes account for approximately 25% of ischemic strokes (Kolominsky-Rabas et al., 2001). However, perfusion deficits from lacunar infarcts are usually not apparent on standard CTP maps, especially for small deep or posterior circulation lesions (Garcia-Esperon et al., 2021). This limitation can lead to underdiagnosis of lacunar stroke on CTP alone (Arba et al., 2020). One reason for these false negatives is the coarse spatial resolution of perfusion CT, along with the tendency of automated algorithms to smooth or average values over small regions. In practice, patients presenting with a lacunar stroke syndrome but a negative CTP study typically undergo additional MRI. MRI with DWI (and FLAIR) has greater sensitivity for detecting recent small infarcts and is generally well-tolerated in patients with lacunar stroke (Wardlaw et al., 2024). However, MRI availability is limited in many stroke centers, and it is time-consuming and resource-intensive. This underscores the value of highly specific CTP software for ruling out lacunar stroke without the need for MRI.

When evaluating patients with suspected acute ischemic stroke (AIS), the ability to confidently exclude ischemia—particularly lacunar infarcts—has significant clinical value. Beyond core and penumbra volumes, recent multi-center and registry analyses indicate that rCBV thresholds and hypoperfusion intensity ratios (HIRs) stratify outcomes in LVO cohorts (Mei et al., 2025; Lakhani et al., 2024). By focusing on specificity in small infarct scenarios, our results complement these selection frameworks by reducing the risk of false positives that could affect treatment decisions.

Robust specificity allows clinicians to avoid unnecessary MRI scans, thereby reducing costs and improving workflow efficiency. In our study, CMN showed a specificity of almost 100%. The difference compared to the syngo.via results in the same cohort was remarkable (Figure 3). syngo.via, across all tested threshold settings, consistently produced false-positive infarct detections. Both syngo.via setting A and setting B wrongly detected strokes in all included patients. Only setting C, using an infarct core threshold of rCBF <30%, correctly detected a 0 mL infarct core in some patients, albeit still with a median core of 21.6 mL and a maximum infarct core detection of 207.9 mL. Conversely, CMN maintained high specificity by consistently reporting negligible core volumes in the patients without true infarcts. CMN's gamma distribution-based model is designed to capture a wider range of flow patterns in low-flow regions, potentially explaining its higher specificity in excluding small infarcts.

The limited immediate availability of MRI in many stroke centers drives reliance on CTP. Our study indicates that CTP is able to add value to NCCT in the setting of ischemic stroke. Our findings highlight the importance of accurate CTP software in the assessment of acute stroke. In clinical practice, a fast and widely available screening tool that can reliably rule out both large-vessel and small-vessel (lacunar) strokes could

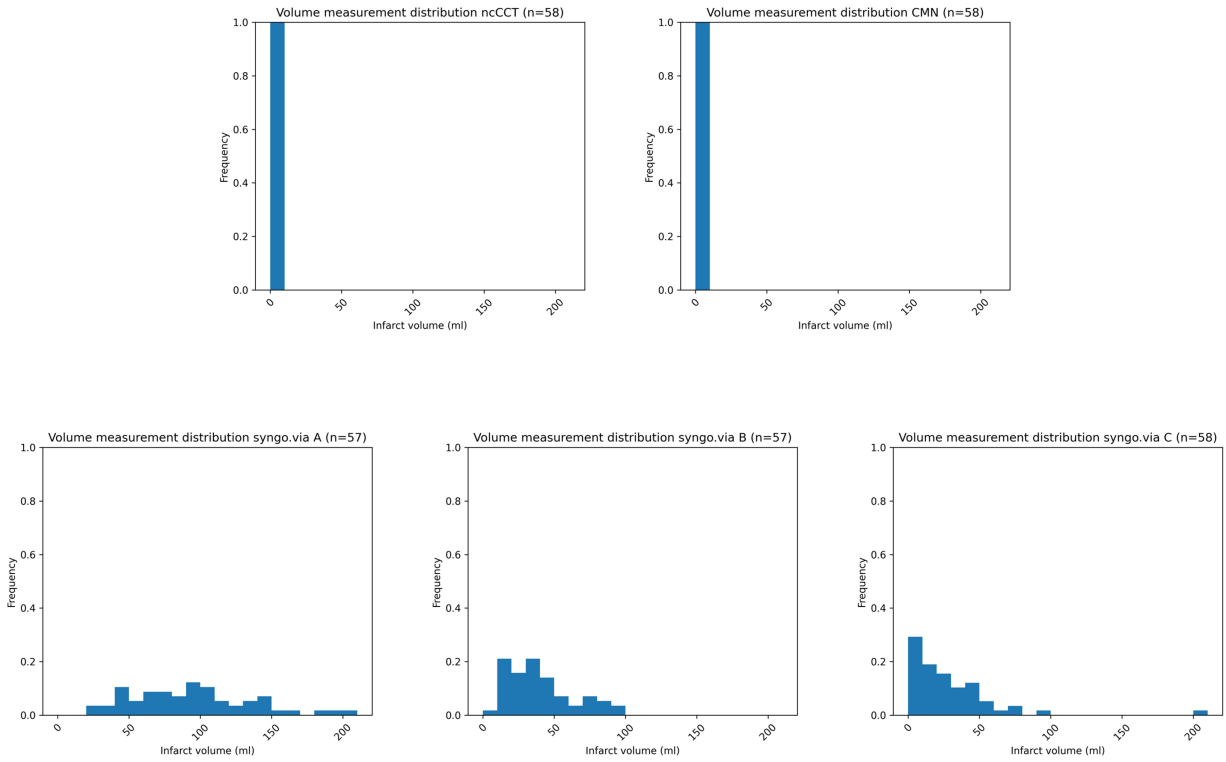

FIGURE 5
Histograms illustrating the distribution of the calculated ischemic core volumes by Cercare Medical Neurosuite (CMN) and the three parameter settings (A, B, and C) of the syngo.via software. CMN consistently shows no infarct volume, aligning with the reference findings. In contrast, the syngo.via settings (A–C) overestimate infarct volumes, showing significant false-positive rates and potentially leading to patient mis-triage.

streamline patient management. If confirmed, accurate CTP results could decrease the need for follow-up MRI in a large proportion of patients with clinical suspicion of acute stroke. Limited MRI slots could be prioritized for patients for whom advanced imaging is crucial.

While our study uniquely examines specificity in stroke-mimic patients using CMN and syngo.via, direct comparisons of CMN with established reference software packages such as RAPID or MIStar are not yet available. However, CMN's FDA clearance was based on demonstrated equivalence to RAPID's analytic approach. Our results suggest that in the specific context of excluding small infarcts, CMN performs strongly. Future studies should confirm if this finding holds true against established platforms in broader populations.

Our study has limitations that need to be acknowledged. It was retrospective in nature and restricted to DWI-negative patients, which allowed us to focus on specificity. Our study did not assess the sensitivity of the included software packages, as AIS-positive cases were excluded by design. While high specificity is desirable to reduce false-positive cores, clinical decision-making requires a balance with sensitivity. Performance in mixed cohorts should be assessed in future studies. The real-world performance of CMN in a standard cohort (with both AIS and non-AIS cases) is not addressed here and should be the subject of future studies. For CMN, we used standard settings only for post-processing. While settings in CMN can be modified, there are no published threshold sensitivity analyses for the software. An extended software-specific threshold analysis was beyond the scope of our study. Our performance estimates reflect the specific software versions tested. Should future vendor updates alter thresholds or deconvolution approaches, the generalizability of our findings may change and would warrant re-evaluation. Follow-up MRI DWI was performed on three different scanners with different field strengths. Scanner heterogeneity may affect small lesion conspicuity and permit interval changes. The average interval to follow-up MRI was long. A total of six patients received IV thrombolysis, potentially influencing the MRI results. Finally, our sample size, while focused on a specific no-stroke cohort, was modest, reflecting the number of eligible patients during the study period.

Our study underscores the value of a highly specific CTP software package for excluding acute stroke, including lacunar subtypes, thereby reducing unnecessary MRI utilization. In our cohort, CMN demonstrated a specificity of almost 100% for small strokes. Despite improvements in various commercial CTP solutions, substantial variability persists, and software selection may have a direct impact on patient triage, treatment decisions, and overall stroke care costs. Accurate CTP core quantification and reliable exclusion of small infarcts will remain critical. Future studies should test integrated pipelines that pair high-specificity core estimation with venous outflow/collateral metrics and mismatch indices, as recently suggested (Barghash et al., 2025), assessing whether combined models enhance accuracy and clinical outcome prediction.

Data availability statement

The raw data supporting the conclusions of this article will be made available by the authors, without undue reservation upon reasonable request.

Ethics statement

The studies involving humans were approved by Ethics committee University of Magdeburg, Nr 19/21. The studies were conducted in accordance with the local legislation and institutional requirements. Written informed consent for participation was not required from the participants or the participants' legal guardians/next of kin in accordance with the national legislation and institutional requirements.

Author contributions

MT: Validation, Resources, Writing – review & editing, Funding acquisition, Project administration, Formal analysis, Writing – original draft, Conceptualization, Software, Methodology, Investigation, Data curation, Supervision, Visualization. MF: Data curation, Investigation, Writing – review & editing, Writing – original draft. RS: Writing – original draft, Formal analysis, Software, Data curation, Investigation, Writing – review & editing, Methodology. SK: Formal analysis, Methodology, Conceptualization, Supervision, Data curation, Validation, Visualization, Writing – review & editing, Software, Writing – original draft, Investigation. DB: Methodology, Writing – original draft, Conceptualization, Investigation, Visualization, Supervision, Project administration, Formal analysis, Software, Writing – review & editing.

Funding

The author(s) declare that financial support was received for the research and/or publication of this article. This study was conducted using a research license granted by Cercare Medical.

Conflict of interest

The authors declare that the research was conducted in the absence of any commercial or financial relationships that could be construed as a potential conflict of interest.

Generative AI statement

The authors declare that no Gen AI was used in the creation of this manuscript.

Any alternative text (alt text) provided alongside figures in this article has been generated by Frontiers with the support of artificial intelligence and reasonable efforts have been made to ensure accuracy, including review by the authors wherever possible. If you identify any issues, please contact us.

Publisher's note

Supplementary material

The Supplementary material for this article can be found online at: https://www.frontiersin.org/articles/10.3389/fnimg.2025.1613078/full#supplementary-material

References

Abdalkader, M., Siegler, J. E., Lee, J. S., Yaghi, S., Qiu, Z., Huo, X., et al. (2023). Neuroimaging of acute ischemic stroke: multimodal imaging approach for acute endovascular therapy. *J Stroke* 25, 55–71. doi: 10.5853/JOS.2022.03286

Alkhiri, A., Alturki, F., Alansari, N. M., Almaghrabi, A. A., Alghamdi, B. A., Alamri, A. F., et al. (2024). Prognosis and distribution of ischemic stroke with negative diffusion-weighted imaging: a systematic review and meta-analysis. *Front. Neurol.* 15:1376439. doi: 10.3389/FNEUR.2024.1376439/BIBTEX

Arba, F., Mair, G., Phillips, S., Sandercock, P., and Wardlaw, J. M. (2020). Improving clinical detection of acute lacunar stroke. *Stroke* 51, 1411–1418. doi: 10.1161/STROKEAHA.119.028402

Barghash, M., Salim, H. A., Mei, J., Tantawi, M., Elnaeem, A. K., Frade, H. C., et al. (2025). Role and prognostic implications of venous outflow assessment in acute ischemic stroke. *J. Neuroimaging* 35:e13256. doi: 10.1111/JON.13256

Benson, J. C., Payabvash, S., Mortazavi, S., Zhang, L., Salazar, P., Hoffman, B., et al. (2016). CT perfusion in acute lacunar stroke: detection capabilities based on infarct location. *AJNR Am. J. Neuroradiol.* 37, 2239–2244. doi: 10.3174/AJNR.A4904

Biesbroek, J. M., Niesten, J. M., Dankbaar, J. W., Biessels, G. J., Velthuis, B. K., Reitsma, J. B., et al. (2013). Diagnostic accuracy of CT perfusion imaging for detecting acute ischemic stroke: a systematic review and meta-analysis. *Cerebrovasc. Dis.* 35, 493–501. doi: 10.1159/000350200

Chalela, J. A., Kidwell, C. S., Nentwich, L. M., Luby, M., Butman, J. A., Demchuk, A. M., et al. (2007). Magnetic resonance imaging and computed tomography in emergency assessment of patients with suspected acute stroke: a prospective comparison. *Lancet* 369, 293–298. doi: 10.1016/S0140-6736(07)60151-2

Eckert, B., Küsel, T., Leppien, A., Michels, P., Müller-Jensen, A., and Fiehler, J. (2011). Clinical outcome and imaging follow-up in acute stroke patients with normal perfusion CT and normal CT angiography. *Neuroradiology* 53, 79–88. doi: 10.1007/S00234-010-0702-9

Edlow, B. L., Hurwitz, S., and Edlow, J. A. (2017). Diagnosis of DWI-negative acute ischemic stroke. *Neurology* 89, 256–262. doi: 10.1212/WNL.0000000000004120

Garcia-Esperon, C., Visser, M., Churilov, L., Miteff, F., Bivard, A., Lillicrap, T., et al. (2021). Role of computed tomography perfusion in identification of acute lacunar stroke syndromes. *Stroke* 52, 339–343. doi: 10.1161/STROKEAHA.120.030455

Hoving, JW, Koopman, MS, Tolhuisen, ML, Voorst, Hvan, Brehm, M, Berkhemer, OA, et al., Accuracy of CT perfusion ischemic core volume and location estimation: a comparison between four ischemic core estimation approaches using syngo.Via. (2022). *PLoS One* 17:e0272276 doi: 10.1371/journal.pone.0272276 PMID: 35917382

Katyal, A., and Bhaskar, S. M. M. (2021). Value of pre-intervention CT perfusion imaging in acute ischemic stroke prognosis. *Diagn. Interv. Radiol.* 27, 774–785. doi: 10.5152/DIR.2021.20805

Kim, N., Ha, S. Y., Park, G. H., Park, J. H., Kim, D., Sunwoo, L., et al. (2024). Comparison of two automated CT perfusion software packages in patients with ischemic stroke presenting within 24 h of onset. *Front. Neurosci.* 18:1398889. doi: 10.3389/FNINS.2024.1398889

Kolominsky-Rabas, P. L., Weber, M., Gefeller, O., Neundoerfer, B., and Heuschmann, P. U. (2001). Epidemiology of ischemic stroke subtypes according to TOAST criteria: incidence, recurrence, and long-term survival in ischemic stroke subtypes: a population-based study. *Stroke* 32, 2735–2740. doi: 10.1161/HS1201.100209

Koopman, M. S., Berkhemer, O. A., Geuskens, R. R. E. G., Emmer, B. J., Van Walderveen, M. A. A., Jenniskens, S. F. M., et al. (2019). Comparison of three commonly used CT perfusion software packages in patients with acute ischemic stroke. *J Neurointerv Surg* 11, 1249–1256. doi: 10.1136/NEURINTSURG-2019-014822

Lakhani, D. A., Balar, A. B., Vagal, V., Salim, H., Mei, J., Koneru, M., et al. (2024). CT perfusion derived relative cerebral blood volume < 42% is negatively associated with poor functional outcomes at discharge in anterior circulation large vessel occlusion stroke. *J. Clin. Neurosci.* 130:130. doi: 10.1016/j.jocn.2024.110907

Lin, K., Do, K. G., Ong, P., Shapiro, M., Babb, J. S., Siller, K. A., et al. (2009). Perfusion CT improves diagnostic accuracy for hyperacute ischemic stroke in the 3-hour window: study of 100 patients with diffusion MRI confirmation. *Cerebrovasc. Dis.* 28, 72–79. doi: 10.1159/000219300

Mei, J., Salim, H. A., Lakhani, D. A., Balar, A., Vagal, V., Koneru, M., et al. (2025). Prolonged venous transit as a superior predictor of functional outcomes in successfully reperfused large vessel occlusions: comparative analysis with cerebral blood volume index and hypoperfusion intensity ratio. *J. Am. Heart Assoc.* 14:39924. doi: 10.1161/JAHA.124.039924/ASSET/95F678DC-06CB-45AF-98D0-30CCFA7DA54C/ASSETS/GRAPHIC/JAH310808-FIG-0002.PNG

Shen, J., Li, X., Li, Y., and Wu, B. (2017). Comparative accuracy of CT perfusion in diagnosing acute ischemic stroke: a systematic review of 27 trials. *PLoS One* 12:e0176622. doi: 10.1371/JOURNAL.PONE.0176622

Simonsen, C. Z., Madsen, M. H., Schmitz, M. L., Mikkelsen, I. K., Fisher, M., and Andersen, G. (2015). Sensitivity of diffusion-and perfusion-weighted imaging for diagnosing acute ischemic stroke is 97.5%. *Stroke* 46, 98–101. doi: 10.1161/STROKEAHA.114.007107

Straka, M., Albers, G. W., and Bammer, R. (2010). Real-time diffusion-perfusion mismatch analysis in acute stroke. *J. Magn. Reson. Imaging* 32, 1024–1037. doi: 10.1002/JMRI.22338

Wardlaw, J. M., Chabriat, H., de Leeuw, F. E., Debette, S., Dichgans, M., Doubal, F., et al. (2024). European stroke organisation (ESO) guideline on cerebral small vessel disease, part 2, lacunar ischaemic stroke. *Eur. Stroke J.* 9, 5–68. doi: 10.1177/23969873231219416

Zedde, M., Napoli, M., Grisendi, I., Assenza, F., Moratti, C., Valzania, F., et al. (2023). CT perfusion in lacunar stroke: a systematic review. *Diagnostics* 13:1564. doi: 10.3390/diagnostics13091564

Frontiers in Medicine

Translating medical research and innovation into improved patient care

A multidisciplinary journal which advances our medical knowledge. It supports the translation of scientific advances into new therapies and diagnostic tools that will improve patient care.

Discover the latest Research Topics

See more →

Frontiers

Avenue du Tribunal-Fédéral 34
1005 Lausanne, Switzerland
frontiersin.org

Contact us

+41 (0)21 510 17 00
frontiersin.org/about/contact